NUMERICAL SIMULATION FOR POLYMER BLEND USING OPENFOAM

Adila Aida Binti Azahar

Submitted in accordance with the requirements
for the degree of Doctor of Philosophy

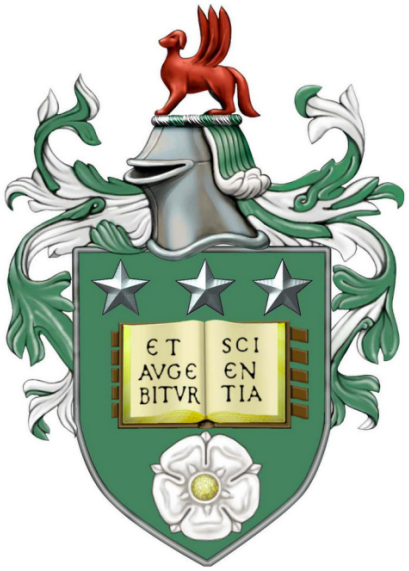

The University of Leeds

Faculty of Engineering and
Physical Sciences
School of Computing

August 2020

Intellectual Property

The candidate confirms that the work submitted is his/her own, except where work which has formed part of a jointly authored publication has been included. The contribution of the candidate and the other authors to this work has been explicitly indicated below. The candidates confirms that appropriate credit has been given where reference has been made to the work of others.

Some parts of the work in this thesis have been published in the following article.

- A. A. Azahar, O. G. Harlen, and M. A. Walkley. Modelling contraction flows of bi-disperse polymer blends using the Rolie-Poly and Rolie-Double-Poly equations. *Korea-Australia Rheology Journal*, 31(4), 203-209, 2019. https://doi.org/10.1007/s13367-019-0021-6.

The above publication is primarily the work of the candidate.

Acknowledgements

First and foremost, thank you to Allah S.W.T, the Almighty God for giving me the strength and patience to finally complete this PhD thesis. The experience that I gained during this PhD journey is priceless and unforgettable. I would like to express my deepest gratitude to my supervisors, Dr. Mark Walkley and Dr. Oliver Harlen for always supporting me throughout this PhD journey over the past four years. I appreciate their encouragement, motivation, patience, assistance and guidance during my PhD studies and I am indebted to my supervisors and grateful for having such supportive supervisors that I could not ask for more.

I would like also to thank my parents, Azahar bin Ahmad and Rosilah binti Mohamad and my brothers, Arman Hadi, Amirul Asyraf, and Aidil Danial for continuously praying for my success and not to forget their motivation, emotional and spiritual supports endlessly that keeps me going stronger and make this thesis becomes surreal.

For my best friend, Nur Soffiah, thank you very much for your time and always be with me through thick and thin. You are indeed a true friend. A special thanks go to my friend in the UK for allowing me to be a part of their family while studying abroad. To Hidayah Badya, Yati, Ana Masara, Rosmaliza, Nurhafizah, Nurul Ain, Najua, Hidayah Aalam, Mashael Al-Johani, Nik and Hanis, the memories that we shared throughout this studies is unforgettable.

I am so thankful to my financial sponsor, the Minister of Education Malaysia and Universiti Sains Malaysia for granting me the scholarship to pursue my PhD studies in the UK. Finally, for those involved directly or indirectly throughout this PhD work, thank you very much. This thesis is not possible to be completed without the supports from everyone.

Abstract

This thesis models the flow behaviour of polymer blends using a new constitutive model derived from tube theory and double reptation called the bidisperse Rolie-Double-Poly equation (Boudara et al., *Journal of Rheology*, 63, 71 (2019)) in two different geometrical flows using finite-volume based OpenFOAM software. This model incorporates the molecular mechanisms of reptation motion, thermal and convective constraint release, chain stretch and accounts for the interactions between polymer chain of different lengths in a polydisperse melt. In this thesis, the model was implemented within OpenFOAM using the RheoTool library. This implementation was validated against published results for the transient extensional viscosity.

Numerical simulations for the bidisperse Rolie-Double-Poly were performed for two different flow geometries used to characterise extension flow properties, the hyperbolic contraction and a cross-slot with both sharp and hyperbolic corners. For each flow the effects of varying the geometric details, the flow-rate and composition of the blend are examined. In addition, we compare the results to those obtained from the equivalent multimode Rolie-Poly model that is based on linear superposition to distinguish the coupling effect predicts by the Rolie-Double-Poly model.

The study of the cross-slot flow is extended to investigate the symmetry-breaking bifurcation for a single mode Rolie-Poly and bidisperse Rolie-Double-Poly model. We find that the bifurcation to a steady asymmetric flow depends on the ratio of the stretch to orientation relaxation times and is not observed when this ratio is small even for high Deborah numbers in the Rolie-Poly model, but is observed in blends described by the Rolie-Double-Poly model.

Contents

List of Figures

List of Tables

Nomenclature

Abbreviation

$\mu-$PIV	Micron resolution particle image velocimetry
ADI	Alternating Direction Implicit
ARC	Advanced Research Computing
BSD	Both-Side-Diffusion
BTCS	Backward-Time Central-Space
CCR	Convective constraint release
CFD	Computational Fluid Dynamic
CONDOR	COnstrained, Non-linear, Direct, parallel Optimization using trust Region method for high-computing load function
CSF	Cross-Slot Flow
CUBISTA	Convergent and Universally Bounded Interpolation Scheme for the Treatment of Advection
DEVSS	Discrete elastic-viscous split-stress
FDM	Finite Difference Method
FEM	Finite Element Method
FENE	Finite-Extensible Nonlinear Elastic

FIB	Flow Induced Birefringence
FTCS	Forward-Time Central-Space
FVM	Finite Volume Method
GLaMM	Graham-Likhman-and-Milner-McLeish
GNF	Generalised Newtonian Fluid
HCF	Hyperbolic Contraction Flow
HRSs	High resolution schemes
HWNP	High Weissenberg Number Problem
LHS	Left Hand Side
LPTT	Linear Phan-Thien and Tanner
LVE	Linear Viscoelastic Envelope
mRP	multimode Rolie-Poly
OpenFOAM	Open Source Field Operation And Manipulation
PDEs	Partial Differential Equations
PISO	Pressure-Implicit with Splitting of Operators
PS2	Polystyrene
PSD	Principal Stress Difference
PTT	Phan-Thien and Tanner
RDP	Rolie-Double-Poly
RHS	Right Hand Side
Rolie-Poly	Rouse Linear Entangled Polymer
RP	Rolie-Poly

SIMPLE	Semi-Implicit Method for Pressure-Linked Equation
SIMPLEC	Semi-Implicit Method for Pressure-Linked Equation-Consistent
UCM	upper-convected Maxwell
VFR	Volumetric flow-rate

Others

$\Delta\pi$	Principal Stress Difference
Δn	birefringence
ΔP	Pressure drop
Δt	time-step
Δx, Δy	spatial-step in x and y direction respectively
$\mathbf{D}$	rate of deformation tensor
$\mathbf{u}$	fluid velocity vector
$\mathbf{u}^{'}$	velocity correction vector
$\mathbf{u}^{*}$	predicted velocity vector
B	Beginning of contraction
C	stress optical coefficient
D	channel full-depth, channel width in cross-slot definition in Chapter 8
d	channel half-depth
E	Elasticity number, End of contraction
h	length scale of the body
$H(x)$	The height of the channel at x position

H_0	The height of the upstream channel for half hyperbolic contraction geometry
H_1	The height of the downstream channel for half hyperbolic contraction geometry
H_d	The height of the downstream channel for full hyperbolic contraction geometry
H_u	The height of the upstream channel for full hyperbolic contraction geometry
np	number of processors
p	pressure
$p^{'}$	pressure correction
p^{*}	known pressure field from previous time iteration
Q	Flow-rate
R	Contraction ratio
t	time
tr	trace
W	Within of contraction (half-way)
$\mathbf{A}$	Conformation tensor
$\mathbf{I}$	Identity tensor
$\mathbf{K}$	Global stiffness matrix
$\mathbf{M}$	Galerkin Mass matrix
$\underline{\mathbf{f}}$	Known vector
De	Deborah number

De_{cr}	critical Deborah number
DQ	bifurcation parameter
N	Number of nodes
R	Radius of rounded corner
Re	Reynolds number
T_{LL}	Trace for a conformation tensor field $\mathbf{A}$ for $L-L$ chain interaction
T_{LS}	Trace for a conformation tensor field $\mathbf{A}$ for $L-S$ chain interaction
U	Fluid velocity
Wi	Weissenberg number
Wi_0	Local Weissenberg number
Wi_R	Weissenberg number based on stretch relaxation time
$\mathrm{Wi}_{eD,i}$	Weissenberg number based on reptation relaxation time in extensional flow for i chain
$\mathrm{Wi}_{eR,i}$	Weissenberg number based on stretch relaxation time in extensional flow for i chain
$\mathrm{Wi}_{sD,i}$	Weissenberg number based on reptation relaxation time in shear flow for i chain
$\mathrm{Wi}_{sR,i}$	Weissenberg number based on stretch relaxation time in shear flow for i chain
Z	entanglement number

Symbols

β	viscosity ratio
β^*	convective constraint release coefficient

β_{th}	thermal constraint release
δ	fitting parameter
$\dot{\gamma}$	shear-rate
$\dot{\varepsilon}$	extension-rate
η	fluid viscosity
η^{+}	transient shear viscosity
$\eta_E(t)$, η_E^{+}	transient extensional viscosity
η_P	polymeric viscosity
η_S	solvent viscosity
η_t	total viscosity
γ	shear strain
λ	relaxation time
$\lambda^{'}$	reciprocal averaged relaxation time for short and long chain based on long-short chain interaction
λ^{**}	relaxation time ratio
λ^{*}	reciprocal averaged reptation relaxation time for short and long chain based on long-long chain interaction
λ_D^{*}	reciprocal averaged reptation relaxation time for short and long chains
λ_R^{*}	reciprocal averaged stretch relaxation time for short and long chains
$\lambda_{R,L}^{eff}$	effective stretch relaxation time
$\lambda_{D,L}$	reptation relaxation time for long chain
$\lambda_{D,S}$	reptation relaxation time for short chain
λ_D	reptation relaxation time

$\lambda_{R,L}$	stretch relaxation time for long chain
$\lambda_{R,S}$	stretch relaxation time for short chain
λ_R	stretch relaxation time
ν	kinematic viscosity
ϕ_L	volume fraction of long chain
ϕ_S	volume fraction of short chain
$\boldsymbol{\tau}$	total stress tensor
$\boldsymbol{\tau}_P$	polymeric stress tensor
$\boldsymbol{\tau}_S$	solvent stress tensor
ρ	Fluid density
σ	chain stretch
σ_{max}	maximum chain stretch
τ_{xy}	shear stress
ε	extension strain
$f_E(\phi)$	finite extensibility function
G	elastic modulus
$G(t)$	relaxation modulus
G_N^0	experimental plateau modulus
N_1	First normal stress difference
$\overset{\nabla}{\boldsymbol{\tau}}$	upper-convected time derivative of a tensor field $\boldsymbol{\tau}$
$\overset{\nabla}{\boldsymbol{A}}$	upper-convected time derivative of a tensor field $\boldsymbol{A}$
L	Long, contraction length
S	Short

Chapter 1

Introduction

This chapter outlines the aims, objectives and background study of this work. It first explains rheology, viscoelastic flow, the governing equation and the constitutive laws that are used in this study. The relevant different numerical approaches are described before a summary of the work in viscoelastic flow using both numerical simulation and experimental studies is presented. This chapter ends with an overview of the whole thesis in Section 1.9.

1.1 Background study

Research on fluid behaviour has received particular attention for many years. One can define fluid as any substance that deforms continuously when subjected to a stress regardless of the amount of stress imposed. There are various properties of fluids that can distinguish one fluid from another. One of the physical properties is its viscosity. Newton's law of viscosity states that the ratio between the shear stress and shear-rate of a fluid is constant for a given pressure and temperature. This ratio defines the viscosity or the coefficient of viscosity. Fluids that obey this law are known as Newtonian fluids. This covers many common fluids including air and water. However, there are many other fluids whose stress does not behave as stated in Newton's law, such as molten polymers or polymeric solutions. These kinds of fluid are classified as non-Newtonian.

Modelling a polymer melt flow in industrial polymer processing is crucial so that the polymeric flow behaviour can be predicted and thus the flow can be controlled. This is to ensure the stability and predictability of the flow and to avoid the wastage of polymeric

fluid during the processing. While research on Newtonian fluids has been explored in depth over many years, researchers also extended their interest to investigate the behaviour of non-Newtonian fluid over the last decades. This includes the development of constitutive models that describe polymeric fluids of different types that include the Oldroyd-B [103], Pom-Pom [94], Phan-Thien-Tanner (PTT) [131], Giesekus [56], Finite-Extensible Nonlinear Elastic (FENE) type [20] models and recently proposed constitutive models describing entangled linear polymers, Rolie-Poly [85] and Rolie-Double-Poly [23] to the extent where comparison between the theoretical model and experimental work using real fluids are possible (see for example [89], [129], [134]).

Numerical simulation techniques play a vital role for flow prediction and are able to produce comparable results to experimental findings. The development of numerical approaches from different techniques (e.g. finite volume, finite element and finite difference approaches) have progressed to the point where three-dimensional time-dependent simulations are possible. Both in-house academic codes for viscoelastic fluid (see for example, [16], [64], [130], [137]) and commercial packages, including OpenFOAM [138], ANSYS polyFlow [1], and COMSOL [3] for instance, are now available to simulate and predict the non-Newtonian phenomena for a wide range of different fluids.

Modelling the flow using Computational Fluid Dynamics, (CFD), open-source packages such as OpenFOAM, a free finite-volume based solver [75], [138], facilitates the study of fluid flow and has widely been used in academic and industrial work to solve various applications and model real world problems (see for example, [27], [61], [68] and [81]). Due to its increasing popularity in the last decade, a number of researchers and practitioners deploy this powerful CFD simulator and additional toolboxes have been proposed for specific applications (e.g. [72], [113]) to extend the capability of the software. The extended toolbox which is relevant to the problem solved in this work is called RheoTool [113] which provides the framework for solvers for rheological problems.

Experimental and industrial polymer processing generally requires a confined geometry. Much research has been conducted to study the behaviour of the various constitutive models in different configurations including slit geometry [87], [89], [134], cross-slot geometry [87], [89], and contraction geometry [99], [100], [113]. This include the 4:1 planar contraction that

has been used here as a benchmark flow problem to test the proposed solvers in order to validate the numerical predictions [54], [113]. Previous studies exposed that this geometry produces a corner vortex and the size of the lip vortex is even more pronounced as the Deborah number increases. This is due to the impact of the intense extensional response of the viscoelastic fluid as a consequence of the abrupt geometrical changes at the re-entrant contraction. During shear and extensional deformation, the material functions (e.g. the viscosity and the stress) are important components to look at in order to understand the behaviour of the fluid. For instance, in shear deformation studies, we can observe the relationship between the shear-rate and shear-stress by plotting the flow curve. This exhibits the shear viscosity prediction at different regimes which illustrates different phenomena. For extensional deformation, the relationship between extension-rate and first normal stress difference also could be observed. However, the measurement of the extensional viscosity is difficult.

The converging flow geometry was initially proposed by Cogswell during 1978 [30]. In an abrupt contraction flow, the formation of lip vortices near the re-entrant contraction and fluid vortices at the sharp corner upstream are observed. However, the smooth hyperbolic contraction configuration with sufficiently long contraction length able to avoid and reduce this problem which is observed in the benchmark 4:1 abrupt contraction flow even for low Weissenberg number for Oldroyd-B, PTT and Giesekus-Leonov fluid as reported in Debbaut et al. [41]. Researchers, [127], [128], [139] then developed the hyperbolic contraction as a measurement tool to capture the extensional properties of the fluid. The configuration was able to generate a uniform extension-rate within the contracting region which facilitates the measurement of the extensional viscosity, one of the important material functions required to understand the behavior of the viscoelastic fluid. This configuration produces complex flow containing both shear and extensional response.

The cross-slot flow geometry is a more recent configuration for understanding the extensional response of viscoelastic fluid. In contrast to the hyperbolic contraction flow, this device generates a two-dimensional flow with a stagnation point at the centre. The change in the flow direction creates high extensional response along the centre-line that accumulate significant macromolecular strain for a sufficiently fast flow. The cross-slot with sharp or

rounded corners is considered for the study of extensional response of different viscoelastic constitutive models including PTT, UCM, Oldroyd-B, FENE type and Rolie-Poly equations (see reference [26], [35], [65], [67], [87], [123] for example).

1.2 Research aims and objectives

The aim of this thesis is to model the behaviour of a latest viscoelastic constitutive law that describes a bidisperse polymer blend, Rolie-Double-Poly (RDP) model [23], derived from tube theory [45], using the OpenFOAM CFD software. In particular, the hyperbolic contraction geometry and cross-slot with hyperbolic corner are considered where some of the physical effects of the geometries are varied to observe the response of the fluid behaviour to the changes. This includes observing the extensional response and the molecular stretch of the polymer when the polymeric fluid experiences the converging and stretching flow and changes in the flow direction for the two-dimensional cross-slot flow. The coupling effect of the polymer chains in the new (bidisperse) model are compared with linear superposition of a non-coupled Rolie-Poly model with the equivalent polydispersity. The summary of the objectives for this work is outlined as follows

- To implement the Rolie-Poly model in OpenFOAM and validate the behaviour of the model in a benchmark flow and against published results before extending the model to the hyperbolic contraction geometry.
- To implement the RDP model in OpenFOAM and validate the rheological behaviour with published results available from the literature.
- To develop the equivalent multimode Rolie-Poly (mRP) model based on the linear viscoelastic limit of the coupled RDP constitutive laws so that the coupling effect between the polymer chains can be observed through comparison of transient shear viscosity and transient elongational viscosity.
- To investigate the RDP model in the hyperbolic contraction geometry with different physical dimensions and the coupling effect on the extensional response and molecular stretch of the polymer. Further to that, the effect of varying the blend composition and channel depth in a three-dimensional geometry are considered.

- To investigate the behaviour of the RDP model in a cross-slot geometry with hyperbolic corner for different physical dimensions. The behaviour of the RDP model and the effect of blend composition are discussed.

- To investigate bifurcation of the flow with the single mode Rolie-Poly and RDP model in the cross-slot flow to find the critical Deborah number where the onset of bifurcation of the flow is observed.

In the next sections, the rheological behaviour and viscoelastic flow for the relevant constitutive models used in this work are described.

1.3 Rheology and viscoelastic flow

Rheology is defined as the study of deformation and flow of matter under the effect of an applied force. More precisely, it is the study of suspensions, foods, polymer, slurries, emulsion, paste and other compounds in order to understand the behaviour of the flow [95]. Rheological studies can characterise the behaviour of fluid with dimensionless numbers, the most common being are the Deborah number (De) and Weissenberg number (Wi). The Deborah number is defined as the ratio of the relaxation time, λ, to the characteristics time of the deformation process being observed,

$$\mathrm{De} = \frac{\lambda}{T}.$$

Lower De flows exhibit liquid-like behaviour while higher De demonstrates solid-like characteristics. When De=0, it represents a Newtonian fluid. In contrast, when De=∞, an elastic solid is expected. Weissenberg number can be defined as the ratio of the elastic forces to the viscous forces which can be defined as the ratio of elastic forces to viscous forces. As reported in Poole [114], the Weissenberg number in a steady simple shear flow for the simplest differential model describing the viscoelastic fluid, the upper-convected Maxwell due to the Oldroyd model can be written as

$$\mathrm{Wi} = \frac{\text{Elastic forces}}{\text{Viscous forces}} = \frac{\tau_{xx} - \tau_{xy}}{\tau_{xy}} = \frac{2\eta\lambda\dot{\gamma}^2}{\eta\lambda\dot{\gamma}} = 2\lambda\dot{\gamma}$$

where $\dot{\gamma}$ is a shear-rate, η is the viscosity and $N_1 = \tau_{xx} - \tau_{yy}$ is a first normal stress difference. Note that, the characteristic shear-rate, $\dot{\gamma}$ can be defined as the ratio of the fluid velocity, U to the length scale of the body, h denoted as U/h.

The primary dimensionless number that classifies the behaviour of a Newtonian fluid is called the Reynolds number, (Re). This dimensionless number is defined as the ratio between the fluid inertia and the viscous force, defined as follows

$$\mathrm{Re} = \frac{\text{Inertial force}}{\text{Viscous force}} = \frac{\rho U h}{\eta_S},$$

where ρ is fluid density and η_S is the dynamic viscosity of the fluid. The Elasticity number, E, of the polymeric fluid can be defined as the ratio of the Weissenberg number to the Reynolds number, where the viscosity is the contribution from both Newtonian and polymeric parts, $\eta_t = \eta_S + \eta_P$. The Elasticity number can be written as

$$E = \frac{\mathrm{Wi}}{\mathrm{Re}} = \frac{\lambda \eta_t}{\rho h^2}.$$

Molten polymer exhibits viscoelastic behaviour which possess both viscous and elastic aspects that is describable by Newtonian viscous liquid and Hookean elastic solid response. Viscoelastic behaviour can be illustrated using a dashpot and a spring, where the dashpot models the viscosity while the spring models the elasticity. When a weight is applied on the spring and removed, it deforms immediately and gives the illustration of the elastic deformation. In contrast, none of the viscous deformation is recovered when a weight is removed from the dashpot model. When the spring and dashpot are placed in series, we get a viscoelastic liquid-like behaviour which, on a short time scale, behaves as an elastic spring but, on a longer time scale, the motion is resisted by the dashpot. The constitutive equation for a spring and dashpot are defined as

$$\tau = G\gamma \qquad \text{and} \qquad \tau = \eta\dot{\gamma}$$

respectively where τ is the stress for the spring and dashpot, G is the elastic modulus, γ is the shear strain. The concept of combining a spring with dashpot in series motivated James

Clerk Maxwell in 1867 to introduce the first constitutive equation to describe the flow of viscoelastic fluid known as the Maxwell model [93]. The illustration of the Maxwell element is presented from the last subfigure in Figure 1.1.

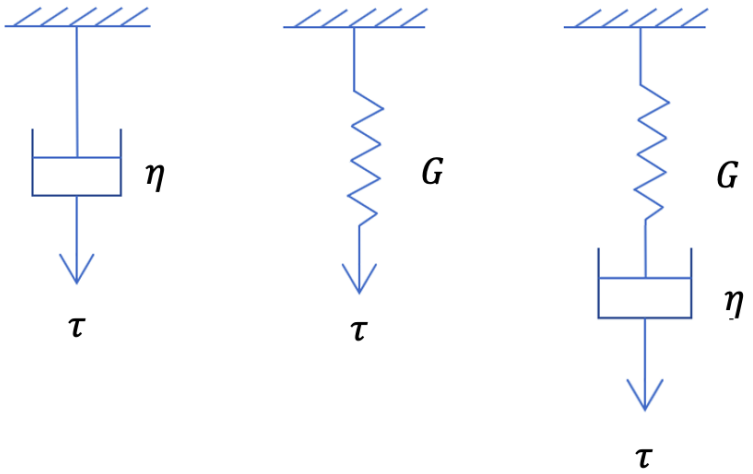

Figure 1.1: The dashpot (left), spring (centre) and Maxwell model (right).

Prior to the constitutive equation for a spring and dashpot defined above, the differential equation for the rate of change with respect to time for a single Maxwell element is the summation of the shear rates of the two constitutive equations. The Maxwell element is then governed by

$$\frac{d\gamma}{dt} = \frac{1}{G}\frac{d\tau}{dt} + \frac{\tau}{\eta},$$

and that can be written in the form of relaxation time, λ as

$$\dot{\tau} + \frac{\tau}{\lambda} = G\dot{\gamma},$$

given $\eta = G\lambda$. Following the development of this model, more modern, complex and sophisticated models, which incorporate the relevant physical mechanisms to make a better prediction of the behaviour of real fluid, are developed. Chronologically, the upper-convected Maxwell (UCM) model was next. Oldroyd [103] then extended the UCM model to a set of rheological equations of state, including the Oldroyd-B model, which can also be derived from the kinetic theory of a suspension of elastic dumbbells in a Newtonian fluid. This model however does not consider a shear-thinning fluid. Graham and Likhtman [57] developed a constitutive law that describes a shear-thinning fluid based on molecular and tube

theory [45] called Rolie-Poly model. This model is similar to the Oldroyd-B model with an additional term describing the stretch response of the fluid and the convective constraint release of the entangled chain. Boudara et al. [23] extended this to a new constitutive law called the Rolie-Double-Poly which describes a polydisperse polymer for shear-thinning fluid. The details of these models are described in the next section. Other constitutive laws derived from different theories, including kinetic, network, molecular and tube theory, are PTT [111], [131], FENE-P and FENE-CR [20], Giesekus [56], Pom-Pom [94] and extended Pom-Pom [136]. A brief description of these models is summarised in Table 1.1.

Table 1.1: The summary of the viscoelastic constitutive model

Constitutive model	Theory	Description	Reference
Maxwell	Spring and dashpot (series)	Linear unentangled polymer	Maxwell [93]
Generalised Upper Convected Maxwell (UCM)	Maxwell element with upper convected derivative	Linear unentangled polymer	Oldroyd [103]
Oldroyd-B	1) Structural theory 2) Can be derived using kinetic theory (Dumbbells model)	Linear polymer	Oldroyd [103]
PTT	Network theory	Linear entangled polymer	Thien and Tanner [111]
FENE (Finite extensibility)	Kinetic theory	Unentangled polymer	Bird et al. [20]
FENE-P	Kinetic theory Closure approximation	Unentangled polymer	Bird et al. [20]
FENE-CR	Kinetic theory Closure approximation	Unentangled polymer	Chilcott and Rallison [29]
Giesekus quadratic stress term	Kinetic theory	Linear polymer	Giesekus [56]
Pom-Pom	Tube theory	Branched entangled polymer	McLeish and Larson [94]
Extended Pom-Pom	Tube theory	Branched entangled polymer	Verbeteen et al. [136]

Constitutive model	Theory	Description	Reference
Graham-Likhman-and-Milner-McLeish (GLaMM)	Tube theory	Monodisperse linear entangled polymer	Graham et al. [57]
Rolie-Poly	Reptation/ Tube theory	Monodisperse linear entangled polymer	Likhtman and Graham [85]
Rolie-Double-Poly	Tube, double reptation theory	Polydisperse linear entangled polymer	Boudara et al. [23]

1.4 Governing equations and viscoelastic constitutive laws

The physics behind rheology are described by the conservation laws of mass, momentum and energy and the constitutive laws that relate the stress to deformation for a particular fluid model chosen under a specific flow condition. A set of governing equation for isothermal, incompressible, single-phase viscoelastic fluid consists of mass and momentum conservation defined as follows

$$\nabla \cdot \mathbf{u} = 0, \tag{1.1}$$

$$\rho\left(\frac{\partial \mathbf{u}}{\partial t} + \mathbf{u} \cdot \nabla \mathbf{u}\right) = -\nabla p + \nabla \cdot \boldsymbol{\tau}, \tag{1.2}$$

where ρ is a fluid density, $\mathbf{u}$ is the velocity vector, t is time, p is a pressure, $\mathbf{I}$ is the identity tensor, $\boldsymbol{\tau}$ is the total stress tensor, that can be decomposed into $\boldsymbol{\tau} = \boldsymbol{\tau}_S + \boldsymbol{\tau}_P$ where $\boldsymbol{\tau}_S = 2\eta_S \mathbf{D}$ is the solvent stress contribution, η_S is the solvent viscosity, $\mathbf{D}$ is the rate of deformation tensor, defined as $\mathbf{D} = \frac{1}{2}(\nabla \mathbf{u} + \nabla \mathbf{u}^T)$, and $\boldsymbol{\tau}_P$ is polymeric stress.

1.4.1 Oldroyd-B constitutive equation

The Oldroyd-B viscoelastic model [103] is a standard model used to observe the behaviour of a polymeric solution under general flow conditions. The equations can be derived from the kinetic theory of an elastic dumbbell made up of two beads with interconnected spring which is immersed in a Newtonian solvent, as described by Bird et al. [19]. The total viscosity in this model is the summation of the contribution from the polymer and the Newtonian solvent. This model is used as the initial study to illustrate the mathematical models for the polymer flows before more advanced models are considered. The constitutive laws for Oldroyd-B model in terms of conformation tensor, $\mathbf{A}$, can be mathematically described as follows,

$$\underbrace{\frac{\partial \mathbf{A}}{\partial t} + \mathbf{u} \cdot \nabla \mathbf{A}}_{\text{Time derivative}} - \underbrace{[\nabla \mathbf{u} \cdot \mathbf{A} + \mathbf{A} \cdot (\nabla \mathbf{u})^T]}_{\text{Deformation tensor}} = \underbrace{-\frac{1}{\lambda_D}(\mathbf{A} - \mathbf{I})}_{\text{Orientation}}, \tag{1.3}$$

where λ_D is the orientation relaxation time. Let $\overset{\nabla}{\boldsymbol{A}}$ be the upper-convected time derivative of a conformation tensor defined as,

$$\overset{\nabla}{\boldsymbol{A}} = \frac{\partial \mathbf{A}}{\partial t} + \mathbf{u} \cdot \nabla \mathbf{A} - [\nabla \mathbf{u} \cdot \mathbf{A} + \mathbf{A} \cdot (\nabla \mathbf{u})^T],$$

then, in a compact form, equation (1.3) can be reduced to

$$\overset{\nabla}{\boldsymbol{A}} = -\frac{1}{\lambda_D}(\mathbf{A} - \mathbf{I}). \tag{1.4}$$

Extension to the Oldroyd-B model with an additional term that describes the polymer stretch using tube theory, are next presented.

1.4.2 Rolie-Poly constitutive equation

The Rouse linear entangled polymer (Rolie-Poly) constitutive model [85], derived based on tube theory, is the simplest version of the sophisticated constitutive models known as the GLaMM model [57]. This model is derived using the tube theory concept of de Gennes [39], [45] and incorporates several mechanisms including reptation, convective constraint

release [91], and chain stretch.

The linear entangled polymer melts can be visualised as being analogous to a plate of spaghetti where each of the spaghetti strand represents a polymer chain.

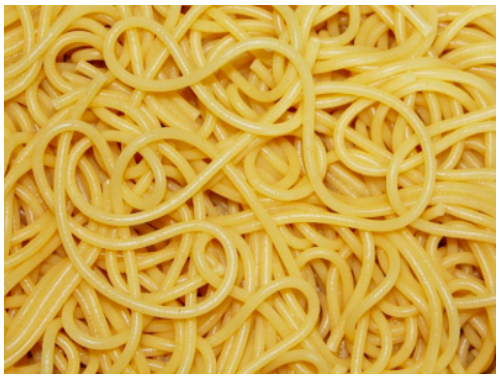

Figure 1.2: The representation of the entangled polymer chain as a plate of spaghetti [92].

Each of the chains is constrained by a "tube" that is made up by the neighbouring chains. The movement of the chain inside the tube incorporates reptation and the retraction of the chain back and forth along the tube contour. We can visualise the motion of the single chain in a tube from the following figure.

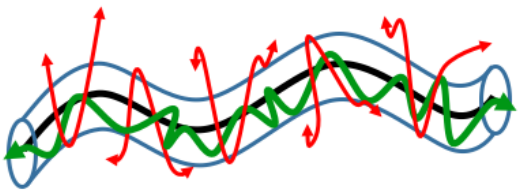

Figure 1.3: The tube theory representation for a single polymer chain where the tube (represented by a blue tube) is determined by neighbouring chains (illustrated by the red chains).

The reptation motion can be explained by reptation theory that describes the motion of the chains along the tube which allows the chains to diffuse out of the tube. This is depicted in Figure 1.4.

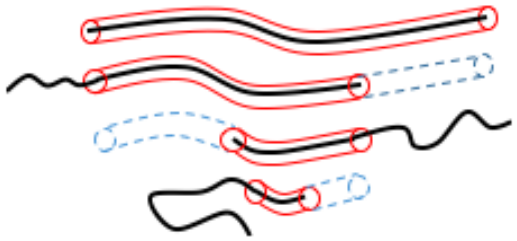

Figure 1.4: The reptation motion of the polymer chain (from top to bottom) illustrating the chain to diffuse out of the tube releasing the entanglement made by surrounding polymer chains.

There are two relaxation modes involved in the constitutive equation that describes the Rolie-Poly model. These are the reptation relaxation time, denoted by λ_D, that governs the orientation and motion of the chain along the tube. The other relaxation mode is stretch relaxation time, λ_R, that governs the spring-like fluctuation of the chain length. In physical terms, the reptation relaxation time should be greater than the stretch relaxation time, i.e. $\lambda_D > \lambda_R$ with the limit $\lambda_D \to \lambda_R$ representing in an approximate way unentangled chains. The constitutive laws for Rolie-Poly model in terms of the conformation tensor can be mathematically described as follows

$$\overset{\nabla}{\boldsymbol{A}} = \underbrace{-\frac{1}{\lambda_D}(\mathbf{A}-\mathbf{I})}_{\text{Reptation}} \underbrace{-\frac{2}{\lambda_R}(1-\sigma^{-1})[\mathbf{A}+\beta^*\sigma^{2\delta}(\mathbf{A}-\mathbf{I})]}_{\text{Retraction and CCR}}, \tag{1.5}$$

where $\mathbf{A}$ is a stress conformation tensor such that $\boldsymbol{\tau}_p = G\mathbf{A}$ and G is the elastic modulus. Here, β^* is convective constraint release, (CCR) coefficient, δ is the fitting parameter, set to $\delta = -0.5$, and $\sigma = \sqrt{\frac{tr(\mathbf{A})}{3}}$ is the molecular stretch. The rheological behaviour of the Rolie-Poly model under shear deformation can be visualised in Figure 1.5 and 1.6.

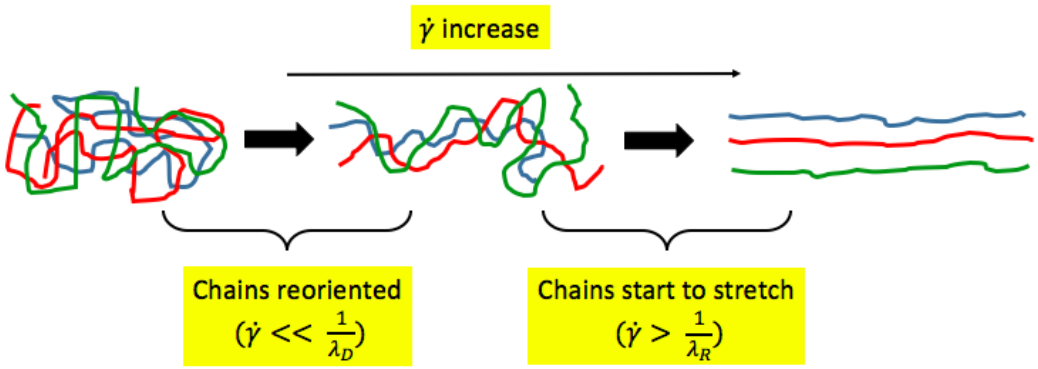

Figure 1.5: Polymer chain alignment.

Figure 1.5 depicts the transformation of the polymer melt from chain entanglement until the chains get stretched under the shear deformation. In this case, three different colours are used to distinguish the different polymer chains which are entangled to each other. Each of the polymer chains will start to move along the tube contour by retraction motion and release the constraint made by other polymer chains as the imposed shear-rate is sufficiently high the chains are reoriented. For higher shear-rates, the polymer chains start to align and the emergence of polymer stretch can be observed when $\dot{\gamma}\lambda_R > 1$. The importance of looking at the polymer stretch is that the onset of crystallisation of the polymer is observed when the chain is stretched beyond the yield point as noted in [37]. Crystallisation however, is governed by the orientation and stretch of the polymer molecules and we do not include and discuss the crystallisation problem further in this work.

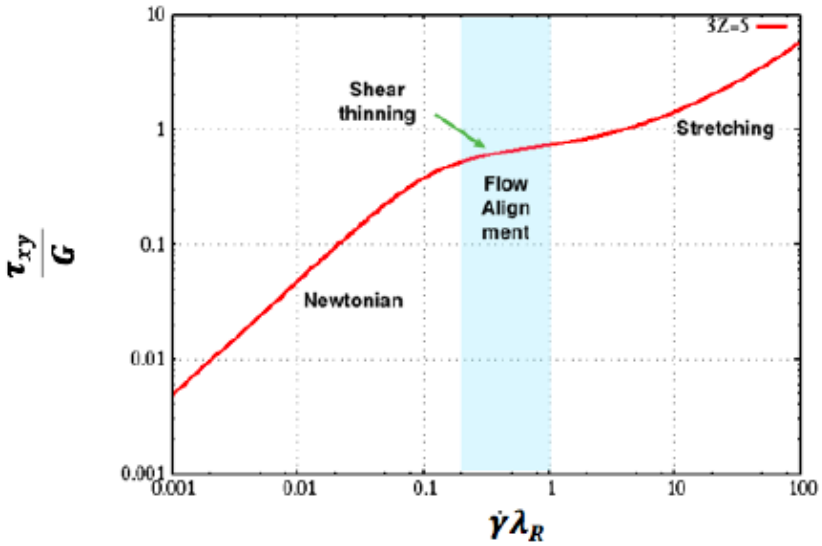

Figure 1.6: The flow curve for Rolie-Poly model when $3Z = 5$ where Z is the entanglement number [83] defined by $Z = \frac{\lambda_D}{3\lambda_R}$.

Figure 1.6 shows the flow curve of the shear deformation for shear stress as a function of Weissenberg number based on stretch relaxation, $\mathrm{Wi}_R = \dot{\gamma}\lambda_R$. The flow curve divides the rheological behaviour of the model in three different regimes: slow, intermediate and fast regime. Under slow deformation, that is when $\dot{\gamma}\lambda_D < 1$, the Rolie-Poly fluid is approximately Newtonian and the viscosity shown by the slope of the graph is constant. In the intermediate regime, when $\dot{\gamma}\lambda_D \approx 1$ and $\dot{\gamma}\lambda_R < 1$, the viscosity of the fluid is decreasing. This indicates the shear thinning region where the polymer chains start to align. The polymer chain starts to stretch in the fast flow regime when $\dot{\gamma}\lambda_R > 1$.

1.4.3 Multimode model

Modelling the fluid behaviour using a single mode model is inadequate to represent real polymer behaviour. This is because most viscoelastic materials are polydisperse and consist of different molecular weights of polymer chain, where the relaxation times for both reptation and stretch are not the same for different molecular weights. Due to this fact, the prediction of a real fluid using a single mode is insufficient to make a good numerical prediction. Thus, more modes (termed multimode) are required to ensure a better prediction can be obtained that is consistent to experimental results. The total polymeric stress, $\boldsymbol{\tau}_P$ of the multimode model is defined as

$$\boldsymbol{\tau}_P = \sum_{M=1}^{n} \boldsymbol{\tau}_M. \tag{1.6}$$

where $\boldsymbol{\tau}_M$ is the polymeric stress of mode M and n is the total number of modes. Note that, each mode has a different elastic modulus and relaxation time.

Based on literature survey, many research works have been carried out using the multimode model for various viscoelastic constitutive laws. These include the enhancement of the numerical method proposed, [34] to simulation studies in polymer processing, for instance, extrusion process, die design, [136], planar contraction flows [129], planar elongational flow [42].

However, the multimode model is based on linear superposition in which the total polymeric stress of the model is simply the summation of the individual polymeric stress contribution of different modes. In this model the chains of the viscoelastic material are treated independently and neglects the interaction between the different polymer chains of the material. However, different species involved in a polydisperse polymer melt will interact with each other (which from now on will be termed as the coupling between different species) and the stress of the coupling between the polymer species contributes to the total polymeric stress, which will then contribute to the prediction of the velocity and pressure of the flow when the governing equation is solved numerically.

In recent years, a new constitutive equation which describes the non-linear rheological response for a bidisperse blend of long and short linear polymers was introduced theoretically by Read et al., [119]. This model extends the previous work of Likhtman and Graham, [85] for linear polymer melts to the full-chain bidisperse blend of linear material. In this work, we use the simplified version the tube model which was recently introduced by Boudara et al. [23]. This is based on the Rolie-Poly model [85] and double reptation theory [44] where the model is generalised to describe the polydisperse blend type of polymer. In this work, the entanglement of two chain species from the same polymer material having the same plateau modulus is considered.

In contrast to the linear superposition multimode model, the new constitutive model for the binary blend includes the coupling between the short and long chain where the polymeric stress for each coupled mode depends on the interaction of the chains. The total polymeric

stress contribution of the coupled blend model now depends on more modes defining the coupling between different polymer species. The mathematical model is presented in the next subsection for the case of the two chain species.

1.4.4 Rolie-Double-Poly - Mathematical model for bidisperse blends.

The bidisperse blends described by the RDP model [23] incorporates the interaction between two different polymer chain lengths, the short (S) and the long (L). The chain entanglements are termed $L-L$, $S-S$, $L-S$ and $S-L$ interactions. The entanglements with chains from the same species are described using a Rolie-Poly constitutive model while the entanglements of the chain from different species are defined in slightly different way that takes account of the release of constraints through thermal and convective constraint release. The total polymeric stress tensor, $\boldsymbol{\tau}_P$ is written as

$$\boldsymbol{\tau}_P = G_N^0[\phi_S f_E(\sigma_S)\mathbf{A}_S + \phi_L f_E(\sigma_L)\mathbf{A}_L], \tag{1.7}$$

where G_N^0 is the experimental plateau modulus, ϕ_S and ϕ_L are the volume fraction of the short and long chain respectively. The elastic modulus, G, for the short and long chains are defined as $G_L = G_N^0\phi_L$ and $G_S = G_N^0\phi_S$. The conformation tensors for short and long chains are denoted by $\mathbf{A}_S$ and $\mathbf{A}_L$ respectively. These tensors represent the mean conformation tensor of the entanglement for short and long chain species. The short and long chain stretch are represented by σ_S and σ_L and the finite extensibility function, $f_E(\sigma)$ has the following definition

$$\sigma_S = \sqrt{\frac{tr(\mathbf{A}_S)}{3}}, \qquad \sigma_L = \sqrt{\frac{tr(\mathbf{A}_L)}{3}}, \qquad f_E(\sigma) = \frac{1-\sigma_{max}^{-2}}{1-\sigma^2\sigma_{max}^{-2}}.$$

Here, σ_{max} is the maximum chain stretch proportion in extension. In this work, we negelect the finite extensibility of the polymer chain and set $f_E(\sigma) = 1.0$. The two mean conformation tensors, $\mathbf{A}_S$ and $\mathbf{A}_L$ are defined as

$$\mathbf{A}_S = \phi_S \mathbf{A}_{SS} + \phi_L \mathbf{A}_{SL}, \tag{1.8}$$

$$\mathbf{A}_L = \phi_S \mathbf{A}_{LS} + \phi_L \mathbf{A}_{LL}, \tag{1.9}$$

This leads to the introduction of four conformation tensors which incorporate the interaction for short and long chains with the different type of entanglement effects, $\mathbf{A}_{MN}$ where MN represents the chain species, L or S. The time derivative of the conformation tensors for $L-L$ and $S-S$ are described similar to the conventional way of defining the single mode Rolie-Poly as in equation (1.5). The four-mode coupled polymer blend constitutive equations are defined as

$$\overset{\nabla}{\boldsymbol{A}}_{SS} = \underbrace{-\frac{1+\beta_{th}}{\lambda_{D,S}}(\mathbf{A}_{SS}-\mathbf{I})}_{\text{Reptation and CR}} \underbrace{-\frac{2}{\lambda_{R,S}}(1-\sigma_S^{-1})f_E(\sigma_S)[\mathbf{A}_{SS}+\beta^*\sigma_S^{2\delta}(\mathbf{A}_{SS}-\mathbf{I})]}_{\text{Retraction and CCR}}, \tag{1.10}$$

$$\overset{\nabla}{\boldsymbol{A}}_{LL} = -\frac{1+\beta_{th}}{\lambda_{D,L}}(\mathbf{A}_{LL}-\mathbf{I}) - \frac{2}{\lambda_{R,L}}(1-\sigma_L^{-1})f_E(\sigma_L)[\mathbf{A}_{LL}+\beta^*\sigma_L^{2\delta}(\mathbf{A}_{LL}-\mathbf{I})], \tag{1.11}$$

$$\overset{\nabla}{\boldsymbol{A}}_{SL} = \underbrace{-\frac{1}{\lambda_{D,S}}(\mathbf{A}_{SL}-\mathbf{I})}_{\text{Reptation}} \underbrace{-\frac{2}{\lambda_{R,S}}(1-\sigma_S^{-1})f_E(\sigma_S)\mathbf{A}_{SL}}_{\text{Retraction}} \underbrace{-(\mathbf{A}_{SL}-\mathbf{I})\left[\frac{\beta_{th}}{\lambda_{D,L}}+\frac{2\beta^*}{\lambda_{R,L}}(1-\sigma_L^{-1})f_E(\sigma_L)\sigma_S^{2\delta}\right]}_{\text{CR and CCR}}, \tag{1.12}$$

$$\overset{\nabla}{\boldsymbol{A}}_{LS} = -\frac{1}{\lambda_{D,L}}(\mathbf{A}_{LS}-\mathbf{I}) - \frac{2}{\lambda_{R,L}}(1-\sigma_L^{-1})f_E(\sigma_L)\mathbf{A}_{LS} - (\mathbf{A}_{LS}-\mathbf{I})\left[\frac{\beta_{th}}{\lambda_{D,S}}+\frac{2\beta^*}{\lambda_{R,S}}(1-\sigma_S^{-1})f_E(\sigma_S)\sigma_L^{2\delta}\right]. \tag{1.13}$$

While equation (1.10) and (1.11) are defined in a similar way to "classic" Rolie-Poly, the other two equations consider the double reptation theory [44]. Note that the thermal constraint release is set to $\beta_{th} = 1.0$ to be consistent with the double reptation theory. This theory describes the constraint release of two entanglements where each of the entanglement

involves the interaction of two chains of different species. Based on tube theory [45], constraints from different chains can be depicted as two nested tubes of different sizes referred to as the *thin tube* and *fat tube* introduced by Dealy et al. [40]. The *thin tube* is made up of the entanglements of the test chain with of all other chains. On the other hand, the *fat tube* describes the constraints from the long chain only and the environment explored by long chains over times when the short chains diffuse away. The illustration of the following figures facilitate the description of the complex polymer blends of short and long chains.

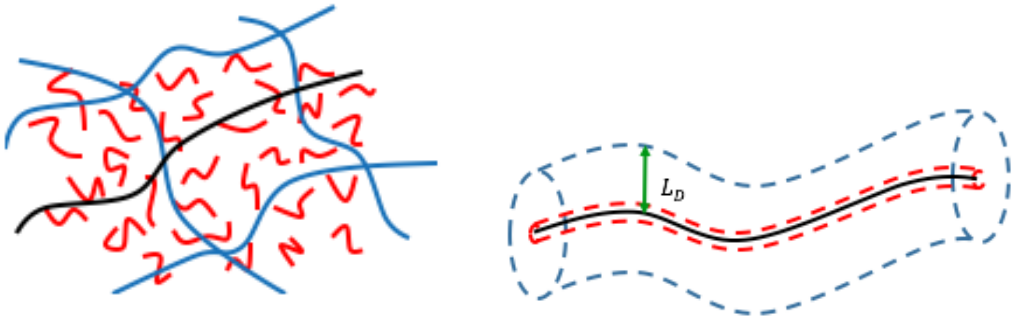

Figure 1.7: The interaction between the chain with different chain lengths of the same material is presented from the left hand side (LHS) figure and the representation of the double reptation tube in the right hand side (RHS) figure.

The interaction between the chains and double reptation theory via tube theory can be visualized in Figure 1.7. From the left of Figure 1.7, the short chains are represented by red line curve while the blue and black line curve are for long chains and test chain respectively. Transforming the interactions to a tube, leads to double reptation theory which can be illustrated from the RHS figure of Figure 1.7. This theory describes the constraint release in a simple way of two different entanglements. Two tubes of different diameters, i.e. *thin* and *fat tube* are used to describe the entanglements where L_D from the figure is denoted as the distance between the long chain species.

1.4.4.1 Enhanced stretch relaxation time

One phenomena resulting from the coupling between modes in the RDP model is the enhanced stretch relaxation time, which was observed experimentally in bimodal blends of linear monodisperse polyisoprene [9]. This set of experiments considered the influence cause of dilution of the long component on the transient elongational viscosity and found that

elongational hardening occurred at lower elongational rates with increasing dilution which suggests that dilution increases the effective stretch relaxation time of the polymer chains. In a short letter, Auhl et al. [9], describe the effective stretch relaxation time by considering two different polymer chain lengths of the same material. For a sufficiently slow elongational flow (i.e. $\dot{\varepsilon}\lambda_{R,L} < 1$), the effective stretch relaxation time is visualised based on the deformation and the reorientation of the long test chain in a thin tube where the increase in the length of the long test chain in a thin tube along the fat tube contour is entirely imposed by the constraints made by the fat tube. The effective stretch relaxation time of the long chains in the bidisperse blend model is given by

$$\lambda_{R,L}^{eff} = \frac{\lambda_{R,L}}{\phi_L},$$

where $\lambda_{R,L}$, is the stretch relaxation time for the long chain and ϕ_L is the long chain concentration in the blend. Further explanation regarding this relaxation mode is available in letter [9]. In the next section, the linear viscoelastic limit for the Rolie-Poly model is described.

1.5 Linear viscoelastic envelope

The linear viscoelastic envelope, (LVE) for Rolie-Poly model is derived by considering the relaxation from an infinitesimal step-strain. We consider a fluid between two plates as depicted in Figure 1.8. The top plate is moved a small distance, instantaneously and a very small strain ε is suddenly imposed. The subsequent relaxation of the shear stress $\tau_{xy}(t)$ is given by $\tau_{xy}(t) = \varepsilon G(t)$ where $G(t)$ is the relaxation modulus.

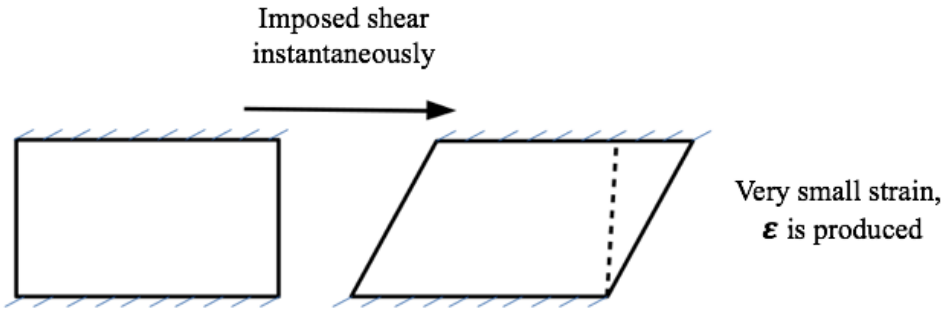

Figure 1.8: The infinitesimal strain resulted from deformation.

In the LVE, the transient uniaxial extensional viscosity is calculated using

$$\eta_E(t) = 3\int_0^t G(t)dt. \tag{1.14}$$

The LVE derivation for single and multimode Rolie-Poly, (mRP) model is presented in the following section while the derivation for the RDP, and equivalent mRP, are provided in Chapter 5.

1.5.1 LVE for single and mRP models

The relaxation modulus, $G(t)$ can be calculated by setting the flow terms to zero. The LVE can only be captured in a Newtonian regime and thus no molecular stretch is observable. Therefore, the stretch in equation (1.5) is set to one. The single mode Oldroyd-B model and the Rolie-Poly model from equation (1.5) is then reduces to the same equation,

$$\frac{d\mathbf{A}}{dt} = -\frac{1}{\lambda_D}(\mathbf{A} - \mathbf{I}), \tag{1.15}$$

where the total polymeric stress can be defined as $\boldsymbol{\tau}_P = G(\mathbf{A} - \mathbf{I})$ and G is the elastic modulus of a single mode. Considering the shear case, where a single stress component, A_{xy} is non-zero, the above equation is reduced to

$$\frac{dA_{xy}}{dt} = -\frac{1}{\lambda_D}(A_{xy}). \tag{1.16}$$

Solving the equation by separation of variable with initial condition $A_{xy} = \varepsilon$ at $t = 0$, the polymeric stress tensor for a single mode is $\tau_{xy} = \varepsilon G(t)$ where $G(t) = Ge^{-t/\lambda_D}$. For the case of the mRP model, the total polymeric shear stress is given by

$$\tau_{xy} = \varepsilon \sum_{i=1}^{N} G_i e^{(-t/\lambda_{D,i})},$$

where $G(t) = \sum_{i=1}^{N} G_i e^{(-t/\lambda_{D,i})}$, N is the total number of modes, i is the i^{th} mode. The transient elongational viscosity can then be calculated using equation (1.14) to give

$$\begin{aligned}\eta_E(t) &= 3\int_0^t G(t)dt \\ &= 3\sum_{i=1}^{N} G_i\lambda_{D,i}(1-e^{(-t/\lambda_{D,i})}) \\ &= 3\sum_{i=1}^{N} \eta_i(1-e^{(-t/\lambda_{D,i})}),\end{aligned} \tag{1.17}$$

where $\eta_i = G_i\lambda_{D,i}$ is the polymeric viscosity for mode i.

1.6 Flow Induced Birefringence

The stress with a flowing polymer melt can be investigated through a phenomenon called flow induced birefringence (FIB). This phenomenon is due to the anisotropic stress in flowing polymer melt producing an anisotropy of the refractive index. FIB is a convenient technique used in experimental work to measure the stress distribution in a molten polymer flow.

FIB is used extensively in research area of polymer melt flow to compare the prediction made by a numerical approximation to experimental results (see for example [70], [87], [130], [129]). The stress-optical equation defines the relationship between birefringence and stress anisotropy as being directly proportional and for a two-dimensional flow can be mathematically presented as

$$\Delta n = C\Delta\pi = \sqrt{(\pi_{xx}-\pi_{yy})^2 + 4\pi_{xy}^2}, \tag{1.18}$$

where Δn is the birefringence, $\Delta\pi$ denotes the Principal Stress Difference (PSD) with $\boldsymbol{\pi} = -\nabla p + \eta_S(\nabla\mathbf{u} + [\nabla\mathbf{u})^T] + \boldsymbol{\tau}_P$ and C is the stress-optical coefficient. In this work, we will implement the birefringence described in equation (1.18) to visualise the stress distribution of the flowing polymer melt.

1.7 Numerical techniques

In this section, a review of numerical techniques will be presented with a focus on the relevant techniques used in this work.

Mathematical models based on PDEs are widely used in scientific disciplines and arise in different fields to describe phenomena related to physics, engineering and applied mathematics. These include the Navier-Stokes equation in fluid dynamic problem, wave propagation, Maxwell's equation of electromagnetism, quantum mechanics, heat conduction and diffusion and general relativity. Some simple PDE problems can be solved analytically, however, solving a complex PDE analytically is difficult and sometimes impossible. Thus, it is common to obtain an approximate solution of the PDE problem using different numerical approaches. These include the Finite Difference Method (FDM), Finite Element Method (FEM) and Finite Volume Method (FVM). In this thesis, we use the FDM and FEM to solve one- and two-dimensional channel flow problems and comparison is made with the available analytical solutions. We mainly use the OpenFOAM CFD software that used a FVM spatial discretisation to solve more complex geometrical flow. There are other techniques of discretisation that are not considered in this thesis including spectral methods [80], collocation methods, discontinuous Galerkin methods [122] and boundary element method [24]. We present a general explanation for the methods we use in the following section and the details of the application of the methods to viscoelastic flow is described in a later chapter.

1.7.1 Temporal discretisation

Temporal discretisation is necessary if we consider a transient or time-dependent problem. A time step, Δt is defined between two time levels. The temporal discretisation can be divided into explicit and implicit methods. The forward Euler method is classified as an explicit method. This method is easy in implementation and computationally cheap where the value at the next time level can be computed explicitly given the known values at the current level. However, it is generally only conditionally stable and restricted to a certain limit for the time step. The possible value of time step is satisfied by the following inequality equation: $\Delta t < \frac{(\Delta x)^2}{2}$ for second order parabolic equation.

On the other hand, the implicit methods, for example backward Euler and Crank-Nicolson, require more time in computation as compared to forward Euler since a linear system needs to be solved for every time step. However, the stability of the implicit methods is unconditional and allows the choice of a larger time step as compared to explicit

methods.

1.7.2 Spatial discretisation

The first step of the spatial discretisation is generally to divide the spatial domain into a finite set of sub-domains without overlapping. The number of sub-domain that has been used influences the numerical accuracy. In general, a finer size of the sub-domain gives a closer approximate solution to the true PDE solution. Three different spatial dicretization (i.e. FDM, FVM and FEM) techniques are presented in the following sections. Solving the PDE requires the following steps: a) grid generation, b) discretisation and c) solution of equations; where the details of each step are different from one approach to another.

1.7.2.1 Finite difference method

FDM is the oldest and simplest method used to obtain approximate solutions of differential equations. This method has been widely used as a numerical tool in many research areas because it is intuitive and simple in its implementation. This method works well for two-dimensional regions where the boundaries are parallel to the coordinate axes. The drawback of this method is that it is only easily applicable for regular spatial domains.

The spatial discretisation of this method works by discretizing the domain into a set of nodes. For use of notation, will shall assume a uniform spatial length scale as Δx. For instance, consider the interval $[x_A, x_B]$, then the spatial length scale for a set of N modes can be defined as

$$\Delta x = \frac{x_B - x_A}{N-1},$$

where N is the number of discretisation points (nodes). The value of x at a specific point after discretisation is given by $x_i = x_A + i\Delta x$ where $i = 0, 1, 2..., N-1$. From the interval, x_A is the left boundary and x_B is the right boundary. Field variables $\mathbf{u}$ are evaluated at nodes is denoted by $u_i = u(x_i)$. A numerical approximation to the spatial derivative is obtained from a Taylor's series expansion as follows

$$u^n_{i+1} = u^n_i + \Delta x \frac{\partial u^n_i}{\partial x} + \frac{\Delta x^2}{2!}\frac{\partial^2 u^n_i}{\partial x^2} + \frac{\Delta x^3}{3!}\frac{\partial^3 u^n_i}{\partial x^3} + \frac{\Delta x^4}{4!}\frac{\partial^4 u^n_i}{\partial x^4} + ..., \tag{1.19}$$

$$u_{i-1}^n = u_i^n - \Delta x \frac{\partial u_i^n}{\partial x} + \frac{\Delta x^2}{2!}\frac{\partial^2 u_i^n}{\partial x^2} - \frac{\Delta x^3}{3!}\frac{\partial^3 u_i^n}{\partial x^3} + \frac{\Delta x^4}{4!}\frac{\partial^4 u_i^n}{\partial x^4} + ... \tag{1.20}$$

Based on the Taylor's series expansion, the first and second derivative in space for the central difference approximation can be obtained by adding or subtracting equation (1.19) and (1.20) and making the first or second derivative as the subject. These yield the central difference approximations of the following derivatives: The first derivative in space is:

$$\frac{\partial u(x_i)}{\partial x} \approx \frac{u_{i+1}^n - u_{i-1}^n}{2\Delta x} + \mathcal{O}(\Delta x^2), \tag{1.21}$$

and the second derivative in space:

$$\frac{\partial^2 u(x_i)}{\partial x^2} \approx \frac{u_{i+1}^n - 2u_i^n + u_{i-1}^n}{\Delta x^2} + \mathcal{O}(\Delta x^2), \tag{1.22}$$

where subscript i denotes the spatial location and superscript n denotes current time level.

1.7.2.2 Finite element method

FEM is an established numerical procedure and has been widely used in various applications of engineering, physics and computational science. Due to a more general approach to spatial discretisation, this method is used extensively to solve problems with complex geometrical structure.

FEM works by first dividing the domain into a number of non-overlapping sub-domain. Each sub-domain is termed an element. The advantage of this method is that this discretisation does not need to be structured, thus making it flexible to discretize complex spatial domain. In a one-dimensional FEM, the spatial length scale for each element is defined as

$$\Delta x_i = x_{i+1} - x_i,$$

where $i = 0, 1, ..., N-1$, N is the number of nodes, $N-1$ is the total number of element and x_{i+1} and x_i are two neighbouring nodes.

This method relies on the weak formulation of the PDE, produced by transforming the

strong formulation through mutiplying with a weight function and integrating over spatial domain.

Integrating the weak formulation over the elements forms a system of linear equation that can be solved computationally. The details for one- and two-dimensional for FEM are presented in Chapter 3 where the channel flow problems are solved using this approach.

1.7.2.3 Finite volume method

FVM is a spatial discretisation technique that is used to approximate PDEs that typically arise from physical conservation law. FVM was developed by Spalding and Patankar [107] and was commonly used as a numerical approximation computational fluid dynamics. One of the advantages of using the FVM is it can be used on unstructured grids which is therefore suitable for complex geometry. It is relatively simple compared to FEM which make it suitable to use in solving large three-dimensional problems in CFD. This method is the basis for the OpenFOAM CFD software.

In FVM, an integral formulation of the problem with a finite set of non-overlapping partitions is used to discretise the equation. Grid generation and the details of the partition for a one-dimensional geometry is shown in the following figure.

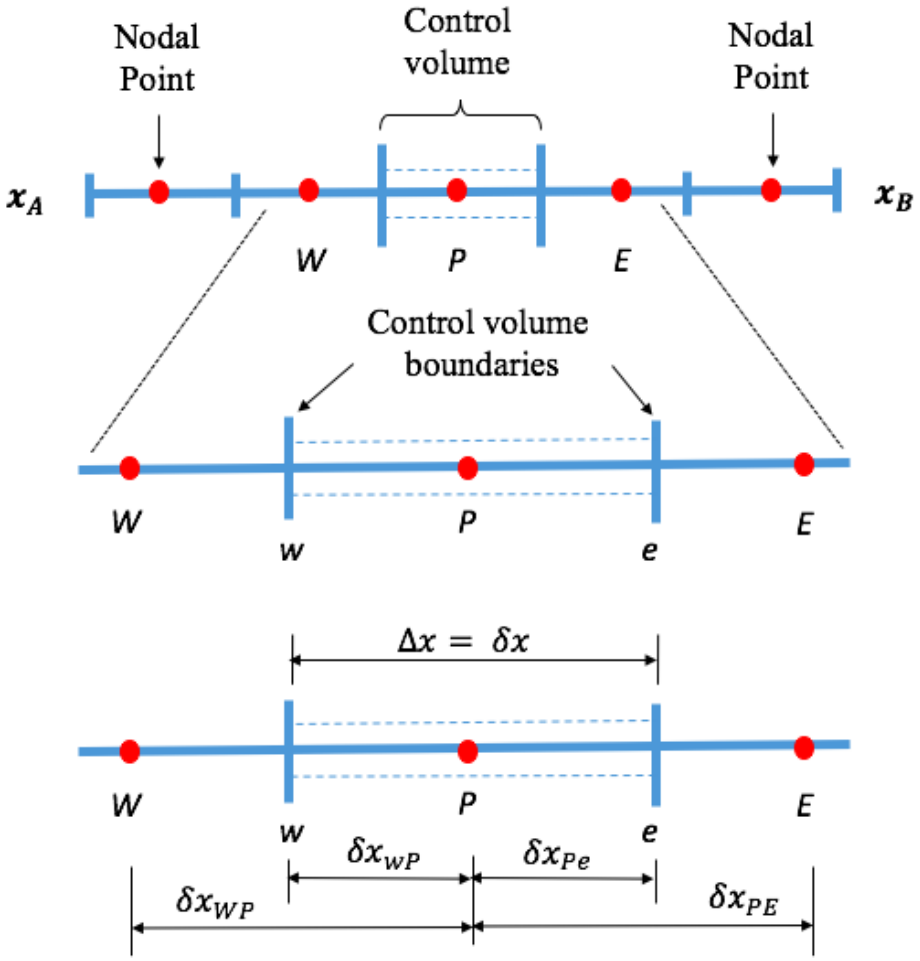

Figure 1.9: Finite volume grid for x on the range $[x_A, x_B]$.

The partition set is known as the control volumes or elements and the unknown value for the variable of interest is located at the centre of the control volume. After the domain is discretized, the integral of the differential form of the governing equation is considered for each control volume. This then results in a single discrete equation for each control volume, where typically the divergence theorem is used to convert the spatial derivatives to surface integrals. Consider the conservation form of the unsteady diffusion problem defined as

$$\frac{\partial u}{\partial t} - \alpha \frac{\partial^2 u}{\partial x^2} = 0.$$

The integral form over a control volume of the equation is written as

$$\int_{cv} \frac{\partial u}{\partial t} dV - \underbrace{\int_{cv} \frac{\partial}{\partial x}\left(\alpha \frac{\partial u}{\partial x}\right) dV}_{\text{divergence theorem}} = 0.$$

Applying the divergence theorem, the equation reduces to

$$\int_{cv} \frac{\partial u}{\partial t} dV - \int_{s} \alpha \frac{\partial u}{\partial x} \mathbf{n} dS = 0$$

where s is the surface area of the cell with outward normal vector, $\mathbf{n}$.

In the one-dimensional case, integrating the previous equation over a control volume for node P shown in Figure 1.9 gives

$$v_i \frac{\partial u}{\partial t} + \left[\left(\alpha A \frac{\partial u}{\partial x}\right)_e - \left(\alpha A \frac{\partial u}{\partial x}\right)_w\right] = 0,$$

where v_i is the volume (length) of cell i, and the time derivative is constant on cell i. The spatial derivative is approximated using central differencing (i.e. $\left(\frac{\partial u}{\partial x}\right)_e = \frac{u_E - u_P}{\delta x_{PE}}$ for example).

1.8 A review on viscoelasic flow studies

In this section, a review of viscoelastic flow problem including both numerical and experimental related to this research is presented.

The early work on numerical simulation since the late 1960's and early 1970's provides the basis to develop the numerical techniques which nowadays act as the main tools for solving many partial differential equations describing different phenomena including the viscoelastic molten polymer fluid flows. Conducting experimental procedures to investigate the real polymer melts behaviour is expensive and the experimental prediction can be affected by the external factors. Thus, mathematical constitutive laws describing different types of polymer molecular architecture, including linear, branched and entangled polymers have been developed. These are used by the researchers to provide numerical prediction of polymer flow. In this context, numerical simulation is crucial for predicting industrial flows

including polymer processing applications (for example [106]).

Numerical simulation for complex viscoelastic fluid flow began to develop in the 1970's. In 1977, Perera and Walter [109], [110] implemented a finite difference approach to solve complex fluid problems while Kawahara and Takeuchi [77] used FEM to analyse viscoelastic fluid flow. Since many decades, the literature survey reveals a huge amount of research on solving viscoelastic fluid flow using a variety of numerical techniques. These include the finite difference method (e.g. [7], [43], [133]), finite element method (e.g. [18], [46], [64], [65], [84], [97], [130]), finite volume method (e.g [35], [87], [104], [123], [140]) and mixed finite volume and finite element method (e.g [74], [98], [99], [100], [101]).

There are several common geometries used to study viscoelastic flow and some of them have been considered as benchmark geometrical flows. These include the 4:1 abrupt contraction, the cross-slot, the exit-entry slit, flow past a cylinder, the contraction-expansion and the hyperbolic contraction geometry for example. These flows have been studied in physical experiment and numerical simulation over recent decades.

The abrupt contraction flow is one of the benchmark geometrical flows used to compare both experiment and numerical prediction. This geometry creates shear at the wall and pure extension (no shear) at the centre-line, where the combination of both allows complex flow to be formed. Measuring the extensional viscosity as well as the shear viscosity is of great significance in numerous applications as they have a role in characterising the rheological behaviour of the fluid. However, measuring the extensional viscosity is quite challenging in the abrupt contraction due to the intense elongational flow created when the flow accelerates from the upstream to the downstream of the configuration. For sufficiently fast flow, recirculation of the fluid will be generated at the sharp corner of the upstream which reduces the smoothness of the flow during processing. The earlier work on the abrupt contraction geometry includes the work in references [12] [13], [18], [117] and [118]. Quinzani et al. [117] conducted an experiment to investigate the behaviour of polyisobutylene in tetradecane, a shear-thinning fluid, in an approximately 4:1 planar contraction where laser Doppler velocimetry is used to capture the velocity field and flow induced birefringence is used to visualise the stress field. The work is then extended [118] to the comparison between the prediction of the extension-rate and normal stresses in unsteady extensional flow. Bern-

stein et al. [18] performed the numerical prediction based on a finite element approach for KBKZ-type fluid in a 4:1 sudden (axisymmetric) contraction flow. This configuration has also been used in research conducted by Azaiez et al. [13] where the behaviour of viscoelastic fluids (i.e. PTT, FENE-CR and Carreau) and the fiber orientation in polymeric fluid is presented where the comparison for different closure approximations are made. Research works by [53], [61], [69] use this benchmark geometry problem to compare their results with the numerical results [12] and the experimental result [117] that used the same geometry in their research. More research works using this contraction geometry can be found in references [21], [32], [48], [79], [112], [116], [141]. More recently, Nystrom et al. [99] reported that a uniform extensional rate is not able to be created in an abrupt contraction, since the fluid flow experiences a rapid change as a result of the sudden geometrical changes from the upstream to the contraction region.

The challenge to understand the extensional response of the viscoelastic fluid in a contraction flow motivated Cogswell [30] to examine the fluid flow in several converging geometries. These geometries were used to investigate the rheology of the fluid undergoing stretching flow. He found that the die with a hyperbolic contraction profile was able to provide a region of constant extension-rate which could be used as a tool to measure and predict the extensional viscosity. Among the earlier studies using this configuration, James et al. [74] investigate a Newtonian fluid through a converging channel at high Reynolds number before considering the lower Reynolds number [73] to understand the extensional behaviour of the non-Newtonian fluid through the constriction region. This is part of their preliminary study where only the Newtonian fluid was considered before extending their work to look at a viscoelastic fluid as part of the development of the rheometer. Later, Kim et al. [78] and Collier et al. [31] use the hyperbolic die configuration to demonstrate the behaviour of polypropylene and the low-density polyethylene experimentally in elongational flow for lubrication related studies. Baird and Huang [15], [14], utilised this configuration to measure and evaluate elongational flow in the hyperbolic contraction. Oliveira et al. [104] used this technique to design and investigate the utility of this die profile as an extensional microrheometer. Nystrom et al. [99] presented work on numerical prediction of contraction geometries with different configurations including a sudden contraction, tapered geome-

try, hyperbolic contraction (with sharp and rounded corner) to understand the behaviour of Newtonian and Boger fluid (i.e. FENE-CR). They developed a measuring tool for extensional viscosity using a hybrid finite element and finite volume scheme. The extended version of their work [101], using the same numerical scheme focuses on the investigation of the fluid in a hyperbolic contraction geometry that exhibits extensional flow in a converging region and considers the rheological response. The hyperbolic contraction configuration has also been used in microfluidic flow to predict the extensional viscosity of a complex fluid as reported in Ober et al., [102] and Campo-Deano et al. [25]. They used this die profile to study the evolution of a Boger fluid with low viscosity. Lanzaro et al. [82] conducted the experiment to investigate the behaviour of polyacrylamide solution in a microfluidic hyperbolic contraction flow with high contraction ratio and characterized the polyacrylamide aqeous solution using a μ-PIV technique. Nystrom et al. [100] extended their work [99] to investigate the influence of the hyperbolic contraction with different contraction ratios to observe the flow behaviour for Oldroyd-B fluid and FENE-CR models [20] as well as the shear-thinning LPTT model [131] for fixed Deborah number. The hyperbolic contraction flow has also been used in other relevant processes. For instance, references [127], [128], [139] also deploy this technique in food processing and investigate the behaviour of the material during and after processing through this hyperbolic nozzle.

While the planar contraction flow is very popular and has been addressed as a benchmark flow for polymeric fluids in past decades, it is limited in the amount of strain that the fluid experiences. The cross-slot device is an alternative that is used in many viscoelastic flow studies to enhance the understanding of the extensional response of the viscoelastic fluid under strong elongational flow. This geometry was suggested as a new benchmark flow by Cruz et al. [35]. The simplest version of this geometry consists of two straight channels intersecting at right angles, with fluid forced inwards in both directions along one of the channels creating a hyperbolic stagnation point at the intersection. This device generates high extensional deformation along the inlet-outlet (symmetrical plane) centre-line. This geometry was initiated by Scrivener et al. [125] to study drag-reducing polymers. Among the earlier research work using the cross-slot device as a tool to measure the elongational flow includes the work that has been done using the polyethylene oxide in Lyazid et al.

[90] and the polystyrene solution in Gardner et al. [55] that measures the velocity profile at the upstream and downstream of the channel. Studies of the viscoelastic flow in this device have been explored numerically and compared with experimental data as reported in Harlen et al. [63], Schoonen et al. [124] and Bogaerds et al. [22]. The numerical simulation through this geometry also has been performed in Singh and Leal [126] and Remmelgas et al. [120] using a similar finite element approach. The use of this device has become popular, being utilised to reinforce the understanding of non-linear response in complex flow. Recent research work includes comparing the numerical simulation based on different numerical techniques [26], [35], [88], and experimental work [66], [67]. These allow both numerical simulation and experimental observation producing comparable results with the use of appropriate comparable viscoelastic models (see for example [65], [87], [89]).

The main purpose of the cross-slot is to examine the extensional flow at the stagnation point at the centre of the device. However, the corners formed at the intersections of the channels generate flow singularities. In 2008, Alves [5] designed an optimized cross-slot channel using a finite volume approach with the CONDOR optimizer [17], to obtain the shape that maximised the size of the region of linear extensional flow near the stagnation point. The proposed optimized cross-slot design (with cut-out at the corners) was tested numerically for Newtonian, upper-convected Maxwell, Oldroyd-B [103] and PTT [131] models and it was claimed that the designed optimized cross-slot was able to produce a velocity field that is not influenced by inertial and elastic effect. Haward et al. [67] used this design to fabricate an optimized cross-slot geometry as a tool for microfluidic extensional rheometry that can be used to measure the extensional viscosity for dilute polymeric solutions. Cruz et al. [35] considered both sharp and the rounded corners to observe the influence of the corner type on the viscoelastic flows predicted by UCM, Oldroyd-B and PTT model. They reported that the numerical prediction of the fluid flowing through this configuration having different corner types gives only a small change in the prediction and thus can be neglected.

Other benchmark problem such as the flow past a cylinder in a channel have been used in [130] for Oldroyd-B [103] model to validate the developed two-dimensional code before the code is implemented in a contraction geometry for the Rolie-Poly [85] and Pom-Pom

model [94] in three-dimensions.

Nowadays, CFD commercial packages and software such as OpenFOAM [138], ANSYS [1] and REM3D are typically becoming the standard option and used to produce the numerical simulation of flow involving liquids and gases to observe and analyse the behaviour of the fluid flow. They are typically based on finite volume and finite element approaches. A number of researchers have conducted their work with CFD software to study viscoelastic flow. Favero et al., [53] used the parameters described in Quinzani et al. [117] and the Oldroyd-B constitutive model to validate a solver that has been implemented in OpenFOAM and good agreement was observed. Pimenta and Alves, in the documentation of the RheoTool toolbox, reproduce the results in a recent benchmark problem for the two-dimensional cross-slot flow [35] using the `rheoFoam` solver with log-conformation approach [49] to ensure the numerical stability at high Weissenberg number. Other related research articles (see [53], [54], [61], [62], [69] for example) are using the OpenFOAM software to simulate viscoelastic fluid flows. Another open source library code written in C++, deal.ii, is used by Yoon et al. [142] in their research to develop an effective numerical simulation to study the suspension of the particles in viscoelastic flow using the finite element framework.

The research on viscoelastic flow in OpenFOAM is not only restricted to a confined geometry. It has also been conducted in free surface flow and two-phase flow for example (see [54], [61]) to study the viscoelastic free-surface effect such as die-swell and Weissenberg effect. Guranov et al. [60] presented their work on numerical studies of viscoelastic flow using the OpenFOAM software. They consider two constitutive models, the upper convected Maxwell (UCM) and the Oldroyd-B model and aim to test the `viscoelasticFluidFoam` solver [53] from the OpenFOAM software. Each model has been tested in three cases: the start-up flow in the channel, pulsating flow in the channel and start-up flow in a circular pipe. The assumption of a fully developed planar flow has been made due to the specific problems considered. The analytical solution found in Duarte et al. [47] for these problems makes it possible to compare with the numerical solution obtained with OpenFOAM using the `viscoelasticFluidFoam` solver. The results demonstrate good agreement between the analytical and the numerical approximation.

In this section, we have presented a review for both experiment and numerical solution (both in house code and OpenFOAM CFD software) on viscoelastic fluid flow in a confined geometry. We focus on a sudden contraction, hyperbolic contraction and a cross-slot flow since these geometries are key to this work. In the next section, the outline of the thesis is presented.

1.9 Thesis structure

This thesis consists of 9 chapters including the introduction chapter. Chapter 2 presents the OpenFOAM software and the solver used for the rheological problems including the numerical techniques and strategy proposed to tackle the stability issues. The implementation of the constitutive model within the software is described in this chapter and the differences between the solvers available from different versions of OpenFOAM are considered.

Chapter 3 describes the numerical approximation for Newtonian and non-Newtonian fluid for one- and two-dimensional channel flow problem, where the order of accuracy for each techniques are observed. The comparison between the analytical solution and the numerical predictions using different numerical approaches for one-dimensional Oldroyd-B model is illustrated.

The implementation of the Rolie-Poly model in OpenFOAM is documented in Chapter 4 and validated against published results for a benchmark 4:1 contraction flow. The work is then extended to look at the behaviour of the polymer in a hyperbolic contraction flow.

In Chapter 5, the RDP model is implemented and validation against the published results is made. The linear viscoelastic limit for RDP is described to create the equivalent uncoupled mRP model for the purpose of comparison of the transient extensional and transient shear viscosity.

Having validated the RDP model in Chapter 5, in Chapter 6 the hyperbolic contraction flow is considered where the behaviour of this model is investigated by observing the extensional response as a consequence of varying the geometrical effects, the extension-rate and blend composition. The coupling effect is explored by comparing uncoupled mRP and coupled RDP models.

Chapter 7 focuses on the two-dimensional cross-slot flow with a hyperbolic corner where

the extensional behaviour of the RDP model is investigated. The geometrical effects as well as the effect of different extension-rate, blend composition and the coupling effect are presented and discussed. The comparison between the hyperbolic contraction flow and cross-slot flow is also discussed.

Chapter 8 extends the work in Chapter 7 where the numerical prediction for the cross-slot geometry is simulated at high Deborah number until the flow of the RDP fluid bifurcates. The influence of the blend composition in the RDP model in order to determine the critical Deborah number where the onset for the symmetry breaking is investigated.

In Chapter 9, we conclude and recap the chapters that have been presented in this thesis, emphasizing the contribution of this work. The potential of extending the current work in several directions is described.

Chapter 2

Viscoelastic Simulation using OpenFOAM

2.1 Introduction

OpenFOAM (Open Source Field Operation And Manipulation) [138] numerical models are written in the high-level C++ object-oriented language where the mathematical models are translated into C++ code almost analogous to the partial differential equations that describes the model mathematically. In general, this software was designed to solve a wide range of CFD problems. Alongside the solvers created in this software, libraries containing a set of standard PDE models are available and the relevant libraries are described in a later section. While OpenFOAM is the original project developed by Weller [75], [138] and endorsed by the ESI group, foam-extend [58] is the project developed by the community which is not endorsed by any groups. The foam-extend version provides the platform for new contributions in CFD from the users and developers.

This chapter describes the capability of the software to deal with CFD problems for non-Newtonian viscoelastic flow. A brief introduction and chapter outline are presented in this section. Section 2.2 describes the strategies used for viscoelastic flow simulation in OpenFOAM. The libraries available are the RheoTool solver, called `rheoFoam`, and the earlier viscoelastic solver, available in foam-extend version 3.2 and 4.0, known as `viscoelasticFluidFoam`. This is then followed by the basic OpenFOAM structure that is presented briefly in

Section 2.3. In Section 2.4, a discussion of creating new models within the OpenFOAM libraries is presented to provide guidance to the reader for the compilation of a new model that is relevant to their research interest.

2.2 Viscoelastic flow simulations using OpenFOAM

2.2.1 The `viscoelasticFluidFoam` solver

The general viscoelastic solver was first introduced by Favero et al., [52] known as `viscoelasticFluidFoam`. This solver was available in `foam-extend` library version 3.2 and 4.0 alongside a variety of viscoelastic constitutive models from different ranges. This solver uses a technique called Discrete elastic-viscous split-stress, DEVSS, [59] that is used to deal with the numerical instabilities. DEVSS technique is sometimes referred to as Both-Sides-Diffusion (BSD) in the literature and it works by adding a diffusive term on both sides of the momentum equation (1.2) that gives

$$\rho\left(\frac{\partial \mathbf{u}}{\partial t} + \mathbf{u}\cdot\nabla\mathbf{u}\right) - \underbrace{\nabla\cdot(\eta_S+\eta_P)\nabla\mathbf{u}}_{\text{added } \eta_P \text{ implicitly}} = -\nabla p - \underbrace{\nabla\cdot(\eta_P\nabla\mathbf{u})}_{\text{added } \eta_P \text{ explicitly}} + \nabla\cdot\boldsymbol{\tau}. \tag{2.1}$$

The extra diffusion terms cancel each other when the steady-state solution is achieved. This method can increase the ellipticity of the momentum equation in nature and thus give a numerical stabilizing effect. Note that, from equation (2.1), the polymeric viscosity, η_P is used to scale the both-sides diffusive terms and has been commonly used in the literature, for example [28], [51].

In 2017, Pimenta and Alves [113] claimed that the `viscoelasticFluidFoam` solver was prone to stability issues under certain circumstances, including in the simulation of high Weissenberg number and simulation when the Newtonian viscosity contribution is absent. Relying only on a DEVSS technique alone is insufficient to deal with the high Weissenberg number problem. Thus, to strengthen and enhance the numerical stability, the additional technique called log-conformation tensor [49] is applied in this context to minimize the stability issues. This leads to the introduction of a new toolbox for solving viscoelastic flow

problems called RheoTool [113].

2.2.2 The RheoTool toolbox

Recently, RheoTool toolbox [113] extended the OpenFOAM to include further Generalized Newtonian fluid and viscoelastic constitutive models. While the `viscoelasticFluidFoam` solver was only accessible from foam-extend, RheoTool solvers are available in both OpenFOAM and foam-extend versions. This toolbox is developed to tackle the High Weissenberg Number Problem (HWNP) using a log-conformation technique [49] to increase the numerical stability. At high Weissenberg number flows, numerical simulations struggle to get convergence of the prediction due to loss of positive definiteness of the conformation tensor which leads to the growth of the stresses at the critical point and finally result in numerical instability. Thus, Fattal and Kupferman [49], [50] introduced the log-conformation tensor approach to conserve the positive definiteness of the conformation tensor and improve the numerical stability, ensuring the linearity of the exponential growth of the stress at the critical point. The details of this approach are not described in this chapter since the standard constitutive models is used throughout this work. However, the details of the methodology for this approach is available in the literature [49], [50], [113].

The comparable solver to `viscoelasticFluidFoam` in the RheoTool toolbox solver is called `rheoFoam` solver. There are some features that distinguish the difference between these two solvers for example the algorithm used for solving the pressure-velocity coupling. The `rheoFoam` solver is designed by considering the SIMPLEC (SIMPLE-Consistent) algorithm to solve the pressure-velocity coupling. On the other hand, `viscoelasticFluidFoam` solver uses the PISO [71] algorithm for the coupling. SIMPLEC algorithm used in `rheoFoam` solver allows a larger-time step to be used which reduces the computational cost without encountering any decoupling problems. With the exception for pressure in a non-orthogonal grid, the use of under-relaxation is not required when SIMPLEC algorithm is used for solving the pressure-velocity coupling. This enhances the efficiency of the numerical simulation. For the `viscoelasticFluidFoam` solver, the PISO algorithm for pressure-velocity coupling also do not require the under-relaxation. However, under certain circumstances, for example for sufficiently fast flow, the under-relaxation may be required to deal with numerical

instabilities. Otherwise, a smaller time step is needed to ensure numerical stability and this is is some times computationally expensive especially when dealing with huge amount computational cell and complex model.

There are a few new utilities within this toolbox. These include new boundary conditions and an additional scheme for convective terms. The approximate boundary condition for stress near the wall called `linearExtrapolation` was introduced to provide a better approximation value instead of only specifying a `zeroGradient` boundary condition at the wall. The `zeroGradient` boundary condition at the wall for stress gives rise to a deviation for the stress profile across the geometry where the stress measured at the centre of the computational cell near the wall is forced to obey the boundary condition of the `zeroGradient` at the wall. Although this issue can be minimised using a finer mesh grid, a coarser mesh shows a poor approximation of the stress at the wall. This is can be seen clearly when the stress component is plotted across the geometry using a coarse mesh resolution. On the other hand, the `linearExtrapolation` boundary condition for stress at the wall introduced in RheoTool toolbox provides a better approximation where the stress calculated at the centre of the cell is linearly extrapolated to the wall and preserving the stress prediction at the wall from the stress profile across the geometry without any deviation.

The high-resolution schemes, (HRSs), are proposed in RheoTool which are used to discretize the convective terms. There are seven available schemes accessible including `"no convection"` where the convective term is deleted. Other available choices of the schemes are UPWIND, CUBISTA, MINMOD, SMART, WACEB and SUPERBEE that are defined using a Normalized Weighting Factor approach [96]. To avoid the numerical instabilities, the HRSs are available in a component-wise and deferred correction approach where the details of these are described in Pimenta and Alves [113]. To date, the latest version of the RheoTool toolbox has expanded with the addition of further libraries, boundary conditions and utilities although these are out of the scope of this research.

2.2.2.1 The RheoTool solvers

The RheoTool toolbox was first introduced with three solvers, called `rheoFoam`, `rheoInterFoam` and `rheoTestFoam`. While the `rheoFoam` and `rheoTestFoam` are ready to use, the

`rheoInterFoam` was under development during that time. To date, based on the latest version of RheoTool (version 4.1), there are five solvers available in total with three additional solvers, `rheoInterFoam`, `rheoEFoam` and `rheoBDFoam`. In this thesis, we use two RheoTool solvers, `rheoFoam` and `rheoTestFoam` that are relevant to the problems considered.

The `rheoTestFoam` solver by default is designed to look at the behaviour of the constitutive model for shear and extensional deformation on a single computational cell having a single relaxation time. The Rolie-Poly model, however, having two relaxation times, requires some additional declarations to be made from a file called, `createFields.H`. There are other header files relevant to this solver, `reStartOrEnd.H` and `timeWrite.H`. These files and the main file of the solver, `rheoTestFoam.C` are available from the following directory `src/solver/rheoTestFoam/`. In `createFields.H`, there is part of the code from the `if else` conditional statement for a model with a single relaxation time written as,

```
dimensionedScalar lambdatmp(constitutiveProperties.subDict
                   ("parameters").lookup("lambda"));
lambdaMax = lambdatmp.value();
lambdaMin = lambdaMax;
```

For Rolie-Poly model, we extend the above to

```
dimensionedScalar lambdatmp(constitutiveProperties.subDict
                    ("parameters").lookup("lambda"));
dimensionedScalar lambdaRtmp(constitutiveProperties.subDict
                   ("parameters").lookup("lambdaR"));
lambdaMax = lambdatmp.value();
lambdaMin = lambdaRtmp.value();
```

This `rheoTestFoam` software helps to validate the correctness of the implementation for the model within the OpenFOAM solver since the analytical solution for pure shear or pure extension computed on a single computational cell usually exists and can be used for

validation purposes. The requirement of only a single computational cell disallows a spatial discretization. Therefore, during the computation for the transient flow, the contribution of the numerical error is caused only by the temporal discretization.

A single computational cell by default is a square domain with a 1m edge length. This domain is used for different canonical flows specified by the velocity gradient during the pre-processing. Even though the `rheoTestFoam` solver is designed to solve the polymeric constitutive equation including a solvent stress contribution, the solver can be modified to not include the solvent part.

In this solver, there are two modes available to compute the material functions of the polymer: the transient mode and ramp mode. The transient mode computes the evolution of the stress components given a fixed value of deformation rate to the specified end. In ramp mode, the deformation rate imposed on a single computational cell is increased ("ramped up") after a set time interval and the stress components with respect to the deformation rate are retrieved. Thereby mimicking a strain-rate sweep experiment on a rheometer. The data can be obtained from a file called `Report` that is produced during the simulation.

On the other hand, the `rheoFoam` solver is used to solve a single-phase flow specifically for transient incompressible flow of the Generalised Newtonian fluid, (GNF) and viscoelastic fluids. The solver is solved iteratively in a C++ subroutine and uses the SIMPLEC algorithm [135] to solve the pressure-velocity coupling. Similar to `rheoTestFoam`, the `rheoFoam` solver is accessible through `src/solver/rheoFoam/` directory.

The main file from this directory is `rheoFoam.C` where the source code of the solver is built with the appropriate headers that are also available in the same directory. The headers include `createFields.H, UEqn.H, pEqn.H, CEqn.H`. Figure 2.1 summarises the solving sequence for the `rheoFoam` solver and locate the headers when the function is calling to solve the equation in the sequence. The detailed explanation of the methodology used in the `rheoFoam` solver with respect to Figure 2.1 is available in the user-guide and Alves and Pimenta [113].

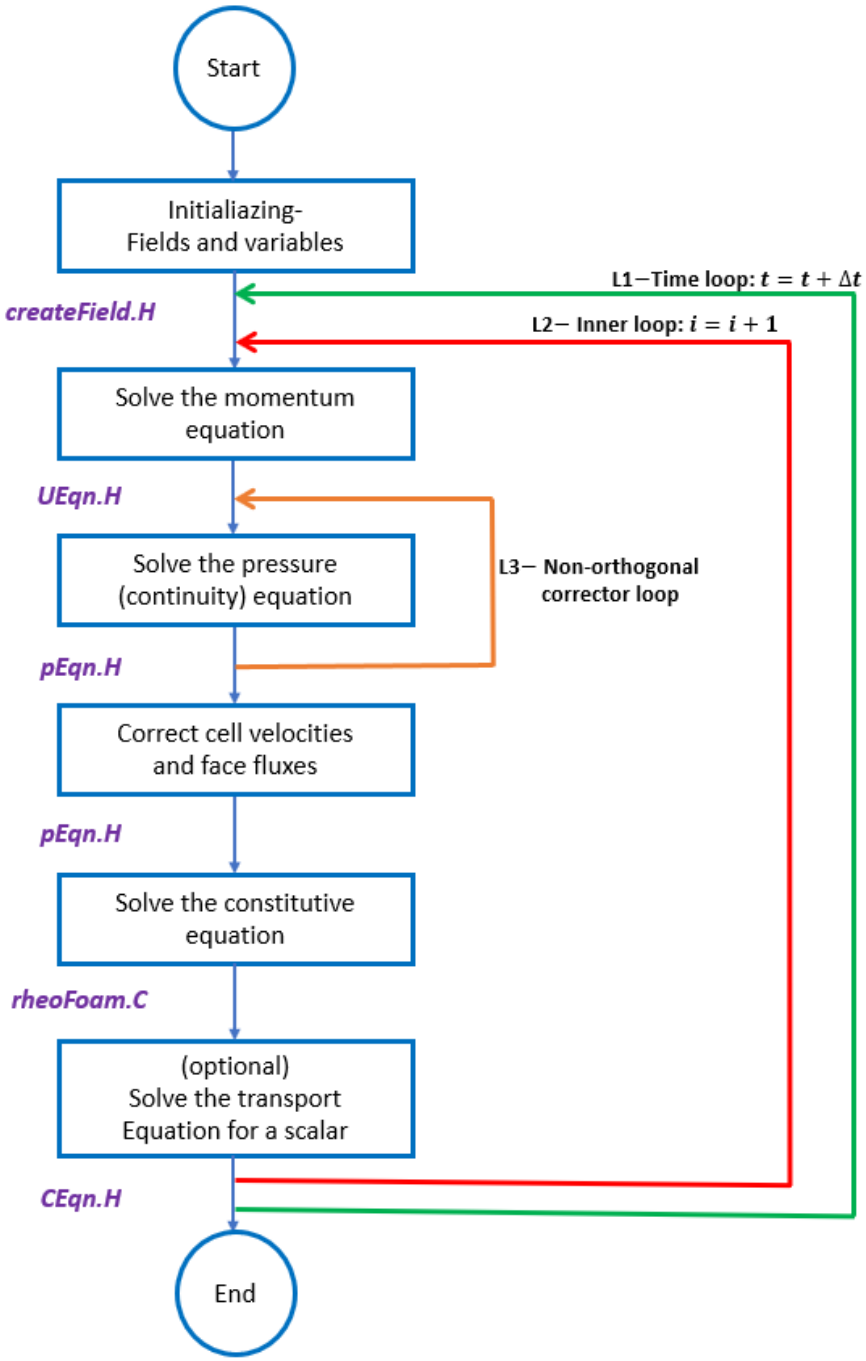

Figure 2.1: The solving sequence for `rheoFoam` solver available in user-guide RheoTool toolbox (adapted from the RheoTool toolbox user-guide).

2.2.2.2 The SIMPLEC algorithm for pressure-velocity coupling

The brief idea for the SIMPLEC algorithm [135] is illustrated as follows.

- **Step 1** : The momentum equation is solved implicitly using the known value of pressure from previous time step or inner-iteration to obtain estimated velocity field,

$\mathbf{u}^*$. This algorithm is initialised by guessing the pressure field, $p^* = p^n$, where p^n is the pressure from the previous time iteration. These two solutions, $\mathbf{u}^*$ and p^* need to satisfy the momentum equation but not necessarily the continuity equation. Thus, the correction needs to be done for both $\mathbf{u}$ and p to ensure the continuity equation is obeyed.

- **Step 2** : The correction for both $\mathbf{u}^*$ and p^* are carried out to obtain corrected values of u and p. This is done using

$$\mathbf{u} = \mathbf{u}^* + \mathbf{u}^{'}$$

and

$$p = p^* + p'$$

where $\mathbf{u}^{'}$ and p' are velocity and pressure correction respectively. These corrected values, ($\mathbf{u}$ and p) are continuity-compliant.

- **Step 3** : The corrected values of $\mathbf{u}$ and p are substituted in the momentum balance yielding the semi-discretized equations.

Note that, the SIMPLE and SIMPLEC algorithm are usually used for pressure-velocity coupling for the steady-state solver. However, at low Reynolds number, Pimenta and Alves [113] claim that SIMPLEC algorithm is applicable for time-dependent viscoelastic fluid flow where the accuracy and stability are ensured. In Pimenta and Alves [113], the continuity equation for pressure field resulted from the SIMPLEC algorithm can be implicitly written as

$$\nabla \cdot \left(\frac{1}{a_P - H_1} (\nabla p)_P \right) = \nabla \cdot \left[\frac{\mathbf{H}}{a_P} + \left(\frac{1}{a_P - H_1} - \frac{1}{a_P} \right) (\nabla p^*)_P \right]. \tag{2.2}$$

Solving equation (2.2) implicitly produces the corrected pressure, p. This value is then used to find the corrected velocity from the following equation,

$$\mathbf{u} = \frac{1}{a_P}\mathbf{H} + \left(\frac{1}{a_P - H_1} - \frac{1}{a_P} \right) (\nabla p^*)_P - \frac{1}{a_P - H_1} (\nabla p)_P. \tag{2.3}$$

Note that, the pressure (p) and velocity correction ($\mathbf{u}$) obey the mass conservation. From the

equations, a_P represents the coefficients in the diagonal entry from the momentum equation, $H_1 = -\sum_{nb} a_{nb}$ is a negative value obtained based on the summation of the off-diagonal entries in the momentum equation, whereas $\mathbf{H} = \sum_a a_{nb}\mathbf{u}^*_{nb} + \mathbf{b}$ is a vector contributed by the off-diagonal with addition of the source term in the momentum equation.

As reported in Pimenta and Alves [113], a standard Rhie and Chow interpolation [121] is used to interpolate the face velocity for the cell-centred velocity from the collocated grid to avoid the unphysical checkerboard pressure and velocity field from happening. However, the disadvantage of this method can be seen when the time-step is set to a small value approaching zero, the simulation may crash [76], [143]. A corrective term introduced in the OpenFOAM toolbox is used to tackle this issue. The detailed derivation for the pressure-velocity coupling derived from SIMPLEC algorithm is available in Pimenta and Alves [113].

2.2.2.3 Stress-velocity coupling

Pimenta and Alves [113] introduced a new stress-velocity coupling method to avoid the same potential decoupling issues. This usually takes place when the face centre field of the stress from the divergence term of polymeric stress in momentum equation (1.2) is discretised by linear interpolation from the cell-centred field. In Pimenta and Alves [113], the polymeric stress tensor at face centres, $\boldsymbol{\tau}_f$ is defined as

$$\boldsymbol{\tau}_f = \overline{\boldsymbol{\tau}}_f + \eta_P[(\nabla\mathbf{u}|_f + (\nabla\mathbf{u})^T|_f) - (\overline{\nabla\mathbf{u})}|_f + \overline{\nabla\mathbf{u})^T}|_f] \tag{2.4}$$

where the overbar terms for the polymeric stress and velocity gradient are linearly interpolated from the cell-centred values. The velocities at the cell-centres are used to compute the normal velocity gradient from the second term of equation (2.4). Substituting this equation in the momentum equation with the DEVSS term included as in equation, (2.1), yields the following equation

$$\rho\left(\frac{\partial\mathbf{u}}{\partial t} + \mathbf{u}\cdot\nabla\mathbf{u}\right) - \nabla\cdot(\eta_S + \eta_P)\nabla\mathbf{u} = -\nabla p - \overline{\nabla\cdot\eta_P\nabla\mathbf{u}} + \nabla\cdot\overline{\boldsymbol{\tau}} + \mathbf{f}. \tag{2.5}$$

Note that, from the equation, the overbar term is dissimilar to the Laplacian term because the velocity gradient as part of the overbar term is evaluated by linearly interpolating

from the cell-centred values. The remaining term from the equation (2.4) is dropped out as a consequence of the continuity imposed. In the next section, a brief description of the OpenFOAM case folder with the sub-folders is presented.

2.3 OpenFOAM structure

Like other commercial CFD software (e.g. ANSYS Fluent and STAR-CCM+), OpenFOAM works by three fundamental stages: the pre-processing, processing and post-processing. OpenFOAM requires a basic structure of the case directory which in general is composed of three main sub-directories namely, **0**, **constant**, and **system** folder as pre-processing data. For viscoelastic flow case, the structure of the case file from OpenFOAM can be illustrated as follows.

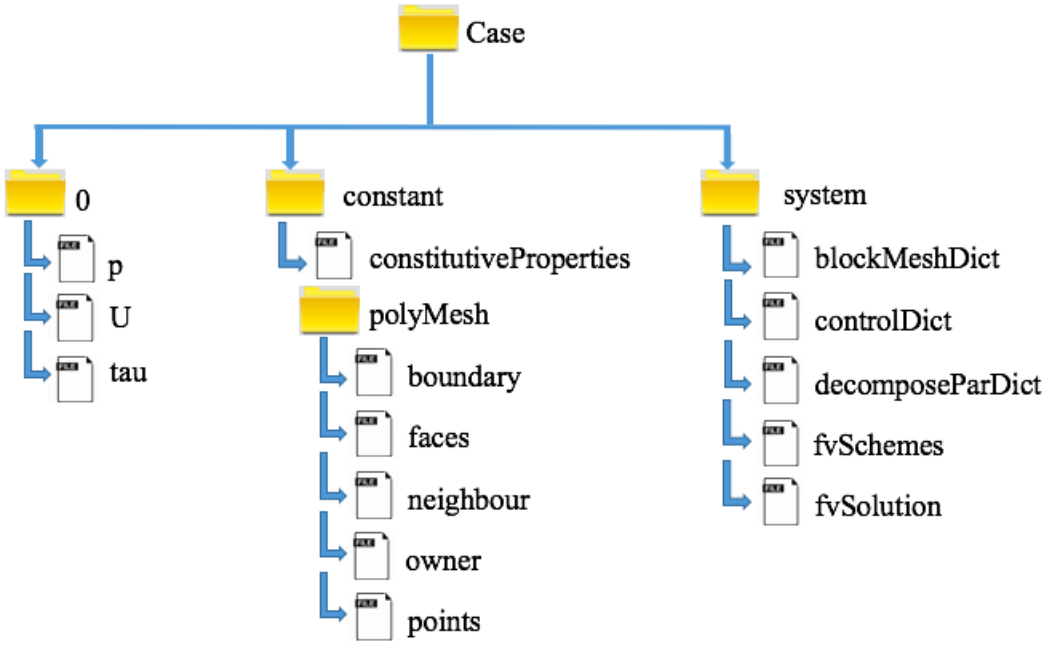

Figure 2.2: The case directory structure for solving viscoelastic flow problem in OpenFOAM including the `decomposeParDict` file for a case solved in parallel.

The case file from Figure 2.2 is accessible from **$FOAM_TUTORIAL**. The user is advised to copy the file to the local run directory, **$FOAM_RUN** which allows the simulation to be performed. From this directory, the user is allowed to modify the pre-processing data in the time directory folder, **0** which comprises the initial and boundary conditions for pressure (p), velocity (U) and stress (tau) field. A set of parameters of the constitutive model

can be set up in the `constitutiveProperties` file from the **constant** directory. There is a sub-directory in **constant** called **polyMesh** which stores the details of the geometry configuration used. This folder is only created when the `blockMesh` utility is performed. The quality of the mesh can be confirmed by performing the **checkMesh** utility from the terminal window. A set of geometrical checking analysis is printed to justify the precision of the configuration. At the end of the geometry checking, there are two possible conclusions reported: i) Mesh OK or ii) Failed mesh check. The case problem is ready to be simulated if the mesh is OK. Otherwise, modification in the setup file, `blockMeshDict` need to be done to ensure the correct geometrical domain with the appropriate mesh structure is built.

In the **system** directory, there are five files as listed in Figure 2.2. The mesh generation, blocks, including the specification of the patches (e.g. inlet, outlet, walls, etc.) is written in `blockMeshDict` file. The `controlDict` file manages the time, reading and writing of the solution data. The `decomposeParDict` is important when the case is solved using parallel execution. This file is responsible to decompose the mesh and fields according to the number of sub-domains and method of parallel processing specified in this file. The schemes used for time and spatial discretization for the partial differential terms are specified in the `fvSchemes` dictionary file. Finally is the `fvSolution` dictionary file. This file is made up of two dictionaries: `solvers`, which specifies the linear solvers with appropriate preconditioner and tolerance used for pressure, velocity and stress equation; `fvSolution`, the algorithm control dictionary, for SIMPLE that stores the number of iterations, residual control and relaxation factors for pressure field, the stress and momentum equation.

Tutorials for solving viscoelastic flow in different flow problems, including channel flow, contraction flow and cross-slot flow, are available online and can be downloaded from the RheoTool github page that is accessible through the following link `https://github.com/fppimenta/rheoTool`. Explicit guidelines to setup the flow case are available and described in details from the user-guide which is available from the above link.

2.4 Compilation of new constitutive models

As well as the free open-source package, this software allows full access to modify the source code. The user can customize the model and implement more complex and sophisticated

mathematical models for more specific problems for various CFD applications.

In this section, the procedures needed to implement a new constitutive model within the library are presented in a step by step manner. In general, the model can be implemented from **$FOAM_SRC** path in the OpenFOAM environment. However, to be consistent with the work presented in this thesis that used the RheoTool toolbox [113], the model can be implemented from the path for this toolbox.

The RheoTool toolbox is available in both OpenFOAM and foam-extend version. The readers are advised to read the user-guide document available from the downloaded documents for installation. This toolbox provides the library that is used by its solvers to simulate the GNF and viscoelastic models. If the OpenFOAM version 4.0 is used, a new model within the RheoTool toolbox can be implemented from the following path, `rheoTool/rheoTool-master/of40/src/libs/constitutiveEquations/constitutiveEqs/...`

A set of viscoelastic constitutive equations was firstly presented from **$FOAM_SRC** in foam-extend/4.0 based on the library used by `viscoelasticFluidFoam` solver [54]. This RheoTool toolbox version extended some of the models with the log-conformation approach. The following constitutive laws are accessible through the library path mentioned above with additional source code using log-conformation approach for some of the models. The following common viscoelastic models are available in the folder.

```
FENE-CR     FENE-P     GNF     Giesekus     Oldroyd-B     PTT
WhiteMetzner     XPomPom     multiMode
```

A new viscoelastic model (e.g. RDP model) can be created by first copying one of the available models from the path using the following command.

```
cp -r Oldroyd-B RDP
```

Now we have created a new directory for the RDP model with three files having `.C`, `.H` and `.dep` file extension which at the moment having `Oldroyd_B.C`, `Oldroyd_B.H` and

`Oldroyd_B.dep`. These three files are available in the `../constitutiveEqs/RDP` directory that needs to be renamed accordingly using the folder name, i.e. RDP.C, RDP.H, RDP.dep. Note that, the `.dep` file extension is only created if the model is successfully compiled. Therefore, this file can be initially removed.

Now, within each file, there is the occurrence of the old class name that needs to be changed to the new class name. Once the changes have been made and saved, a new RDP class is successfully created. The next step that needs to be completed is the compilation of the model. For the new model to be recognised by the library, the path to the RDP model (where the `RDP.C` and `RDP.H` file extension are available) need to be included from the `Make/files` file. This is written as `constitutiveEqs/RDP/RDP.C` in the file. Finally, the `wmake libso` command is launched from the terminal window for compilation. The successful compilation will print out the "up to date" status of the shared object library, for instance, `libconstitutiveEquations.so` at the end of the compilation. The example of the status is displayed as follows,

```
'/home/home01/scaaaz/OpenFOAM/scaaaz-4.1/platforms/
linux64Gcc48DPInt64Opt/lib/libconstitutiveEquations.so' is up to date.
```

The currently created model is a copy of the Oldroyd-B model. Further code development is then required to implement the alternative RDP model and then recompilation is required. The new model can now be used to simulate the case problem with the relevant application of the viscoelastic flow problem as it is now recognised as a part of the RheoTool library by OpenFOAM.

2.5 Summary

This chapter presents the OpenFOAM software that is used in this work. The comparison between the previous viscoelastic solver, `viscoelasticFluidFoam`, with the recent solver `rheoFoam` that has been improved to strengthen the numerical stability is described. Also, the new added utilities available in the RheoTool toolbox that increase the order of the accuracy of the numerical solution are also highlighted. A brief description for the pre-

processing data setup for solving a flow case problem is presented. The details about the new model implementation is described in depth to guide OpenFOAM user in the implementation and compilation of the model of interest within the software.

Even though the RDP model with log-conformation approach would be more stable for simulation in both low and high Deborah number, however in this thesis, we restrict our work to investigate the multimode version of Rolie-Poly and the RDP bidisperse blend model without implementing the log-conformation technique that was introduced in the RheoTool toolbox. As the complexity of the model is concerned, it is crucial to look at the behaviour of the model at low Weissenberg Number first, to get a good understanding about the coupling effect towards the flow behaviour, before extending it to higher Weissenberg numbers.

Chapter 3

Newtonian and Oldroyd-B flow through a straight channel

In this chapter, the numerical predictions of Newtonian and non-Newtonian (i.e. Oldroyd-B constitutive equation) through a straight channel in one- and two-dimensions are presented. Here the problems are solved numerically using different spatial and temporal discretisations and the order of accuracy for each of the numerical schemes is compared.

3.1 Definition of problem

This section defines the channel flow problem for one- and two-dimensions and the transient and steady-state exact solution for the Newtonian fluid respectively. The one-dimensional Oldroyd-B problem is also presented in this section with analytical solution at the steady-state.

Numerical calculations of the one- and two-dimensional channel flow problems were performed for the Newtonian fluid before extending the one-dimensional problem to the Oldroyd-B model using the finite difference and finite element method. The Oldroyd-B results are then compared to the three-dimensional OpenFOAM finite volume (`rheoFoam`) solver.

3.1.1 One-dimensional Channel flow

We consider pressure driven flow between two parallel planes located at $y = \pm h$. We define x as the coordinate in the direction of downstream pressure gradient, such that $\nabla p = -c\underline{\hat{x}}$. The fluid velocity is in the $\underline{\hat{x}}$ direction and is a function only of y and t. For a Newtonian fluid of viscosity, η_S, u satisfies the partial differential equation that is used to formulate the channel flow problem involving several variables as follows

$$\rho\frac{\partial u}{\partial t} = -\frac{\partial p}{\partial x} + \eta_S\frac{\partial^2 u}{\partial y^2}. \tag{3.1}$$

Dividing equation (3.1) by ρ we obtain

$$\frac{\partial u}{\partial t} = \frac{\eta_S}{\rho}\frac{\partial^2 u}{\partial y^2} + \frac{c}{\rho}. \tag{3.2}$$

The first term of the right-hand side represents the viscous resistance. Let the kinematic viscosity, $\nu = \frac{\eta_S}{\rho}$. If the fluid is initially at rest at $t = 0$, then the initial and boundary conditions are given as

- Initial condition: $u(y, 0) = 0$,
- Boundary condition: $u(-h, t) = u(h, t) = 0$.

The exact solution to this problem is [4]

$$u(y,t) = \frac{c}{2\eta_S}\left[h^2 - y^2 - h^2\sum_{N=0}^{\infty}\frac{4(-1)^N}{(N+\frac{1}{2})^3\pi^3}e^{-(N+\frac{1}{2})^2\pi^2\frac{\nu t}{h^2}}\cos\left(N+\frac{1}{2}\right)\frac{\pi y}{h}\right] \tag{3.3}$$

for $y \in [-h, h]$.

3.1.2 Two-dimensional Channel flow

We can extend the previous problem to a rectangular duct in the domain $[-a, a] \times [-b, b]$ and $t > 0$ such that $\underline{u} = [0, 0, u(x, y, t)]$. This two-dimensional cross-sectional channel flow

problem for a Newtonian fluid is described by the following equation

$$\rho\frac{\partial u}{\partial t} = -\frac{\partial p}{\partial z} + \eta_S\left(\frac{\partial^2 u}{\partial x^2} + \frac{\partial^2 u}{\partial y^2}\right). \tag{3.4}$$

Again taking $\frac{\partial p}{\partial z} = -c$, we have

$$\frac{\partial u}{\partial t} = \frac{\eta_S}{\rho}\left(\frac{\partial^2 u}{\partial x^2} + \frac{\partial^2 u}{\partial y^2}\right) + \frac{c}{\rho} \tag{3.5}$$

with the initial and boundary conditions given by

- Initial condition: $u(x, y, 0) = 0$,
- Boundary conditions: $u(-a, y, t) = u(a, y, t) = u(x, -b, t) = u(x, b, t) = 0$.

Due to the unavailability of the analytical solution for the time-dependent problem, this problem will be solved until it reaches steady-state to compare with the available analytical solution. The exact solution at steady-state is [36]

$$u(x, y) = \frac{16a^2 c}{\eta_S \pi^3} \sum_{i=1,3,5,\ldots}^{+\infty} (-1)^{\frac{i-1}{2}} \left[1 - \frac{\cosh(\frac{i\pi y}{2a})}{\cosh(\frac{i\pi b}{2a})}\right] \frac{\cos(\frac{i\pi x}{2a})}{i^3}. \tag{3.6}$$

3.1.3 Oldroyd-B Channel flow

We now consider extending the one-dimensional channel flow problem to the Oldroyd-B model. For a general flow the governing equations are given by

$$\nabla \cdot \mathbf{u} = 0$$

$$\rho\left(\frac{\partial \mathbf{u}}{\partial t} + \mathbf{u} \cdot \nabla \mathbf{u}\right) = -\nabla p + \nabla \cdot \boldsymbol{\tau}$$

$$\boldsymbol{\tau} = \eta_S[(\nabla \mathbf{u}) + (\nabla \mathbf{u})^T] + G\mathbf{A}$$

$$\frac{\partial \mathbf{A}}{\partial t} + (\mathbf{u} \cdot \nabla)\mathbf{A} - \mathbf{A} \cdot \nabla \mathbf{u} - (\nabla \mathbf{u})^T \cdot \mathbf{A} = -\frac{1}{\lambda}(\mathbf{A} - \mathbf{I})$$

where $\boldsymbol{\tau}$ is the total stress, $\mathbf{A}$ is the polymer conformation tensor. Here, η_S is the solvent viscosity, G is the elastic modulus and λ is the relaxation time. The polymer viscosity is given by $G\lambda$ so that the total viscosity is $\eta_S + G\lambda$.

Extending the one-dimensional channel flow equation described in the earlier section to the Oldroyd-B model, since $\mathbf{u} = [u(y,t), 0]$, from flow symmetry it follows that the deformation tensor is of the form, $\mathbf{A} = \begin{pmatrix} A_{xx} & A_{xy} & 0 \\ A_{xy} & A_{yy} & 0 \\ 0 & 0 & A_{zz} \end{pmatrix}$, where $\mathbf{A}$ is a function only of y and t. The momentum equation therefore reduces to

$$\rho \frac{\partial u}{\partial t} = -\frac{\partial p}{\partial x} + \frac{\partial \tau_{xy}}{\partial y}, \tag{3.7}$$

where τ_{xy} for the Oldroyd-B model is given by

$$\tau_{xy} = \eta_S \frac{\partial u}{\partial y} + G A_{xy}.$$

Substituting τ_{xy} into (3.7) with $\frac{\partial p}{\partial x} = -c$ gives the following

$$\rho \frac{\partial u}{\partial t} = c + \eta_S \frac{\partial^2 u}{\partial y^2} + G \frac{\partial A_{xy}}{\partial y} \ , \tag{3.8}$$

where A_{xy} satisfies the following constitutive equation

$$\frac{\partial A_{xy}}{\partial t} = -\frac{1}{\lambda} A_{xy} + \frac{\partial u}{\partial y} \ , \tag{3.9}$$

since $A_{yy} = 1$. The problem is solved within the range of $\pm h$ in the $y-$direction. We specify the boundary and initial conditions as

- Initial condition: $u(y,0) = 0$ and $A_{xy}(y,0) = 0$,
- Boundary condition: $u(-h,t) = u(h,t) = 0$.

The analytical solution available from [47] is given as follows

$$u(y,t) = \frac{c(h^2 - y^2)}{2(\eta_S + G\lambda)} - 48 \sum_{n'=1}^{\infty} \left[\frac{1}{n^3} \sin\left(\frac{n(1 + \frac{y}{h})}{2} \right) \right] e^{-(\frac{\alpha_n t}{2\lambda})} W\left(\frac{t}{\lambda} \right) \ . \tag{3.10}$$

The definition of $W(\frac{t}{\lambda})$ depends on the elasticity number. For $\alpha_n^2 - En^2 \geq 0$, and Elasticity number, $E = \frac{\lambda(\eta_S + G\lambda)}{\rho h^2}$,

$$W\left(\frac{t}{\lambda}\right) = \cosh\left(\frac{\beta_n t}{2\lambda}\right) + \frac{\gamma_n}{\beta_n}\sinh\left(\frac{\beta_n t}{2\lambda}\right), \tag{3.11}$$

$$n = (2n' - 1)\pi, \quad \alpha_n = 1 + \frac{1}{4}\beta En^2, \quad \beta_n = \sqrt{\alpha_n^2 - En^2}, \quad \gamma_n = 1 - \frac{1}{4}(2 - \beta)En^2 ,$$

whereas if $\alpha_n^2 - En^2 < 0$, then

$$W\left(\frac{t}{\lambda}\right) = \cos\left(\frac{\beta_n t}{2\lambda}\right) + \frac{\gamma_n}{\beta_n}\sin\left(\frac{\beta_n t}{2\lambda}\right),$$

where $\beta_n = \sqrt{En^2 - \alpha_n^2}$ and β is the retardation ratio defined as $\frac{\eta_S}{\eta_S + G\lambda}$ where η_S is the viscosity of the solvent and $\eta_S + G\lambda$ is the total viscosity.

3.2 Temporal discretisation

In order to solve equation (3.2), (3.5), (3.8) and (3.9) numerically we must introduce a discretisation both in space and time. Discretisation in space, either through finite differences or finite elements, has the effect of replacing the continuous variable $u(\underline{x}, t)$ with an array $\underline{\bar{u}}^{(t)}$ of the velocities at the mesh nodes where $\underline{\bar{u}}$ satisfies an equation of the form

$$\mathbf{M}\frac{d\underline{\bar{u}}}{dt} = -\mathbf{K}\underline{\bar{u}} + f,$$

where $\mathbf{M}$ and $\mathbf{K}$ are symmetric and positive definite matrices. Applying the $\theta-$method discretisation in time, the equation then becomes

$$\mathbf{M}\frac{\underline{\bar{u}}^{n+1} - \bar{u}^n}{\Delta t} = (1 - \theta)(-\mathbf{K}\underline{\bar{u}}^n) + \theta(-\mathbf{K}\underline{\bar{u}}^{n+1}) + f,$$

where Δt is the time step and $0 \geq \theta \geq 1$, which can be rearranged and yields the following general numerical (finite element) scheme

$$(\mathbf{M} + \Delta t\theta\mathbf{K})\underline{\bar{u}}^{n+1} = (\mathbf{M} - \Delta t(1-\theta)\mathbf{K})\underline{\bar{u}}^{n} + \Delta t f. \tag{3.12}$$

The symmetric and positive definite matrices of the system is ensured provided $\theta \geq 0$. Different values of θ are chosen to illustrate the performance of the numerical approximation based on the order of accuracy. The details of the numerical schemes for both finite difference and finite element are presented in the next subsection while the results for solving one- and two-dimensional problems are available in the section that follows.

3.3 The numerical schemes

The numerical schemes for different time discretisation techniques for one- and two-dimensional channel flow problem in equation (3.2), (3.5), (3.8) and (3.9) are described in the following subsections.

3.3.1 One-dimensional finite difference scheme for Newtonian fluid problem

The one-dimension channel flow problem for Newtonian fluid in equation (3.2) can be non-dimensionalised to

$$\frac{\partial u}{\partial t} - \nu\frac{\partial^2 u}{\partial y^2} = 1. \tag{3.13}$$

Applying the temporal and spatial discretisation using FDM, for FTCS explicit scheme, this yields

$$\underbrace{\frac{u_j^{n+1} - u_j^n}{\Delta t}}_{\text{Forward Time}} = \nu \underbrace{\frac{u_{j+1}^n - 2u_j^n + u_{j-1}^n}{\Delta y^2}}_{\text{Centred Space}} + 1 + \underbrace{\mathcal{O}(\Delta t, \Delta y^2)}_{\text{Order of accuracy}}. \tag{3.14}$$

Note that, from equation (3.14), the forward difference in time and central difference in space is used to discretise the partial derivative. This scheme is explicit because the velocity u_i^{n+1} at the next time step $(n+1)$ can be solved explicitly due to the availability of the known quantities from the previous time step (n). However, this scheme proved to be conditionally stable from von Neumann stability analysis [105]. On the other hand, the implicit scheme is obtained when the backward difference approximation is used for temporal discretisation

and central difference approximation in spatial discretisation. Now, the implicit scheme becomes

$$\underbrace{\frac{u_j^{n+1}-u_j^n}{\Delta t}}_{\text{Backward Time}} = \nu \underbrace{\frac{u_{j+1}^{n+1}-2u_j^{n+1}+u_{j-1}^{n+1}}{\Delta y^2}}_{\text{Centred Space}} + 1 + \underbrace{\mathcal{O}(\Delta t, \Delta y^2)}_{\text{Order of accuracy}} . \tag{3.15}$$

Notice that now, the scheme consists of more nodal points at the next time step $(n+1)$. This scheme reduces to a set of linear equation which can be expressed in the form of $[\mathbf{A}]\{\mathbf{u}\} = \{\mathbf{b}\}$ where $\mathbf{A}$ is a tridiagonal matrix, $\{\mathbf{u}\}$ is the unknown vector and $\{\mathbf{b}\}$ is the known vector. Thomas algorithm [132] is often used to solve the tridiagonal system of linear equation since it is more efficient than Gaussian elimination. An alternative implicit scheme is a Crank-Nicolson method [33]. This method is second order accurate in both time and space and unconditionaly stable. The scheme can be written as

$$\frac{u_j^{n+1}-u_j^n}{\Delta t} = \underbrace{\frac{\nu}{2}\left[\frac{u_{j+1}^{n+1}-2u_j^{n+1}+u_{j-1}^{n+1}}{\Delta y^2} + \frac{u_{j+1}^{n}-2u_j^{n}+u_{j-1}^{n}}{\Delta y^2}\right]}_{\text{Average value - centred space}} + 1 + \underbrace{\mathcal{O}(\Delta t^2, \Delta y^2)}_{\text{Order of accuracy}} .$$

Similar to the backward Euler implicit scheme, the tridiagonal system of linear equation resulted in the Crank-Nicolson scheme can be solved using Thomas algorithm from Algorithm 3 in Appendix A.

For equally spaced points equation (3.2) reduces to the following numerical schemes,

- Explicit scheme: Forward Euler time discretisation with central difference approximation for spatial, (FTCS) when $\theta = 0$, the scheme reduces to

$$u_j^{n+1} = r\nu u_{j+1}^n + (1-2r\nu)u_j^n + r\nu u_{j-1}^n + \Delta t$$

  where $r = \frac{\Delta t}{(\Delta y)^2}$, suffix denotes spatial coordinate and superfix the time coordinate.

- Implicit scheme: Backward Euler time discretisation with central difference approximation for spatial, (BTCS) when $\theta = 1$, the scheme is

$$-r\nu u_{j+1}^{n+1} + (1+2r\nu)u_j^{n+1} - r\nu u_{j-1}^{n+1} = u_j^n + \Delta t.$$

Since this scheme is implicit, the Thomas algorithm (Algorithm 3 in Appendix A) is used to solve the resulting tridiagonal system.

- Implicit scheme: Crank-Nicolson time discretisation with central difference approximation for spatial when $\theta = \frac{1}{2}$, the scheme is

$$-r\nu u_{j+1}^{n+1} + (2 + 2r\nu)u_j^{n+1} - r\nu u_{j-1}^{n+1} = r\nu u_{j+1}^n + (2 - 2r\nu)u_j^n + r\nu u_{j-1}^n + 2\Delta t.$$

Pseudocode for these 3 schemes are presented as Algorithms 1,2,4 in Appendix A. The convergence and accuracy of these schemes is summarised in Table 1.

Table 3.1: The features of one-dimensional numerical schemes using finite difference method

Scheme	FTCS	BTCS	Crank-Nicolson
Method	Explicit	Implicit	Implicit
Taylor expansion	$u(y_j, t^n)$	$u(y_j, t^{n+1})$	$u(y_j, t^{n+\frac{1}{2}})$
Order of accuracy	$\mathcal{O}(\Delta t, \Delta y^2)$	$\mathcal{O}(\Delta t, \Delta y^2)$	$\mathcal{O}(\Delta t^2, \Delta y^2)$
Stability	cond. stable	uncond. stable	uncond. stable

The abbreviations cond. stable and uncond. stable in Table 3.1 and 3.2 refer to conditional and unconditional stability respectively, with respect to time step Δt.

3.3.2 Two-dimensional finite difference numerical schemes

Extending the one-dimensional channel flow problem to two-dimensional, the non-dimensionalised equation from equation (3.5) gives the following equation

$$\frac{\partial u}{\partial t} - \nu\left(\frac{\partial^2 u}{\partial x^2} + \frac{\partial^2 u}{\partial y^2}\right) = 1.$$

This problem can be solved using both explicit, fully implicit and semi-implicit method. However, solving the problem explicitly restricted to a choice of time step and spatial step which sometimes requires a small time step especially when the grid gets finer to ensure numerical stability. Since explicit scheme is first order accurate in time and second order accurate in space, when a smaller mesh grid size is used that is reduced by factor 2 from

the coarser mesh grid for example, the time step needs to be reduced by factor 4 to ensure stability of the numerical approximation. Otherwise, if the fully implicit backward Euler centred space (BTCS) scheme is used, for two-dimenisonal case, the system of linear equation resulting in pentadiagonal algebraic system that is computationally expensive.

Alternatively, the Alternating Direction Implicit (ADI) [108] scheme can be used to solve this problem. This scheme is unconditionally stable with order of accuracy, $\mathcal{O}(\Delta t^2, \Delta x^2, \Delta y^2)$. This scheme having two steps iteration process with two equations with $x-$ and $y-$sweep that solved the tridiagonal system independently. Each equation is solved at half time step. The two schemes can be written as

- The first half time

$$\frac{u_{i,j}^{n+\frac{1}{2}} - u_{i,j}^{n}}{\Delta t} = \frac{\nu}{2}\left(\frac{u_{i+1,j}^{n+\frac{1}{2}} - 2u_{i,j}^{n+\frac{1}{2}} + u_{i-1,j}^{n+\frac{1}{2}}}{\Delta x^2} + \frac{u_{i,j+1}^{n} - 2u_{i,j}^{n} + u_{i,j-1}^{n}}{\Delta y^2}\right) + \frac{1}{2}.$$

- The second half time

$$\frac{u_{i,j}^{n+1} - u_{i,j}^{n+\frac{1}{2}}}{\Delta t} = \frac{\nu}{2}\left(\frac{u_{i+1,j}^{n+\frac{1}{2}} - 2u_{i,j}^{n+\frac{1}{2}} + u_{i-1,j}^{n+\frac{1}{2}}}{\Delta x^2} + \frac{u_{i,j+1}^{n+1} - 2u_{i,j}^{n+1} + u_{i,j-1}^{n+1}}{\Delta y^2}\right) + \frac{1}{2}.$$

Notice that for the first half time step, the compact notation showing the implicit and explicit in $x-$ and $y-$direction respectively. The known vector in the $y-$direction for the first half time equation allows the solution in the $x-$direction from the first half time equation to be made. The results from the first half time step is then used to find the solution in the $y-$direction. The process is repeated until the whole two-dimensional domain is covered for every time step.

Thus we shall consider two finite difference numerical schemes for solving a two-dimensional channel flow problem: an explicit scheme which is computational cheap, but only conditionally stable and a semi-implicit numerical scheme called the Alternating Direction Implicit (ADI) method that is unconditionally stable.

- Explicit scheme: two-dimensional FTCS, $\theta = 0$

$$u_j^{n+1} = u_{i,j}^{n} + r_x\nu(u_{i-1,j}^{n} + 2u_{i,j}^{n} + u_{i+1,j}^{n}) + r_y\nu(u_{i,j-1}^{n} - 2u_{i,j}^{n} + u_{i,j+1}^{n}) + \Delta t$$

- Semi-implicit scheme: two-dimensional ADI scheme.

  For $\theta > 0$, the resulting linear system involves the inversion of a sparse matrix. However unconditional stability can be achieved using a two-step semi-implicit scheme in which the x, and y directions are solved consecutively. This is presented in the following points.

  ⋆ First half-time ($x-$sweep)

$$\underbrace{-\frac{\nu r_x}{2}(u_{i-1,j}^{n+\frac{1}{2}} + u_{i+1,j}^{n+\frac{1}{2}}) + (1+\nu r_x)u_{i,j}^{n+\frac{1}{2}}}_{x\text{-direction - implicit}} = \underbrace{\frac{\nu r_y}{2}(u_{i,j-1}^{n} + u_{i,j+1}^{n}) + (1-\nu r_y)u_{i,j}^{n} + \frac{\Delta t}{2}}_{y\text{-direction - explicit}}.$$

  ⋆ Second half-time ($y-$sweep)

$$\underbrace{-\frac{\nu r_y}{2}(u_{i,j-1}^{n+1} + u_{i,j+1}^{n+1}) + (1+\nu r_y)u_{i,j}^{n+1}}_{\text{unknown}} = \underbrace{\frac{\nu r_x}{2}(u_{i-1,j}^{n+\frac{1}{2}} + u_{i+1,j}^{n+\frac{1}{2}}) + (1-\nu r_x)u_{i,j}^{n+\frac{1}{2}} + \frac{\Delta t}{2}}_{\text{known-obtained from first step}}.$$

  From the numerical scheme for the first and second half-time, $r_x = \frac{\Delta t}{(\Delta x)^2}$ and $r_y = \frac{\Delta t}{(\Delta y)^2}$.

We summarise the features of the numerical schemes in Table 3.2.

Table 3.2: The features of two-dimensional numerical schemes using finite difference method

Scheme	FTCS	ADI
Method	Explicit	Semi-implicit
Taylor expansion	$u(x_{i,j}, t^n)$	$u(x_{i,j}, t^{n+\frac{1}{2}})$
Order of accuracy	$\mathcal{O}(\Delta t, \Delta x^2, \Delta y^2)$	$\mathcal{O}(\Delta t^2, \Delta x^2, \Delta y^2)$
Stability	cond. stable	uncond. stable

In the next subsection, the finite element spatial discretisation for one- and two-dimensional models are presented with respective numerical schemes.

3.3.3 One-dimensional finite element numerical scheme

For solution by finite elements, we define a set of basis functions, $N_i(y)$ such that $u(y,t) = \bar{u}_i(t)N_i(y)$ where the summation convention is assumed and $N_i(y)$ is a linear function which

has value 1 at i^{th} node of the mesh and zero elsewhere. Then the Galerkin weak form gives

$$\left(\int_{-h}^{h} N_j N_i dy\right)\frac{\partial \overline{u}_i}{\partial t} = -\nu\left(\int_{-h}^{h} \frac{\partial N_j}{\partial y}\frac{\partial N_i}{\partial y}dy\right)\overline{u}_i + \cancelto{0}{\left[\nu N_j \frac{\partial u}{\partial y}\right]_{-h}^{h}} + f_j, \tag{3.16}$$

applying Dirichlet boundary condition so that $N_j = 0$ on $y = \pm h$. Equation (3.16) then becomes

$$\left(\int_{-h}^{h} N_j N_i dy\right)\frac{\partial \overline{u}_i}{\partial t} = -\nu\left(\int_{-h}^{h} \frac{\partial N_j}{\partial y}\frac{\partial N_i}{\partial y}dy\right)\overline{u}_i + f_j. \tag{3.17}$$

Over the whole domain, Ω, equation (3.17) reduces to the following system of ordinary differential equations that is written as

$$\mathbf{M}_1\frac{\partial \underline{\bar{u}}}{\partial t} = -\mathbf{K}_1\underline{\bar{u}} + \underline{f}$$

where

$$M_{ji} = \int_{-h}^{h} N_j N_i dy, \qquad K_{ji} = \nu\int_{-h}^{h} \frac{\partial N_j}{\partial y}\frac{\partial N_i}{\partial y}dy, \quad \text{and} \quad f_j = \int_{-h}^{h} N_j dy.$$

Now applying the θ method, we obtain

$$(\mathbf{M} + \theta\Delta t\mathbf{K})\underline{\bar{u}}^{n+1} = (\mathbf{M} - (1-\theta)\Delta t\mathbf{K})\underline{\bar{u}}^{n} + \Delta t\underline{f}.$$

For different temporal discretisation technique following the θ-method, the three numerical schemes are presented as follows

- Explicit scheme: Explicit Euler numerical scheme when $\theta = 0$ is

$$\mathbf{M}_1\underline{\bar{u}}^{n+1} = (\mathbf{M}_1 - \Delta t\mathbf{K}_1)\underline{\bar{u}}^{n} + \Delta t\underline{f}$$

- Implicit scheme: Implicit numerical scheme when $\theta = 1$ is

$$(\mathbf{M}_1 + \Delta t\mathbf{K}_1)\underline{\bar{u}}^{n+1} = \mathbf{M}_1\underline{\bar{u}}^{n} + \Delta t\underline{f}$$

- Implicit scheme: Crank-Nicolson numerical scheme when $\theta = \frac{1}{2}$ is

$$(\mathbf{M}_1 + \frac{1}{2}\Delta t\mathbf{K}_1)\underline{\bar{u}}^{n+1} = (\mathbf{M}_1 - \frac{1}{2}\Delta t\mathbf{K}_1)\underline{\bar{u}}^{n} + \Delta t\underline{f}$$

3.3.4 Two-dimensional finite element numerical schemes

For solving a two-dimensional channel flow problem, the domain is divided into a number of triangular element with basis function, $N(\underline{x})$ (where $\underline{x} = (x, y)$) such that the fluid velocity can be written as $u(\underline{x}, t) = \sum N(\underline{x})\overline{u}(t)$ and $\overline{u}(t_n) = \overline{u}^n$. The Galerkin weak formulation for the two dimensional channel flow problem can then be written as follows

$$\int_\Omega N_j \frac{\partial u_i}{\partial t} N_i d\Omega = \nu \int_S N_j u_i \nabla N_i \cdot dS - \nu \int_\Omega \nabla N_j \cdot \nabla N_i u_i d\Omega + \int_\Omega N_j d\Omega \tag{3.18}$$

which implies

$$\left(\int_\Omega N_j N_i d\Omega\right)\frac{\partial u_i}{\partial t} = -\nu\left(\int_\Omega \nabla N_j \cdot \nabla N_i d\Omega\right)u_i + \nu \cancelto{0}{\int_S N_j \frac{\partial u}{\partial n} dS} + f, \tag{3.19}$$

where N_j is a basis function taken the value 1 at the j^{th} node and the basis function for a triangular element, N_i is defined as

$$N_i = \frac{a_i + b_i x + c_i y}{2A}, \text{ for } i = 1, 2, 3 \text{ is the vertices of an element}$$

where

$$a_1 = s_{2x}s_{3y} - s_{3x}s_{2y} \quad , \quad b_1 = s_{2y} - s_{3y} \quad , \quad c_1 = s_{3x} - s_{2x}$$

$$a_2 = s_{3x}s_{1y} - s_{1x}s_{3y} \quad , \quad b_2 = s_{3y} - s_{1y} \quad , \quad c_2 = s_{1x} - s_{3x}$$

$$a_3 = s_{1x}s_{2y} - s_{2x}s_{1y} \quad , \quad b_3 = s_{1y} - s_{2y} \quad , \quad c_2 = s_{2x} - s_{1x},$$

and A is the area of an element defined as

$$2A = c_3b_2 - c_2b_3 = |(s_2 - s_1) \times (s_3 - s_1)| = 2 \times \text{Area}(\Omega_e),$$

where s_{ix} and s_{iy}, for $i = 1, 2, 3$ represent the coordinate of the three vertices for each of the triangular element.

For Dirichlet boundary condition again we get

$$\mathbf{M}_2 \frac{d\underline{u}}{dt} = -\mathbf{K}_2\underline{u} + \underline{f}$$

where the Galerkin mass matrix, $\mathbf{M_2}$, and global stiffness matrix, $\mathbf{K_2}$ are given as

$$\mathbf{M}_2 = \int_\Omega N_j N_i d\Omega; \qquad \mathbf{K}_2 = \nu \int_\Omega \nabla N_j \cdot \nabla N_i d\Omega \qquad \& \qquad f = \int_\Omega N_j d\Omega.$$

The explicit and implicit numerical schemes for two-dimensional finite element channel flow problem when $\nu = 1.0$ are defined as

- Explicit scheme: Forward Euler numerical scheme when $\theta = 0$ is

$$\mathbf{M}_2\bar{\underline{u}}^{n+1} = (\mathbf{M}_2 - \Delta t\mathbf{K}_2)\bar{\underline{u}}^n + \Delta t\underline{f}$$

- Implicit scheme: Backward Euler numerical scheme when $\theta = 1$ is

$$(\mathbf{M}_2 + \Delta t\mathbf{K}_2)\bar{\underline{u}}^{n+1} = \mathbf{M}_2\bar{\underline{u}}^n + \Delta t\underline{f}$$

- Implicit scheme: Crank Nicolson numerical scheme when $\theta = \frac{1}{2}$ is

$$(\mathbf{M}_2 + \frac{1}{2}\Delta t\mathbf{K}_2)\bar{\underline{u}}^{n+1} = (\mathbf{M}_2 - \frac{1}{2}\Delta t\mathbf{K}_2)\bar{\underline{u}}^n + \Delta t\underline{f}.$$

We have now described the methodology to generate the numerical schemes using different spatial and temporal discretisation approaches for one- and two-dimensional channel flow problem for Newtonian fluid. In the next subsection, we will derive the numerical schemes for one-dimensional channel flow for Oldroyd-B model.

3.3.5 Channel flow for Oldroyd-B

We used a staggered grid finite difference method for spatial discretisation where the stress conformation shear component, A_{xy}, for the Oldroyd-B viscoelastic constitutive model is defined at points that are intermediate between points where u are defined in Figure 3.1.

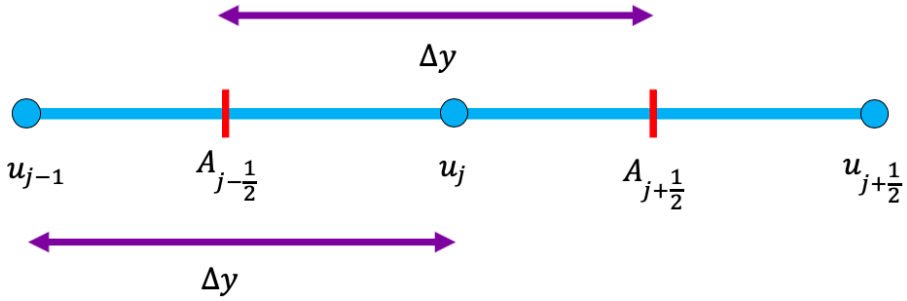

Figure 3.1: Staggered grid approach used to solve the one-dimensional channel flow problem for Oldroyd-B model.

The finite difference numerical schemes based on this spatial discretisation strategy (for both momentum and conformation stress equation) are defined as follows, where $r_1 = \frac{\Delta t}{(\Delta y)^2}$, $r_2 = \frac{\Delta t}{\rho \Delta y}$, $r_3 = \frac{c\Delta t}{\rho}$, $s_1 = \frac{\Delta t}{\lambda}$ and $s_2 = \frac{\Delta t}{\Delta y}$.

- Explicit scheme: The momentum equation in equation (3.8) is discretised using forward Euler in the following manner

$$u_j^{n+1} = \nu r_1 (u_{j+1}^n - 2u_j^n + u_{j-1}^n) + Gr_2 (A_{j+\frac{1}{2}}^n - A_{j-\frac{1}{2}}^n) + r_3 + u_i^n.$$

  On the other hand, the stress equation from equation (3.9) is discretised as

$$A_{j+\frac{1}{2}}^{n+1} = -s_1 A_{j+\frac{1}{2}}^n + s_2 (u_{j+1}^n - u_j^n) + A_{j+\frac{1}{2}}^n.$$

- Implicit scheme: The momentum equation in equation (3.8) is discretised using backward Euler in the following manner

$$-\nu r_1 u_{j-1}^{n+1} + (1 + 2\nu r_1) u_j^{n+1} - \nu r_1 u_{j+1}^{n+1} + Gr_2 A_{j-\frac{1}{2}}^{n+1} - Gr_2 A_{j+\frac{1}{2}}^{n+1} = u_i^n + r_3$$

and the discretised stress equation from equation (3.9) as

$$s_2 u_j^{n+1} - s_2 u_{j+1}^{n+1} + (s_1 + 1) A_{j+\frac{1}{2}}^{n+1} = A_{j+\frac{1}{2}}^{n}.$$

These numerical schemes are used to get the approximate solution for one- and two-dimensional channel flow problems and the order of accuracy for each scheme are observed. The results are presented and discussed in the following section.

3.4 Results and discussion

The results for the one- and two-dimensional channel flow problem for Newtonian fluid are solved using different numerical schemes discussed from the previous section. This is then followed by the numerical results for one-dimensional non-Newtonian fluid for the Oldroyd-B model that is solved using the finite difference approach with forward and backward Euler time discretisation. The comparison for different spatial discretisation techniques, including the finite volume approach used in the RheoTool solver `rheoFoam`, against the analytical solution for both Newtonian and non-Newtonian flows are presented by plotting the transient velocity at the centre point.

3.4.1 Finite difference numerical approximation for one-dimensional channel flow problem

To examine the accuracy of the solutions we shall compare the value for the fluid velocity at $y = 0$ at $t = 1$. For a Newtonian fluid with $\nu = 1$ the exact solution to 10 significant figures is given by $u(0.0, 1.0) = 0.4562385522$. The numerical simulation with different values of the spatial step (Δy) and time step (Δt) are carried out to observe the order of accuracy for each schemes by looking at the absolute error column. Note that, the absolute error is simply defined by Error $= |u(y,t) - u(y_j, t^n)|$ where $u(y,t)$ is the exact solution and $u(y_j, t^n)$ is the approximate solution obtained from the numerical scheme at value of the measured y position with respective time. The results are recorded in the Table 3.3, 3.4 and 3.7.

In Table 3.3, we have varied both Δy and Δt to keep $r = \frac{\Delta t}{(\Delta y)^2}$ constant. This is necessary to ensure the stability of the FTCS numerical scheme, but as both the BTCS and

Crank-Nicolson are unconditionally stable, we provide additional results which demonstrates the behaviour of the error where Δy and Δt are varied independently in Table 3.5, 3.6, 3.8 and 3.9.

Table 3.3: The FTCS finite difference approximate solution and the error for one-dimensional channel flow problem.

Δy	Δt	r	$u(0.0, 1.0)$	Error
0.1	2.5×10^{-3}	0.25	0.45634971	1.112×10^{-4}
0.05	6.25×10^{-4}	0.25	0.45626631	2.776×10^{-5}
0.025	1.5625×10^{-4}	0.25	0.45624549	6.939×10^{-6}
0.0125	3.90625×10^{-5}	0.25	0.45624029	1.735×10^{-6}

Table 3.4: The BTCS finite difference approximate solution and the error for one-dimensional channel flow problem.

Δy	Δt	r	$u(0.0, 1.0)$	Error
0.1	1.0×10^{-2}	1.0	0.45468461	1.554×10^{-3}
0.05	2.5×10^{-3}	1.0	0.45585002	3.885×10^{-4}
0.025	6.25×10^{-4}	1.0	0.45614141	9.713×10^{-5}
0.0125	1.5625×10^{-4}	1.0	0.45621427	2.428×10^{-5}

Based on the accuracy obtained from Taylor's series expansion, both FTCS and BTCS numerical schemes have the same order of accuracy that is first order accurate in time and second order accurate in space (i.e. $\mathcal{O}(\Delta t, \Delta y^2)$). The only difference is the choice for Δt in FTCS is restricted to being smaller than or equal to $2r(\Delta y)^2$ to ensure numerical stability. From Table 3.3 and 3.4, it can be seen that by reducing the value of the grid size by factor 2 and time step by factor 4, the error is reduced consistently by factor 4 as expected.

The results presented in Table 3.5 and 3.6 show the effect of varying spatial and temporal discretisation on the error contribution. This is done by looking at the effect of varying the time step with the fixed value of spatial step and varying the spatial step with the fixed value of temporal discretisation.

Table 3.5: The BTCS finite difference approximate solution and the error for the channel flow problem when $\Delta y = 0.025$ and time step is varied.

Δt	r	$u(0.0, 1.0)$	Error
1.0×10^{-2}	16.0	0.45489418	1.344×10^{-3}
2.5×10^{-3}	4.0	0.45589173	3.468×10^{-4}
6.25×10^{-4}	1.0	0.45614142	9.713×10^{-5}
1.5625×10^{-4}	0.25	0.45620386	3.469×10^{-5}

In Table 3.5, when the spatial step is fixed to $\Delta y = 0.025$ while the time step is varied (and reduced) by a factor 4, we see error is reduced by factor slightly less than four. This is still consistent with the scheme being first order in time, but the absolute error also contains a contribution from the spatial discretisation which is present even in the limit $\Delta t \to 0$.

Table 3.6: The BTCS finite difference approximate solution and the error for the channel flow problem when $\Delta t = 6.25 \times 10^{-4}$ and spatial step is varied.

Δy	r	$u(0.0, 1.0)$	Error
0.1	0.0625	0.45593293	3.056×10^{-4}
0.05	0.25	0.45609976	1.388×10^{-4}
0.025	1.0	0.45614142	9.713×10^{-5}
0.0125	4.0	0.45615183	8.672×10^{-5}

On the other hand, when Δt is fixed to $\Delta t = 6.25 \times 10^{-4}$ and Δy is varies in the range of $\Delta y = 0.1, 0.05, 0.025, 0.0125$, it produces the results for the error presented in Table 3.6. For larger values of Δy the error decreases roughly in proportion to Δy^2 however between 0.025 and 0.0125 there is only a small improvement as the error is now dominated by the time discretisation.

Table 3.7: The Crank-Nicolson finite difference approximate solution and the error for one-dimensional channel flow problem.

Δy	Δt	r	$u(0.0, 1.0)$	Error
0.1	1.0×10^{-2}	1.0	0.45602174	2.168×10^{-4}
0.05	5.0×10^{-3}	2.0	0.45618440	5.415×10^{-5}
0.025	2.5×10^{-3}	4.0	0.45622502	1.353×10^{-5}
0.0125	1.25×10^{-3}	8.0	0.45623517	3.38×10^{-6}

Both the FTCS and BTCS are first order in time and second order in space. However the Crank-Nicolson scheme is expected to second order accurate in both time and space. This is illustrated in Table 3.8 where a decrease in the values of Δy and Δt by a factor 2 reduces the error by approximately a factor 4.

Table 3.8: The Crank-Nicolson finite difference approximate solution and the error for one-dimensional channel flow problem when $\Delta y = 0.025$ and time step is varied.

Δt	r	$u(0.0, 1.0)$	Error
1.0×10^{-2}	16.0	0.45623015	8.399×10^{-6}
5.0×10^{-3}	8.0	0.45622604	1.251×10^{-5}
2.5×10^{-3}	4.0	0.45622502	1.353×10^{-5}
1.25×10^{-3}	2.0	0.45622476	1.379×10^{-5}

If the spatial step is fixed to $\Delta y = 0.025$ and the value of Δt is varied by reducing by factor 2 as recorded in Table 3.8, reducing the time step below 5.0×10^{-3} has little effect on the error as it is dominated by the spatial discretisation error. On the other hand, in Table 3.9, when the temporal step is fixed to $\Delta t = 6.25 \times 10^{-4}$ and spatial step is decreased by factor 2, the error is reduced consistently by factor 4. With the evidence in Table 3.8 and 3.9, this suggests that the spatial step dominates the error since the temporal discretisation is more accurate in the Crank-Nicolson scheme than the BTCS numerical scheme.

Table 3.9: The Crank-Nicolson finite difference approximate solution and the error for one-dimensional channel flow problem when $\Delta t = 6.25 \times 10^{-4}$ and spatial step is varied.

Δy	r	$u(0.0, 1.0)$	Error
0.1	0.25	0.45601629	2.222×10^{-4}
0.05	1.0	0.45618305	5.55×10^{-5}
0.025	4.0	0.45622470	1.386×10^{-5}
0.0125	16.0	0.45623510	3.45×10^{-6}

It is worth mentioning that the advantage of the numerical stability for the Crank-Nicolson and BTCS scheme allows the use of larger time step during the computation which produces the numerical solution more efficiently. However both schemes are implicit and so in one-dimension require the solution of a tridiagonal system.

3.4.2 Finite element numerical approximation for one-dimensional channel flow problem

We now repeat this error analysis for the finite element method again by examining the value at $u(0, 1)$ where the exact solution is 0.4562385522 to 10 significant figures when $\nu = 1.0$. Although we have implemented both forward and backward Euler time discretisation, we shall only consider the results for the Crank-Nicolson scheme, for which the error should be second order in both space and time.

Table 3.10: The Crank-Nicolson time integration finite element approximation and the error for one-dimensional channel flow problem.

Δy	Δt	$u(0.0, 1.0)$	Error
0.1	1.0×10^{-2}	0.4564657849	2.272×10^{-4}
0.05	5.0×10^{-3}	0.4562954099	5.686×10^{-5}
0.025	2.5×10^{-3}	0.4562527697	1.422×10^{-5}
0.0125	1.25×10^{-3}	0.4562421067	3.555×10^{-6}

Table 3.10 demonstrates that the error decreases by a factor of 4 as the spatial and time is reduced by factor 2 going down the table. Moreover comparing the absolute values of the errors between Table 3.10 and 3.7 we see that the finite element and finite difference

schemes provide absolute errors that a very similar at the same resolution. This can also be seen when we compare the error for a fixed time step of $\Delta t = 6.25 \times 10^{-4}$ between Table 3.9 and 3.11.

Table 3.11: The Crank-Nicolson time integration finite element approximation and the error for one-dimensional channel flow problem when $\Delta t = 6.25 \times 10^{-4}$ and spatial step is varies.

Δy	$u(0.0, 1.0)$	Error
0.1	0.4564603221	2.218×10^{-4}
0.05	0.4562940614	5.551×10^{-5}
0.025	0.4562524487	1.390×10^{-5}
0.0125	0.4562420425	3.490×10^{-6}

Thus for this simple one-dimensional problem the finite element scheme produces results of equivalent accuracy to the finite difference scheme at the same level of resolution.

3.4.3 Finite difference numerical approximation for two-dimensional Channel flow problem

We next examine the solution for the flow in a square channel. Since a transient analytical solution is unavailable for this problem, we will compare the computed solutions with a steady-state analytical solution presented in equation (3.6). At the point $x = 0$ and $y = 0$, $u = 0.2946851553$ to 10 significant figure. Two different numerical schemes the FTCS and ADI are used to solve the two-dimensional channel flow problem where the results for accuracy are presented in Table 3.12 and 3.13 respectively.

Table 3.12: The forward Euler time integration finite element approximation and the error for two-dimensional channel flow problem.

$\Delta x \& \Delta y$	Δt	$r_x \& r_y$	$u(0.0, 0.0, 7.0)$	Error
0.1	2.5×10^{-3}	0.25	0.29410684	5.783×10^{-4}
0.05	6.25×10^{-4}	0.25	0.29454041	1.448×10^{-4}
0.025	1.5625×10^{-4}	0.25	0.29464914	3.602×10^{-5}
0.0125	3.90625×10^{-5}	0.25	0.29467634	8.82×10^{-6}

Table 3.12 reveals the accuracy of the two-dimensional FTCS method that is second-

order accurate in space, $\mathcal{O}(\Delta x^2, \Delta y^2)$. This can be seen when Δx and Δy are reduced by factor 2 (and Δt is reduced by factor 4), the error column is showing a consistent error reduction that is by factor 4.

Table 3.13: The ADI finite difference approximate solution and the error for the two-dimensional channel flow problem.

$\Delta x \& \Delta y$	Δt	$r_x \& r_y$	$u(0.0, 0.0, 7.0)$	Error
0.1	1.0×10^{-2}	1.0	0.29410684	5.783×10^{-4}
0.05	5.0×10^{-3}	2.0	0.29454041	1.448×10^{-4}
0.025	2.5×10^{-3}	4.0	0.29464914	3.602×10^{-5}
0.0125	1.25×10^{-3}	8.0	0.29467634	8.82×10^{-6}

The order of accuracy from the Taylor's series expansion for ADI scheme is second-order accurate in both temporal and spatial, that is $\mathcal{O}(\Delta t^2, \Delta x^2, \Delta y^2)$. The error columns in Table 3.13 reveals that the error is reduced by factor 4 as a consequence of reducing Δx,Δy and Δt by factor 2 which confirms the order of accuracy being second-order accurate in space and time. However it should be noted that since the calculations are run to steady-state that the temporal accuracy is not really being tested here.

Notice that, Table 3.12 and 3.13 give identical values of fluid velocity at the same resolution regardless of the different time integration schemes used. This is because the spatial discretisation is identical.

3.4.4 Finite element numerical approximation for two-dimensional Channel flow problem

We have also considered this problem using the two dimensional finite element scheme, using a square lattice divided into pairs of triangular finite elements. This is shown in Figure 3.2 where uniform refinement of the mesh for two-dimensional domain is discretised using the triangular mesh type. The detail of the data used to approximate the solution is recorded in Table 3.14 and these data are obtained from the in-house Fortran code. The data used to approximate the solution at this point is summarised as follows

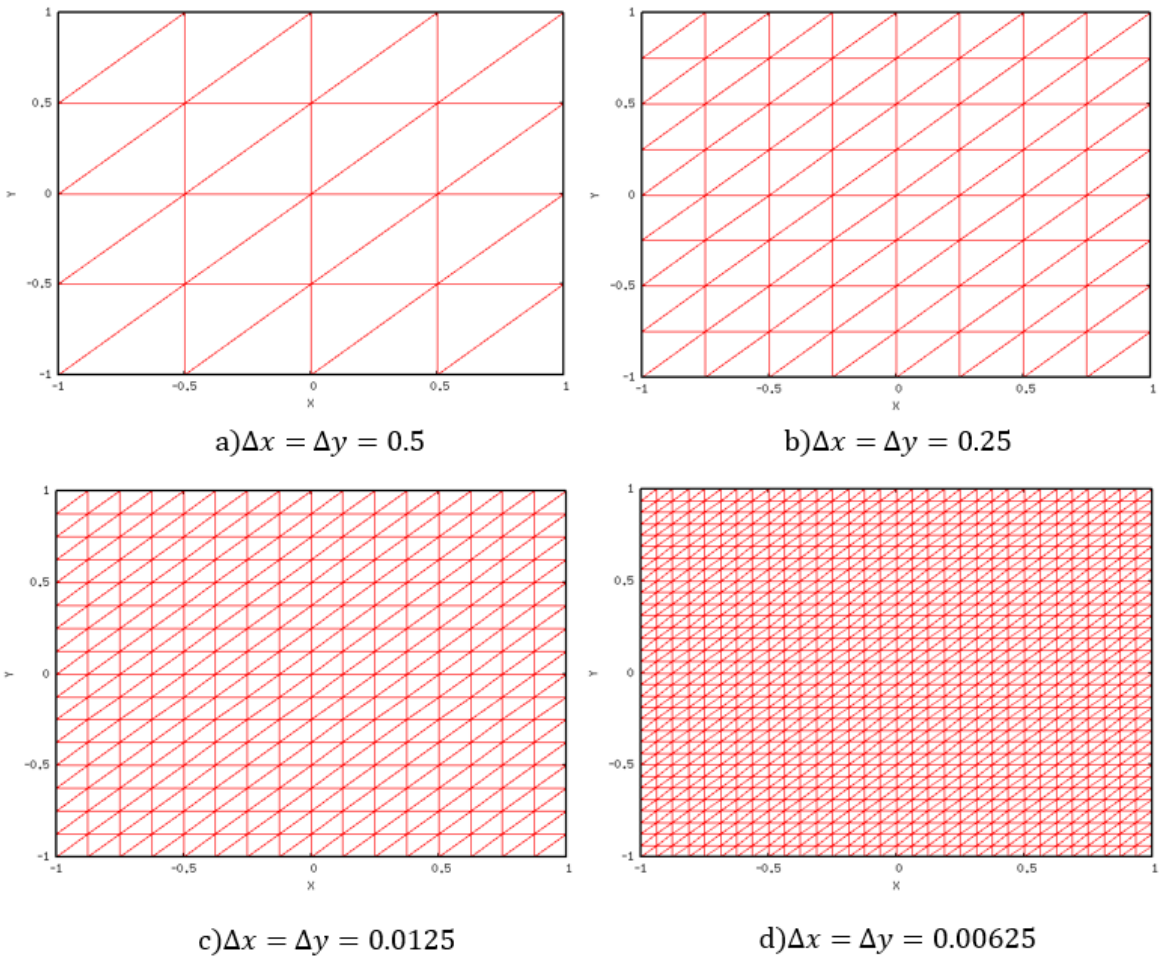

Figure 3.2: The refinement of the mesh for two-dimensional finite element with triangular mesh type.

Table 3.14: The data for solving two-dimensional channel flow problem using finite element approximation.

Δx & Δy	Element	Point	Boundary	Int. point	Int. matrix
0.5	32	25	16	9	9×9
0.25	128	81	32	49	49×49
0.125	512	289	64	225	225×225
0.0625	2048	1089	128	961	961×961

Table 3.15: The Crank-Nicolson time integration finite element approximate solution and the error for two-dimensional channel flow problem.

Δx & Δy	Δt	$u(0.0, 0.0, 7.0)$	Error
0.5	1.0×10^{-2}	0.28125	1.3435×10^{-2}
0.25	5.0×10^{-3}	0.291130514	3.5546×10^{-3}
0.125	2.5×10^{-3}	0.2937830663	9.02089×10^{-4}
0.0625	1.25×10^{-3}	0.2944589494	2.262×10^{-4}

We have implemented Forward, Backward Euler and Crank-Nicolson schemes, however the same value of error for the steady-state solution is found with all three schemes so only show the results for Crank-Nicolson scheme. Interpolating the results between Δx, Δy of 0.125 and 0.0625 in the Table 3.15 we find that the error for $\Delta x = \Delta y = 0.1$ is consistent with the finite difference scheme. However, the finite element scheme is computationally more expensive due to the need to solve a linear system at each time step.

3.4.5 One-dimensional Channel flow problem for Oldroyd-B fluid

Finally we consider the solution to the one-dimensional channel flow problem for an Oldroyd-B fluid. We compare the solution at $y = 0$ for a fluid with parameters $\lambda = 1$, $G = 1$ and $\eta_S = 1.0$. The exact solution at $t = 1$, $u(0, \lambda) = 0.345058$. The forward and backward Euler prediction for different mesh grid sizes with the appropriate time step values simulated up to steady-state are presented in Table 3.16 and 3.17 respectively. It can be observed from the tables that it takes about four times the relaxation time to reach the steady-state where the velocity at this point $u(0, 4\lambda) \approx 0.25$ (the steady-state analytical solution).

Table 3.16: The forward Euler approximate solution for different time at point $u(0.0, t)$.

Δx	Δt	t= λ	t= 2λ	t= 4λ	t= 8λ	t= 16λ
0.1	2.5×10^{-3}	0.344108	0.263839	0.24943	0.249999	0.25
0.05	6.25×10^{-4}	0.343911	0.263943	0.249426	0.249999	0.25
0.025	1.5625×10^{-4}	0.343862	0.263969	0.249426	0.249999	0.25
0.0125	3.90625×10^{-5}	0.34385	0.263975	0.249425	0.249999	0.25

Table 3.17: The backward Euler approximate solution for different time at point $u(0.0, t)$.

Δx	Δ	t= λ	t= 2λ	t=4λ	t= 8λ	t= 16λ
0.1	1.0×10^{-2}	0.342788	0.264879	0.249384	0.249999	0.25
0.05	2.5×10^{-3}	0.343582	0.264205	0.249415	0.249999	0.25
0.025	6.25×10^{-4}	0.34378	0.264035	0.249423	0.249999	0.25
0.0125	1.5625×10^{-5}	0.343829	0.263992	0.249425	0.249999	0.25

In the next section, the comparison between the prediction made by different numerical techniques (including the OpenFOAM finite volume scheme) is used to validate the capability for solving the one-dimensional channel flow problem for Newtonian and Oldroyd-B model with the benchmark of the analytical solution.

3.4.6 Comparison between analytical, finite difference and finite volume (OpenFOAM) approximation

We first compare the solution for the flow of a Newtonian fluid for one-dimensional channel flow problem described in Section 3.1.1. A square domain $[-h, h]$ for both $x-$ and $y-$ direction is simulated within OpenFOAM using the `icoFoam` solver. The square channel for this domain is divided into $20 \times 20 \times 1$ which gives 400 control volumes to be computed with $\Delta x = \Delta y = 0.1$ when $h = 1$. The mesh for computational domain of the square channel is shown in Figure 3.3 and the boundary conditions used to solve this problem is provided in Table 3.18.

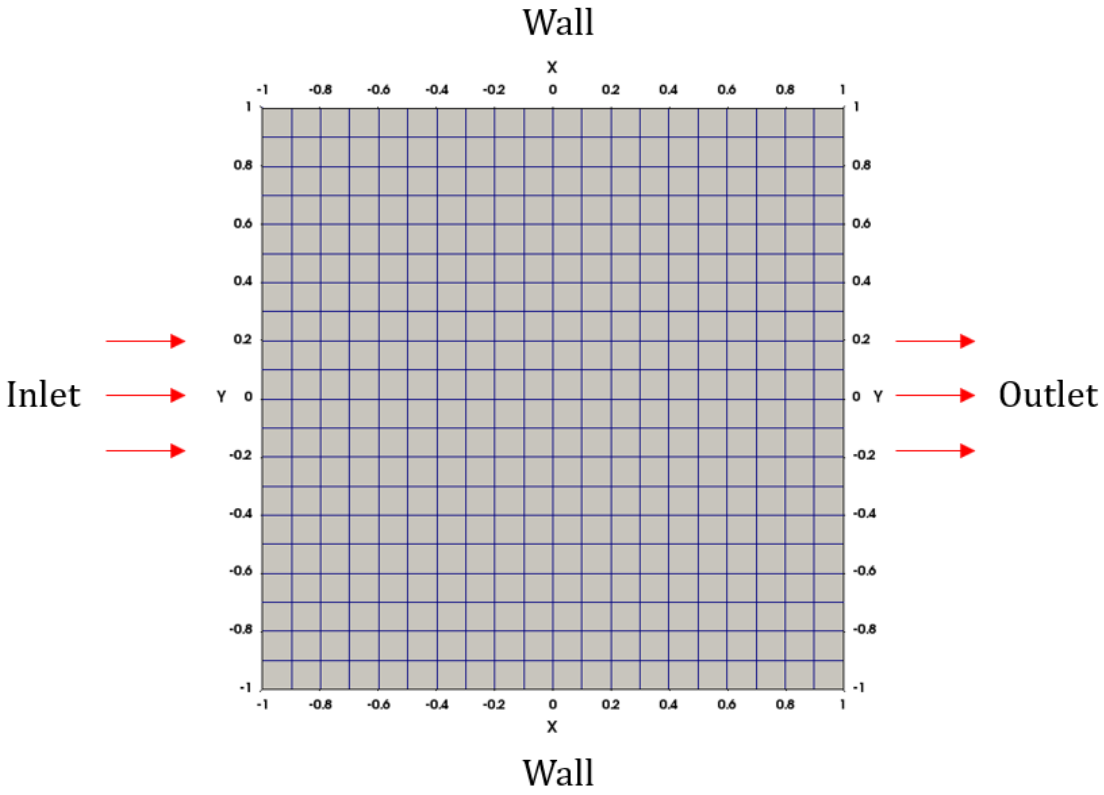

Figure 3.3: The mesh for the square channel with specified boundary for $\Delta x = \Delta y = 0.1$

Table 3.18: The boundary condition for the two-dimensional square channel defined in OpenFOAM.

Boundary	Boundary conditions		
	p	$\mathbf{U}$	$\boldsymbol{\tau}_i$
Inlet	`fixedValue`	`zeroGradient`	`zeroGradient`
Outlet	`fixedValue`	`zeroGradient`	`zeroGradient`
Walls	`zeroGradient`	`noSlip`	`linearExtrapolation`

Figure 3.4 shows an excellent agreement between the analytical solution and the numerical solutions obtained with finite difference, finite element and finite volume (i.e. OpenFOAM solver) at point $u(0, t)$ when $\eta_S = 1.0$ and $\rho = 1.0$. Here the fluid velocity increases monotonically towards the steady-state solution.

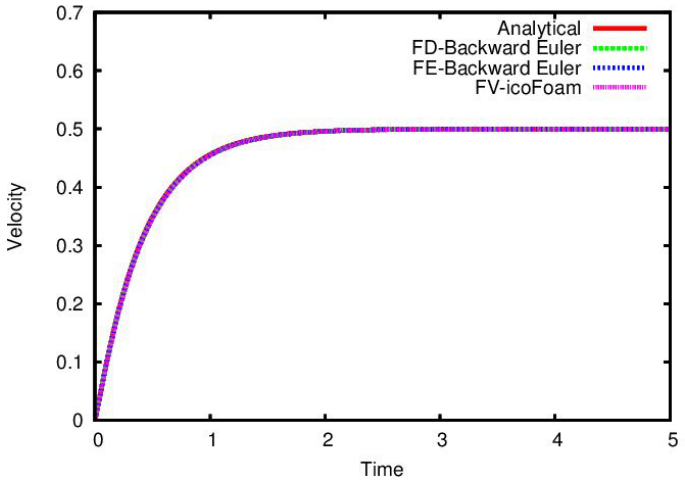

Figure 3.4: The analytical and numerical predictions (finite difference, finite element and OpenFOAM (`icoFoam`) finite volume solver) for transient velocity at the centre point for one-dimensional channel flow problem for Newtonian fluid when $\eta_S = 1.0$ and $\rho = 1.0$ with $\Delta y = 0.1$ and $\Delta t = 0.01$.

In contrast, the elasticity of the Oldroyd-B model leads to an overshoot of the fluid velocity. This is depicted in Figure 3.5 where the transient velocity at point $u(0, t)$ is plotted for both Newtonian and Oldroyd-B model on the same graph with the parameters set to $G = 1.0, \lambda = 1.0, \eta_S = 1.0$ and $\rho = 1.0$. The Oldroyd-B model gives a lower steady-state velocity compared to Newtonian. This is because the total viscosity for this choice of parameters in the Oldroyd-B model is double that of the Newtonian fluid (i.e. $\eta_{total} = \eta_S + \eta_P = \eta_S + G\lambda$).

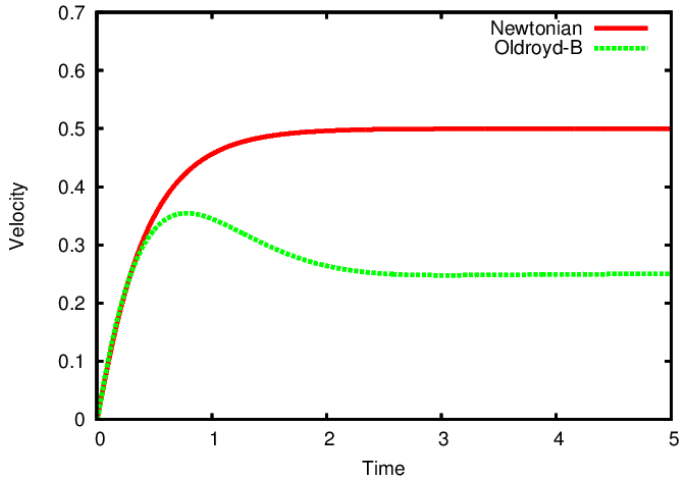

Figure 3.5: The comparison between the analytical solution for Newtonian (from equation (3.2)) and Oldroyd-B model through one-dimensional channel flow (from equation (3.8)) when $G = 1.0$, $c = 1.0$, $\lambda = 1.0$, $\eta_S = 1.0$ and $\rho = 1.0$.

The analytical solution for the Oldroyd-B model is compared with the spatial discretisation for forward and backward Euler time discretisation with $\Delta t = 0.01$ and $\Delta y = 0.1$. Figure 3.6 shows that the prediction agrees well with the analytical solution with a slight difference visible only at the maximum overshoot.

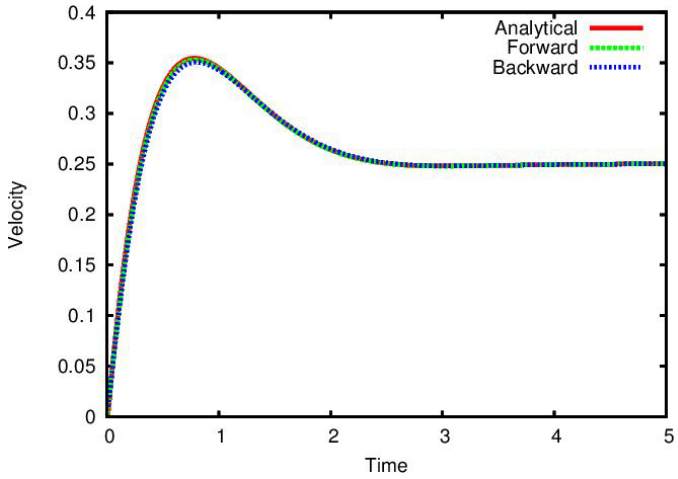

Figure 3.6: The comparison between the analytical solution with numerical approximation predicted by forward and backward Euler numerical schemes when $\eta_S = 1.0$, $G = 1.0$, $\lambda = 1.0$ and $\rho = 1.0$ at the centre point for one-dimension channel flow problem for Oldroyd-B fluid.

In Section 3.1.3 we noted that the solution for the velocity depends on the Elasticity number, $E = \frac{\lambda(\eta_S + G\lambda)}{\rho h^2}$. For this, the value of parameters are assigned as $\eta_S = \frac{1}{9}$, $G = \frac{8}{9}$ and relaxation time $\lambda = 1.0$, so that time is non-dimensionalised with respect to relaxation time. The value of fluid density ρ, is varied to give different Elasticity numbers. These parameter values were chosen to coincide with those used by Duarte et al. [47]. The results for different elasticity number are presented in Figure 3.7 as a comparison between the analytical, finite difference (using backward Euler time-integration) and finite volume `rheoFoam` solver solutions.

The following pre-processing data for density and (fixed value) inlet pressure is set up. In OpenFOAM RheoTool toolbox, the pressure is defined as kinematic pressure, $P = \frac{P_d}{\rho}$ (where P_d is the dynamic pressure), thus pressure set in the pre-processing must take account of the changes to the fluid density. Note that the same domain shown in Figure 3.3 is used here with the same spatial resolution as the simulation for the Newtonian fluid that is $\Delta y = 0.1$ (Duarte et al. [47] use $\Delta y = 0.01$ in their computation).

Table 3.19: The pre-processing data for solving one-dimensional channel flow problem for Oldroyd-B model in OpenFOAM

E	ρ	P_{inlet}	Δt
1	1.0	2	1.25×10^{-3}
10	0.1	20	1.25×10^{-4}
100	0.01	200	2.5×10^{-5}

The transient velocity at the centre point of the channel is taken to compare with the analytical solution and prediction made by the finite difference approach. The details of the results can be visualised in Figure 3.7.

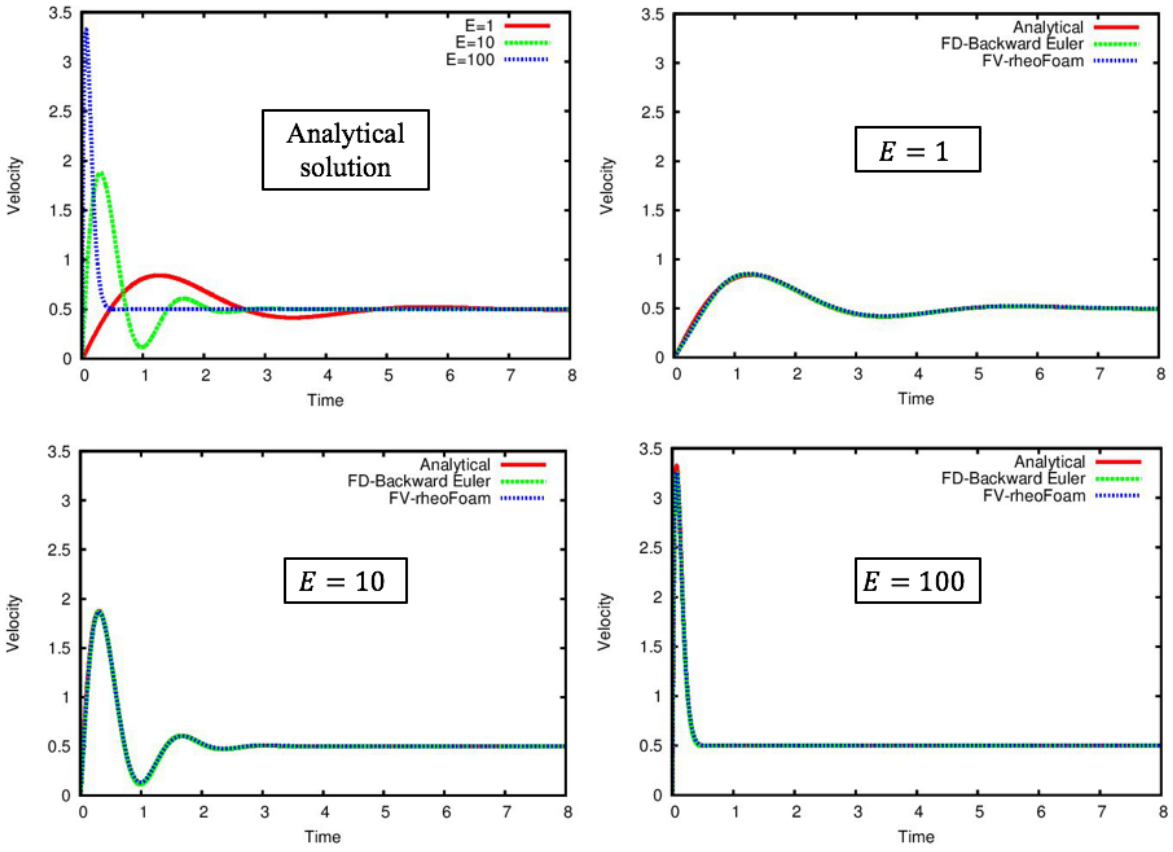

Figure 3.7: The analytical solution and the comparison between the analytical solution with numerical predictions (i.e. finite difference and finite volume) for different Elasticity numbers for one-dimensional channel flow problem for Oldroyd-B model when $\eta_S = \frac{1}{9}, \eta_P = \frac{8}{9}, \lambda = 1.0$ and $G = \frac{8}{9}$ at the centre point of the channel.

The Elasticity number is the ratio between the fluids elasticity and inertia. Note that it does not affect the steady-state velocity only the transient velocity. High Elasticity numbers

correspond to low inertia meaning that the inertial terms are only important at the initial onset of the flow. At moderate Elasticity numbers the inertial terms remain important during the time when the viscoelastic stresses are growing and this leads to oscillations in the velocity.

3.5 Conclusion

In this chapter, the results for one- and two-dimensional channel flow for Newtonian and Oldroyd-B fluids are presented where different numerical approaches for spatial descretisation (i.e. finite difference and finite element) are compared with different time integration techniques. The order of accuracy for different schemes used are compared and shown to agree with the expected behaviour of these schemes.

In the final section of this chapter, we compare the different numerical approaches to solve the channel flow problem and reproduce the results from Duarte et al., [47] plotted in Figure 3.7. Here we have compared the analytic solution with both the finite difference scheme and the `rheoFoam` finite volume scheme and find excellent agreement. This provides a good (simple) benchmark to validate the reliability of the solvers which complements other validations on more complicated geometrical problems [113]. In the later chapters, we will simulate more complex geometrical flow using the `rheoFoam` solver for more sophisticated constitutive equations.

Chapter 4

Polymer Melt Flow Through a Hyperbolic Contraction

This chapter presents the implementation of the Rolie-Poly constitutive equation in OpenFOAM software and a study of the behaviour of the model in a contraction flow. The implementation is validated for a multimode Rolie-Poly model with the published results [129] in a benchmark 4:1 sudden contraction for PS2 commercial polymer fluid. The work is then extended to study the behaviour of PS2 in a hyperbolic contraction where the effect of the contraction length is observed and the birefringence pattern for different contraction lengths are visualised.

4.1 Motivation

Contraction flows have been widely studied as a prototypical processing geometry containing regions of both shear and extensional flow. The sudden 4:1 contraction was established as a benchmark flow for viscoelastic flow computations and so has been extensively studied both numerical and experimentally. Although the sudden contraction flow is a popular choice for a flow with an extensional component, the strain-rate history through the contraction is complex and depends strongly upon the rheological properties of the fluid (as this affects the flow pattern upstream of the contraction). In this chapter, we consider a contraction with a hyperbolic geometry. In the case of perfect slip at the walls the polymer will experience

a constant rate of extension through the contraction and so has been used to measure extensional properties [31], [74] of polymeric fluids.

The capability of the hyperbolic contraction in producing a relatively uniform extension-rate, and a smooth flow through the contracting region, can avoid the formation of vortices at the upstream corner near the wall. This could also increase the measuring range. There is no published work for recent rheological models, specifically monodisperse Rolie-Poly and bi-disperse Rolie-Double-Poly models (presented in later chapter), in hyperbolic contraction flow. With this motivation, this research aims to investigate the behaviour of the shear-thinning Rolie-Poly fluid and explore the effect of geometrical changes of this contraction configuration and the influence of this on the prediction of the constitutive model.

4.2 Rolie-Poly implementation in OpenFOAM

The Rolie-Poly (RP) model defined in equation (1.5) in terms of conformation tensor is redefined as follows

$$\overset{\nabla}{\boldsymbol{A}} = -\frac{1}{\lambda_D}(\mathbf{A}-\mathbf{I}) - \frac{2}{\lambda_R}(1-\sigma^{-1})[\mathbf{A}+\beta^*\sigma^{2\delta}(\mathbf{A}-\mathbf{I})].$$

The RP equation is rewritten in terms of a polymeric stress tensor as $\boldsymbol{\tau} = G(\mathbf{A}-\mathbf{I})$. Note that, here we have written the notation for polymeric stress tensor as $\boldsymbol{\tau}$ without the subscript p used before. This is to ensure the consistency with the implemented source code that is presented later in this section. Also, not to be confused with the previous notation where we used $\boldsymbol{\tau}_p$ for polymeric stress is used to distinguish the stress contribution from the polymer and solvent. Henceforth, the notation for the polymeric stress is written as $\boldsymbol{\tau}$ for simplicity. Rewritten the polymeric stress expression implies that $\overset{\nabla}{\boldsymbol{\tau}} = G\overset{\nabla}{\boldsymbol{A}} + 2G\mathbf{D}$ which is obtained from the following derivation.

$$\underbrace{\frac{D\boldsymbol{\tau}}{Dt} - (\nabla\mathbf{u})\cdot\boldsymbol{\tau} - \boldsymbol{\tau}\cdot(\nabla\mathbf{u})^T}_{\overset{\nabla}{\boldsymbol{\tau}}} = \frac{D}{Dt}G(\mathbf{A}-\mathbf{I}) - (\nabla\mathbf{u})\cdot G(\mathbf{A}-\mathbf{I})$$

$$\begin{aligned}
&\quad - G(\mathbf{A}-\mathbf{I})\cdot(\nabla\mathbf{u})^T \\
&= G\left(\frac{D\mathbf{A}}{Dt} - (\nabla\mathbf{u})\cdot\mathbf{A} - \mathbf{A}\cdot(\nabla\mathbf{u})^T\right) \\
&\quad - G\left(\frac{D\mathbf{I}}{Dt} - (\nabla\mathbf{u})\cdot\mathbf{I} - \mathbf{I}\cdot(\nabla\mathbf{u})^T\right) \\
&= G\overset{\nabla}{\boldsymbol{A}} + G[(\nabla\mathbf{u}) + (\nabla\mathbf{u})^T] \\
&= G\overset{\nabla}{\boldsymbol{A}} + 2G\mathbf{D} \\
\therefore\ \overset{\nabla}{\boldsymbol{\tau}} &= G\overset{\nabla}{\boldsymbol{A}} + 2G\mathbf{D}
\end{aligned}$$

where $\mathbf{D} = \frac{1}{2}[(\nabla\mathbf{u}) + (\nabla\mathbf{u})^T] \implies 2\mathbf{D} = (\nabla\mathbf{u}) + (\nabla\mathbf{u})^T$ and $\mathbf{I}$ do not depend on time, and the substantive derivative of the identity matrix, $\frac{D\mathbf{I}}{Dt}$, is zero. We have

$$\begin{aligned}
G\overset{\nabla}{\boldsymbol{A}} &= -\frac{1}{\lambda_D}G(\mathbf{A}-\mathbf{I}) - \frac{2}{\lambda_R}(1-\sigma^{-1})[G\mathbf{A} + \beta^*\sigma^{2\delta}G(\mathbf{A}-\mathbf{I})] \\
&= -\frac{1}{\lambda_D}\boldsymbol{\tau} - \frac{2}{\lambda_R}(1-\sigma^{-1})(\boldsymbol{\tau} + G\mathbf{I} + \beta^*\sigma^{2\delta}\boldsymbol{\tau}).
\end{aligned}$$

This implies that the Rolie-Poly model written in term of $\overset{\nabla}{\boldsymbol{\tau}}$ can be written as follows

$$\begin{aligned}
\overset{\nabla}{\boldsymbol{\tau}} - 2G\mathbf{D} &= -\frac{1}{\lambda_D}\boldsymbol{\tau} - \frac{2}{\lambda_R}(1-\sigma^{-1})(\boldsymbol{\tau} + G\mathbf{I} + \beta^*\sigma^{2\delta}\boldsymbol{\tau}) \\
\overset{\nabla}{\boldsymbol{\tau}} &= 2G\mathbf{D} - \frac{1}{\lambda_D}\boldsymbol{\tau} - \frac{2}{\lambda_R}(1-\sigma^{-1})(\boldsymbol{\tau} + G\mathbf{I} + \beta^*\sigma^{2\delta}\boldsymbol{\tau}).
\end{aligned}$$

Separating the like terms (i.e. $\boldsymbol{\tau}$ and $\mathbf{I}$) accordingly, yields the following equation

$$\overset{\nabla}{\boldsymbol{\tau}} = 2G\mathbf{D} - \left[\frac{1}{\lambda_D} - \frac{2}{\lambda_R}(1-\sigma^{-1})(1+\beta^*\sigma^{2\delta})\right]\boldsymbol{\tau} - \frac{2}{\lambda_R}(1-\sigma^{-1})G\mathbf{I}.$$

To make it more consistent to the way the equation is "translated" to high level C++ code

in OpenFOAM, the above equation can be further broken down to the following equation

$$\frac{\partial \boldsymbol{\tau}}{\partial t} + \mathbf{u}\cdot\nabla\boldsymbol{\tau} = 2\frac{\eta_P}{\lambda_D}\mathbf{D} + \mathbf{u}\cdot(\nabla\boldsymbol{\tau}) + \boldsymbol{\tau}\cdot(\nabla\mathbf{u})^T - \left[\frac{1}{\lambda_D} - \frac{2}{\lambda_R}(1-\sigma^{-1})(1+\beta^*\sigma^{2\delta})\right]\boldsymbol{\tau} - \frac{2\eta_P}{\lambda_D\lambda_R}(1-\sigma^{-1})\mathbf{I}.$$

Let $g(\sigma) = 2(1-\frac{1}{\sigma})$, $f(\sigma) = g(\sigma)(1+\beta^*\sigma^{2\delta})$ where σ in terms of $\boldsymbol{\tau}$ is written as, $\sigma = \sqrt{\frac{tr(\boldsymbol{\tau})}{3G}+1}$. The above Rolie-Poly model written in high level C++ code in OpenFOAM can be represented as follows

Member functions in Rolie-Poly.C file

```
//***************** Member Functions *****************//

void Foam::constitutiveEqs::Rolie_Poly::correct()

{


volTensorField L = fvc::grad(U());

volTensorField C = tau_ & L;

volSymmTensorField twoD = twoSymm(L);

Stretch_ = Foam::sqrt(1+tr(tau_)*lambdaD_/3/etaP_);

volScalarField gSigma = 2*(1-1/Stretch_);

volScalarField fSigma = gSigma*

(1+beta_*Foam::pow(Stretch_,2*delta_));


fvSymmTensorMatrix tauEqn

(

fvm::ddt(tau_) + fvm::div(phi(), tau_)

==

etaP_/lambdaD_*twoD + twoSymm(C) - fvm::Sp(1/lambdaD_

+1/lambdaR_*fSigma, tau_)

- etaP_/(lambdaD_*lambdaR_)*gSigma*I_

);


tauEqn.relax();

tauEqn.solve();

}
```

The above C++ coding is the main part of the Rolie-Poly code that been implemented in `Rolie_Poly.C`. This file is available in the following path directory `../src/libs/constitutiveEquations/constitutiveEqs/Rolie-Poly`. Table 4.1 demonstrates the implementation of the C++ code which is "translated" almost analogous to the mathematical operator. Note

that, the `twoSymm(C)` from Table 4.1 has been defined and recognised by the OpenFOAM software as the summation between the tensor field C (i.e. $\nabla \boldsymbol{u} \cdot \boldsymbol{\tau}$) with its transpose.

Table 4.1: The mathematical operator with respective high level C++ coding implementation in OpenFOAM software.

Mathematical Operator	**OpenFOAM implementation**
$\frac{\partial \boldsymbol{\tau}}{\partial t} + \boldsymbol{u}.\nabla \boldsymbol{\tau}$	`fvm::ddt(tau_) + fvm::div(phi(), tau_)`
$\frac{2\eta_P \mathbf{D}}{\lambda_D}$	`etaP_/lambdaD_*twoD`
$\nabla \boldsymbol{u} \cdot \boldsymbol{\tau} + \boldsymbol{\tau} \cdot (\nabla \boldsymbol{u})^T$	`twoSymm(C)`
$\frac{1}{\lambda_D} + \frac{2}{\lambda_R} f(\sigma)$	`fvm::Sp(1/lambdaD_ + 1/lambdaR_*fSigma_, tau_)`
$\frac{\eta_P}{(\lambda_D \lambda_R)} g(\sigma) \boldsymbol{I}$	`etaP_/(lambdaD_*lambdaR_)* gSigma_*I_`
$g(\sigma)$	`2*(1-1/stretch_)`
$f(\sigma)$	`gSigma_* (1+beta_*Foam::pow(stretch_,2*delta_))`
σ	`Foam::sqrt(1+tr(tau_))*lambdaD_/3/etaP_`

We have successfully extended the monodisperse Rolie-Poly constitutive law in OpenFOAM software. In the next section, we present computations based on the implemented Rolie-Poly model where we validate our implementation in a 4:1 planar contraction flow and compared with the published results reported in Tenchev et al. [129] that uses the multimode Rolie-Poly model to describe PS2. In OpenFOAM, the multimode model is available within the library where the multimode Rolie-Poly model can be specified under multimode constitutive model with different set of Rolie-Poly parameters that describes PS2.

4.3 Two-dimensional hyperbolic contraction geometry

The whole two-dimensional hyperbolic geometry can be depicted in Figure 4.1 where H_1 and H_2 are the height of the upstream and downstream channel respectively.

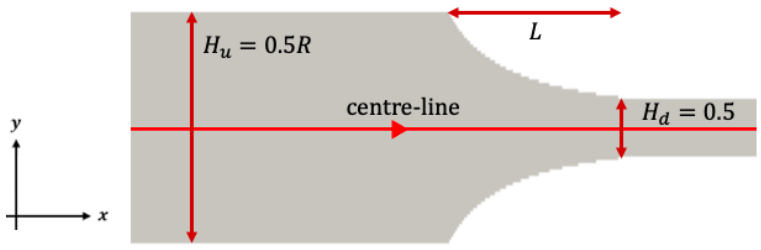

Figure 4.1: Whole two-dimensional hyperbolic contraction geometry.

The contraction ratio, R, is defined as $R = H_1/H_2$. The centre-line of this geometry is where the extension-rate, $\dot{\varepsilon}$, and stretch will be observed in order to demonstrate whether this configuration is able to generate a region of constant extension-rate. This is observable within the contraction region where the velocity of the fluid is increasing due to the effect of geometrical changes.

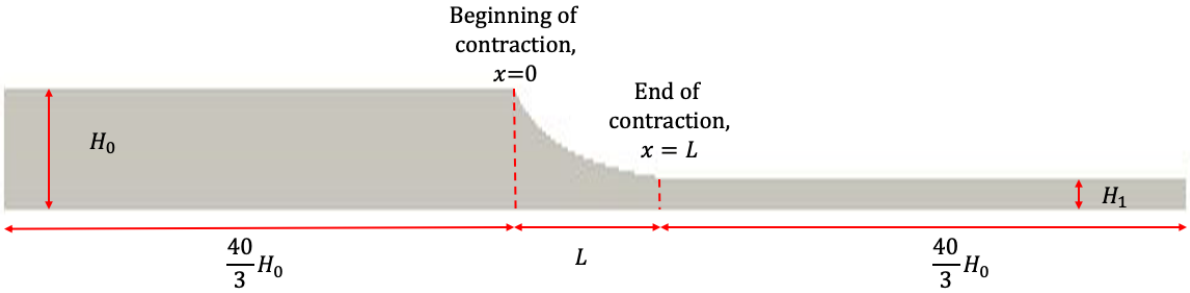

Figure 4.2: The the two-dimensional half hyperbolic contraction computational domain as a consequence of the symmetry with the upstream and downstream straight channel length. The contraction length shown by the figure is around 30% of the upstream (or downstream) straight channel.

The numerical simulations for the multimode Rolie-Poly constitutive equation are carried out through two-dimensional 4:1 (R=4) sudden and hyperbolic planar contractions for different contraction lengths. As a consequence of the symmetry, only half of the whole domain is considered as shown in Figure 4.2. Let the half-width of the upstream channel be $\frac{1}{2}H_u = H_0$, then the half-width of the downstream channel is $0.25H_0$. The upstream and downstream straight channels are $\frac{40}{3}H_0$ long. The contraction begins at $x = 0$ and the contraction ends at $x = L$. The long straight channels are required so that the fully-developed velocity is able to be generated before the velocity changes due to the geometrical configuration when the flow passes through the contracting region. This ensures that any effect of an undeveloped velocity profile on the prediction of the result before the contraction can be

avoided. The half height of the hyperbolic within the contracting region, $H(x)$, is defined as follows

$$H(x) = \begin{cases} H_0, & x \leq 0 \\ \dfrac{H_0 L}{L + (H_0/H_1 - 1)x}, & 0 < x < L \\ H_1 & x \geq L \end{cases}$$

so that the channel-half height contracts from H_0 to H_1 over a length L. Further explanations on the boundary condition specification, the meshing strategies and the pressure ramping protocol are described in the subsections that follows.

4.3.1 Boundary condition

The boundary conditions for p, U, and τ_i are recorded in the following table, where τ_i is the polymeric stress for the i^{th} mode. The no-slip boundary condition is imposed at the wall. This geometry creates the maximum shear at the wall. However, at the centre-line, when there is no shear, a pure extensional flow is developed. The shear at the wall can be reduced using a partial slip boundary condition which is available in OpenFOAM software. Nevertheless, we do not intend to discuss the effect of partial slip on the fluid flow in this research and focus purely on the no-slip effect.

Table 4.2: The boundary condition for two-dimensional 4:1 contraction flow used in RheoTool.

Boundary	Boundary conditions		
	p	$\mathbf{U}$	$\boldsymbol{\tau}_i$
Inlet	`uniformFixedValue`	`zeroGradient`	`zeroGradient`
Outlet	`fixedValue`	`zeroGradient`	`zeroGradient`
Walls	`zeroGradient`	`noSlip`	`linearExtrapolation`
Symmetry	`symmetryPlane`	`symmetryPlane`	`symmetryPlane`
frontAndBack	`Empty`	`Empty`	`Empty`

In Table 4.2, we specify a pressure gradient with a pressure ramping protocol for inlet pressure. The polymeric stress tensor τ has boundary condition of `linearExtrapolation` introduced in [113] near the wall and the stress at the wall is linearly extrapolated from the predicted stress at the cell next to the wall. The front and back plane are set to empty to

treat the default three-dimensional mesh as purely two-dimensional.

4.3.2 Pressure ramping protocol

In our simulations, the flow is developed by imposing non-zero pressure at the inlet and zero pressure at the outlet. We consider a pressure ramping protocol in this research at the inlet of the geometrical flow as this will help the transient evolution of the fluid velocity and avoid a rapid change of the flow at the start which can cause the failure of our simulation. We do not impose the velocity at the inlet of the geometry as the prediction of the velocity profile depends on the shear-thinning phenomena. The following pressure formula is used, $P = \alpha(1 - e^{-\beta t})$ where α is the target pressure drop value, $\beta = 1.0$, typically and t is time. How fast the pressure ramping during the transient is depends on the value specified for β and the best choice of β when dealing with the real polymer behaviour depends on the material properties of the polymer and type of the geometry considered. However, we do not consider the detail of the flow during pressure ramping, only after a steady flow is established. In the next sections, we present the results for PS2 flowing through planar contraction and extended to the hyperbolic contraction flow in the following section solving using RheoTool solver.

4.4 4:1 Planar Contraction flow for PS2

The multimode Rolie-Poly model is used to represent the commercial-grade polystyrene known as PS2 where the rheological parameters were obtained using the Reptate software package [86]. We compare the results produced by our pressure ramping approach with `rheoFoam` solver against published results [129] where the flow is evolved by imposing the velocity at the inlet of the geometry and solved using a finite element algorithm. The full three-dimensional geometry for the 4:1 sudden contraction with $15mm$ inflow channel height, $3.75mm$ outflow channel height and $25mm$ deep is used. Since we are solving two-dimensional flow, the effect of depth in this context is not considered. The Bradford Mk2 4:1 contraction die geometrical definition is available in Tenchev et al. [129].

The detail of the rheological parameters used are recorded in Table 4.3. The CCR coefficient and fitting parameter are set to $\beta^* = 0.0$ and $\delta = -0.5$ respectively. The

solvent viscosity, which is obtained from the 7 slowest Rolie-Poly modes (out of 12 modes) is $\eta_S = 1580Pas$.

Table 4.3: The elastic modulus and relaxation times for both reptation and stretch of different Rolie-Poly modes for PS2.

$G(Pa)$	$\lambda_D(s)$	$\lambda_R(s)$
183	10	0.683
800	3.162	0.342
3365	1.0	0.171
10737	0.3162	0.0852
18724	0.1	0.0428

We consider the mesh convergence of our OpenFOAM solver first. Then we compare the predictions made by OpenFOAM and the published finite element solver for the same contraction problem for the same material.

4.4.1 Mesh convergence

We consider several meshes from coarser to finer as shown Figure 4.3 to demonstrate the convergence of the solution using the RheoTool solver. The 4:1 sudden contraction benchmark problem flow is reproduced and the result is compared to [129] to observe the agreement of the solution with the two different numerical approaches. The detail of the mesh and the mesh data are presented in Table 4.4 and Figure 4.3 respectively.

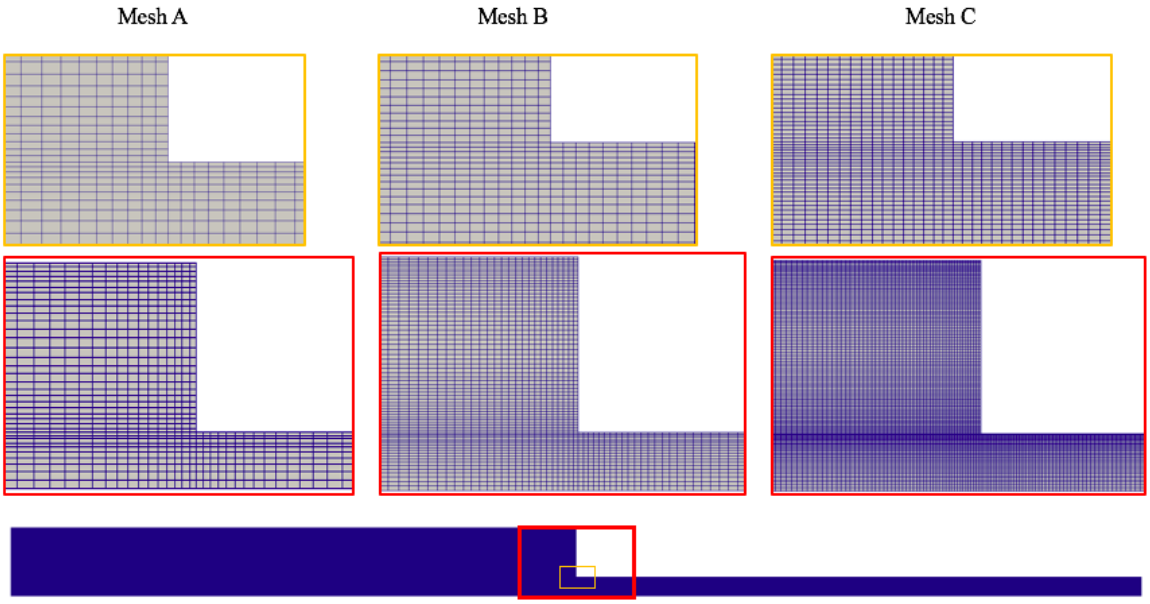

Figure 4.3: The mesh refinement.

The meshes are graded such that the walls and the re-entrant corner are resolved more finely. This is because high stress is expected in these regions and should be well resolved to avoid loss of accuracy.

Table 4.4: Mesh information for different mesh refinements.

Mesh		A	B	C
Points		4874	18542	73082
Cells		2300	9000	36000
Faces		9336	36270	144540
Internal faces		4464	17730	71460
Minimum cell size (in mm)	x	0.311	0.157	0.128
	y	0.099	0.0498	0.0463

The mesh convergence is presented in Figure 4.5 by plotting the velocity profile near the re-entrant region and the downstream channel just after the contraction at $x = -2mm$ and $x = 2mm$ respectively, as shown in Figure 4.4. Note that, the CUBISTA high resolution scheme [6] is used to discretise the convective term which theoretically has a third order accuracy. It can be seen that the convergence of the solution is ensured as the mesh grid gets finer.

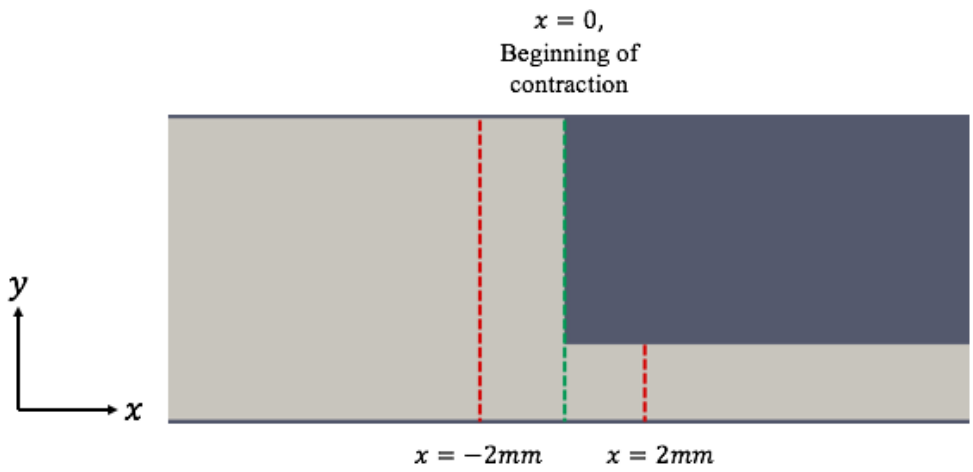

Figure 4.4: Comparison for velocity distribution at the centre-line towards the contracting region between `rheoFoam` (current work) and finite element solver [129].

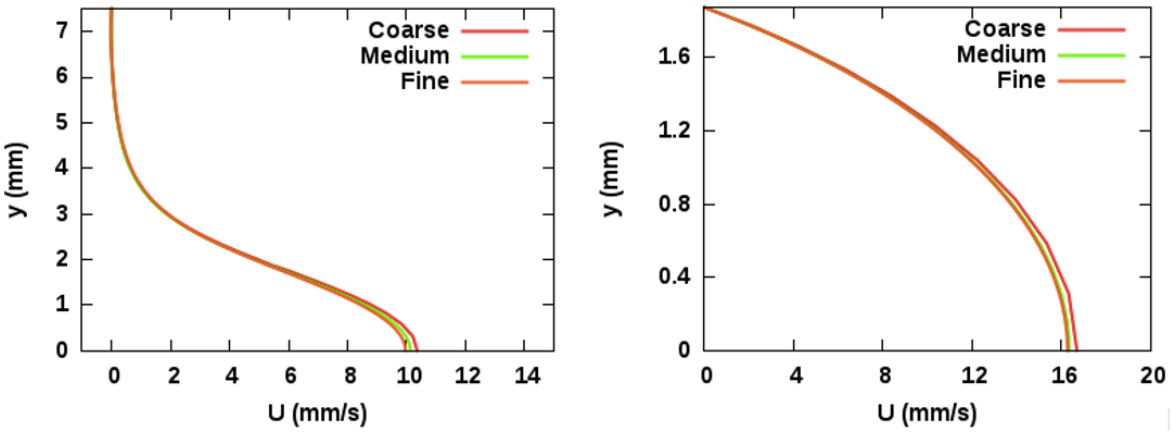

Figure 4.5: The half domain of the velocity profile at x=-2mm (LHS) and x=2mm (RHS) across the geometry before the contraction comparing the velocity profile predicted using different mesh resolution: Coarse-Mesh A, Medium-Mesh B, Fine-Mesh C.

4.4.2 Result and Validation

The comparison between the finite element solver used in [129] is made by observing the velocity distribution on the centre-line before the contraction and the two-dimensional birefringence pattern as presented from Figure 4.6 and 4.7. While Tenchev et al. [129] imposed a parabolic profile boundary condition for velocity at the inlet, the approach used in this research is different as mentioned earlier. Even so, we are able to reproduce the results from Tenchev et al. [129] with good agreement to the previous study as depicted in Figure 4.6 for velocity and Figure 4.7 for the birefringence stress pattern.

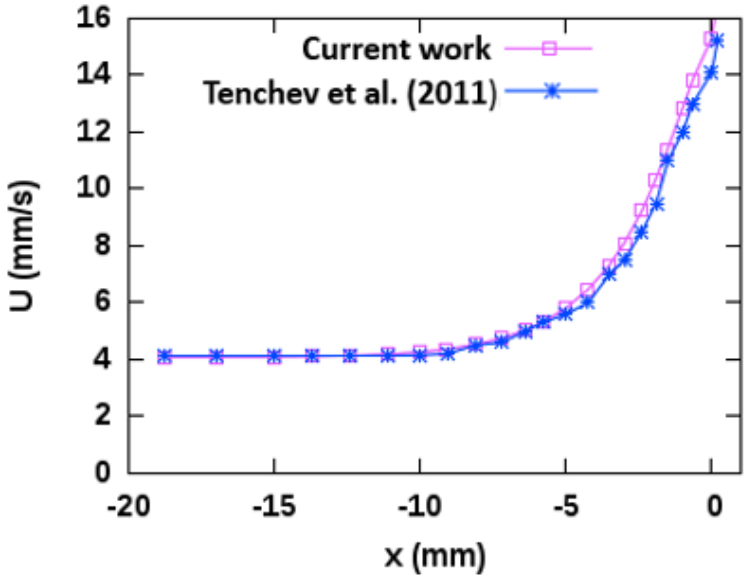

Figure 4.6: Comparison for velocity distribution at the centre-line towards the contracting region between `rheoFoam` (current work) and the finite element solver [129].

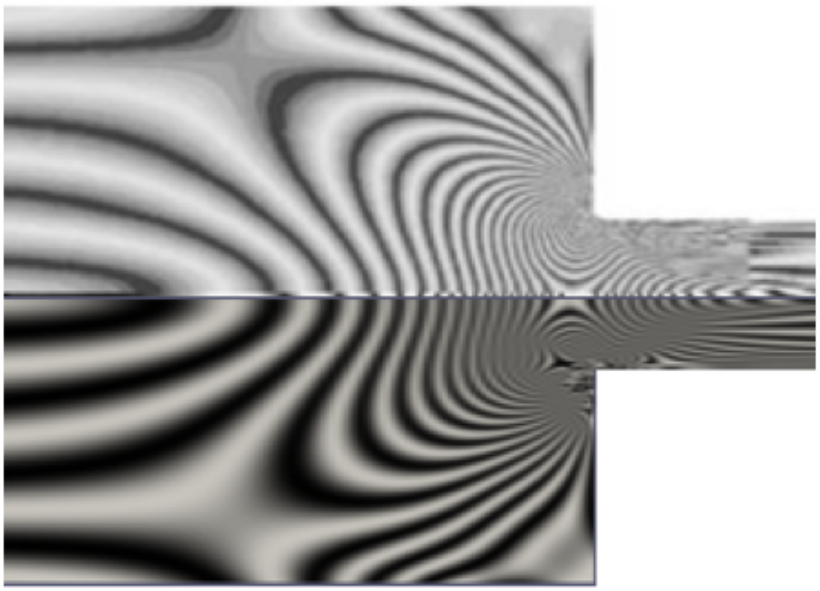

Figure 4.7: Two-dimensional birefringence for PS2 contraction flow at 15 RPM screw speed: Finite element [129] (upper half) and `rheoFoam` solver (lower half).

This validation demonstrates that the RheoTool solver can capture the behaviour of a multimode Rolie-Poly fluid in non-trivial flow conditions.

4.5 4:1 Hyperbolic Contraction Flow for PS2

The work is then proceeded by investigating the behaviour the PS2 fluid in the hyperbolic planar contraction. We aim to look at the behaviour of the model in different contraction lengths, L, and determine the hyperbolic contraction required to achieve constant extension-rate within the contracting region. We let $L = 2, 4, 8, 16, 32, 64mm$ and compare with the abrupt contraction ($L = 0$), from the previous subsection. The changes of the flow are observed by capturing the birefringence stress pattern and the extension-rate along the centre-line to illustrate the evolution from peak to uniform extension-rate generated by the hyperbolic contraction given sufficient contraction length. In line with that, the stretch of the chain with highest molecular weight, which has the longest relaxation time, is measured along the centre-line to observe the effect of different contraction lengths.

4.5.1 Mesh generation strategies

Hexahedral mesh generation involving curvature requires a careful strategy to ensure adequate mesh quality. This is to ensure that the simulation does not experience any "difficulties" due to computational cells with high skewness as a result of geometrical changes caused by the hyperbolic curvature. The following mesh strategies are used to ensure the mesh smoothness such that the simulation can proceed until steady-state is achieved.

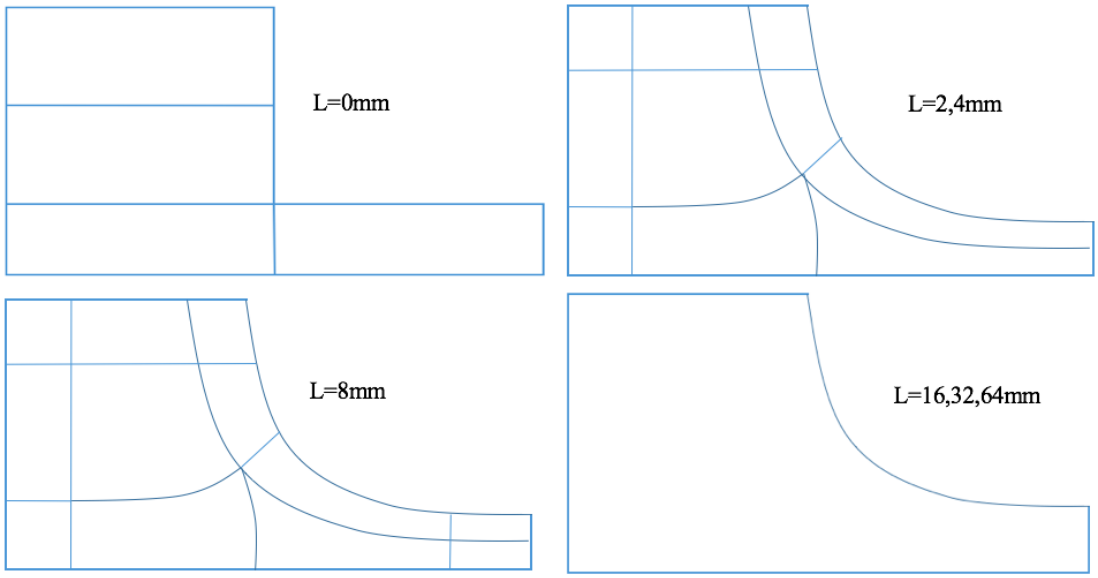

Figure 4.8: The sketch for different mesh block strategies for different contraction lengths.

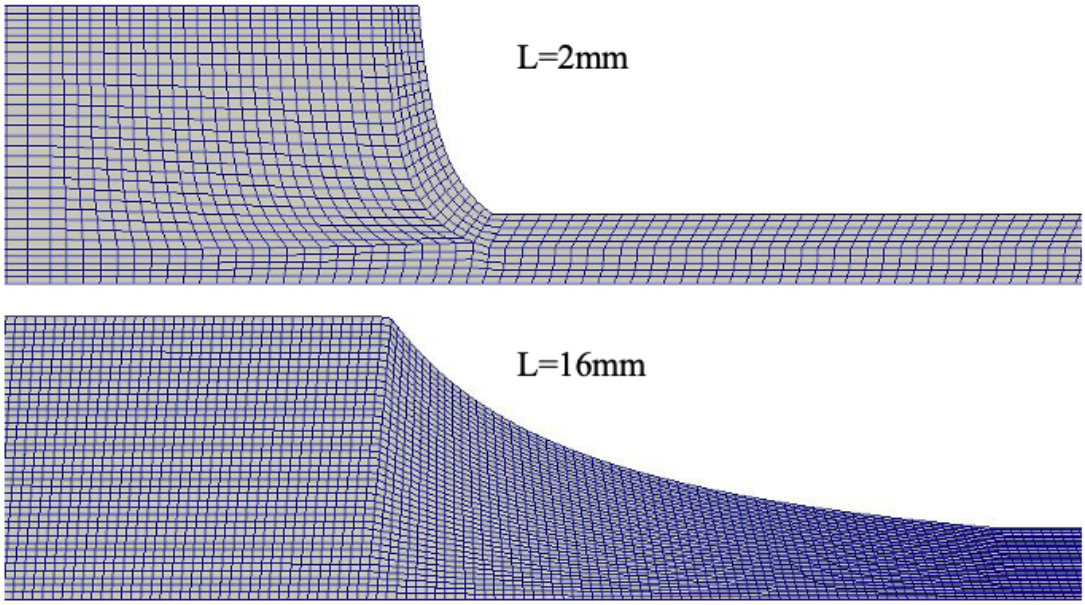

Figure 4.9: The example of the mesh for $L = 2mm$ and $L = 16mm$ generated in OpenFOAM.

With the meshes depicted from Figure 4.8 and the example of the mesh shown Figure 4.9, the results presented in the following subsection are generated by defining a mesh resolution and grading within each block. As before, grading is used near the wall and the centre-line to improve flow resolution there.

4.5.2 Contraction design conclusion

This section presents the results for the hyperbolic contraction flow for PS2. In the hyperbolic contraction, we set the upstream and the downstream channel to be long enough to let the flow to be fully developed before reaching the contracting region. The upstream and downstream straight channel are set to be the same length, that is $100mm$. The length for the whole downstream (the contracting region and straight downstream channel) part depends on the contraction length, $(100 + L)mm$. In order to ensure the same flow-rate for different contraction lengths, the pressure drop imposed for $L = 0$ is used as the benchmark to identify the pressure drop value requires for other contraction lengths in order to produce the same flow-rate. Therefore, the pressure drop imposed at the inlet boundary for each contraction lengths is different as the total length of the whole domain of the configurations are not the same. Table 4.5 provides the details of the pressure drop used for each

contraction length.

Table 4.5: Pressure drop, ΔP for different contraction length, L

Total length, (mm)	$L(mm)$	$\Delta P(Pa)$
200	0	380
202	2	380
204	4	382
208	8	386
216	16	397
232	32	420
264	64	467

As mentioned previously in Section 4.3 the length for the upstream channel should be sufficiently long so that the velocity as well as the stress is fully developed before the constriction. In Figure 4.10, we showed that velocity and stress profile taken at half-way upstream for contraction length, $L = 0, 4, 16, 64$. Even though we are not presenting the profile predicted by $L = 2, 8, 32$, it it worth noting that, the similar prediction are observed for these contraction lengths.

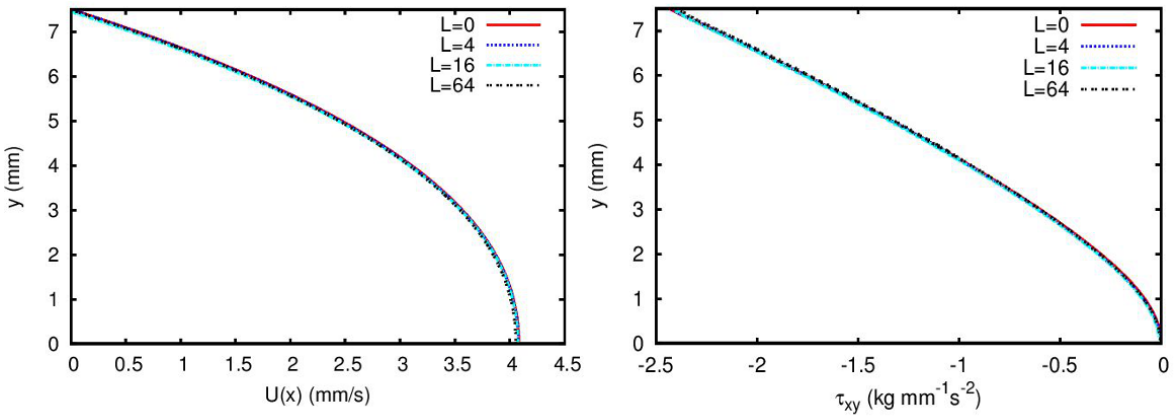

Figure 4.10: The fully-developed velocity and the total polymeric stress profile (xy-component) for different hyperbolic contraction lengths taken at the half-way upstream channel, $x = -\frac{40}{6}H_0$ flowing at the same flow-rate.

We present the results for various contraction lengths where the velocity, extension-rate and the stretch for the mode with highest relaxation time are plotted on the centre-line. The individual effect of the contraction length on the birefringence pattern are observed by presenting the contour plot of the birefringence with the same contour interval in each case.

Plotting the velocity gradient of the x-component on the centre-line, $\frac{du}{dx}$ reveals the level of uniformity of the extension-rate within the contracting region. This predicts what could be an appropriate contraction to be used in production of a hyperbolic die that can be used experimentally. This would allow experimental study of the behaviour of the real fluid, for example PS2, that has been used in these numerical simulation studies.

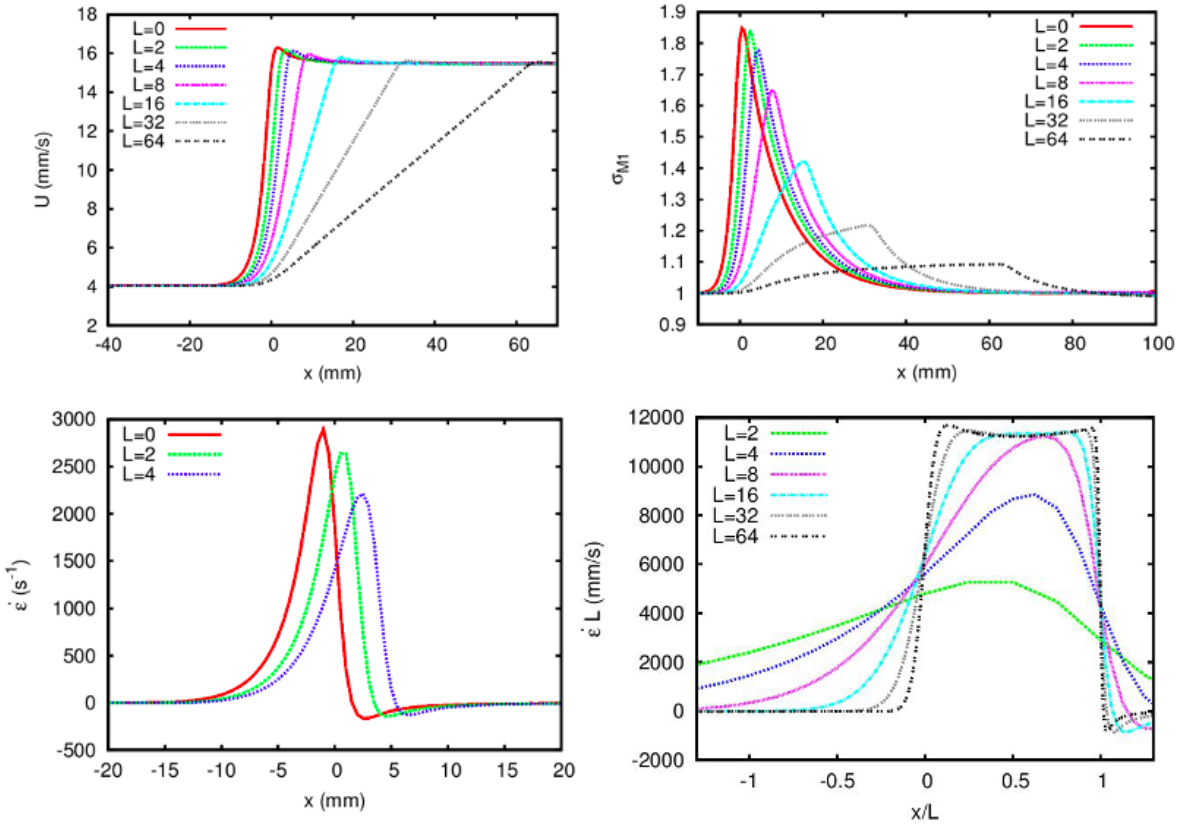

Figure 4.11: The centre-line plot for: velocity of the fluid, longest polymer chain stretch, σ_{M1} (i.e. having the highest reptation relaxation time) and extension-rate with different contraction lengths for PS2 fluid using pressure drop values as presented in Table 4.5. The dimension of the contraction length from the legend of the subfigures is measured in millimetre (mm).

Figure 4.11 illustrates the fluid velocity, extension-rate and the longest chain stretch at the centre-line when the configuration of the planar contraction is changed from abrupt contraction, $L = 0$, to hyperbolic contraction of different lengths. As depicted from the left top figure in Figure 4.11, the velocity gradient changes from a steep slope (i.e. highest for $L = 0mm$) to lower (i.e. lowest for $L = 64mm$) as the contraction length increases. This is because the fluid flow is accelerating rapidly as the result of sudden geometrical changes in

the configuration. Increasing the contraction length hyperbolically, the geometry produces a smoother contracting region and thus allows the fluid velocity to change more gradually throughout the contracting region.

The variation of the contraction lengths also affects the stretch of the polymer chains. The mode with highest relaxation time, $\lambda_D = 10s$ from Table 4.3, is used to demonstrate this. The pressure drop imposed for the abrupt contraction is sufficient to generate high stretch as shown in Figure 4.11. The pressure drop for all different contraction lengths are able to produce noticeable stretch of the chain. The stretch is more pronounced for lower contraction length because the flow resistance due to the geometrical constraint is more prominent and cause the extension-rate to be more significant in the downstream region.

The two bottom sub-figures in Figure 4.11 demonstrates the level of uniformity of the extension-rate that we expect using the superior hyperbolic contraction geometry. When $L = 0mm$, the abrupt contraction, a peak extension-rate is produced but not maintained. Increasing the contraction length is an attempt to promote a region of constant extension-rate. The figures reveal that a consistent extension-rate starts to be observed when $L = 16mm$ which is about 1:2.1333 ratio comparing the height of the half upstream channel to the contraction length itself.

In previous research, (see for example, [87], [89], [129] and [134]), the comparison between the numerical result using a proposed solver and experimental procedures conducted on a real fluid show the PSD contour or so called birefringence. We present the predicted birefringence contour for each contraction length, L, with the stress optical coefficient, $C = 1.0$.

To the best of our knowledge, no work on the Rolie-Poly model in the hyperbolic contraction has been published either numerically or experimentally. Thus, relying on the benchmark problem in the 4:1 abrupt contraction, we extend the work to observe the PSD with grayscale color representation as depicted from Figure 4.12 that is obtained using the different mesh strategies from Figure 4.8 with contour interval = 5564.73 $kgm^{-1}s^{-2}$ and $\eta_S = 1580Pas$. The same PSD result is also plotted by looking at the contour of the PSD for each contraction length as depicted from Figure 4.13 and 4.14.

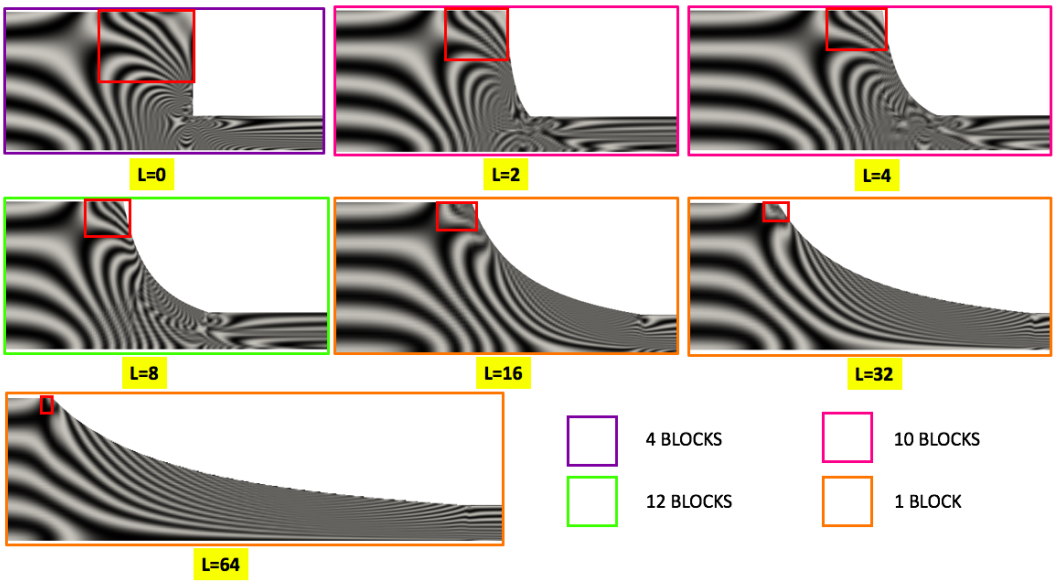

Figure 4.12: The birefringence pattern with contour interval = $5564.73 kgm^{-1}s^{-2}$, $\eta_S = 1580 Pas$ and pressure drop values as specified in Table 4.5.

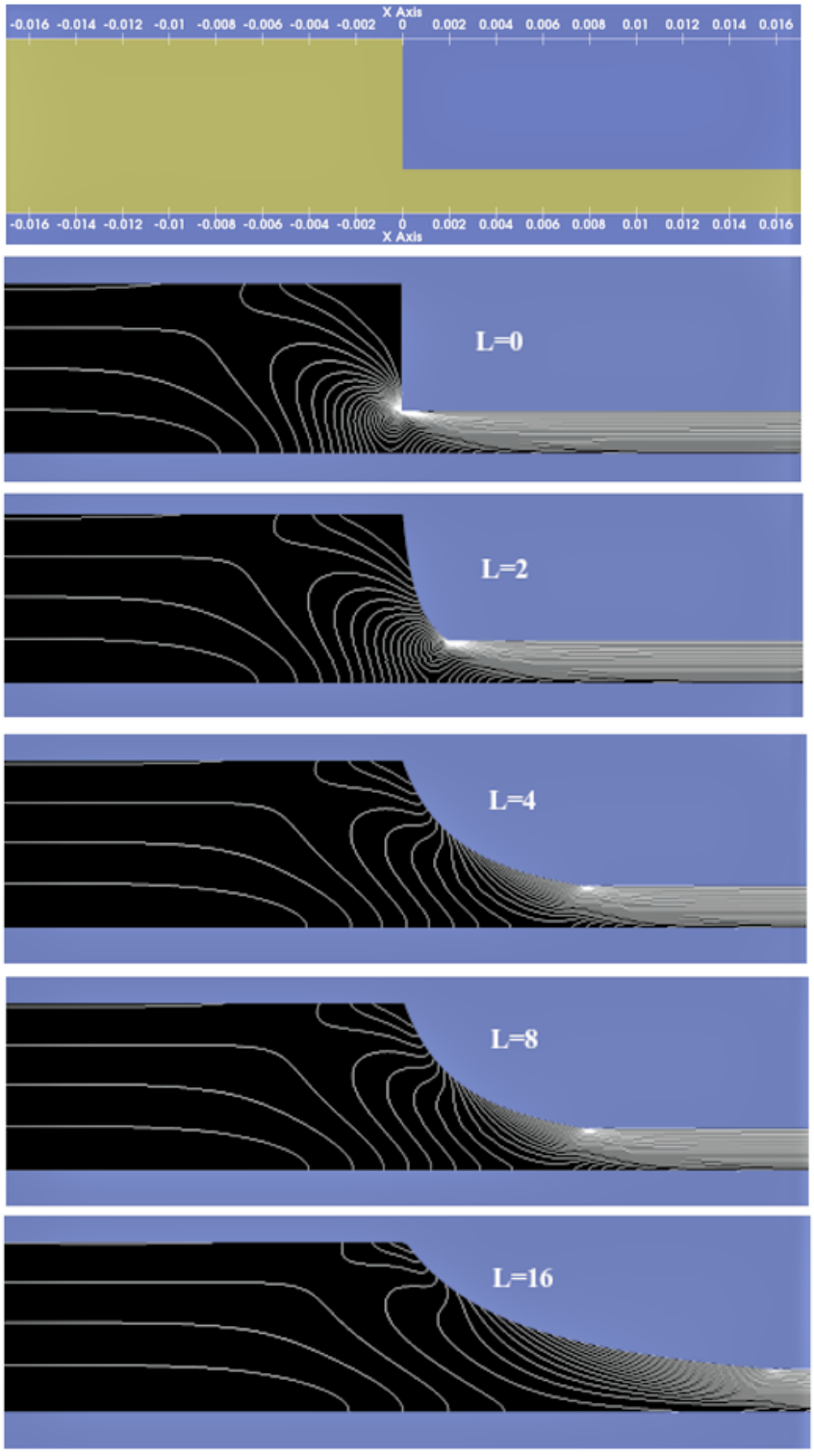

Figure 4.13: The steady-state two-dimensional PS2 birefringence contour for $L = 0, 2, 4, 8, 16mm$.

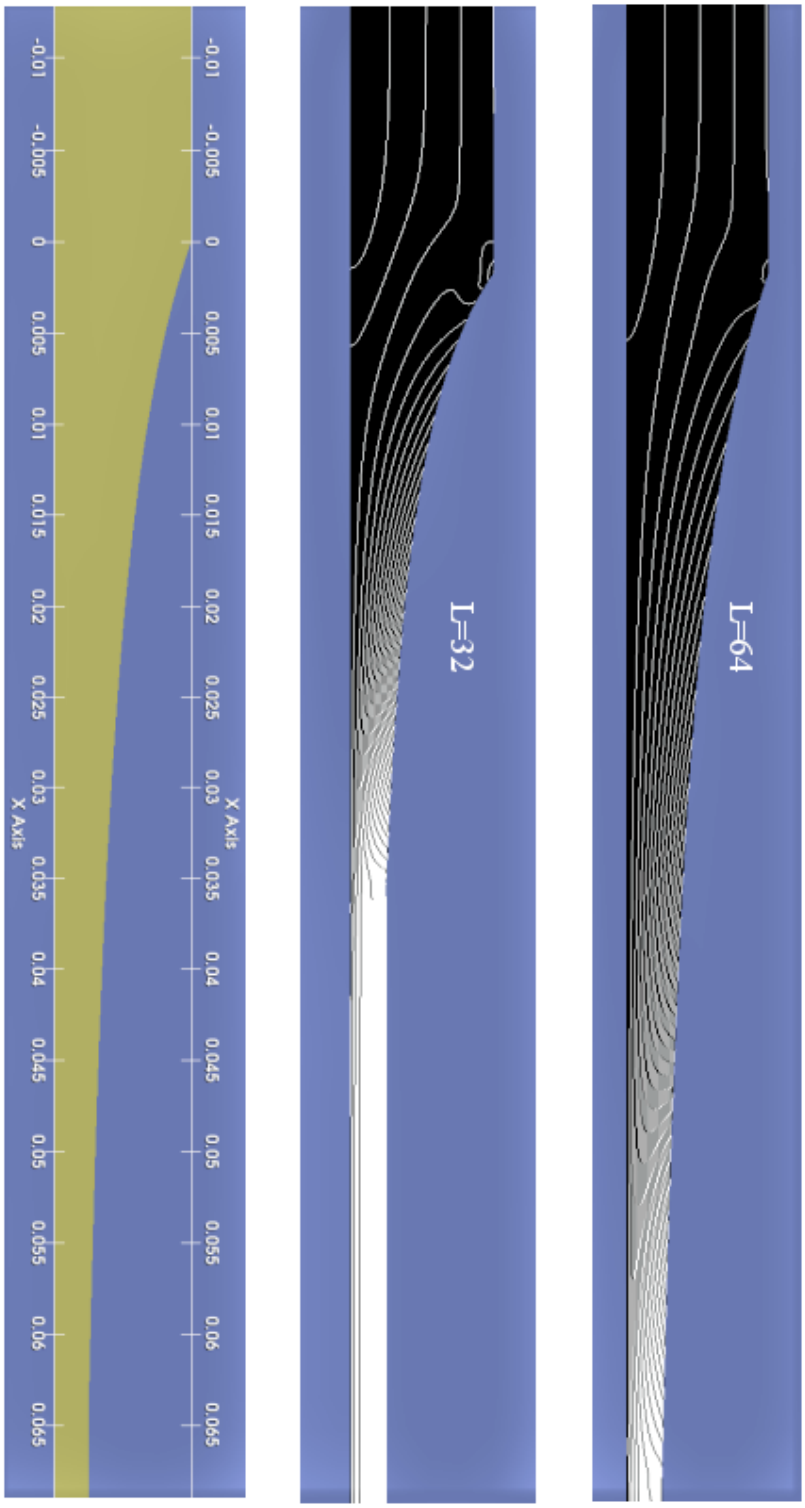

Figure 4.14: The steady-state two-dimensional PS2 birefringence contour for longer contraction length $L = 32, 64mm$.

The results show that the stress contour at the upstream sharp corner is reduced consistently as the contraction length increases and almost disappears for the longest contraction

length. This is because, as the contraction length increases, the flow resistance at the re-entrant of the geometry is decreased and thus the flow becomes smoother through the contracting region as a result of stress reducing at the sharp corner of the upstream channel. This also promotes the wider measuring range when investigating the fluid behaviour through this hyperbolic die which is one of the advantages of using this geometry.

The density of the PSD contour is more pronounced at the end of the contraction length before the fluid continues flowing in the straight channel downstream. This can clearly be seen for shorter contraction lengths. However, the stress is reduced in line with the increment of the contraction length which allow the fringes to be decreased gradually. This is because, in terms of the configuration, the shorter contraction lengths are not sufficient to produce a smooth transition from the end contraction to the straight channel due to the continuation point connecting the end of the hyperbolic contraction length and the straight channel. There is still a corner which affects the flow because of the resistance experienced by the fluid at that point. This explains why the stress in the fluid is more pronounced at that particular point.

In terms of the density of the fringes, this is not affected at the upstream channel, except at the sharp corner upstream and the reasons for that are as explained in the above discussion. At the re-entrant, corner and within the contraction, the fringes are observed to be perpendicular to the wall which can be seen clearly for sudden contraction, $L = 0mm$, and $L = 2mm$. This indicates that the flow through the contraction is dominated by the extensional flow and thus produces a higher extension-rate as shown in the sub-figure (bottom left) from Figure 4.11. As the contraction length is increased the fringe pattern is observed to become more parallel which indicates the flow is dominated by shear flow. Even though the consistent extension-rate is more uniform for the longest contraction length, it is shear dominated and gives low extension-rate. A higher pressure drop is required for the higher extension-rate prediction if the longer contraction length is considered.

4.6 Conclusion

We have presented work on the multimode Rolie-Poly model, where the model was implemented within the OpenFOAM software. This model is developed using the RheoTool

solver, `rheoFoam`. We impose a pressure drop to evolve the fluid velocity in the fluid domain. We validated our model with a benchmark two-dimensional 4:1 sudden contraction flow problem with Tenchev et al. [129] which used different boundary condition and numerical solver and we found agreement between these two approaches. The work is then extended to a hyperbolic contraction geometry where different contraction lengths are used to find the contraction length that are able to generate a uniform extension-rate within the contracting region. We discovered that, the minimum ratio of the height of the half upstream channel to the contraction length is 1:2.1333 such that one may observe the constant extension-rate of the fluid. This is consistent with the finding in Zagrafos et al. [144], that used the hyperbolic contraction approach to design the optimised microfluidic converging and diverging channel for homogeneous extensional deformation. They found that as the contraction length increases approaching the ideal hyperbolic shape, the optimal geometry can be achieved through the optimisation procedure. In real experiments, this observation will aid the prediction of the fluid extensional viscosity. However, the flow through a contraction can only be transient and the lower strain rate reached means non-linear response will be affected.

In the next chapter, we will extend the work further to the binary blend model. Comparison between the rheological behaviour for both coupled RDP and uncoupled mutimode Rolie-Poly models is made to distinguish the newer, coupled blend model from recently published work [23] which describes the dynamics in a more precise way.

Chapter 5

The rheological behaviour of the multimode Rolie-Poly and Rolie-Double-Poly

This chapter presents the implementation in OpenFOAM of the recently published model, Rolie-Double Poly (RDP) binary blend constitutive law. The implementation of the RDP model is first described and validated against published results [23]. The predictions of this model are compared with a multimode Rolie-Poly (mRP) model, chosen to have the same linear viscoelastic behaviour, to assess the effect of the additional coupling between modes in the RDP that is not present when mRP modes are superimposed. The differences in non-linear rheology between uncoupled and coupled models are explored by comparing the transient elongational viscosity and transient shear viscosity. Some results in Section 5.5.2 have been published in Azahar et al. [11] and are described in the following reference

- A. A. Azahar, O. G. Harlen, and M. A. Walkley. Modelling contraction flows of bi-disperse polymer blends using the Rolie-Poly and Rolie-Double-Poly equations. *Korea-Australia Rheology Journal*, 31(4), 203-209, 2019. https://doi.org/10.1007/s13367-019-0021-6.

5.1 Introduction

The RDP model for a binary blend of short and long molecules requires 4 conformation tensors describing the conformation of each of the two species with the constraining tubes formed by long and short chains. These are denoted as $\mathbf{A}_{IJ}$ where I denotes the conformation of chains of type I in the constraining tube formed of chains of type J. The total polymeric stress is given as

$$\boldsymbol{\tau} = G_N^0[\phi_L^2 f_E(\sigma_L)\boldsymbol{A}_{LL} + \phi_L\phi_S f_E(\sigma_L)\boldsymbol{A}_{LS} + \phi_S\phi_L f_E(\sigma_S)\boldsymbol{A}_{SL} + \phi_S^2 f_E(\sigma_S)\boldsymbol{A}_{SS}]. \tag{5.1}$$

The separate evolution equations are linked by the stretch of each chain defined by, $\sigma_I = \sqrt{\frac{1}{3}tr(\phi_L A_{IL} + \phi_S A_{IS})}$ where ϕ_L and ϕ_S are the concentration of long and short chains respectively. For convenience, the equations of the four conformation tensors defined in Chapter 1 are rewritten here.

$$\overset{\nabla}{\boldsymbol{A}}_{SS} = \underbrace{-\frac{1+\beta_{th}}{\lambda_{D,S}}(\mathbf{A}_{SS}-\mathbf{I})}_{\text{Reptation and CR}} \underbrace{-\frac{2}{\lambda_{R,S}}(1-\sigma_S^{-1})f_E(\sigma_S)[\mathbf{A}_{SS}+\beta^*\sigma_S^{2\delta}(\mathbf{A}_{SS}-\mathbf{I})]}_{\text{Retraction and CCR}} \tag{5.2}$$

$$\overset{\nabla}{\boldsymbol{A}}_{LL} = -\frac{1+\beta_{th}}{\lambda_{D,L}}(\mathbf{A}_{LL}-\mathbf{I}) - \frac{2}{\lambda_{R,L}}(1-\sigma_L^{-1})f_E(\sigma_L)[\mathbf{A}_{LL}+\beta^*\sigma_L^{2\delta}(\mathbf{A}_{LL}-\mathbf{I})] \tag{5.3}$$

$$\begin{aligned}\overset{\nabla}{\boldsymbol{A}}_{SL} = &\underbrace{-\frac{1}{\lambda_{D,S}}(\mathbf{A}_{SL}-\mathbf{I})}_{\text{Reptation}} \underbrace{-\frac{2}{\lambda_{R,S}}(1-\sigma_S^{-1})f_E(\sigma_S)\mathbf{A}_{SL}}_{\text{Retraction}} \\ &\underbrace{-(\mathbf{A}_{SL}-\mathbf{I})\left[\frac{\beta_{th}}{\lambda_{D,L}}+\frac{2\beta^*}{\lambda_{R,L}}(1-\sigma_L^{-1})f_E(\sigma_L)\sigma_S^{2\delta}\right]}_{\text{CR and CCR}}\end{aligned} \tag{5.4}$$

$$\overset{\nabla}{\boldsymbol{A}}_{LS} = -\frac{1}{\lambda_{D,L}}(\mathbf{A}_{LS} - \mathbf{I}) - \frac{2}{\lambda_{R,L}}(1 - \sigma_L^{-1}) f_E(\sigma_L)\mathbf{A}_{LS} - (\mathbf{A}_{LS} - \mathbf{I})\left[\frac{\beta_{th}}{\lambda_{D,S}} + \frac{2\beta^*}{\lambda_{R,S}}(1 - \sigma_S^{-1}) f_E(\sigma_S)\sigma_L^{2\delta}\right], \quad (5.5)$$

where $\overset{\nabla}{\boldsymbol{A}}_{IJ} = \frac{\partial \mathbf{A}_{IJ}}{\partial t} + \mathbf{u}\cdot\nabla\mathbf{A}_{IJ} - [\nabla\mathbf{u}\cdot\mathbf{A}_{IJ} + \mathbf{A}_{IJ}\cdot(\nabla\mathbf{u})^T]$, is the upper convected derivative. The equations (5.2)-(5.5) of the RDP model are referred for the implementation purposes within the OpenFOAM as described in the next section.

5.2 RDP implementation in OpenFOAM

The evolution equation for the tensor for the same species are similar to the Rolie-Poly model as defined in equation (1.5). Note that the reptation term in the Rolie-Poly model includes thermal constraint release, while in the RDP model the reptation and constraint release terms are written separately. Boudara et al. [23] also include the finite extensibility function, denoted by $f_E(\sigma_I)$, to limit the stretch extensibility of the polymer chain. However this is not included here, so $f_E(\sigma) = 1$. The implementation follows the RP model presented in the previous chapter, in that we replace the conformation tensor $\boldsymbol{A}_{IJ}$ with its contribution to the stress,

$$\boldsymbol{\tau}_{IJ} = \frac{\eta_{P,I}}{\lambda_{D,I}}(\mathbf{A}_{IJ} - \mathbf{I}),$$

where $G_I = \frac{\eta_{P,I}}{\lambda_{D,I}}$ is the elastic modulus for chain I defined as $G_I = G_N^0\phi_I$ for G_N^0 is the plateau modulus.

Rewriting the conformation tensors $\boldsymbol{A}_{IJ}$ described in equation (5.2)-(5.5) in terms of polymeric stress, $\boldsymbol{\tau}_{IJ}$, yields the following equations. The conformation of the same species can be compactly written as

Same species equation

$$\frac{\partial \boldsymbol{\tau}_{II}}{\partial t} + \mathbf{u}\cdot\nabla\boldsymbol{\tau}_{II} = 2\frac{\eta_{P,I}}{\lambda_{D,I}}\mathbf{D} + \mathbf{u}\cdot(\nabla\boldsymbol{\tau}_{II}) + \boldsymbol{\tau}_{II}\cdot(\nabla\mathbf{u})^T - \left[\frac{1+\beta_{th}}{\lambda_{D,I}} + \frac{2}{\lambda_{R,I}}(1-\sigma_I^{-1})f_E(\sigma_I)(1+\beta^*\sigma^{2\delta})\right]\boldsymbol{\tau}_{II} - \frac{2\eta_{P,I}}{\lambda_{D,I}\lambda_{R,I}}(1-\sigma_I^{-1})\mathbf{I},$$

where we have written out the upper convected derivative term and the subscript II represents either short-short or long-long species interaction. Having the equation as stated in equation (5.4) and (5.5), the compact form for different species entanglement can be written in terms of the polymeric stress $\boldsymbol{\tau}$ as follows

Different species equation

$$\frac{\partial \boldsymbol{\tau}_{IJ}}{\partial t} + \mathbf{u}\cdot\nabla\boldsymbol{\tau}_{IJ} = 2\frac{\eta_{P,I}}{\lambda_{D,I}}\mathbf{D} + \mathbf{u}\cdot(\nabla\boldsymbol{\tau}_{IJ}) + \boldsymbol{\tau}_{IJ}\cdot(\nabla\mathbf{u})^T - \left[\frac{1}{\lambda_{D,I}} + \frac{2}{\lambda_{R,I}}(1-\sigma_I^{-1})f_E(\sigma_I) + \frac{\beta_{th}}{\lambda_{D,J}} + \frac{2}{\lambda_{R,J}}\beta^*(1-\sigma_J^{-1})f_E(\sigma_J)\sigma_I^{2\delta})\right]\boldsymbol{\tau}_{IJ} - \frac{2}{\lambda_{D,I}\lambda_{R,I}}f_E(\sigma_I)\eta_{P,I}\mathbf{I},$$

where the subscript IJ is either the short-long interation or long short interaction (e.g. I=S or L and J=L or S respectively). These four equations are implemented in the high level C++ code used by OpenFOAM as `Rolie-Double-Poly.C`, which is detailed in Appendix B.

5.3 Validation of the implementation

It is crucial to validate the implementation before the model is used to study the behaviour of the model in the geometrical flow. The RDP model implemented within OpenFOAM is validated by reproducing one of the results from Boudara et al. [23]. The non-dimensional

relaxation time parameters are set to $\lambda_{D,L} = 200$, $\lambda_{R,L} = 1.0$, $\lambda_{D,S} = 0.1$ and $\lambda_{R,S} = 0.01$. The blend composition is $\phi_L = 0.05$ and $\phi_S = 0.95$ for long and short chains respectively. The maximum stretch is $\sigma_{max} = 100$. With the absence of solvent viscosity and convective constraint release parameter, $\beta^* = 1.0$, the following result is reproduced. In OpenFOAM, we use the solver called `rheoTestFoam` to simulate the rheology of the bidisperse RDP model in a single periodic computational cell.

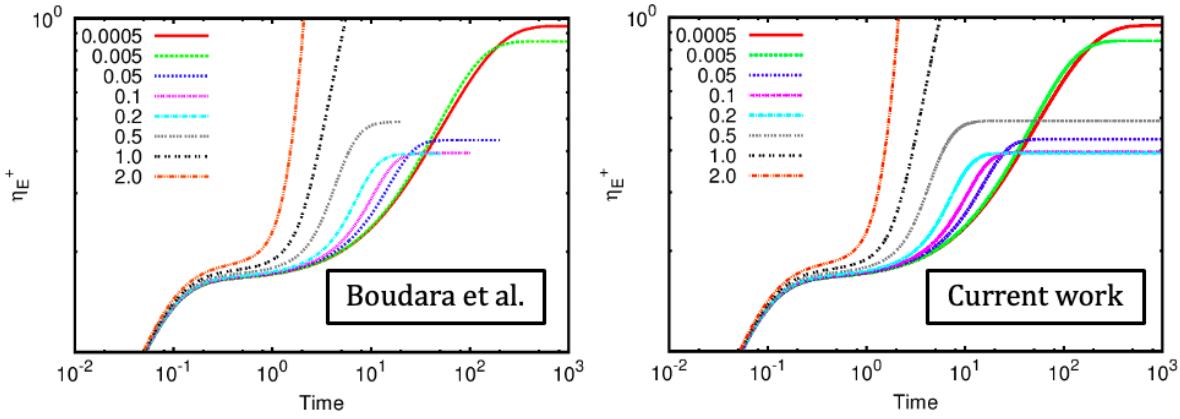

Figure 5.1: Validation of the implemented RDP model by comparing the transient uniaxial extensional viscosity from the published results by Boudara et al. [23] (LHS) with current work (RHS) for 5% long chain blend with 95% short chain having relaxation times of $\lambda_{D,L} = 200$, $\lambda_{R,L} = 1.0, \lambda_{D,S} = 0.1$, $\lambda_{R,S} = 0.01$.

Figure 5.1 shows the perfect agreement between both predictions demonstrating the correct implementation of the RDP model within the software. In the next section, the comparison of the rheological behaviour for RDP with an equivalent linear superposition mRP models is presented.

5.4 Parameters for the RDP model

The RDP model parameters used by Boudara et al. [23] were chosen such that the stretch relaxation time for the long chain was longer than the reptation time of the short chains. However the particular values chosen result in four orders of magnitude difference between the longest and shortest relaxation times, which is computationally challenging for a full computational fluid dynamics simulation. Therefore, we will use a different set of parameters that retain the relative ordering of the relaxation times but reduce the ratio between the longest and shortest time. The chosen parameters for the RDP coupled model are presented

in Table 5.1. The units are chosen such that the plateau modulus, G_N^0 for this bidisperse blends model is set to $G_N^0 = 1.0$. The elastic modulus for both short and long chains are defined as $G_S = G_N^0\phi_S$ and $G_L = G_N^0\phi_L$ respectively. The data in Table 5.1 do not represent a particular polymer blend, but are chosen to give a sufficient difference between $\lambda_{D,L}$, $\lambda_{R,L}$ and $\lambda_{D,S}$ to see the effects of the enhanced stretch relaxation times, but without too large a range of relaxation times for computational convenience.

Table 5.1: The default RDP parameters for the bidisperse polymer blend.

Parameter	Long (L)	Short (S)
$\eta_{P,i}$	0.05	0.095
$\lambda_{D,i}$	10.0	0.1
$\lambda_{R,i}$	0.2	0.05
ϕ_i	0.05	0.95

Note that, the subscript i from the Table 5.1 represents $i = S$ or L. The solvent viscosity and the total polymeric viscosity are defined as $\eta_S = 0.01$ and $\eta_P = \eta_{P,L} + \eta_{P,S}$ respectively. Hence we will use the following non-dimensional relaxation times $\lambda_{D,L} = 10, \lambda_{R,L} = 0.2, \lambda_{D,S} = 0.1$ and $\lambda_{R,S} = 0.05$ where each of the relaxation time is non-dimensionalised by dividing with $5\lambda_{R,L}$. This reduces the ratio $\lambda_{D,L}/\lambda_{R,S}$ to 200 compared to 20 000. The other dimensionless parameters are $t = \frac{t}{5\lambda_{R,L}}$, $\dot{\varepsilon} = 5\dot{\varepsilon}\lambda_{R,L}$, $\eta_E^+ = \frac{\eta_E^+}{5G_N^0\lambda_{R,L}}$ and $\eta^+ = \frac{\eta^+}{5G_N^0\lambda_{R,L}}$. We next consider the effect of changing the degree of entanglement of the long chains by examining how $\lambda_{D,L}$ influences the prediction of elongational and shear viscosity. Figure 5.2 illustrates the influence of $\lambda_{D,L}$ on the elongational viscosity while keeping other parameters the same.

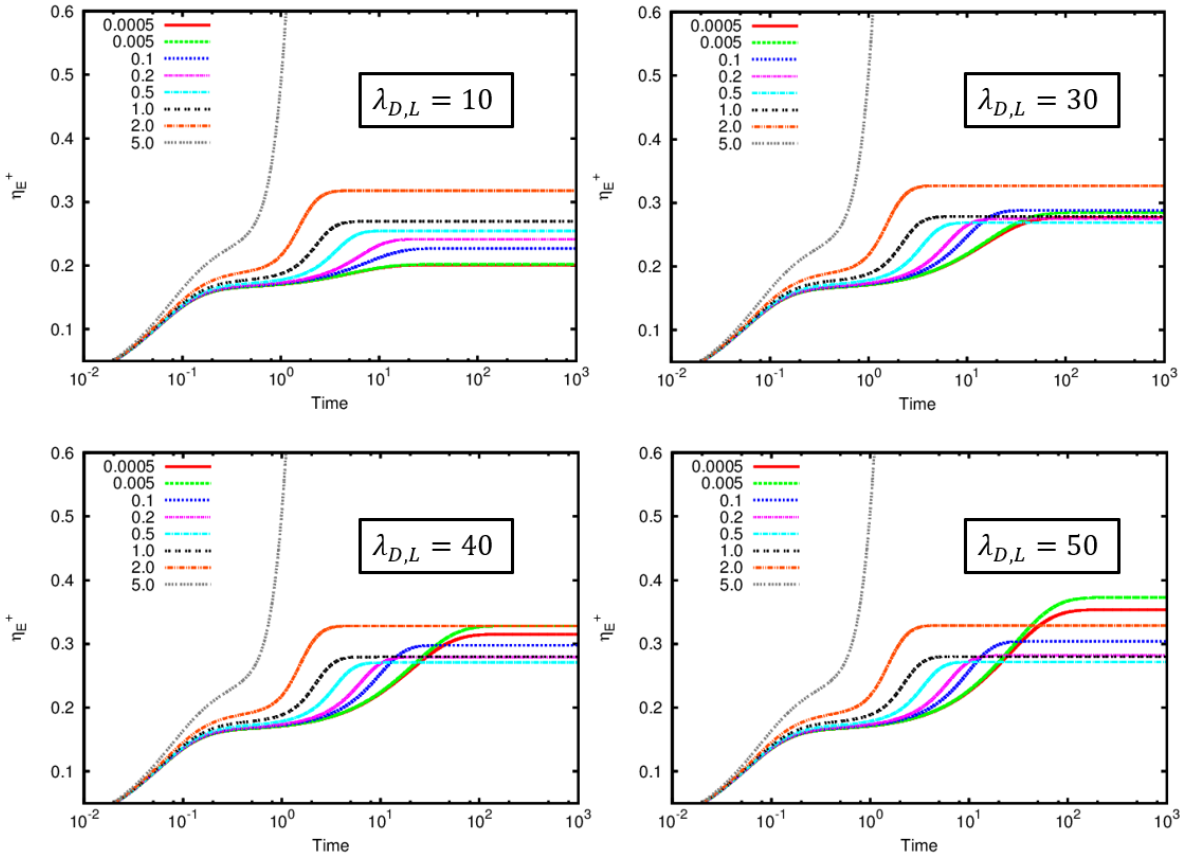

Figure 5.2: The transient uniaxial elongational viscosity for different values of reptation relaxation time for the long chain, with 5% long chain concentration, predicted by the RDP model when $\lambda_{R,L} = 0.2$, $\lambda_{D,S} = 0.1$ and $\lambda_{R,S} = 0.05$. The legend value represents the different extension-rate used.

In Figure 5.2, we can observe the changes of the elongational viscosity at steady-state predicted at the lower extension-rates, (i.e. $\dot{\varepsilon} = 0.0005, 0.005, 0.1$) is increased as $\lambda_{D,L}$ is increased. This is to be expected as increasing the reptation relaxation time of the long chain increases the zero shear-rate viscosity. Once the extension-rate exceeds $\lambda_{D,L}^{-1}$ the extensional viscosity reduces (extension thins). This would be expected to continue until the emergence of the elongational hardening when $\dot{\varepsilon} > \lambda_{R,L}^{-1}$, that is $\dot{\varepsilon} > 5.0$. However, we find that this increase occurs at a lower rate because of the phenomenon of enhanced stretch relaxation time. The onset of the elongational hardening starts to be observed when $\dot{\varepsilon}\lambda_{R,L}^{eff} > 1.0$, where $\dot{\varepsilon} > 0.25$. Therefore, we see that the onset of the elongational hardening is observed within $(\lambda_{R,L}^{eff})^{-1} < \dot{\varepsilon} < (\lambda_{R,L})^{-1}$ as stated in Boudara et al. [23]. It is worth noting that in order to see the extension-rate thinning before the onset of stretch requires that $\lambda_{D,L} >> \lambda_{R,L}^{eff}$ so that $Z = \frac{\lambda_{D,L}}{3\lambda_{R,L}} > \phi_L^{-1}$, meaning that the long chains must be entangled by other long

chains. In particular we find that for $\lambda_{D,L} = 10$ we do not find an extension thinning region.

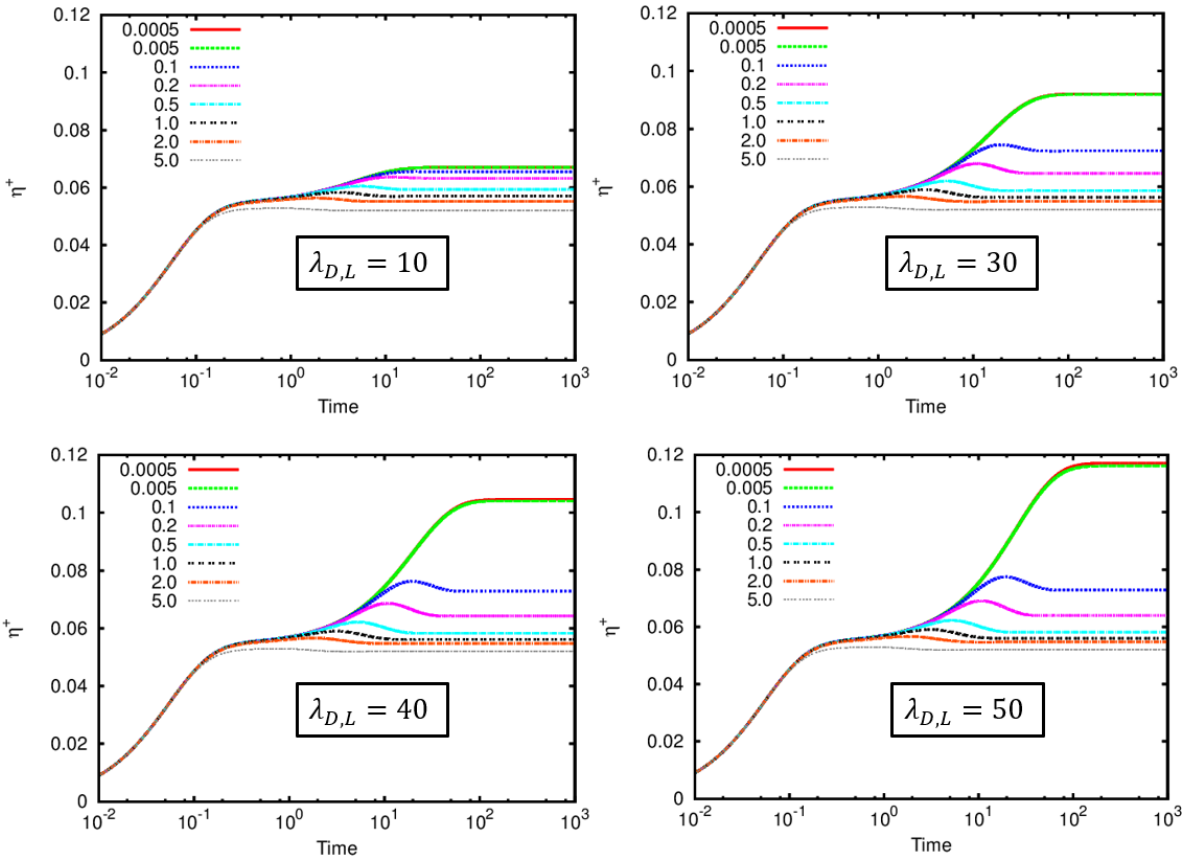

Figure 5.3: The transient shear viscosity for different value of reptation relaxation time for the long chain with 5% long chain concentration predicted by the RDP model when $\lambda_{R,L} = 0.2$, $\lambda_{D,S} = 0.1$ and $\lambda_{R,S} = 0.05$. The legend value represents the different shear-rate used.

Figure 5.3 shows the time dependent shear viscosity by varying the reptation relaxation time for the long chain, $\lambda_{D,L}$. In contrast to extensional viscosity, the prediction for shear viscosity shows only shear-rate thinning. Notice that the viscosity at the higher shear-rates is not affected by the reptation relaxation time for the long chain, while the lower shear rate, (i.e. $\dot{\gamma} = 0.0005$ and 0.005) shows significant changes in line with the increase in the zero shear-rate viscosity. The overshoot of viscosity illustrated by higher $\lambda_{D,L}$ is more obvious compared to the lower one. This is because, as the $\lambda_{D,L}$ increases, the entanglement number [83], $Z = \frac{\lambda_{D,L}}{3\lambda_{R,L}}$, for the $L - L$ interaction, (defined by the ratio of two relaxation times) also increases. This means the entanglement between the long chains get stronger and the orientation effects of the chain during the constraint release explains the overshoot

viscosity response for the intermediate shear-rate.

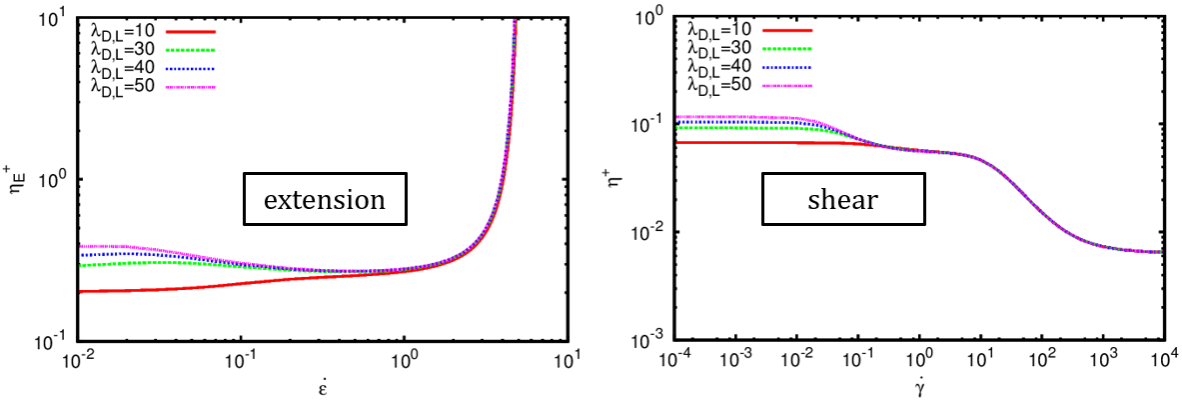

Figure 5.4: The extension (LHS) and shear (RHS) viscosity predicted by the RDP model by varying the reptation relaxation time of the long chain, $\lambda_{D,L}$ for 5% long chain contribution when $\lambda_{R,L} = 0.2$, $\lambda_{D,S} = 0.1$, $\lambda_{R,S}$ and $\beta^* = 0.0$.

The extensional viscosity and shear viscosity of the total polymeric stress for the RDP model, depicted in Figure 5.4, illustrates the rheological behaviour of the model. Looking at the extensional viscosity plotted against extension-rates, the extensional viscosity for the same material (having the same plateau modulus) is higher at the lower extension-rates as the reptation relaxation time of the long chain increases. Imposing higher extension-rate allows the extension-thinning phenomena to take place where the onset of the extension-thinning occurs at a different extension rate depending on the reciprocal of the reptation relaxation time of the long chain considered. However, when $\lambda_{D,L} = 10$, the extension-thinning is not taking place. The extension viscosity predicted by different $\lambda_{D,L}$ converges to the same value within the intermediate regime before extension hardening is observed when $\dot{\varepsilon} > \frac{1}{\lambda_{R,L}} = 5$. In this regime, the molecular stretch of the polymer chain will continuously grow to infinity, unless the finite extensibility function is considered in the RDP model.

Noting the fact that the viscosity of the polymeric solution depends on the molecular weight of the polymer (i.e. the higher the molecular weight, the longer the polymeric chain and thus the reptation relaxation time is longer), the right-hand Figure 5.4 shows a constant shear viscosity at a lower shear-rate (Newtonian regime). However, when a higher shear-rate is imposed, the viscosity decreases which indicates the shear-thinning phenomena. Notice that, from the shear flow figure, there are double humps spotted for higher relaxation times. This is as the consequence of the four relaxation times scales involved in the RDP model

separate the shear viscosity into different regimes indicating the shear-thinning for the short and long chains within the intermediate regime.

5.5 Comparison between uncoupled and coupled models

In order to examine the role played by the coupling terms in the RDP model, it is useful to compare with the predictions of a mRP model that does not have these coupling terms. One possible comparison would be with a 2-mode RP model where the two modes correspond to the long and short chains respectively. However this model gives a different response even in the limit of linear viscoelasticity. Instead we shall construct a mRP model that has the same linear viscoelasticity in order to look at the differences in the nonlinear rheology. In particular we will compare the transient uniaxial elongational viscosity. This demonstrates the effect of the enhanced stretch in the RDP model that is not captured by the linear superposition of the mRP model. The transient uniaxial extensional viscosity is plotted for different extension-rate values for the (3-mode) mRP model and RDP binary blend model.

5.5.1 Linear viscoelastic envelope - Rolie-Double-Poly (bidisperse model)

Deriving the linear viscoelastic limit for RDP will lead to the development of the equivalent mRP model. It is not as straight forward as defining monodisperse and mRP models because the model now contains extra stress terms (i.e. the average stress incorporates the interaction between different species) that need to be taken into account. Taking an infinitesimal step strain, $\boldsymbol{\varepsilon}$ and setting $\beta_{th} = 1.0$ the evolution equations (5.2) -(5.5), reduce to

$$
\begin{aligned}
\frac{d\mathbf{A}_{LL}}{dt} &= -\frac{2}{\lambda_{D,L}}\mathbf{A}_{LL}, && \implies \mathbf{A}_{LL} = \boldsymbol{\varepsilon} e^{-2t/\lambda_{D,L}},\\
\frac{d\mathbf{A}_{SS}}{dt} &= -\frac{2}{\lambda_{D,S}}\mathbf{A}_{SS}, && \implies \mathbf{A}_{SS} = \boldsymbol{\varepsilon} e^{-2t/\lambda_{D,S}},\\
\frac{d\mathbf{A}_{LS}}{dt} &= -\left(\frac{1}{\lambda_{D,L}} + \frac{1}{\lambda_{D,S}}\right)\mathbf{A}_{LS} \\
&= \frac{-2}{\lambda_D^*}\mathbf{A}_{LS}, && \implies \mathbf{A}_{LS} = \boldsymbol{\varepsilon} e^{-2t/\lambda^*},\\
\frac{d\mathbf{A}_{SL}}{dt} &= -\left(\frac{1}{\lambda_{D,S}} + \frac{1}{\lambda_{D,L}}\right)\mathbf{A}_{SL} \\
&= \frac{-2}{\lambda_D^*}\mathbf{A}_{SL}, && \implies \mathbf{A}_{SL} = \boldsymbol{\varepsilon} e^{-2t/\lambda^*} = \mathbf{A}_{LS}.
\end{aligned}
$$

Here λ_D^* is the reciprocal averaged reptation relaxation time for short and long chains defined by $\lambda_D^* = \frac{2\lambda_{D,S}\lambda_{D,L}}{\lambda_{D,S}+\lambda_{D,L}}$. Substituting $\mathbf{A}_{LL}$, $\mathbf{A}_{SS}$, $\mathbf{A}_{SL}$ and $\mathbf{A}_{LS}$ into the equation (5.1) yields the following equation,

$$
\boldsymbol{\tau} = \boldsymbol{\varepsilon}\underbrace{G_0(\phi_L^2 e^{-2t/\lambda_{D,L}} + 2\phi_L\phi_S e^{-2t/\lambda_D^*} + \phi_S^2 e^{-2t/\lambda_{D,S}})}_{G(t)}.
$$

Rewriting $G(t)$ as a square power gives

$$
G(t) = G_0(\phi_L e^{-t/\lambda_{D,L}} + \phi_S e^{-t/\lambda_{D,S}})^2
$$

which is consistent with the elastic modulus defined by double reptation theory [44] that is used to develop the RDP model. Hence, the transient linear elongational viscosity is given by

$$
\begin{aligned}
\eta_E(t) &= 3\int_0^t G(t)dt \\
&= 3G_0\int_0^t (\phi_L^2 e^{-2t/\lambda_{D,L}} + 2\phi_L\phi_S e^{-2t/\lambda_D^*} + \phi_S^2 e^{-2t/\lambda_{D,S}})dt \\
&= 3G_0\left[\frac{\phi_L^2\lambda_{D,L}}{2}(1 - e^{-2t/\lambda_{D,L}}) + \phi_L\phi_S\lambda_D^*(1 - e^{-2t/\lambda_D^*}) + \frac{\phi_L^2\lambda_{D,S}}{2}(1 - e^{-2t/\lambda_{D,S}})\right].
\end{aligned}
\tag{5.6}
$$

Comparing this with the linear viscoelastic prediction for the mRP model we see that this requires a 3-mode model, such that

$$\eta_E(t) = 3[\underbrace{\eta_{P,1}(1-e^{-2t/\lambda_{D,L}})}_{\textbf{Mode 1}} + \underbrace{\eta_{P,2}(1-e^{-2t/\lambda^*_D})}_{\textbf{Mode 2}} + \underbrace{\eta_{P,3}(1-e^{-2t/\lambda_{D,S}})}_{\textbf{Mode 3}}]$$

where the viscosity for each mode can be rewritten in terms of a set of parameters that we define for the RDP model as follows

$$\begin{aligned}
\eta_{P,1} &= \frac{G_0\phi_L^2\lambda_{D,L}}{2} \implies \eta_{P,L}\frac{\phi_L}{2}, \\
\eta_{P,2} &= G_0\phi_L\phi_S\lambda^*_D \implies \eta_{P,L}\phi_S\frac{\lambda^*_D}{\lambda_{D,L}}, \\
\eta_{P,3} &= \frac{G_0\phi_S^2\lambda_{D,S}}{2} \implies \eta_{P,S}\frac{\phi_S}{2}.
\end{aligned}$$

As the LVE does not include the stretch terms from the mRP and RDP models, relaxation parameters (i.e. $\lambda_{R,i}$ where i is the i^{th} mode in 3-mode description or L or S in RDP model definition) remain to be defined. Since the reptation times of modes 1 and 3 are determined by the reptation times of the long and short molecules respectively, we assign the corresponding stretch relaxation times to $\lambda_{R,1}$ and $\lambda_{R,3}$. Mode 2 represents interactions between long and short chains. So here we use the same reciprocal average of relaxation times as the corresponding reptation time for this mode. Hence, we have

$$\begin{aligned}
\lambda_{D,1} &= \frac{\lambda_{D,L}}{2} \qquad \lambda_{R,1} = \lambda_{R,L} \qquad G_1 = G_0\phi_L^2, \\
\lambda_{D,2} &= \frac{\lambda^*_D}{2} \qquad \lambda_{R,2} = \lambda^*_R \qquad G_2 = 2G_0\phi_L\phi_S, \\
\lambda_{D,3} &= \frac{\lambda_{D,S}}{2} \qquad \lambda_{R,3} = \lambda_{R,S} \qquad G_3 = G_0\phi_S^2,
\end{aligned}$$

where $\lambda^*_R = \frac{2\lambda_{R,L}\lambda_{R,S}}{\lambda_{R,L}+\lambda_{R,S}}$ is the reciprocal averaged stretch relaxation time for short and long chains.

5.5.2 Comparison between mRP, RDP and LVE

In Figure 5.5 we compare the transient extensional viscosity at very low extension-rate, $\dot{\varepsilon} = 0.0005$ (that is expected to be in the LVE) between the OpenFOAM implementation of the mRP model (uncoupled case) and the RDP binary blend (coupled case) with the LVE prediction. A set of parameters of RDP with $\lambda_{D,L} = 10$, $\lambda_{D,L} = 0.2$, $\lambda_{D,L} = 0.1$, $\lambda_{D,L} = 0.05$, $\phi_L = 0.05$, $\phi_S = 0.95$, $G = 1.0$ and respective polymeric viscosity, $\eta_{P,L} = 0.5$ and $\eta_{P,S} = 0.095$ are considered.

Table 5.2: The (3-mode) mRP parameters.

Parameter	Mode 1	Mode 2	Mode 3
$\eta_{P,j}$	0.0125	0.009406	0.045125
$\lambda_{D,j}$	5.0	0.0990099	0.05
$\lambda_{R,j}$	0.2	0.08	0.05

The equivalent set of parameters for the 3-mode model are presented in Table 5.2. Other parameters for both models are set to $\beta_{th} = 1.0$, $\beta^* = 0$ and $\delta = -0.5$.

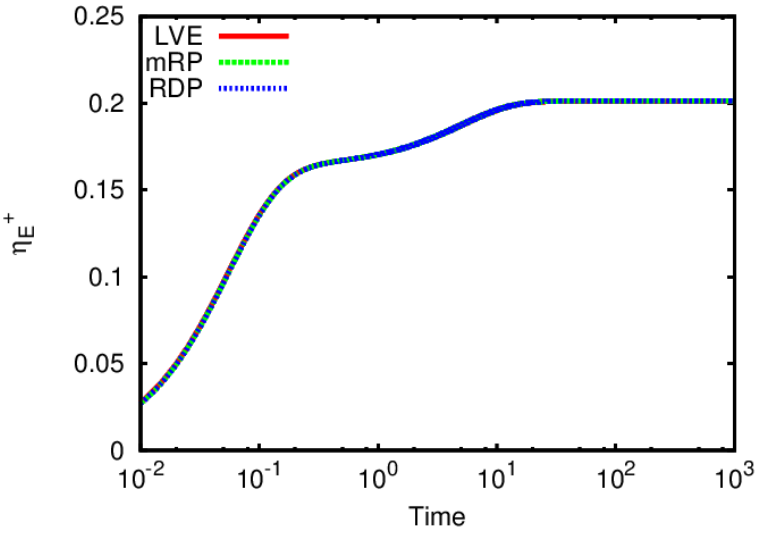

Figure 5.5: Comparison between LVE with (uncoupled 3-mode) mRP and (coupled) RDP blend prediction at low extension-rate, $\dot{\varepsilon} = 0.0005$ obtained using `rheoTestFoam` solver.

The results plotted in Figure 5.2 show an excellent agreement between the theoretical LVE definition for mRP and RDP models with the results produced by the `rheoTestFoam` solver for both models in the linear viscoelastic regime. The agreement shown in Figure 5.5

validates our prediction that the two models should be able to produce the same results in the linear viscoelastic envelope.

We next examine the nonlinear behaviour by comparing the prediction of the transient elongational viscosity at higher extension-rates, $\dot{\varepsilon} = 0.0005, 0.005, 0.1, 0.2, 0.5, 1.0, 2.0, 5.0$. We illustrate the prediction for the transient shear viscosity for both coupled and uncoupled models in Figure 5.6.

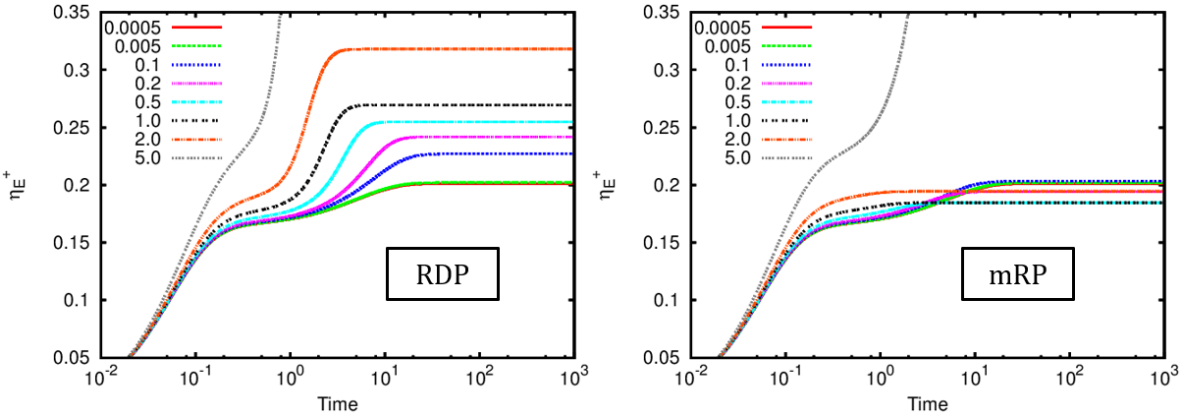

Figure 5.6: The transient uniaxial elongational viscosity predicted by RDP (coupled) and 3-mode mRP (uncoupled) for 5% long chain with $\lambda_{D,L} = 10$, $\lambda_{R,L} = 0.2$, $\lambda_{D,S} = 0.1$ and $\lambda_{R,S} = 0.05$.

Figure 5.6 depicts the prediction made by the RDP and mRP model. The difference in prediction made by the two models can be observed very clearly as the extension-rate increases.

Note that the first two lowest extension-rate, (i.e. $\dot{\varepsilon} = 0.0005$ and 0.005) do not show any significant difference between the models. This is due to the fact that these rates are still in the linear regime which can be captured by the LVE. However, from $\dot{\varepsilon} = 0.1$ and above the models are showing significant difference where the elongational viscosity predicted by the RDP model is increasing gradually above the linear viscoelastic prediction. This illustrates the elongational hardening phenomena at higher extension-rate resulting from the stretching of the polymer chains. In contrast, the mRP model shows less strain hardening than the RDP. In particular the steady-state extensional viscosity decreases for $\dot{\varepsilon} = 0.2$ to 1.0 before it increases again when $\dot{\varepsilon} = 2.0$. For $\dot{\varepsilon} = 5.0$, the prediction made by both models shows strain hardening.

The difference between the predictions made by these models is due to the coupling in

the RDP model that leads to the enhanced stretch of the long chain which is not observable in the mRP model. It is worth emphasizing here that the effective stretch relaxation time of the long chain has been investigated experimentally [9], by observing how the dilution of the long chains in shorter chains influences when the strain-rate at chain stretch is first observed. They found that the critical extension-rate for the onset of the chain stretch, and emergence of the elongational hardening, is lower than would be predicted by the chain Rouse time, as a result of the dilution of long chains by short chains. The effective stretch relaxation time for the long chain at a concentration ϕ_L is given by $\lambda_{R,L}^{eff} = \frac{\lambda_{R,L}}{\phi_L}$ [9]. For the RDP in Figure 5.6, $\lambda_{R,L}^{eff} = 4$ as $\lambda_{R,L} = 0.2$ and $\phi_L = 0.05$. Note that the elongational hardening is expected at $\dot{\varepsilon}\lambda_{R,L}^{eff} > 1$. Therefore, the onset of the elongational hardening from Figure 5.6 can be seen for $\dot{\varepsilon} = 0.5$ and above.

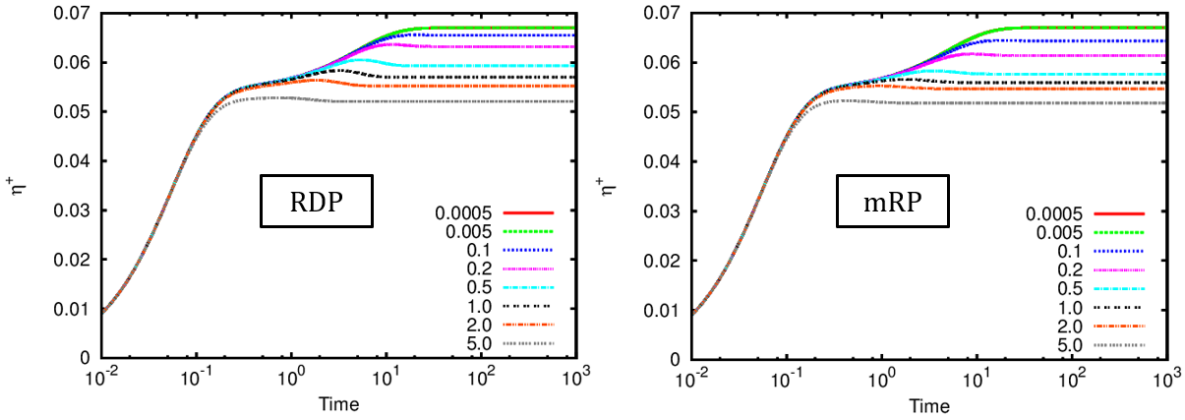

Figure 5.7: The transient shear viscosity predicted by RDP (coupled) and 3-modes mRP (uncoupled) for 5% long chain with $\lambda_{D,L} = 10$, $\lambda_{R,L} = 0.2$, $\lambda_{D,S} = 0.1$ and $\lambda_{R,S} = 0.05$.

The transient shear viscosity for both RDP and mRP models are also plotted by varying the shear-rate $\dot{\gamma} = 0.0005, 0.005, 0.1, 0.2, 0.5, 1.0, 2.0, 5.0$. The results for both models are shown in Figure 5.7. From the figure, the shear viscosity decreases as the shear-rate increases. In contrast to the extensional flow, the predictions of these two models in shear flow are very similar. However, it can be seen that the prediction made for both RDP and mRP models for lower shear-rates (i.e. $\dot{\gamma} = 0.0005$ and 0.005) are identical since these shear-rates are still in the linear viscoelastic envelope. While for $\dot{\gamma} = 0.1, 0.2, 0.5,$ and 1.0 the RDP model predicts a slightly higher shear viscosity at steady-state compared to the mRP model. Higher shear-rates predict the same steady-state shear viscosity for both mod-

els. The overshoot shown by RDP is also more pronounced than the mRP model. These slight differences between the models are because of the coupling effect in the RDP model that is more observable at high shear-rates.

5.6 RDP in a steady extension

The stretch in the thin and fat tube can be explained mathematically by considering steady extensional flow. Recalling the stretch for the thin and fat tubes as

$$\sigma_L = \sqrt{\frac{tr(\mathbf{A}_L)}{3}}, \qquad \sigma_{LL} = \sqrt{\frac{tr(\mathbf{A}_{LL})}{3}}.$$

Under planar extensional flow where $\nabla \mathbf{u} = \begin{pmatrix} \dot{\varepsilon} & 0 & 0 \\ 0 & -\dot{\varepsilon} & 0 \\ 0 & 0 & 0 \end{pmatrix}$, the thin and fat tube stretch can be derived as follows. Let $\beta^* = 0$, $f_E(\sigma) = 1.0$, and $\beta_{th} = 1.0$ the $xx-$component for the upper-convective derivative $\overset{\nabla}{A}_{xx} = -2\dot{\varepsilon}A_{xx}$. The $L - L$ contribution of the RDP model in the $xx-$component reduces to

$$-2\dot{\varepsilon}A_{LL} = \frac{2}{\lambda_{D,L}}(A_{LL} - 1) - \frac{2}{\lambda_{R,L}}\left(1 - \frac{1}{\sigma_L}\right)A_{LL} \tag{5.7}$$

and the $L - S$ contribution for the $xx-$component reduces to

$$-2\dot{\varepsilon}A_{LS} = -\left(\frac{1}{\lambda_{D,L}} + \frac{1}{\lambda_{D,S}}\right)(A_{LS} - 1) - \frac{2}{\lambda_{R,L}}\left(1 - \frac{1}{\sigma_L}\right)A_{LS}. \tag{5.8}$$

When $\dot{\varepsilon}\lambda_{D,L} >> \dot{\varepsilon}\lambda_{R,L} \approx 1$ and $\dot{\varepsilon}\lambda_{D,S} << 1$, then from equation (5.7) it follows that

$$\dot{\varepsilon}\lambda_{R,L} \approx \left(1 - \frac{1}{\sigma_L}\right) \qquad \Longrightarrow \sigma_L \approx (1 - \dot{\varepsilon}\lambda_{R,L})^{-1}.$$

So, for example if $\dot{\varepsilon}\lambda_{R,L} = 0.5$ then $\sigma_L \approx 2$. Now if $\dot{\varepsilon}\lambda_{D,S} << 1$ then it follows from equation (5.8) that $\mathbf{A}_{LS} = \mathbf{I}$ and therefore $tr(\mathbf{A}_{LS}) \approx 3$. Now from the definition of the thin tube stretch, we have

$$\sigma_L = \sqrt{\frac{tr(\mathbf{A}_L)}{3}} \implies 3\sigma_L^2 = tr[\phi_L \mathbf{A}_{LL} + (1-\phi_L)\mathbf{A}_{LS}]$$
$$= \phi_L tr(\mathbf{A}_{LL}) + (1-\phi_L) tr(\mathbf{A}_{LS}).$$

Since $tr(\mathbf{A}_{LS}) = 3$ the square of the thin tube stretch is given by

$$\sigma_L^2 = \phi_L \sigma_{LL}^2 + (1-\phi_L)1$$
$$= \phi_L \sigma_{LL}^2 - \phi_L + 1$$
$$\sigma_{LL}^2 = \frac{1}{\phi_L}(\sigma_L^2 - 1) + 1. \tag{5.9}$$

Therefore in this limit, where $\frac{1}{\lambda_{D,L}} << \dot{\varepsilon} << \frac{1}{\lambda_{D,S}}$ in a steady extensional flow, thin tube stretch and fat tube stretch are related by equation (5.9) and so fat tube stretch is larger by a factor of $\frac{1}{\sqrt{\phi_L}}$ (depending on how big the stretch is) when $\sigma_L^2 - 1 > 0$.

5.7 Conclusion

In this chapter we described the implementation of the RDP model in OpenFOAM and compared its rheological behaviour for shear and extensional flow with a mRP model with the same linear rheology. The implementation of the RDP model is presented in Section 5.2 and and validated against published results. The effect of varying $\lambda_{D,L}$ is also considered and showed that for strain-rate thinning to be observed the long chain components must be entangled by other chains, i.e. $\phi_L Z = \frac{\phi_L \lambda_{D,L}}{3\lambda_{R,L}} > 1$. The derivation for the equivalent 3-mode model is discussed in the following section. The prediction between the coupled and uncoupled models for transient elongational and shear flow, for different extension- and shear-rates above the LVE regime is observed. The enhanced stretch in the RDP model is demonstrated, showing that the main difference between the two models is in extensional flow. This leads to an increase in chain stretch at extension-rates below the inverse stretch relaxation time of the long chains in the non-linear regime. The mathematical analysis for

the RDP model in a steady extension is also presented.

Chapter 6

Rolie-Double-Poly - Hyperbolic contraction flow

In this chapter, we use the constitutive models implemented in Chapter 4 and Chapter 5 to investigate the flow of a polymer blend in a hyperbolic contraction geometry. Some of the results in Section 6.4 have been published in Azahar et al. [11] and are described in the following reference.

- A. A. Azahar, O. G. Harlen, and M. A. Walkley. Modelling contraction flows of bidisperse polymer blends using the Rolie-Poly and Rolie-Double-Poly equations. *Korea-Australia Rheology Journal*, 31(4), 203-209, 2019. https://doi.org/10.1007/s13367-019-0021-6.

6.1 Introduction

Recall that, in Chapter 4, we have considered the hyperbolic contraction flow study comparing different hyperbolic contraction length for a set of parameters with dimension that represent the experimental geometry studied by Tenchev et al. [129] for the PS2 fluid. Throughout this chapter, the behaviour of the bidiperse polymer blend described by the RDP model is investigated in a hyperbolic contraction geometry with different scale from the geometry defined in Chapter 4. This includes the effects of varying relevant physical geometrical quantities and flow rates. These include investigating the effect of different

imposed pressure drops (since we are considering a pressure driven flow), the geometry of the contraction and the effect of varying the blend composition of short and long polymer chains. Although the purpose of the contraction geometry is to generate an elongational flow, the no-slip boundary condition means that the fluid experiences a shear deformation near the walls in addition to the elongational effect at the centre-line as the fluid accelerates through the contraction region. The relative size of the shear and elongation rates is affected by the geometry and the effect on the stress of the geometrical changes can be examined by looking at the birefringence pattern of the polymeric fluid for the whole field of the upper half geometrical domain. Whilst we mainly consider a two-dimensional planar contraction, the work is extended to a three-dimensional geometry with no-slip boundary conditions set at the side wall. The influence of the channel depth in determining the extension-rate along the centre-line of the symmetry plane is observed.

The results for the RDP coupled model are compared to those obtained with a 3-mode mRP uncoupled model for different contraction ratios to examine the effect of the additional coupling terms between long and short chains compare with the conventional way of constructing a multimode model based on linear superposition.

The parameters specified in Table 5.1 are used as the base parameters in this chapter to observe the effect of the imposed pressure drop, contraction length, contraction ratio and contraction width of the three-dimensional geometry. The subscript i from the Table 5.1 represents $i = S$ or L. The dimension of the geometrical configuration used in this chapter is defined in Figure 6.1. The boundary conditions used in this chapter are defined in Table 4.2.

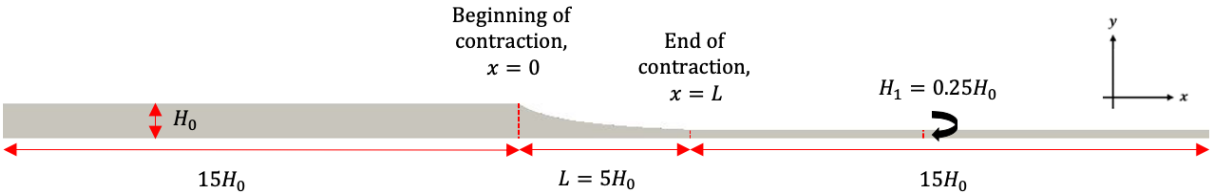

Figure 6.1: The computational domain for the upper half of the hyperbolic contraction used for simulating the HCF using the RDP model with symmetry imposed on $y = 0$. The contraction length shown by the schematic is $L = 5$.

From Figure 6.1 the half-height $H(x)$ is defined as

$$H(x) = \begin{cases} H_0, & x \leq 0 \\ \dfrac{H_0 L}{L + (H_0/H_1 - 1)x}, & 0 < x < L \\ H_1 & x \geq L \end{cases}$$

which is the same expression defined in Chapter 4, so that the channel-half height contracts from H_0 to H_1 over a length L.

6.2 Effect of imposed pressure drop

A range of pressure drop values that span the non-linear rheological behaviour of the model are imposed in a 4:1 hyperbolic contraction geometry in which $H_0 = 1$ and $H_1 = 0.25$ and $L = 5$ using the RDP model with parameters in Table 5.1 to calculate the extension-rate along the centre-line of the contraction and the shear-rate near the wall in both upstream and downstream channel sections. The Weissenberg number for reptation and stretch relaxation time in shear and extensional flow, denoted by $\mathrm{Wi}_{sD,i} = \lambda_{D,i}\dot{\gamma}_j$, $\mathrm{Wi}_{sR,i} = \lambda_{R,i}\dot{\gamma}_j$ for $j = A$ (upstream) or E (downstream), $\mathrm{Wi}_{eD,i} = \lambda_{D,i}\dot{\varepsilon}$, $\mathrm{Wi}_{eR,i} = \lambda_{R,i}\dot{\varepsilon}$ respectively and $i = S$ or L, are calculated for different pressure drop values considered that span the rheological behaviour of the model. The results are presented in Tables 6.1 - 6.3.

Away from the contraction, the shear-rate along the wall is uniform. To be consistent for every pressure drop value, the shear-rates are measured at half-way upstream and downstream in the straight channel, while the extension-rate is taken along the centre-line within the contraction region. In this latter region, the extensional flow is created as a consequence of geometrical changes in the downstream region. Measuring the extension-rate at the centre-line (within the contracting region) that is away from the wall allows a pure extensional flow to be created due to the absence of shear effects on this line. Figure 6.2 illustrates the regions where the shear and extension rates are recorded.

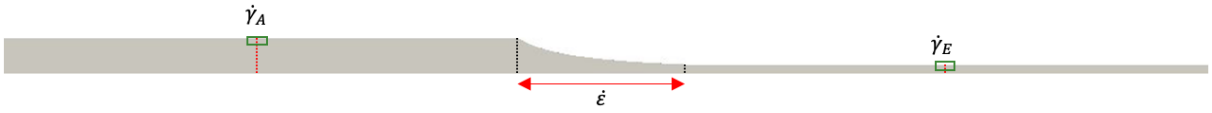

Figure 6.2: The regions where the shear and extension-rate are measured. The shear-rate for both upstream and downstream are measured at $x = -7.5$ and $x = 12.5$ that is the mid-way of the upstream and downstream straight channel. The extension-rate is fairly uniform within the contracting region and to be consistent, the extension-rate is measured at $x = 2.5$ is used to record the data in Table 6.3.

For the 4:1 hyperbolic contraction flow, the fluid velocity downstream is expected to be four times higher than the upstream velocity. As a consequence the ratio for shear-rate downstream to shear-rate upstream channel will be on average higher by a factor of sixteen. Across the straight channel, the shear stress is highest at the wall and decreases linearly to zero approaching the centre-line. However, the velocity profile will depend on the shear rheology of the fluid and will evolve with increasing shear from Newtonian (slow regime), which gives a parabolic profile, shear thinning regime (intermediate), showing a blunted profile, and stretch regime (fast regime with high Weissenberg number) showing similar velocity profile to the Newtonian regime. We shall now discuss the Weissenberg numbers for shear in upstream and downstream channel recorded in Table 6.1 and Table 6.2 respectively followed by Weissenberg number for extension in Table 6.3.

Table 6.1: Upstream shear Weissenberg number in terms of both reptation and stretch for flow near the wall for 4:1 hyperbolic contraction with $L = 5$ for different pressure drop values when $\lambda_{D,L} = 10$, $\lambda_{R,L} = 0.2$, $\lambda_{D,S} = 0.1$, $\lambda_{R,S} = 0.05$ with 5% long chain concentration.

ΔP	8	16	32	64	128	256	512
$\lambda_{R,S}\dot{\gamma}_A$	5.34e-3	1.12e-2	2.38e-2	5.46e-2	1.57e-1	4.69e-1	1.297
$\lambda_{D,S}\dot{\gamma}_A$	1.07e-2	2.24e-2	4.76e-2	1.09e-1	3.15e-1	9.38e-1	2.594
$\lambda_{R,L}\dot{\gamma}_A$	2.14e-2	4.48e-2	9.53e-2	2.18e-1	6.296e-1	1.876	5.188
$\lambda_{D,L}\dot{\gamma}_A$	1.07	2.24	4.76	10.9	31.5	93.8	259.0

As stated earlier, the onset of the shear-thinning and stretch regimes for both short (S) and long (L) polymer chain correspond to $\lambda_{D,i}\dot{\gamma}_j > 1$ and $\lambda_{R,i}\dot{\gamma}_j > 1$ respectively, where $i = S$ or L and $j = A$ or E represent the upstream and downstream respectively. These values are highlighted with two different colors, yellow and green that indicate the shear thinning and stretch regime respectively.

The upstream stretch Weissenberg number for short chain (i.e. $\lambda_{R,S}\dot{\gamma}_A$) recorded in Table 6.1 shows that the onset of the short polymer stretch upstream occurs for pressure drops between $256 < \Delta P < 512$. Looking at the upstream orientation Weissenberg number for the short chain (i.e. $\lambda_{D,S}\dot{\gamma}_A$) in Table 6.1, corresponding to the intermediate regime $\frac{1}{\lambda_{D,S}} \leq \dot{\gamma} \leq \frac{1}{\lambda_{R,S}}$, the short chains align just beyond the pressure drop value of $\Delta P = 256$. At lower pressure drops the upstream shear-rates are small compared to the rate at which the short chains start to reorient and release the entanglements made with other chains.

The reptation relaxation times for the long chain is a hundred time higher than that of the short chains and so requires a much lower pressure drop value for chain orientation to take place and the shear-thinning phenomena to occur. The shear-thinning regime for long chains spans a wider region of shear-rates than the short chains as the long chains are much more entangled. This can be seen very clearly from Table 6.1 which shows that the shear-thinning regime lies between $8 \leq \Delta P < 256$. In this range of shear-rates the long chains are reoriented due to entanglements with other long chains, but entanglements with short chains are released by thermal motion of the short chains.

Table 6.2: Downstream shear Weissenberg number in terms of both reptation and stretch for flow near the wall for 4:1 hyperbolic contraction with $L = 5$ for different pressure drop values when $\lambda_{D,L} = 10$, $\lambda_{R,L} = 0.2$, $\lambda_{D,S} = 0.1$, $\lambda_{R,S} = 0.05$ with 5% long chain concentration.

ΔP	8	16	32	64	128	256	512
$\lambda_{R,S}\dot{\gamma}_E$	7.63e-2	1.57e-1	3.32e-2	7.95e-1	2.381	6.85	16.8
$\lambda_{D,S}\dot{\gamma}_E$	1.53e-1	3.14e-1	6.64e-1	1.59	4.76	13.7e+1	33.6
$\lambda_{R,L}\dot{\gamma}_E$	3.05e-1	6.27e-1	1.329	3.18	9.52	27.4e+1	67.3
$\lambda_{D,L}\dot{\gamma}_E$	15.3	31.4	66.4	159	476	1370	3360

The shear-rates near the wall in the downstream channel are larger on average by a factor of the square of the contraction ratio. This means the pressure drop required for both short and long to orient and stretch is lower than in the upstream channel. As a consequence there is a possibility that the velocity profile across the geometry in both upstream and downstream are different. For example, upstream Weissenberg number for short chains at $\Delta P = 64$ recorded in Table 6.1 is $\lambda_{D,S}\dot{\gamma}_A = 1.09e-1$ corresponding to the slow regime and so a parabolic velocity profile is expected when the velocity profile across the geometry

is plotted. Note that for our choice of parameters the shear-rheology is dominated by the contribution from the short chains. However, when the velocity profile across the geometry in the downstream channel is plotted, a blunted velocity profile is expected. This is because, as highlighted in Table 6.2, when $\Delta P = 64$, $\lambda_{D,S}\dot{\gamma}_E = 1.59$ while $\lambda_{R,S}\dot{\gamma}_E = 7.95e-1$ and so falls in the intermediate regime where the shear-thinning phenomena occur.

Table 6.3: The extension Weissenberg number for both reptation and stretch for flow within the contracting region (along centre-line) when $L = 5$ for different pressure drop values when $\lambda_{D,L} = 10$, $\lambda_{R,L} = 0.2$, $\lambda_{D,S} = 0.1$, $\lambda_{R,S} = 0.05$ with 5% long chain concentration.

ΔP	8	16	32	64	128	256	512
$\lambda_{R,S}\dot{\varepsilon}$	1.65e-3	3.4e-3	7.15e-3	1.6e-2	4.35e-2	0.125	0.339
$\lambda_{D,S}\dot{\varepsilon}$	3.3e-3	6.8e-3	1.43e-2	3.2e-2	8.7e-2	0.25	0.678
$\lambda_{R,L}\dot{\varepsilon}$	6.6e-3	1.36e-2	2.86e-2	6.4e-2	1.74e-1	0.5	1.356
$\lambda_{D,L}\dot{\varepsilon}$	3.3e-1	6.8e-1	1.43	3.2	8.7	25	67.8

The pure extensional flow on the centre-line in the hyperbolic contraction geometry has a similar partition of behaviour as the shear flow at the wall. Thus, the three regimes for the extensional flow are categorised as follows: the slow regime, $\dot{\varepsilon}\lambda_{D,i} < 1$, the intermediate regime, $\frac{1}{\lambda_{D,i}} < \dot{\varepsilon} < \frac{1}{\lambda_{R,i}}$ and the fast regime having $\dot{\varepsilon}\lambda_{R,i} > 1$ where $i = S$ or L. Table 6.3 records the extension Weissenberg number (reptation and stretch) for both short and long chains. Looking at the individual chain, the short chain requires higher pressure than $\Delta P = 512$ before the intermediate regime where the extension thinning is observed.

On the other hand, the extension-thinning region for the long chain is in between $\Delta P = 16$ and $\Delta P = 512$. At $\Delta P = 512$ and above, the extension thickening is predicted and the extensional viscosity will keep growing infinitely, unless the finite extensibility of the chains is included, where at high extension-rate the plateau extension viscosity is predicted when a graph of extensional viscosity against time is plotted.

6.3 Effect of contraction length, L

The design of the hyperbolic contraction presented in Section 4.5.2 reveals that the contraction length plays a vital role in achieving a uniform extension-rate. Based on results in 4.5.2, only two different contraction dimensionless lengths, $L = 1$ and 5, are considered in

this section to observe the creation of uniformity of the extension-rate within the contracting region along the centre-line where $L = L/H_0$, $X = x/H_0$ and $Y = y/H_0$. Note that, in Chapter 4, the dimensional parameters were used in order to compare with the results in Tenchev et al. [129]. Whereas in this Chapter, non-dimensional parameters are used. In comparing geometries to the parameters used in Chapter 4, $L = 1$ corresponds to a length of contraction that is more than $L = 4$ but less than $L = 8$ while for $L = 5$, corresponds to about $L = 32$. To deal with high mesh skewness within the contracting region for the shorter contraction length, $L = 1$, the whole domain is divided into 12 blocks with 31 500 total computational cells. The longer contraction length reduces the skewness issue which allows a single block definition for $L = 5$ with 33 600 quadrilateral computational cells. The volumetric flow-rate, VFR, in the upstream channel is kept the same in each case. For $L = 5$, the pressure drop value is set to $\Delta P = 256$ while for $L = 1$, the pressure drop value is $\Delta P = 230.5$. This gives a volumetric flow rate, VFR ≈ 3.12. The centre-line plot for extension-rate, the stretch in a thin and fat tubes as well as the birefringence contour are presented in the following figures to illustrate the influence of the contraction length on the prediction.

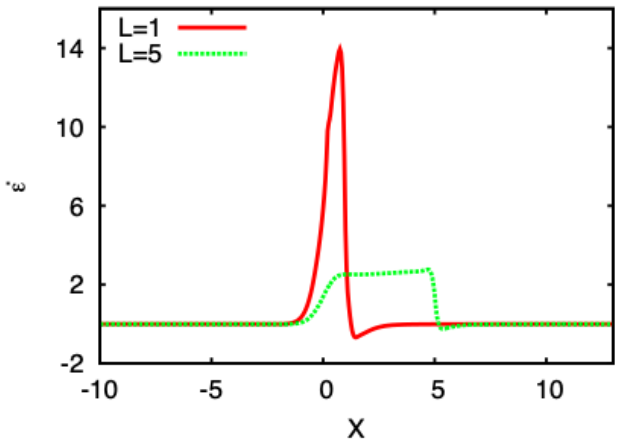

Figure 6.3: The effect of contraction length given $\lambda_{D,L} = 10$, $\lambda_{R,L} = 0.2$, $\lambda_{D,S} = 0.1$ and $\lambda_{R,S} = 0.05$ for VFR ≈ 3.12 on the prediction of extension-rate along the centre-line for 5% long chain concentration.

Looking at Figure 6.3, the longer contraction produces a region of approximately uniform extension-rate along the centre-line of the contraction. However away from this line the flow is dominated by the shear as depicted by the birefringence pattern that is parallel to the wall

in Figure 6.5. For $L = 1$ the results are slightly not smooth through the contracting region due to the skewness issue that is quite challenging near the contracting region. However this will not affect the prediction significantly. Shorter contraction gives a higher but non-uniform extension-rate. It also shows a negative (undershoot) extension-rate at the end of the contraction section due to the elastic recoil. In choosing the length of the contraction there is a compromise between having a long enough contraction to provide a region of uniform extension, but with an extension-rate that is high enough that the flow is not dominated by shear.

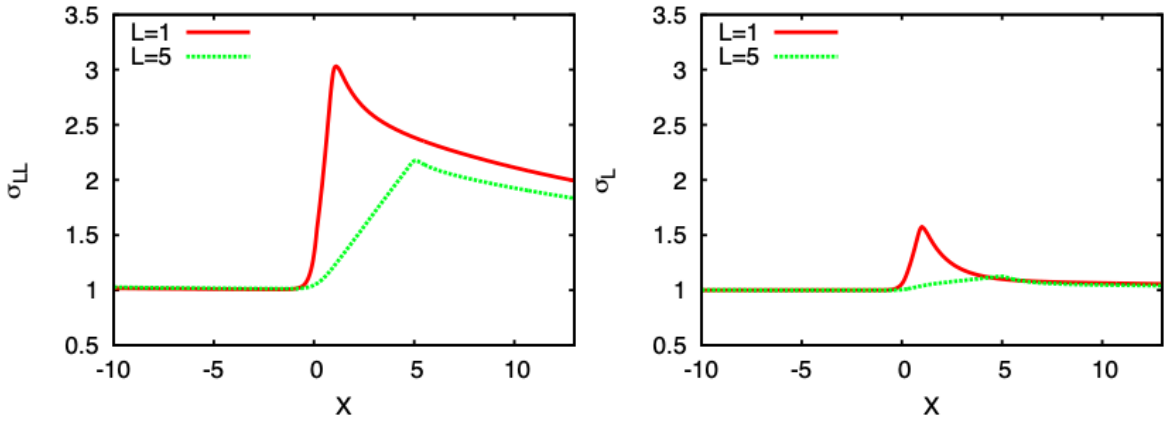

Figure 6.4: The effect of contraction lengths given $\lambda_{D,L} = 10$, $\lambda_{R,L} = 0.2$, $\lambda_{D,S} = 0.1$ and $\lambda_{R,S} = 0.05$ for VFR ≈ 3.12 on the prediction of fat tube stretch (LHS) and thin tube stretch (RHS) along the centre-line for 5% long chain concentration.

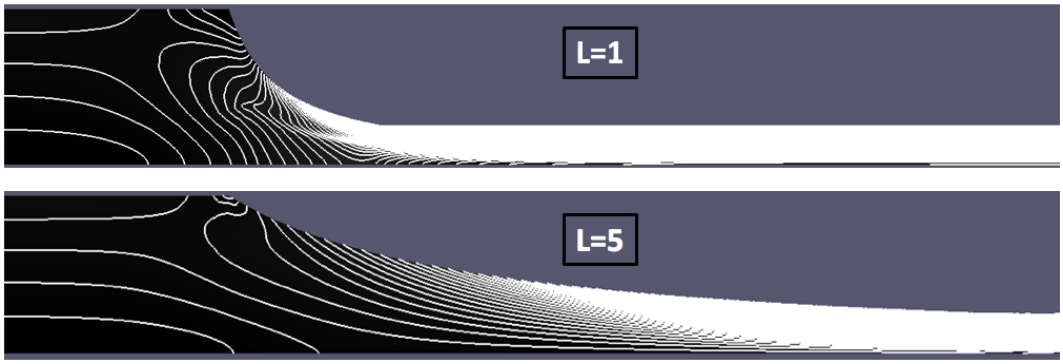

Figure 6.5: The birefringence contour at different contraction lengths, L, for $G_N^0 = 1.0$ $\lambda_{D,L} = 10$, $\lambda_{R,L} = 0.2$, $\lambda_{D,S} = 0.1$ and $\lambda_{R,S} = 0.05$ for VFR ≈ 3.12 with contour interval= 0.25.

Figure 6.5 illustrates the birefringence contours for the $L = 1$ and $L = 5$ contractions. Looking at the upstream birefringence, the contour for both sub-figures shows similar pat-

tern as VFR is kept the same. However, the first birefringence contour at the centre-line for $L = 1$ occurs before the contraction, whereas the first contour for $L = 5$ occurs just after the contraction. Correspondingly, for $L = 1$, the stretch for both thin and fat tubes flowing through the contraction are experienced earlier than the longer contraction length. This can be illustrated from Figure 6.4 where the stretch along the centre-line is more pronounced for the shorter contraction length since the flow experiences intense extensional flow within the contracting region along the centre-line.

In Figure 6.5, different contour patterns are observed immediately upstream and within the contraction. The stress in the downstream channel is not discernable due to the high density of the stress contour indicating higher stress in the downstream channel. This is because the fluid is accelerating through the narrower channel as a consequence of restriction in motion caused by configuration changes. The high density of contour birefringence in the downstream channel arises from the very high shear deformation at the wall.

The stress density at the sharp corner upstream in the shorter contraction is more pronounced than for the longer contraction. This is because, the shorter contraction length causes higher flow resistance due to more rapid geometrical changes compared to the longer contraction length which is showing smoother changes within the contraction. In terms of stress pattern within the contracting region, for the shorter contraction the density of the stress contours is higher and the contours are perpendicular to the flow direction. This shows that this region is dominated by the extensional flow. In contrast, for the longer contraction case, the stress contours are more parallel to the wall which indicates the flow is dominated by the shear. Note that, the discussion and conclusion drawn in this section are consistent to the discussion in presented in Section 4.5.2 as expected.

6.4 Effect of contraction ratio, R

In this section we consider the effect of varying the contraction ratio. This section is divided into four subsections, where the comparison between the contraction ratios is made using the coupled RDP model, before comparing the RDP and mRP models in the subsection that follows. Finally we compare the stretch in the thin and fat tube in the contracting region between the coupled and uncoupled model.

6.4.1 Comparison between 4:1 and 10:1 contraction using RDP model

The effect of two different contraction ratios, R=4:1 and R=10:1 are observed by keeping the contraction length, $L = 5$, the same. The flow-rate is adjusted so that the maximum extension-rate is kept the same, that is at around a dimensionless value of 2.5. We maintain the downstream channel width so that the upstream channel is increased to $H_0 = 2.5$ for the 10:1 case. Whereas the 4:1 contraction requires $\Delta P = 256$ to achieve $\dot{\varepsilon} \approx 2.5$, the 10:1 contraction needs a lower pressure drop value, $\Delta P = 212$ to give the same extension-rate. The velocity as well as the extension-rate profile are depicted in Figure 6.6.

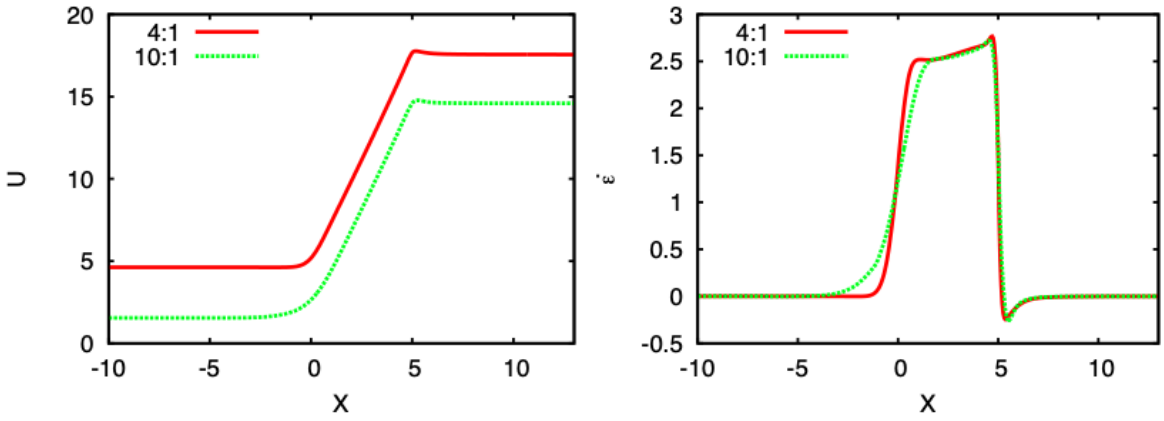

Figure 6.6: The effect of contraction ratios given $\lambda_{D,L} = 10$, $\lambda_{R,L} = 0.2$, $\lambda_{D,S} = 0.1$ and $\lambda_{R,S} = 0.05$ for $\dot{\varepsilon} \approx 2.5$ on the prediction of velocity (LHS) and extension-rate (RHS) along the centre-line between the 4:1 and 10:1 hyperbolic contractions for the RDP model with 5% long chain concentration.

In Figure 6.6, both geometries give an approximately linear increase within the converging region $0 \leq x \leq 5$. The differences in flow-rates in the two channels can be seen clearly from Figure 6.6, where the fluid is flowing faster in the 4:1 contraction while slower in the 10:1 contraction as shown by the centre-line velocity.

From the extensional profile along the centre-line of the figure, the same extension profile for both contraction ratio is achieved as a result of the adjusted flow-rate. Notice that the polymer chain started to stretch before the beginning of the contraction region in the 10:1 contraction. It is worth emphasizing here that the result obtained is due to the larger effective aspect ratio in the 10:1 contraction, where the geometrical resistance is more pronounced in the 10:1 contraction and smoother in the 4:1 contraction, which influences the

fluid flow through the contraction. However although the extension-rates are similar the residence times in the contraction are different.

The maximum extension-rate along the centre-line for both contraction ratios is around 2.5 where, since $\dot{\varepsilon}\lambda_{R,L} < 1$, we would not expect to observe significant chain stretching in a melt consisting completely of L-chains. However the effective stretch relaxation time for 5% long chain concentration of the polymer blend, with $\lambda_{R,L}^{eff} = \lambda_{R,L}/\phi_L = 4$, implies $\dot{\varepsilon}\lambda_{R,L}^{eff} = 10$ so we would possibly expect to observe some stretching of the long chains in a 5% blend.

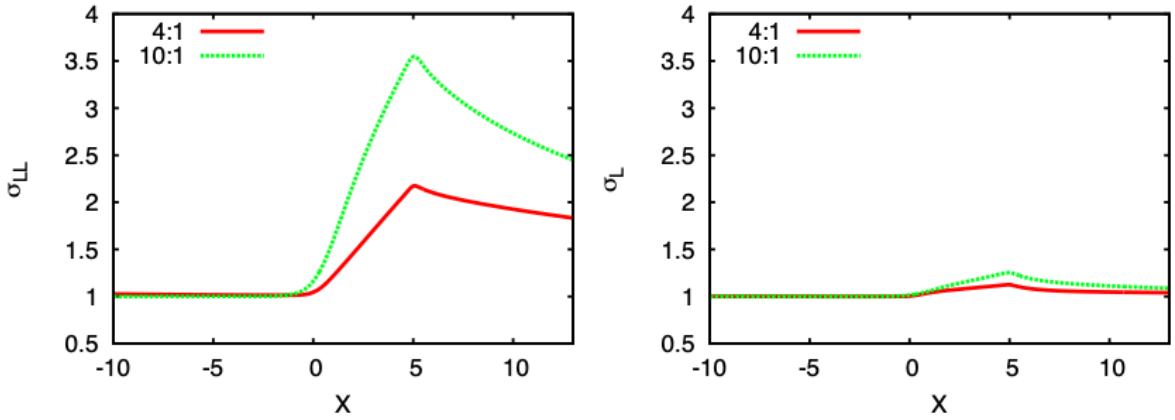

Figure 6.7: The effect of contraction ratio given $\lambda_{D,L} = 10$, $\lambda_{R,L} = 0.2$, $\lambda_{D,S} = 0.1$ and $\lambda_{R,S} = 0.05$ for $\dot{\varepsilon} \approx 2.5$ on the prediction of fat tube stretch, σ_{LL} (LHS) and thin tube stretch, σ_L (RHS) along the centre-line between the 4:1 and 10:1 hyperbolic contractions for the RDP model with 5% long chain concentration.

Figure 6.7 shows the stretch (measured along the tube contour) along the centre-line for fat (σ_{LL}) and thin tube (σ_L) respectively. It can be observed that the stretch predicted in a fat and thin tube for higher contraction ratio is more evident than the lower one. Although the extension-rate is the same, at the higher contraction ratio there is higher extension strain due to longer residence time. This also explains why the stretch in both fat and thin tubes are higher in the 10:1 contraction as shown in Figure 6.7.

As the melt flows through the contraction the stretch within the fat tube, composed of entanglements only with the L-chain species, increases as a consequence of the enhanced stretch relaxation. On the other hand, the stretch in the thin tube, formed of all chain entanglements shows only a slight increment within the contracting region. The 95% of short chains in the blend make up most of the entanglements. However the entanglements

made by short chain are short-lived and diffuse out of the (their own) tube by reptation motion to release the entanglement very quickly. Hence, the relaxation time in a thin tube is due to constraint release.

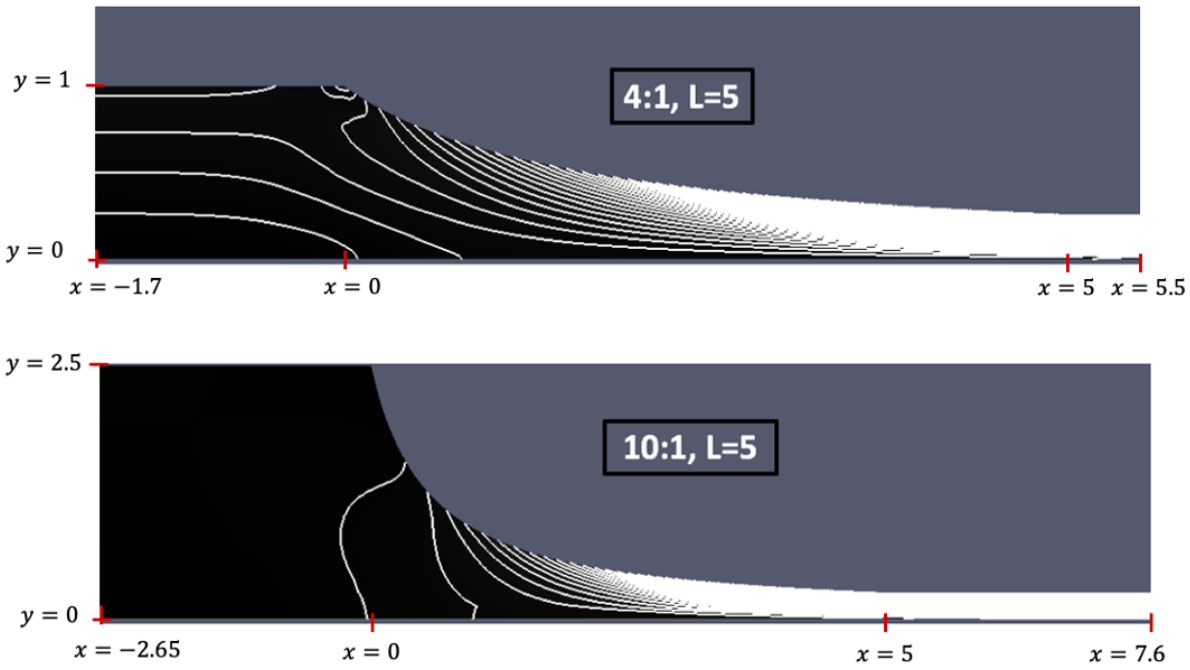

Figure 6.8: The effect of contraction ratio given $\lambda_{D,L} = 10$, $\lambda_{R,L} = 0.2$, $\lambda_{D,S} = 0.1$ and $\lambda_{R,S} = 0.05$ when $\dot{\varepsilon} \approx 2.5$ for the birefringence contour with contour interval= 0.25.

The birefringence patterns in Figure 6.8 show different density of birefringence contour upstream which is explained by the adjusted flow-rate imposed at the inlet to ensure the same extension-rate is achieved. The slower (flow) and wider channel upstream for the 10:1 contraction ratio mean that the shear-rates upstream are much lower. The higher strain due to slower rate of flow through the contraction for 10:1 explains the reason why the stretch for long chain is more pronounced in 10:1 than 4:1 even though the extension-rate is the same.

6.4.2 Comparison between RDP and mRP models

Figures 6.9, 6.10 and 6.11 show the comparison between the RDP (coupled) and mRP (uncoupled) model on the centre-line for velocity, extension-rate and stretch for both 4:1 and 10:1 contraction-ratio. The equivalent parameters for 3-mode mRP model, based on the RDP parameters, as described in Section 5.5.1 are recorded in Table 6.4 and is the same

data recorded in Table 5.2.

Table 6.4: The 3-mode mRP parameters based on RDP parameters.

Parameter	Mode 1	Mode 2	Mode 3
$\eta_{P,j}$	0.0125	0.009406	0.045125
$\lambda_{D,j}$	5.0	0.0990099	0.05
$\lambda_{R,j}$	0.2	0.08	0.05

The lowercase j appears as a subscript of the parameters referring to the j^{th} mode where $j = 1, 2,$ or 3. The linear superposition of the mRP implies that the total polymeric viscosity for 3-mode mRP is defined as $\eta_P = \sum_{j=1}^{3} \eta_{P,j}$.

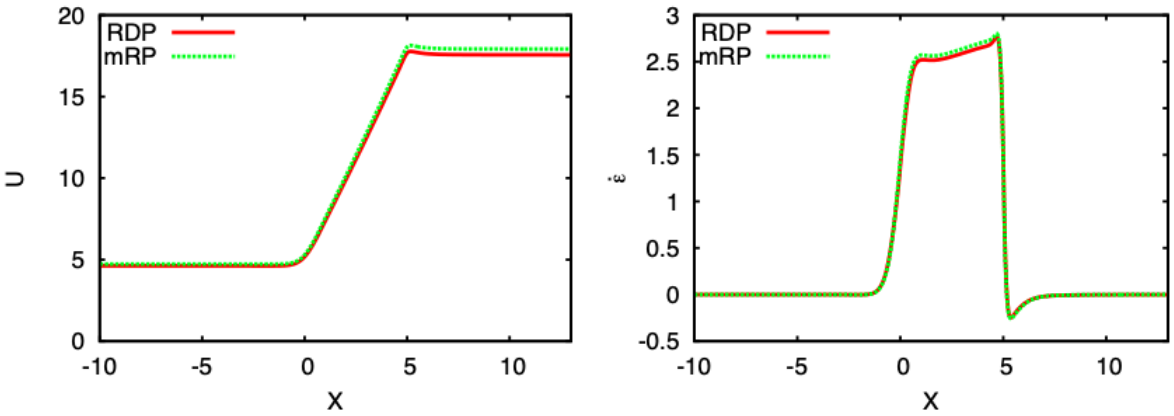

Figure 6.9: Comparison between RDP and 3-mode mRP on the prediction of velocity (LHS) and extension-rate (RHS) for 4:1 contraction ratio when $\Delta P = 256$.

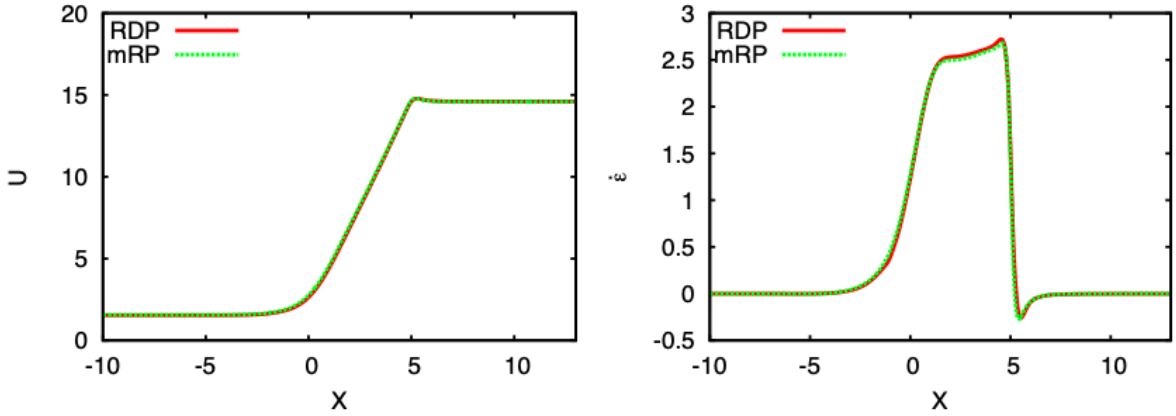

Figure 6.10: Comparison between RDP and (3-mode) mRP on the prediction of velocity (LHS) and extension-rate (RHS) for 10:1 contraction ratio when $\Delta P = 212$.

Figure 6.9 and 6.10 show the prediction made by RDP model and mRP model for 4:1

and 10:1 respectively with the same pressure drop values imposed for both models. The results reveal that the prediction made by both models in both contraction ratios are almost identical with only a slight change observed in the 4:1 contraction as a consequence of a slightly higher flow rate in 4:1 for the mRP.

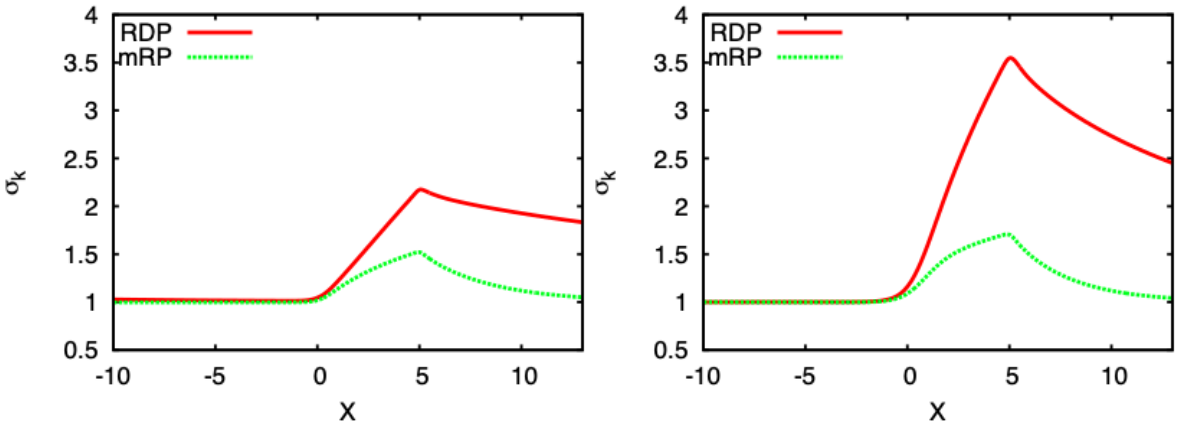

Figure 6.11: Comparison between RDP model and mRP model for both 4:1 (LHS) and 10:1 (RHS) contraction on the prediction of the fat tube stretch along the centre-line.

The stretch for both RDP and mRP model are compared in Figure 6.11. The equivalent stretch for the mRP model to fat tube stretch in the RDP model, σ_{LL}, is the stretch for the longest chain, denoted as σ_{M1}. The notation σ_k on the y-axis of the figure is the standard notation for stretch that represents the RDP and mRP stretch as $\sigma_k = \sigma_{LL}$ or σ_{M1} respectively.

The results shown in Figure 6.11 are the main finding that distinguishes the difference between the prediction made by RDP and mRP model. The results reveal that the RDP model produces significantly more stretch due to the effect of chain coupling in the RDP constitutive model. From the figure, the stretch profile along the centre-line within the contracting region for the mRP model is about $\sigma_{M1} \approx 1.51$ maximum for 4:1 and $\sigma_{M1} \approx 1.7$ maximum for 10:1 contraction ratio.

Comparing the stretch for RDP to mRP model in 4:1 contraction ratio, we can see that the fat tube stretch predicted by RDP is $\sigma_{LL} \approx 2.17$, which is roughly 1.4 times higher than the mRP stretch. The prediction for σ_{LL} in 10:1 case is even higher at about $\sigma_{LL} \approx 3.55$, about double the prediction made by the mRP model. The higher stretch observed for the RDP model is because the slow flow-rate imposed in 10:1 has a longer residence time

in the contraction allowing the strain to accumulate and resulting in higher stretch than the 4:1 contraction. However, the PSD pattern predicted by both models do not show any significant changes and remain the same.

6.4.3 Cross-section of stretch for the thin and fat tubes within the contracting region

The cross-section for both stretches in the fat and thin tube for the RDP model are plotted in the contracting region where the extensional flow is created as the impact of the geometrical configuration from the upstream straight channel to the hyperbolic contracting region. The behaviour of the stretch for thin, σ_L, and fat tube, σ_{LL}, are plotted to observe the effect of the mixed complex flow formed by the combination of shear (at the wall) and extensional flow (at the centre-line) that occurs within the intermediate region. The colour plot of the stretch is presented to observe the prediction of the stretch made by the tubes that distinguish from one to another.

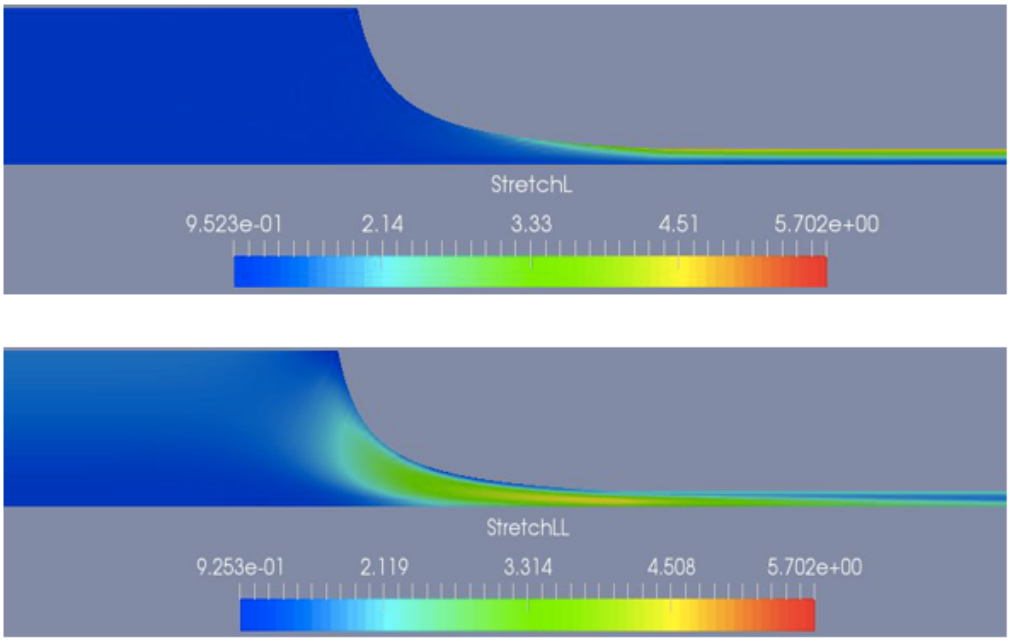

Figure 6.12: The colour maps showing the extension of the L-chain component in the 10:1 hyperbolic contraction for the RDP model. The top figure shows the stretch $\sigma_L = \sqrt{trA_L/3}$ in the thin tube formed from both L and S chains while the bottom figure shows the stretch in the fat tube composed only of L-chains, $\sigma_{LL} = \sqrt{trA_{LL}/3}$.

Figure 6.12 shows the molecular stretch of the polymer chain in the thin and fat tubes

for the 10:1 domain. We do not present the colour plot for the stretch in the 4:1 contraction as it shows the same phenomena. In this figure, the molecular stretch in the thin tube is most pronounced at the wall in the downstream region where the highest shear-rates are found. Although the extension-rate, $\dot{\varepsilon}$, at the centre-line in the contracting region is around 2.5, the shear-rate near the wall of the downstream channel is more than 50 times higher than the extension-rate, that we have measured to be about 140. As a result, away from the centre-line the shear flow is dominant. In contrast, the molecular stretch in the fat tube, the long-long stretch contribution, is quite different with the maximum stretch observed in between the wall and the centre-line.

Figure 6.13 shows the configuration where the stretch for thin and fat tubes are plotted across the geometry at three different positions within the contracting region.

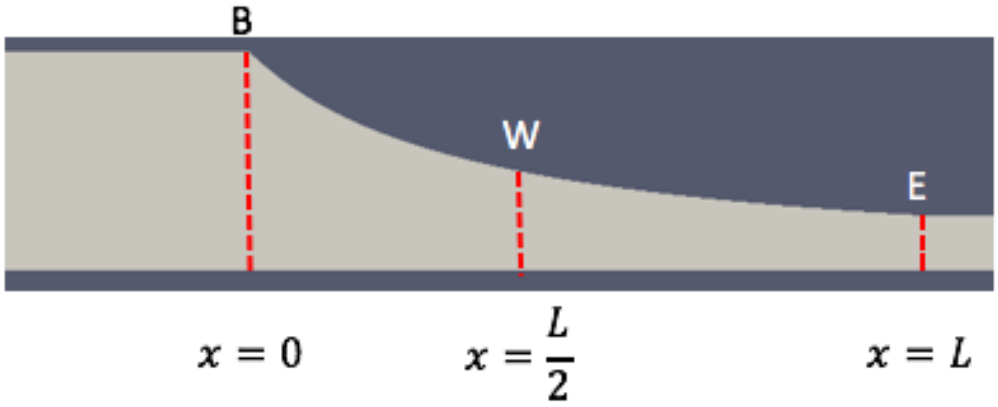

Figure 6.13: The cross-sections (B-beginning, W-midway, E-end of contraction) where the behaviour of the thin and fat tube is observed.

Figure 6.14 and 6.15 show the cross-section of the thin and fat tube stretch at three different cross-sections - the beginning of the contraction, $x = 0$, (denoted by B), half-way contraction, $x = \frac{L}{2}$, (denoted by W) and the end of the contraction, $x = L$, (denoted by E). We show the prediction of the stretch for thin and fat tube on the same graph. The results are presented for both 4:1 and 10:1 contraction ratios with contraction length $L = 5$ and $\Delta P = 256$ and $\Delta P = 212$ respectively.

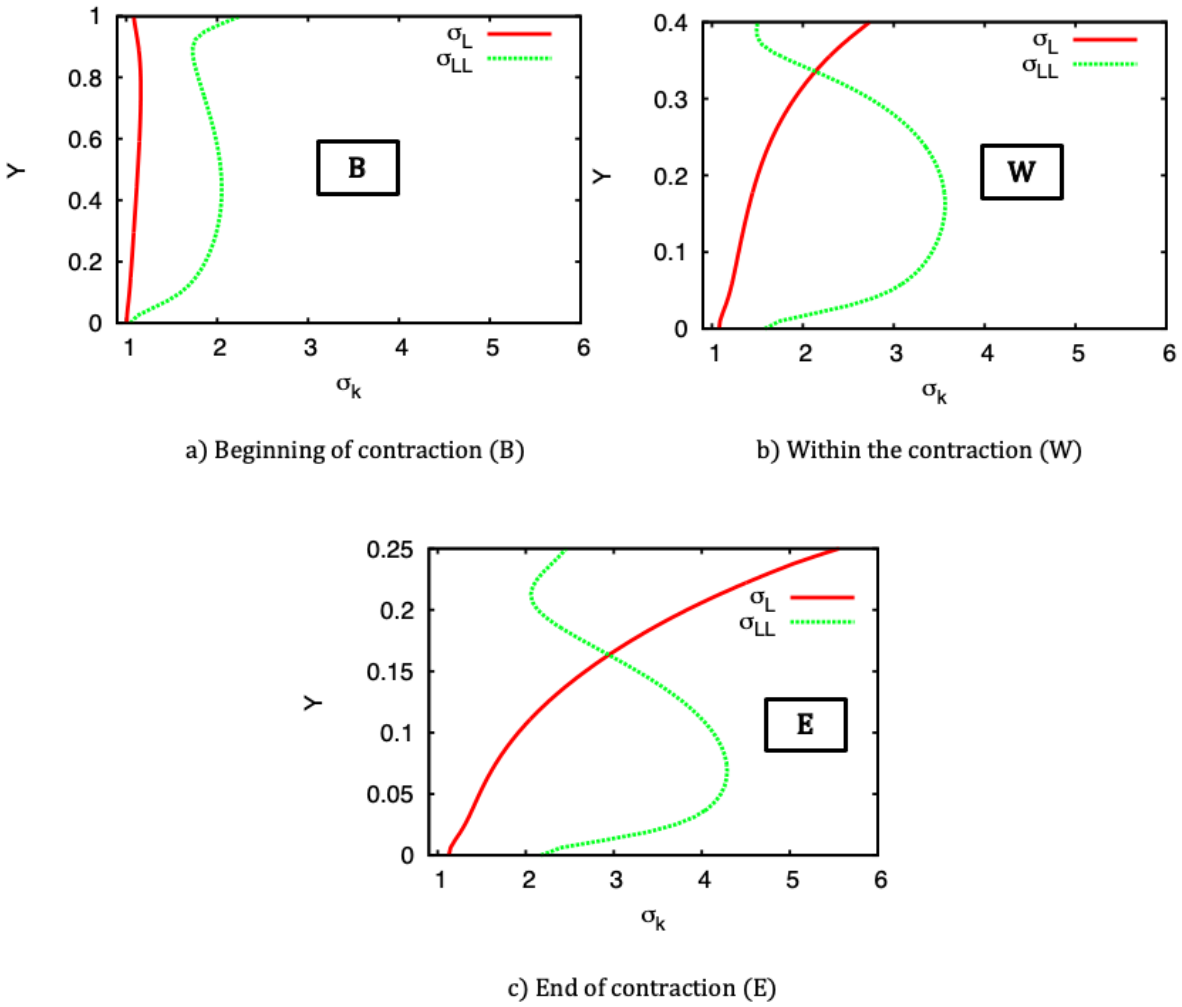

Figure 6.14: The 4:1 cross-sections for stretch in the thin and fat tube.

The 4:1 and 10:1 contraction show a similar trend of prediction in both fat and thin tubes. In general, the stretch predicted by the thin tube across the cross-section increases gradually away from the centre-line, where the flow is dominated by the shear near the wall. The stretch at the end of the contraction shows the highest value as the shear-rate increases with distance down the contraction.

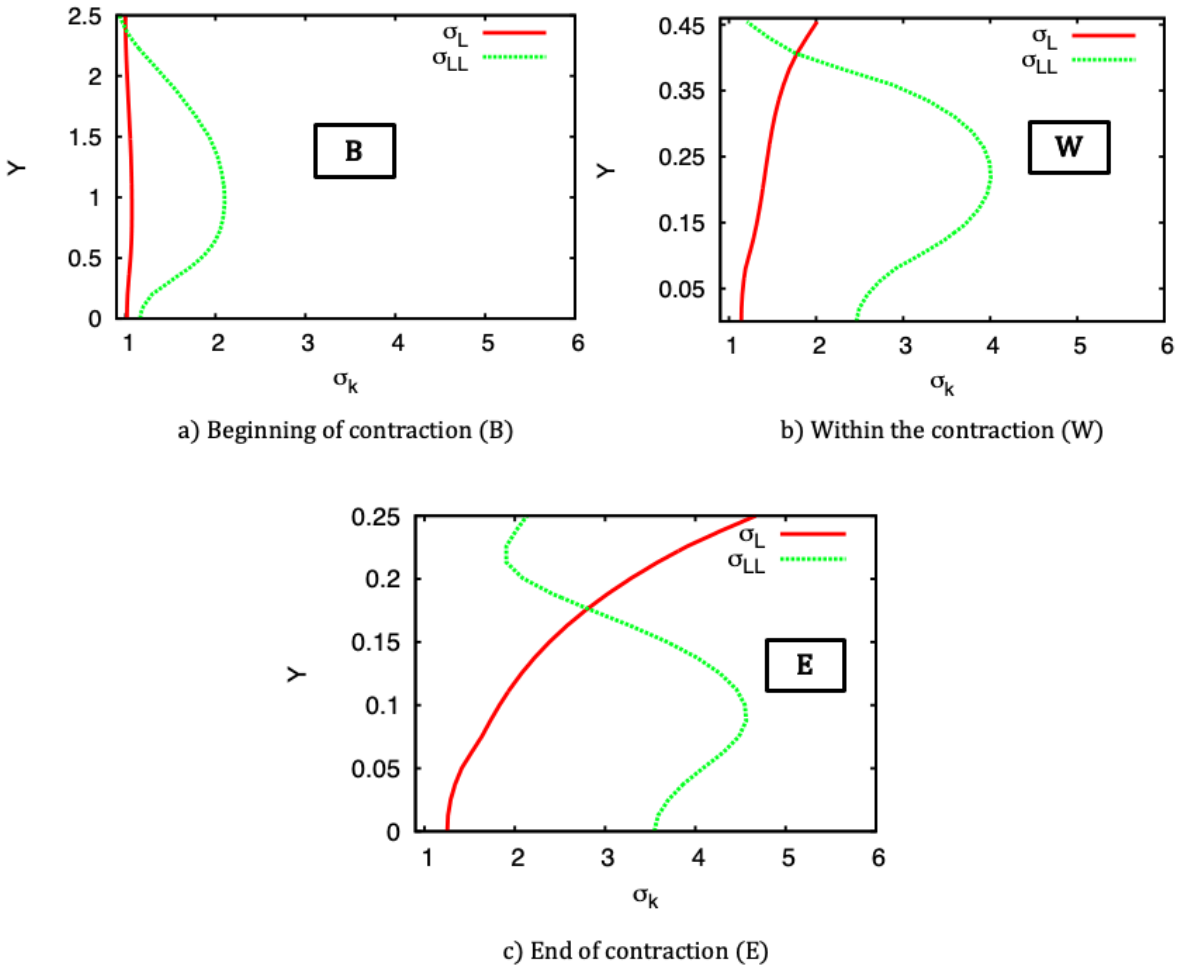

Figure 6.15: The 10:1 cross-sections for stretch in the thin and fat tube.

In contrast, the stretch in the fat tube is observed to have a maximum between the centre-line and the wall. At the centre-line, there is a pure extensional flow which transforms to a pure shear flow approaching the wall, in between there is a mixed flow of shear and extension. One surprising feature is that although the highest velocity gradient occurs at the wall, the stretch predicted in the fat tube is relatively low in this region.

We will explain the prediction of the stretch made by the thin and fat tubes near the wall (where shear dominated) by analyzing the stretch expression for both thin and fat tubes mathematically. The stretch for both thin and fat tube is presented in Chapter 1 as

$$\sigma_L = \sqrt{\frac{tr(\mathbf{A}_L)}{3}} \qquad \text{and} \qquad \sigma_{LL} = \sqrt{\frac{tr(\mathbf{A}_{LL})}{3}}$$

respectively. To explain this we consider the $L-L$ conformation tensor in a steady shear

flow. Recall the $L-L$ contribution conformation tensor satisfies equation (1.11),

$$\overset{\nabla}{\mathbf{A}}_{LL} = -\frac{1+\beta_{th}}{\lambda_{D,L}}(\mathbf{A}_{LL}-\mathbf{I}) - \frac{2}{\lambda_{R,L}}(1-\sigma_L^{-1})f_E(\sigma_L)[\mathbf{A}_{LL}+\beta^*\sigma_L^{2\delta}(\mathbf{A}_{LL}-\mathbf{I})],$$

with $f_E(\sigma) = 1.0$, so that for a steady uniform flow

$$\overset{\nabla}{\mathbf{A}}_{LL} = -\frac{1+\beta_{th}}{\lambda_{D,L}}(\mathbf{A}_{LL}-\mathbf{I}) - \frac{2}{\lambda_{R,L}}(1-\sigma_L^{-1})[\mathbf{A}_{LL}+\beta^*\sigma_L^{2\delta}(\mathbf{A}_{LL}-\mathbf{I})],$$

which implies

$$\overset{\nabla}{\mathbf{A}}_{LL} = -\left[\frac{1+\beta_{th}}{\lambda_{D,L}} + \frac{2}{\lambda_{R,L}}\beta^*\sigma_L^{2\delta}(1-\sigma_L^{-1})\right](\mathbf{A}_{LL}-\mathbf{I}) - \frac{2}{\lambda_{R,L}}(1-\sigma_L^{-1})\mathbf{A}_{LL}.$$

Let $\frac{2}{\lambda_D^*} = \frac{1+\beta_{th}}{\lambda_{D,L}} + \frac{2}{\lambda_{R,L}}\beta^*\sigma_L^{2\delta}(1-\sigma_L^{-1})$, then $\overset{\nabla}{\boldsymbol{A}}_{LL}$ can be written as

$$\overset{\nabla}{\boldsymbol{A}}_{LL} = -\frac{2}{\lambda_D^*}(\boldsymbol{A}_{LL}-\boldsymbol{I}) - \frac{2}{\lambda_{R,L}}(1-\sigma_L^{-1})\boldsymbol{A}_{LL}$$

which is then implies that

$$-(\nabla\mathbf{u})^T\cdot\mathbf{A}_{LL} - \mathbf{A}_{LL}\cdot(\nabla\mathbf{u}) = -\frac{2}{\lambda_D^*}(\boldsymbol{A}_{LL}-\boldsymbol{I}) - \frac{2}{\lambda_{R,L}}(1-\sigma_L^{-1})\boldsymbol{A}_{LL}. \tag{6.1}$$

In a shear, $u_x = \dot{\gamma}y$, the LHS of the equation then reduces to

$$-(\nabla\mathbf{u})^T\cdot\mathbf{A}_{LL} - \mathbf{A}_{LL}\cdot(\nabla\mathbf{u}) = \begin{pmatrix} -2\dot{\gamma}A_{xy} & -\dot{\gamma}A_{yy} & 0 \\ -\dot{\gamma}A_{yy} & 0 & 0 \\ 0 & 0 & 0 \end{pmatrix}, \tag{6.2}$$

where A_{ij} are the components of $\mathbf{A}_{LL}$. The xx, yy, zz, xy components from equation (6.1) are written as

$$
\begin{aligned}
A_{xx} \text{ component} \quad &: \quad -2\dot{\gamma}A_{xy} = -\frac{2}{\lambda_D^*}(A_{xx}-1) - \frac{2}{\lambda_{R,L}}(1-\sigma_L^{-1})A_{xx}, \\
A_{yy} \text{ component} \quad &: \quad 0 \qquad\quad = -\frac{2}{\lambda_D^*}(A_{yy}-1) - \frac{2}{\lambda_{R,L}}(1-\sigma_L^{-1})A_{yy}, \\
A_{zz} \text{ component} \quad &: \quad 0 \qquad\quad = -\frac{2}{\lambda_D^*}(A_{zz}-1) - \frac{2}{\lambda_{R,L}}(1-\sigma_L^{-1})A_{zz}, \\
A_{xy} \text{ component} \quad &: \quad -\dot{\gamma}A_{yy} \;= -\frac{2}{\lambda_D^*}A_{xy} - \frac{2}{\lambda_{R,L}}(1-\sigma_L^{-1})A_{xy}.
\end{aligned}
$$

Solving these equations yields the following

$$
\begin{aligned}
A_{yy} &= \frac{1}{1+\frac{\lambda_D^*}{\lambda_{R,L}}(1-\sigma_L^{-1})}, \\
A_{zz} &= \frac{1}{1+\frac{\lambda_D^*}{\lambda_{R,L}}(1-\sigma_L^{-1})}, \\
A_{xy} &= \frac{\dot{\gamma}\lambda_D^*}{2[1+\frac{\lambda_D^*}{\lambda_{R,L}}(1-\sigma_L^{-1})]^2}, \\
A_{xx} &= \frac{1}{1+\frac{\lambda_D^*}{\lambda_{R,L}}(1-\sigma_L^{-1})} + \frac{\dot{\gamma}^2(\lambda_D^*)^2}{2[1+\frac{\lambda_D^*}{\lambda_{R,L}}(1-\sigma_L^{-1})]^3}.
\end{aligned}
$$

Therefore,

$$
\begin{aligned}
T_{LL} = tr(\mathbf{A}_{LL}) &= A_{xx} + A_{yy} + A_{zz} \\
&= \frac{1}{1+\frac{\lambda_D^*}{\lambda_{R,L}}(1-\sigma_L^{-1})} + \frac{\dot{\gamma}^2(\lambda_D^*)^2}{2[1+\frac{\lambda_D^*}{\lambda_{R,L}}(1-\sigma_L^{-1})]^3} \\
&\quad + \frac{1}{1+\frac{\lambda_D^*}{\lambda_{R,L}}(1-\sigma_L^{-1})} + \frac{1}{1+\frac{\lambda_D^*}{\lambda_{R,L}}(1-\sigma_L^{-1})} \\
&= \frac{3}{1+\frac{\lambda_D^*}{\lambda_{R,L}}(1-\sigma_L^{-1})} + \frac{\dot{\gamma}^2(\lambda_D^*)^2}{2[1+\frac{\lambda_D^*}{\lambda_{R,L}}(1-\sigma_L^{-1})]^3} \\
&= \frac{6[1+\frac{\lambda_D^*}{\lambda_{R,L}}(1-\sigma_L^{-1})]^2 + \dot{\gamma}^2(\lambda_D^*)^2}{2[1+\frac{\lambda_D^*}{\lambda_{R,L}}(1-\sigma_L^{-1})]^3}.
\end{aligned}
$$

Hence the stretch for the fat tube is given by

$$\sigma_{LL} = \sqrt{\frac{18[1+\frac{\lambda_D^*}{\lambda_{R,L}}(1-\sigma_L^{-1})]^2 + 3\dot{\gamma}^2(\lambda_D^*)^2}{2[1+\frac{\lambda_D^*}{\lambda_{R,L}}(1-\sigma_L^{-1})]^3}}.$$

The stretch, σ_L, in a thin tube requires the stress contribution of the $L-S$ interaction, $\mathbf{A}_{LS}$ as well as $\mathbf{A}_{LL}$. For $f_E(\sigma)=1.0$, the component for $\mathbf{A}_{LS}$ from equation (5.5) is given by,

$$\begin{aligned}\overset{\nabla}{\boldsymbol{A}}_{LS} =& -\frac{1}{\lambda_{D,L}}(\mathbf{A}_{LS}-\mathbf{I}) - \frac{2}{\lambda_{R,L}}(1-\sigma_L^{-1})\mathbf{A}_{LS} - \left[\frac{\beta_{th}}{\lambda_{D,S}} + \right.\\ & \left.\frac{2}{\lambda_{R,S}}\beta^*(1-\sigma_S^{-1})\sigma_L^{2\delta}\right](\mathbf{A}_{LS}-\mathbf{I})\\ =& -\left[\frac{1}{\lambda_{D,L}} + \frac{\beta_{th}}{\lambda_{D,S}} - \frac{2}{\lambda_{R,S}}\beta^*(1-\sigma_S^{-1})\sigma_L^{2\delta}\right](\boldsymbol{A}_{LS}-\boldsymbol{I}) -\\ & \frac{2}{\lambda_{R,L}}(1-\sigma_L^{-1})\boldsymbol{A}_{LS},\end{aligned}$$

where $\frac{2}{\lambda_D'} = \frac{1}{\lambda_{D,L}} + \frac{\beta_{th}}{\lambda_{D,S}} - \frac{2}{\lambda_{R,S}}\beta^*(1-\sigma_S^{-1})\sigma_L^{2\delta}$. Notice that the equation for $\overset{\nabla}{\boldsymbol{A}}_{LS}$ is the same as for $\overset{\nabla}{\boldsymbol{A}}_{LL}$ except for the different reptation relaxation times. Thus, the conformation tensor components for $\mathbf{A}_{LS}$ are

$$\begin{aligned}A_{yy} &= \frac{1}{1+\frac{\lambda_D'}{\lambda_{R,L}}(1-\sigma_L^{-1})},\\ A_{zz} &= \frac{1}{1+\frac{\lambda_D'}{\lambda_{R,L}}(1-\sigma_L^{-1})},\\ A_{xy} &= \frac{\dot{\gamma}\lambda_D'}{2[1+\frac{\lambda_D'}{\lambda_{R,L}}(1-\sigma_L^{-1})]^2},\\ A_{xx} &= \frac{1}{1+\frac{\lambda_D'}{\lambda_{R,L}}(1-\sigma_L^{-1})} + \frac{\dot{\gamma}^2(\lambda_D')^2}{2[1+\frac{\lambda_D'}{\lambda_{R,L}}(1-\sigma_L^{-1})]^3}.\end{aligned}$$

The trace for $\mathbf{A}_{LS}$ is

$$\begin{aligned} T_{LS} = tr(\mathbf{A}_{LS}) &= A_{xx} + A_{yy} + A_{zz} \\ &= \frac{3}{1 + \frac{\lambda_D^{'}}{\lambda_{R,L}}(1 - \sigma_L^{-1})} + \frac{\dot{\gamma}^2(\lambda_D^{'})^2}{2[1 + \frac{\lambda_D^{'}}{\lambda_{R,L}}(1 - \sigma_L^{-1})]^3} \\ &= \frac{6[1 + \frac{\lambda_D^{'}}{\lambda_{R,L}}(1 - \sigma_L^{-1})]^2 + \dot{\gamma}^2(\lambda_D^{'})^2}{2[1 + \frac{\lambda_D^{'}}{\lambda_{R,L}}(1 - \sigma_L^{-1})]^3}. \end{aligned}$$

Given that, $tr(\mathbf{A}_L) = \phi_L T_{LL} + (1 - \phi_L) T_{LS}$, the stretch for the thin tube is

$$\sigma_L = \sqrt{\frac{tr(\mathbf{A}_L)}{3}}, \quad \Longrightarrow \quad 3\sigma_L^2 = \phi_L T_{LL} + (1 - \phi_L) T_{LS}.$$

The off-axis stretch predicted for the fat tube, as shown in Figure 6.14 and Figure 6.15, can be explained by considering the limit of small ϕ_L and large reptation relaxation time, $\lambda_{D,L}$. Let ϕ_L be very small, with the following limit,

$$\begin{aligned} \phi_L << 1, \quad &\Longrightarrow 3\sigma_L^2 \approx T_{LS} \text{ (which is mainly } T_{LS}) \\ &\Longrightarrow 3\sigma_L^2 = \frac{3}{1 + \frac{\lambda_D^{'}}{\lambda_{R,L}}(1 - \sigma_L^{-1})} + \frac{\dot{\gamma}^2(\lambda_D^{'})^2}{2[1 + \frac{\lambda_D^{'}}{\lambda_{R,L}}(1 - \sigma_L^{-1})]^3}. \end{aligned}$$

Note that, for $\boldsymbol{A}_{LS}$, we can neglect the CCR term as $\sigma_S \approx 1$. If we now consider the limit where the reptation relaxation time for the long chains is large compared to that of the short chains, for $\beta_{th} = 1$, this gives

$$\begin{aligned} \lambda_{D,L} >> \lambda_{D,S}, \quad &\Longrightarrow \lambda_{D,L} >> \lambda_D^{'} \approx 2\lambda_{D,S} \\ &\Longrightarrow 3\sigma_L^2 = \frac{3}{1 + \frac{2\lambda_{D,S}}{\lambda_{R,L}}(1 - \sigma_L^{-1})} + \frac{\dot{\gamma}^2(2\lambda_{D,S})^2}{2[1 + \frac{2\lambda_{D,S}}{\lambda_{R,L}}(1 - \sigma_L^{-1})]^3}. \end{aligned}$$

Hence in this limit the thin tube stretch depends on the ratio of the short chain reptation and long chain stretch relaxation times and increases with the short chain Weissenberg number, $\dot{\gamma}\lambda_{D,S}$. Thus the stretch for the thin tube is higher near the wall.

To explain why the stretch in the fat tube is small near the wall, even though this is where the shear-rate is dominated, we could formally solve the equation for $tr(\mathbf{A}_{LL})$, (i.e. T_{LL}) with regard to the limits mentioned above. However provided $(1-\sigma_L^{-1}) > 0$ and $\lambda_D^* >> \lambda_{R,L}$ implies that $\lambda_D^* \approx \lambda_{D,L}$, and thus the equation for T_{LL} can be approximated as follows,

$$\begin{aligned} T_{LL} &= \frac{3}{1+\frac{\lambda_{D,L}}{\lambda_{R,L}}(1-\sigma_L^{-1})} + \frac{\dot{\gamma}^2\lambda_{D,L}^2}{2[1+\frac{\lambda_{D,L}}{\lambda_{R,L}}(1-\sigma_L^{-1})]^3} \\ &\approx \frac{3}{\frac{\lambda_{D,L}}{\lambda_{R,L}}(1-\sigma_L^{-1})} + \frac{0.5\dot{\gamma}^2\lambda_{D,L}^2}{[\frac{\lambda_{D,L}}{\lambda_{R,L}}(1-\sigma_L^{-1})]^3} \\ &= \frac{3\lambda_{R,L}}{\lambda_{D,L}(1-\sigma_L^{-1})} + \frac{0.5\dot{\gamma}^2\lambda_{R,L}^3}{\lambda_{D,L}[(1-\sigma_L^{-1})]^3}. \end{aligned}$$

In particular for the case $\beta^* = 0$, the trace for T_{LL} is inversely proportional to $\lambda_{D,L}$ and this implies that the longer the reptation relaxation time of the long chain polymer, $\lambda_{D,L}$ (i.e. in a fat tube), the smaller $tr(\mathbf{A}_{LL})$ is and thus the smaller the stretch becomes in that tube. This is the reason why the stretch in the fat tube collapses in the shear flow (near the wall where the extensional flow is zero) whereas the stretch in the thin tube increases as demonstrated from Figure 6.14 and Figure 6.15.

6.5 Effect of blend composition

In this section, the blend composition of long and short polymer chains of the same material is varied to observe the effect on the hyperbolic contraction flow. The 4:1 contraction with contraction length $L = 5$ is used in this case. The details of the parameters for different volume fractions are presented in Table 6.5. Note that since the different blends have different shear viscosities the pressure gradient is varied in order to give the same VFR of 3.12.

Table 6.5: Different blend composition flowing at the same, VFR=3.12 when $\lambda_{D,L} = 10$, $\lambda_{R,L} = 0.2$, $\lambda_{D,S} = 0.1$ and $\lambda_{R,S} = 0.05$.

Blend	ϕ_S	ϕ_L	$\eta_{P,S}$	$\eta_{P,L}$	ΔP
A	0.95	0.05	0.095	0.5	256
B	0.9	0.1	0.09	1.0	262
C	0.8	0.2	0.08	2.0	271.2

In the hyperbolic contraction flow, the dimensionless upstream wall shear-rate is around 3, so shear-rates upstream are in the range $\frac{1}{\lambda_{D,L}} < \dot{\gamma} < \frac{1}{\lambda_{R,L}}$ where the long chain fraction shear-thins.

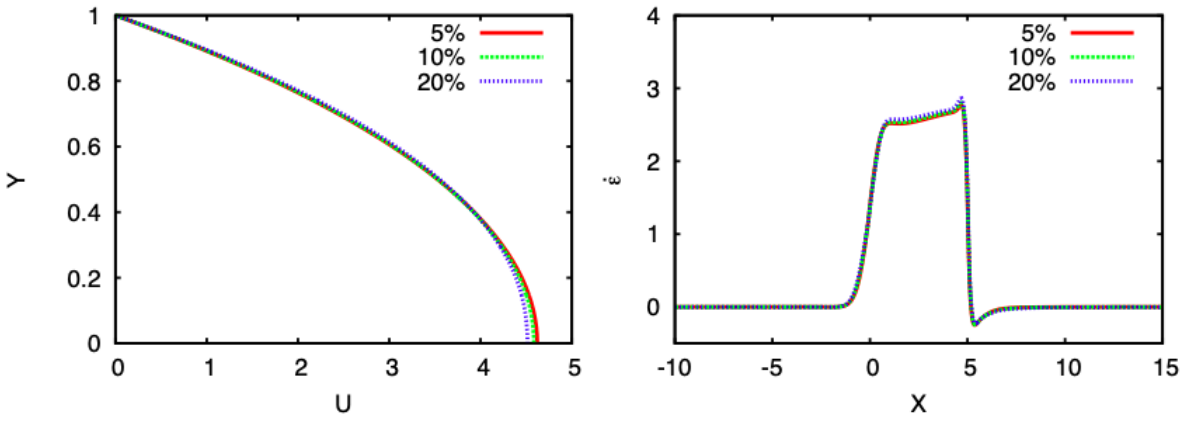

Figure 6.16: LHS figure: Velocity profile across the geometry taking at the half-way upstream (i.e. $x = -7.5$). RHS figure: the extensional profile along the centre-line for different long chain fraction, ϕ_L with constant VFR ≈ 3.12 when $\lambda_{D,L} = 10$, $\lambda_{R,L} = 0.2$, $\lambda_{D,S} = 0.1$ and $\lambda_{R,S} = 0.05$.

The velocity profile depicted in Figure 6.16 shows a parabolic type profile where there is a slight change to the velocity profile with the higher long chain fraction blends that gives a more blunted profile near the centre-line. At 5% long chain concentration, the shear viscosity is dominated by the short chains, and since the short chain Weissenberg number, $\dot{\gamma}\lambda_{D,S}$, is small this leads to a parabolic Newtonian type profile. When ϕ_L is increased, the long chains are oriented but not stretched and thus a shear-thinning profile is observed which is indicated by a more blunted velocity profile. The profile will get more blunted as the fraction of the long chain increases producing a higher shear-thinning effect.

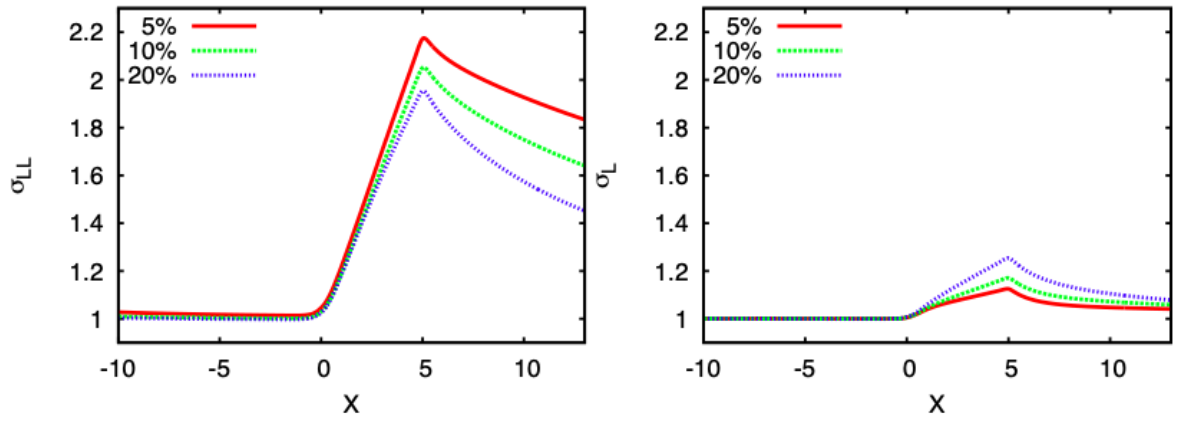

Figure 6.17: Prediction of the stretch for fat and thin tubes along the centre-line for different long chain fraction, ϕ_L with constant VFR ≈ 3.12 when $\lambda_{D,L} = 10$, $\lambda_{R,L} = 0.2$, $\lambda_{D,S} = 0.1$ and $\lambda_{R,S} = 0.05$.

Figure 6.17 shows the effect of increasing the long chain fraction on the predictions of stretch for fat and thin tube along the centre-line of the contraction. Stretch in both fat and thin tubes are showing a different trend as the long chains are diluted (i.e. ϕ_L decreases). While the stretch in the fat tube is increasing as the dilution is increased (i.e. ϕ_L decrease), the stretch in the thin tube decreases. This is because, as the fraction of long chain decreases, the effective stretch relaxation time increases as noted in Boudara et al. [23]. However in the thin tube, we can see that the stretch is increasing with the increment of ϕ_L. The higher density of long chains means that there is a higher possibility of the long chain to get entangled to each other and this increases the fraction of long chain entanglements, which more than compensates for the lower stretch of this fraction.

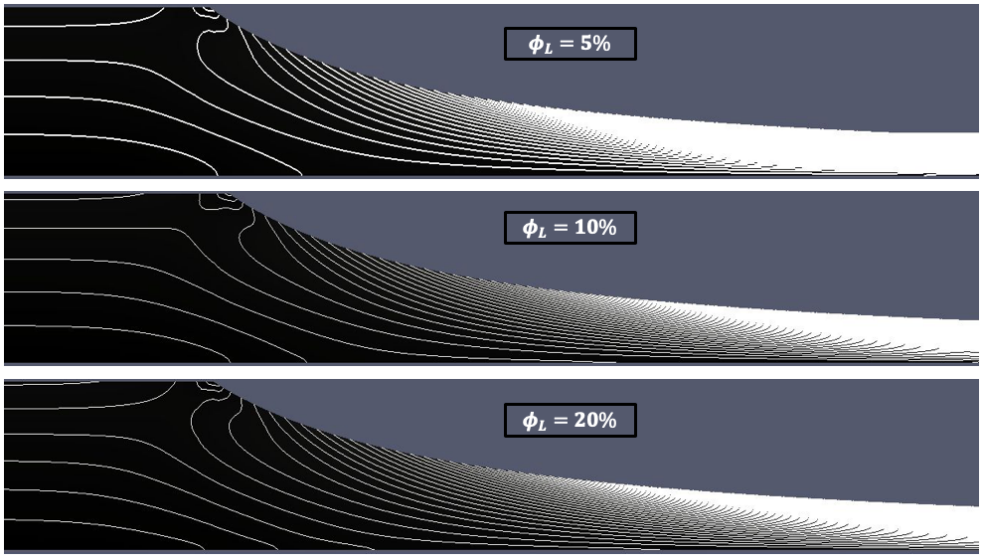

Figure 6.18: The birefringence contour for different blend compositions given $\lambda_{D,L} = 10$, $\lambda_{R,L} = 0.2$, and $\lambda_{D,S} = 0.1$ and $\lambda_{R,S} = 0.05$ for VFR ≈ 3.12 with contour interval=0.25.

The birefringence contour of stress is shown in Figure 6.18 and exhibits a similar stress pattern for the different volume fraction of the long chain. The number of fringes however increases as the concentration of the long chain increases. Even though the melt is flowing with the same VFR upstream, the stress experienced by different blend compositions is not the same. This is because a higher stress is expected in the 20% long chain concentration due to the higher blend viscosity, since the entanglement between the polymer chains in 20% volume fraction of the long species is more pronounced.

6.6 Three-dimensional hyperbolic contraction flow

The hyperbolic contraction flow for the RDP model is further investigated in a more realistic three-dimensional geometry with the presence of the side wall where the no-slip boundary condition is applied. As a consequence of the flow symmetry, only a quarter of the domain is considered for the three-dimensional simulation. The boundary of the three-dimensional hyperbolic contraction geometry is shown in Figure 6.19.

The quarter domain of the geometry promotes the efficiency of solving the three-dimensional flow as the number of computational cells is reduced by factor four from the whole three-dimensional computational domain. However, for the three-dimensional simulation to be

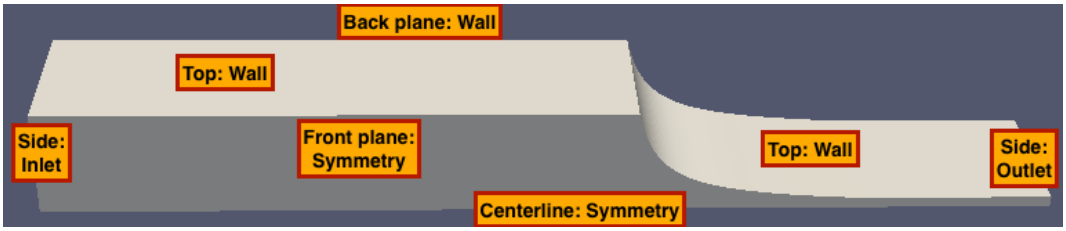

Figure 6.19: The boundaries for a quarter of the three-dimensional hyperbolic contraction domain.

fully practical, a computation strategy based on parallel computing is used here.

The boundary condition for the quarter three-dimensional geometry is treated in a slightly different way to the half domain of the two-dimensional problem. This can be seen from Figure 6.19 where the back plane of the geometry is treated as a wall (i.e. side wall) and the front as a plane of symmetry.

This section is divided into two subsections where the strategy for solving the three-dimensional problem efficiently is first presented before analysing the effect that the presence of side walls has on the flow.

6.6.1 Parallel computing for the three-dimensional problem

Solving a simulation for a large three-dimensional problem requires both large memory and long run times on a serial processor. Here, we used the Advanced Research Computing (ARC) [2] facilities at the University of Leeds to examine the potential efficiency gains of using parallel computing with different numbers of processors. ARC3 consists of 252 nodes where each of the nodes has 24 cores, 128GB of memory and a Solid-State Drive, within the node with 100GB of storage.

For this study, we will simulate the case of a flow cell of depth=0.5. In order to use multiple processors the domain must be divided up between processors. OpenFOAM provides four different methods of domain decomposition. The method of decomposition used in this test is called `simple` where the whole domain is divided geometrically into sub-domains. Here we divide the domain into np sub-domains in the $x-$direction. The full mesh for a quarter of the three-dimensional domain with depth, $d = 0.5$ is $80 \times 40 \times 20$ giving 672 000 hexahedral cells in total. These are then divided equally between the np processors according to their x position. This is depicted in Figure 6.20 for $np = 8$ where each processor has

84 000 cells. The simulations are run for 3 000 time steps with $\Delta t = 10^{-4}$ and the time taken for different number of processors are recorded in Table 6.6 and in Figure 6.21.

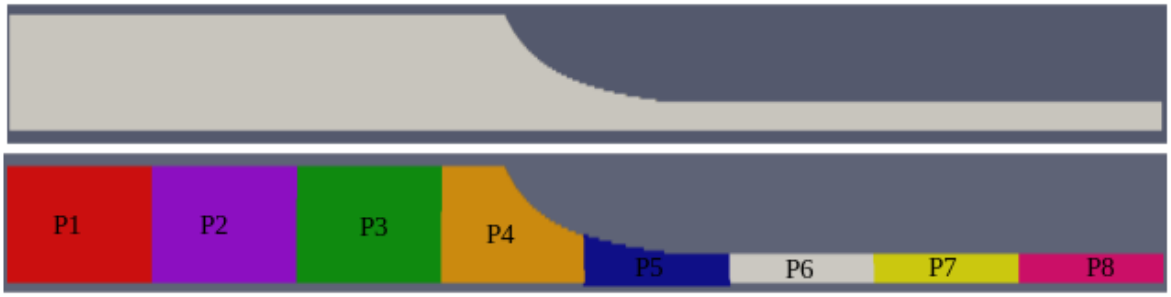

Figure 6.20: The sub-domains when number of processor is set to $np = 8$.

Table 6.6: Efficiency of parallel computing using ARC3 facility.

No of processor (np)	cell/processor	Time taken (s)
2	336000	42581.90
4	168000	19013.20
8	84000	10700.90
16	42000	6346.68
32	21000	3304.80
64	10500	1581.18

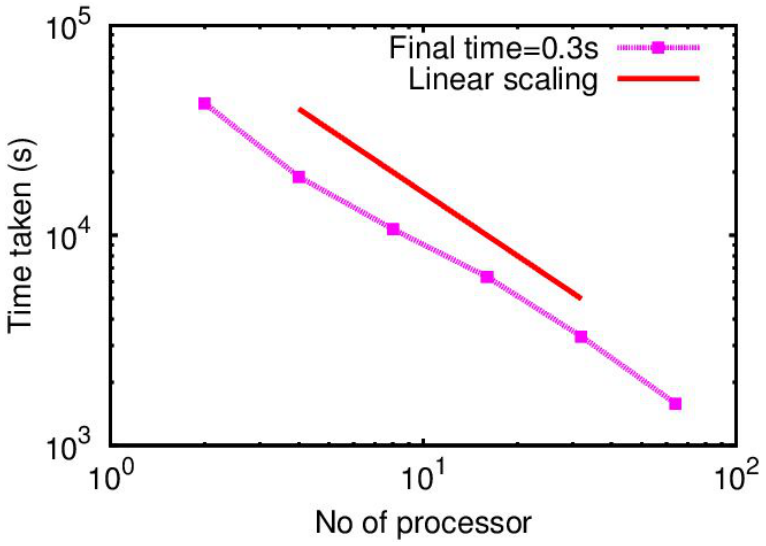

Figure 6.21: The efficiency of the simulation with different processors for the three-dimensional problem when $d = 0.5$.

From Figure 6.21, it can be seen that the time taken for the simulation is decreas-

ing approximately inversely proportional to the number of the processors. This demonstrates the good parallel efficiency of OpenFOAM, and allows practical computation of three-dimensional flows.

6.6.2 The effect of the presence of the side wall

In this section the effect of the presence of the side wall is examined by varying the channel depth, d, and comparing the extension-rate along the centre-line of the centre-plane as shown in Figure 6.22. The extension-rate for different channel depths, d (i.e. $d = 0.5, 1.0, 4.0$) are plotted for 4:1 and 10:1 contraction ratio for a contraction length, $L = 5$. The simulations are carried out with the parameters recorded in Table 5.1. The same pressure drop, ΔP, is used for all different depths with the aim to observe at which channel depth the flow along the centre-line is no longer affected by the presence of the constraining side walls.

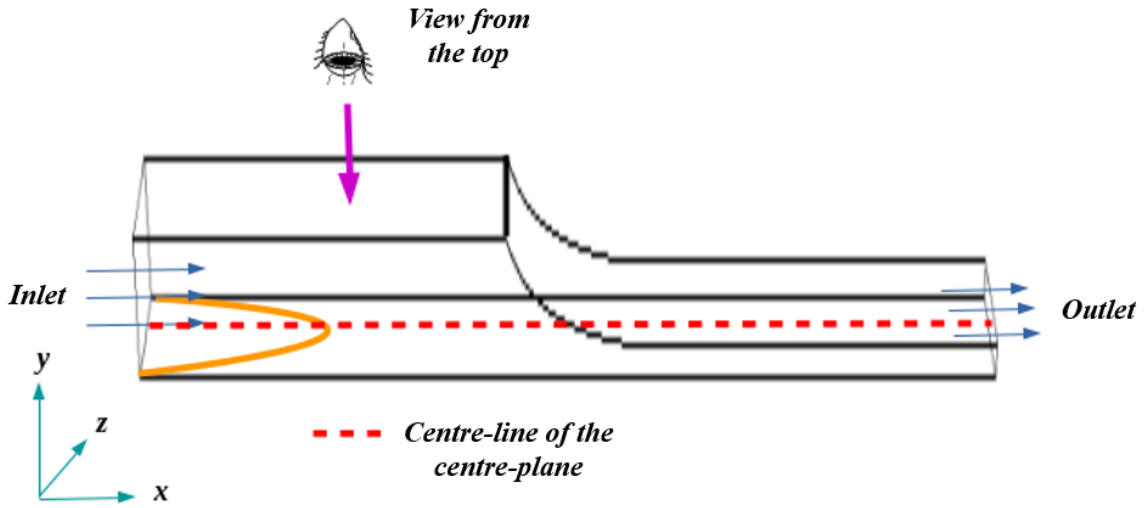

Figure 6.22: The cross-stream flow reflected from the side wall for the half three-dimensional hyperbolic contraction domain.

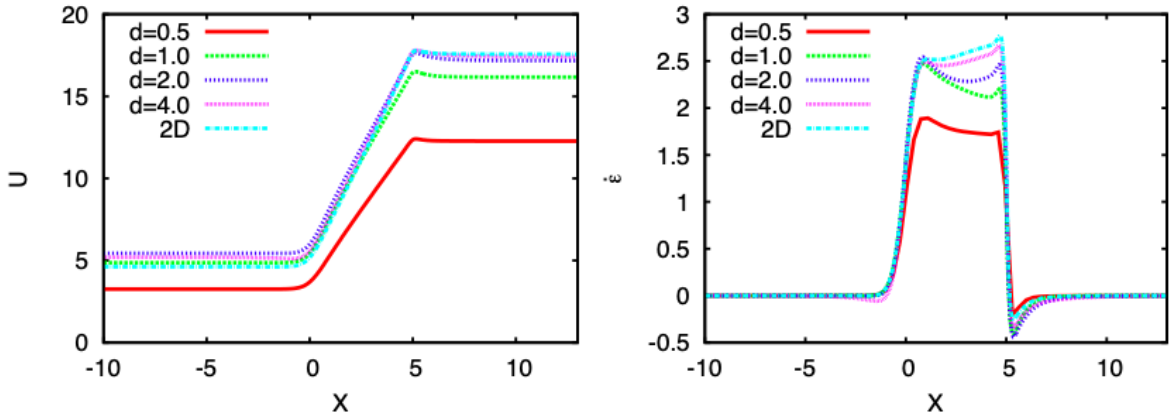

Figure 6.23: The influence of channel depth in 4:1 three-dimensional hyperbolic contraction flow given $\lambda_{D,L} = 10$, $\lambda_{R,L} = 0.2$, $\lambda_{D,S} = 0.1$ and $\lambda_{R,S} = 0.05$ with 5% long chain concentration.

Figure 6.23 shows the centre-line velocity and extension-rate for the 4:1 contraction with different channel depths, $d = 0.5, 1.0, 2.0, 4.0$ for the contraction length, $L = 5$. In terms of the fluid velocity it can be seen that the smallest depth, $d = 0.5$, gives a very different prediction than the others. This is because the ratio of depth to height of the (quarter) geometry at 0.5:1 is too small. However, increasing the depth to $d \geq 1.0$ we find that the extension-rate within the contracting region is within 20% of the $\dot{\varepsilon} = 2.5$ value and approaches the prediction made by the two-dimensional simulation as d increases. The main difference is a reduction in the extension-rate near the end of the contraction section.

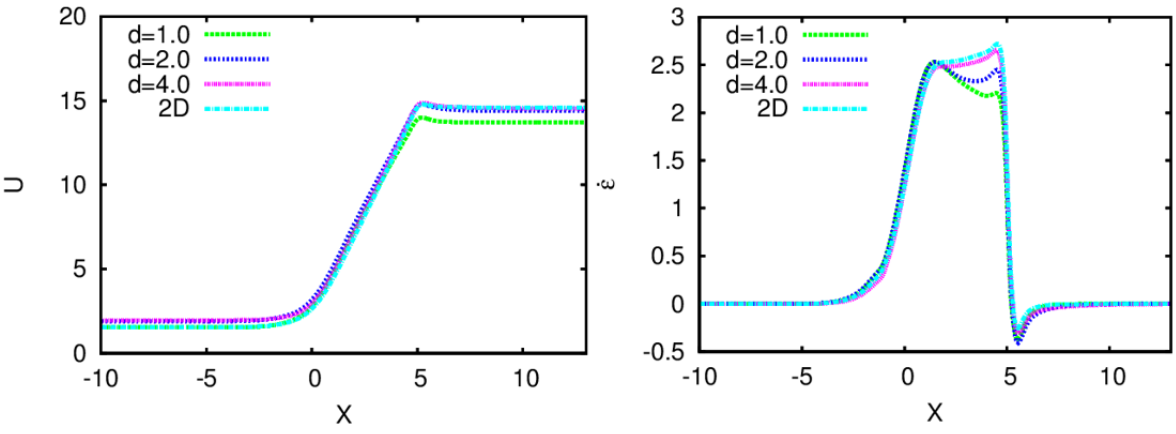

Figure 6.24: The influence of channel depths in a 10:1 three-dimensional hyperbolic contraction flow given $\lambda_{D,L} = 10$, $\lambda_{R,L} = 0.2$, $\lambda_{D,S} = 0.1$ and $\lambda_{R,S} = 0.05$ with 5% long chain concentration.

The results for velocity and the extension-rate profile along the centre-line of the centre-

plane for a 10:1 three-dimensional contraction geometry are plotted as presented in Figure 6.24. The same channel depths to the 4:1 case are considered here. The pressure drop imposed is $\Delta P = 212$ to ensure the same extension-rate to the 4:1 case is achieved for the two-dimensional geometry. For the smallest depth, $d = 0.5$, we find numerical instabilities in the extensional flow region leading to the significant oscillation of the extension-rate within the contraction that continue downstream. This means that we are unable to obtain a steady-state and thus it is not included in the figure.

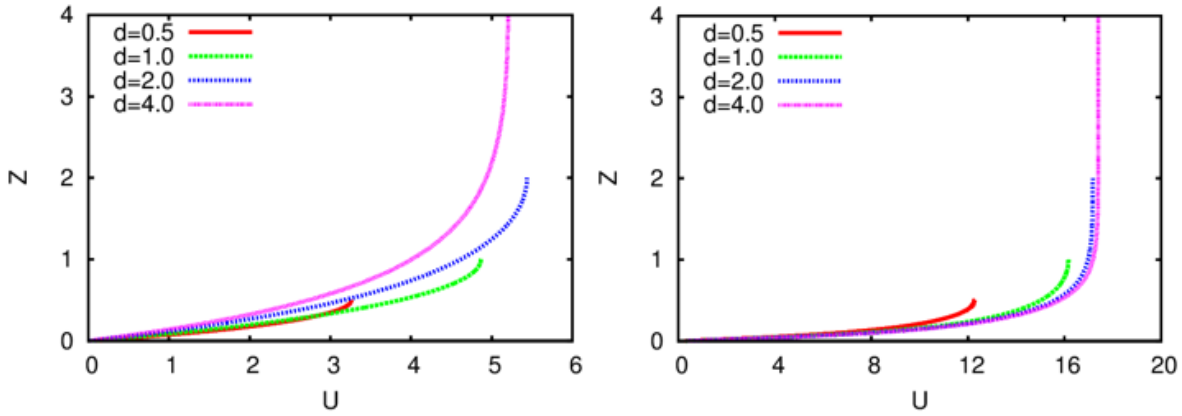

Figure 6.25: The cross-section in z-direction from the centre-line centre-plane (symmetry plane) to the wall for 4:1 contraction ratio for $\lambda_{D,L} = 10.0$, $\lambda_{R,L} = 0.2$, $\lambda_{D,S} = 0.1$ and $\lambda_{R,S} = 0.05$ for 5% long chain concentration with $\Delta P = 256$.

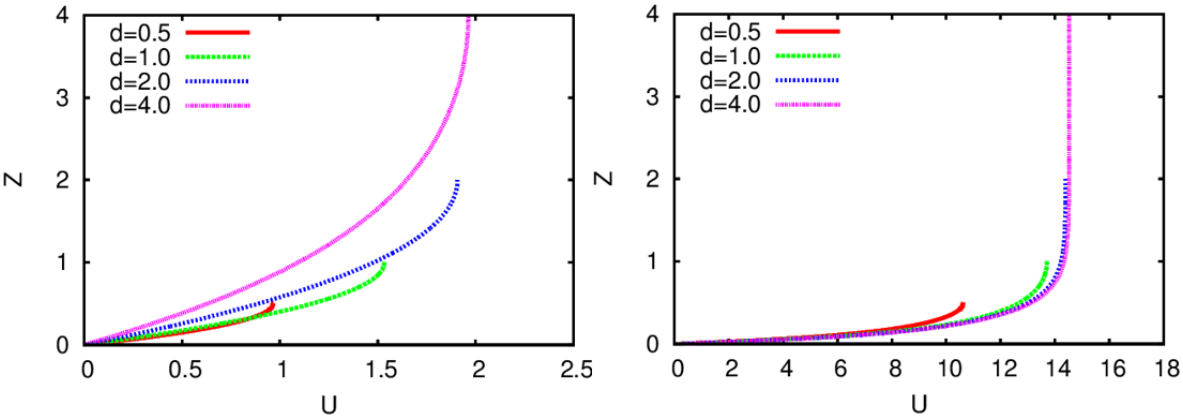

Figure 6.26: The cross-section in z-direction from the centre-line centre-plane (symmetry plane) to the wall for 10:1 contraction ratio for $\lambda_{D,L} = 10.0$, $\lambda_{R,L} = 0.2$, $\lambda_{D,S} = 0.1$ and $\lambda_{R,S} = 0.05$ for 5% long chain concentration with $\Delta P = 212$.

So far we have only examined the flow along the centre-line. Figure 6.25 and 6.26 show the velocity profile across the channel depth (i.e. in z-direction) for halfway upstream (LHS

figure), $x = -7.5$ and halfway downstream of the straight channel (RHS figure), $x = 12.5$. In all cases, $z = 0$ corresponds to the wall. Note that for the 4:1 contraction the half-height of the channel is 1 upstream and 0.25 downstream, so that for $d = 1$ the upstream channel has a square cross-section, while the downstream channel has a cross-section of 1:4. For $d = 4$, the upstream and downstream channels have cross-sections of 1:4 and 1:16 respectively. As a result, for the deepest channel, $d = 4.0$, the velocity is uniform across the central-half of the channel indicating that the flow is free from the effect of the side wall. However reducing the depth to $d = 2.0$ the flow is no longer uniform upstream. Downstream both the 4:1 and 10:1 contractions have the same aspect ratio and hence show similar results.

Comparing the upstream cross-stream velocity profile for both 4:1 and 10:1 contraction ratio for the largest depth, $d = 4.0$, it can be seen that the upstream flow now varies most for the channel depths in the 10:1 case. The ratio of (half) geometry height to its depth explains the difference. While the 4:1 contraction has a 1:4 height to depth ratio, the 10:1 contraction has a higher ratio upstream, that is 1:1.6.

6.7 Conclusion

In this chapter, the behaviour of the RDP model is investigated in a hyperbolic contraction geometry. The effect of contraction length, contraction ratio and channel depth (for three-dimensional geometry) are examined. We found that for a uniform extension-rate to be created within the contracting region, the contraction length should be sufficiently long to give a region of uniform extension-rate through the contraction, however short enough to reduce the ratio of the shear to extensional flow. Increasing the contraction ratio for the same extension-rate allows greater polymer stretch to be accumulated because the lower flow-rate allows the fluid to have a longer residence time within the contracting region, which can accumulate higher strain. In the three-dimensional case, we found that the cross-stream flow in the downstream region can be neglected when the ratio of the half geometry height to channel depth is 1:4 for 4:1 and 1:1.6 for 10:1.

The coupling effect of the RDP and mRP models flowing through the hyperbolic contraction produces different predictions of the thin and fat tube stretch within the contraction region due to the enhanced stretch relaxation time in the RDP model. We present a math-

ematical analysis to explain this. The behaviour of the RDP fluid is further explored by varying the blend composition, where the stretch in the thin and fat tube shows opposite trends with changes in the concentration as a consequence of the effective stretch relaxation time.

Chapter 7

Rolie-Double-Poly - cross-slot flow with hyperbolic corner

This chapter presents simulations for the flow in a cross-slot with hyperbolic corners. The behaviour of the bidisperse RDP model in this configuration is studied by varying the relevant parameters. These include the effect of the hyperbolic (corner) length, comparing the sharp corner ($L = 0$) and hyperbolic corners with different lengths. The effects of this and the cross-slot depth on the prediction of the velocity, extension-rate and stretch profile along the outlet centre-line are presented and discussed. In addition the effect of changing constitutive parameters including the blend composition and differences between the predictions of the RDP and mRP model are considered. The stress birefringence patterns are also calculated to observe the stress distribution in the cross-slot. A comparison between the two different flow geometries considered in this work, the hyperbolic contraction flow and cross-slot flow, is also presented.

7.1 Motivation

As discussed in Chapter 4, the simplest cross-slot geometry consists of two intersecting channels with a right-angled corner similar to the abrupt contraction. Due to the results for the hyperbolic contraction flow discussed in Chapter 6, we also propose to use the cross-slot with hyperbolic corners. No work to date has been published for the cross-slot with hyper-

bolic corners. We expect that homogeneous elongational flow would be generated along the inlet-outlet centre-line based on the findings of the previous chapter. The two-dimensional cross-slot flow simulation is more challenging compared to the hyperbolic contraction flow. In contrast to the hyperbolic contraction flow, in the two-dimensional cross-slot flow there is a stagnation point at the central region of the flow which experiences unbounded extensional strain, due to the infinite residence time at the stagnation point. By probing the stress near the stagnation point the non-linear response to high strain extension flow can be measured. However this local region of highly strained material can modify the fluid dynamics. Gardner et al. [55] observed that the flow along the centre-line, downstream of the stagnation point, is slowed down due to the resistance to extensional flow causing a minimum in the fluid velocity in the downstream region. This was successfully modelled by Harlen et al. [63]. More recently Arriata et al. [8] have shown that for polymer solutions the flow can bifurcate to an asymmetric state. Consequently, although under the assumption of symmetry it would be possible to simulate the flow using a quarter of the geometry, in order to be able to capture the possibility of transition to an asymmetric flow, the whole flow domain is simulated. The simulation results are analysed and discussed in the following sections.

7.2 Two-dimensional cross-slot geometry definition

The dimension of the whole two-dimensional cross-slot geometry and the flow direction are described as shown in Figure 7.1 where the upstream and downstream channel width are set to $H = 1.0$. We let the length of the straight channel for inlet and outlet sections be sufficiently large in the up- and downstream segments to ensure a fully-developed flow and thus avoid end effects.

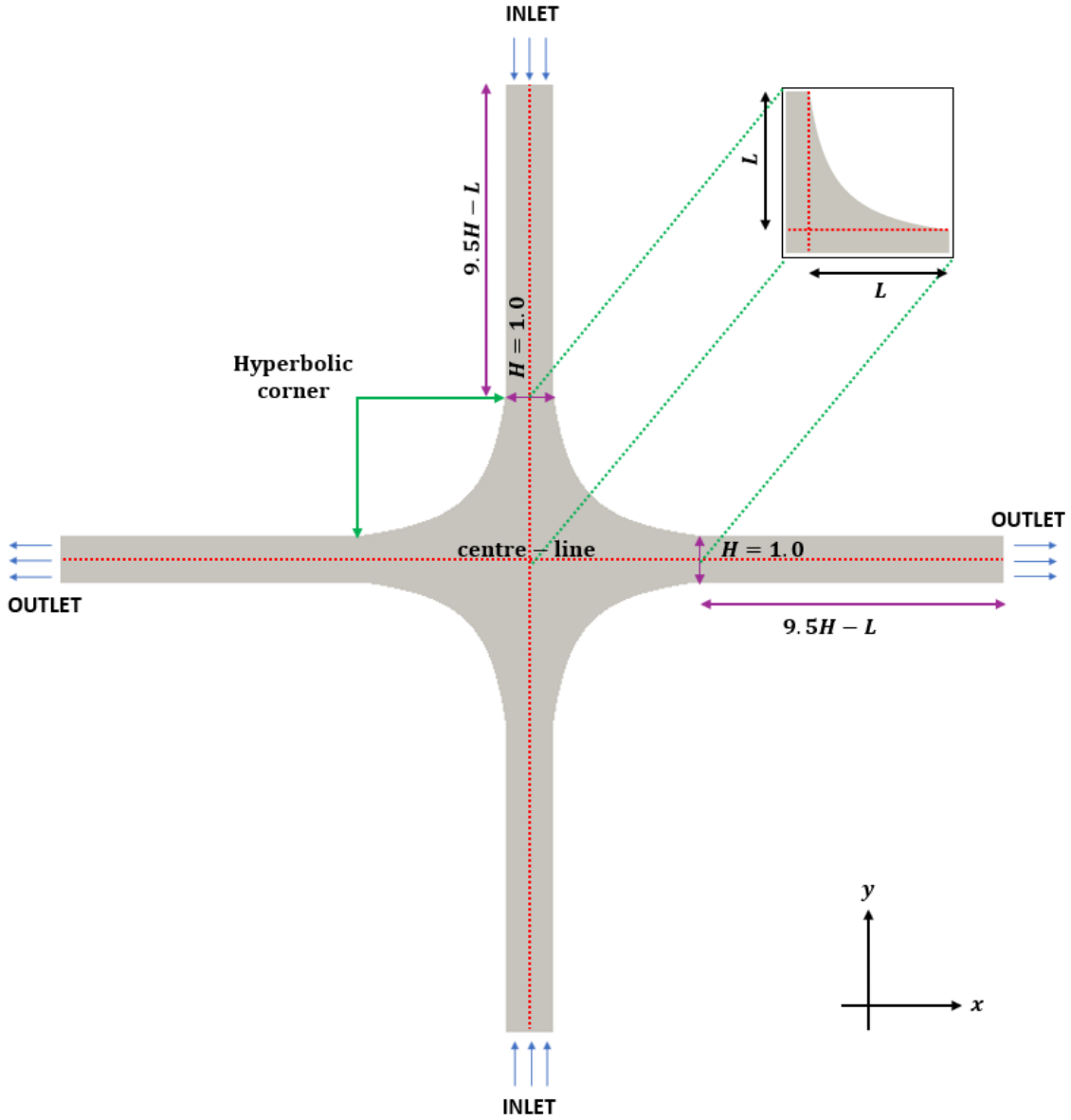

Figure 7.1: Two-dimensional cross-slot geometry with hyperbolic corner and flow direction of the fluid. The origin of the axis is at the stagnation-point that is at the intersection between the inlet-outlet centre-line.

The hyperbolic corners shown in Figure 7.1 are defined according to the quadrant. For a

positive y-axis, $y = H(x)$ takes the value as the following piecewise function

$$H(x) = \begin{cases} 0.5H, & x < -(L + 0.5) \\ \dfrac{-0.5H(L + 0.5)}{x}, & -(L + 0.5) \leq x \leq -0.5 \\ \dfrac{0.5H(L + 0.5)}{x}, & 0.5 \leq x \leq (L + 0.5) \\ 0.5H, & x > L + 0.5. \end{cases}$$

On the other hand, for a negative y-axis, $y = -H(x)$, $H(x)$ is defined as

$$H(x) = \begin{cases} -0.5H, & x < -(L + 0.5) \\ \dfrac{0.5H(L + 0.5)}{x}, & -(L + 0.5) \leq x \leq -0.5 \\ \dfrac{-0.5H(L + 0.5)}{x}, & 0.5 \leq x \leq (L + 0.5) \\ -0.5H, & x > L + 0.5. \end{cases}$$

These piecewise functions make up the full cross-slot geometry shown in Figure 7.1. The dimensionless parameters used in this section are defined as $L = L/H$, $X = x/H$, $Y = y/H$. In the next section, the boundary condition and the meshing strategy for the hyperbolic corner are presented.

7.2.1 Boundary condition

The boundary conditions for the two-dimensional cross-slot flow that is set-up in the OpenFOAM RheoTool software is shown in Table 7.1. Notice that this table is similar to Table 4.2 without the symmetry plane boundary conditions since the whole cross-slot geometry is used here.

Table 7.1: The boundary condition for two-dimensional cross-slot flow.

Boundary	Boundary conditions		
	p	$\mathbf{U}$	$\boldsymbol{\tau}_i$
Inlet	`uniformFixedValue`	`zeroGradient`	`zeroGradient`
Outlet	`fixedValue`	`zeroGradient`	`zeroGradient`
Walls	`zeroGradient`	`noSlip`	`linearExtrapolation`
frontAndBack	`Empty`	`Empty`	`Empty`

The flow domain is represented by the solid grey whole plane shown by the figure with `noSlip` boundary condition indicating that there is no velocity at the wall. Since OpenFOAM uses a three-dimensional geometry we set `empty` boundary conditions at front and back to enable a two-dimensional problem to be solved.

7.2.2 Mesh generation strategies

In this study, the hexahedral type of mesh is used to discretize the whole spatial domain. This type of mesh is the default mesh used in OpenFOAM to discretise a three-dimensional domain. The curved boundaries of the hyperbolic cross-slot geometry requires a meshing strategy that avoids the creation of highly distorted elements, that can lead to numerical difficulties due to mesh skewness. Figure 7.2 shows the different mesh strategies used for the cross-slot with a sharp corner and the cross-slot with hyperbolic corners.

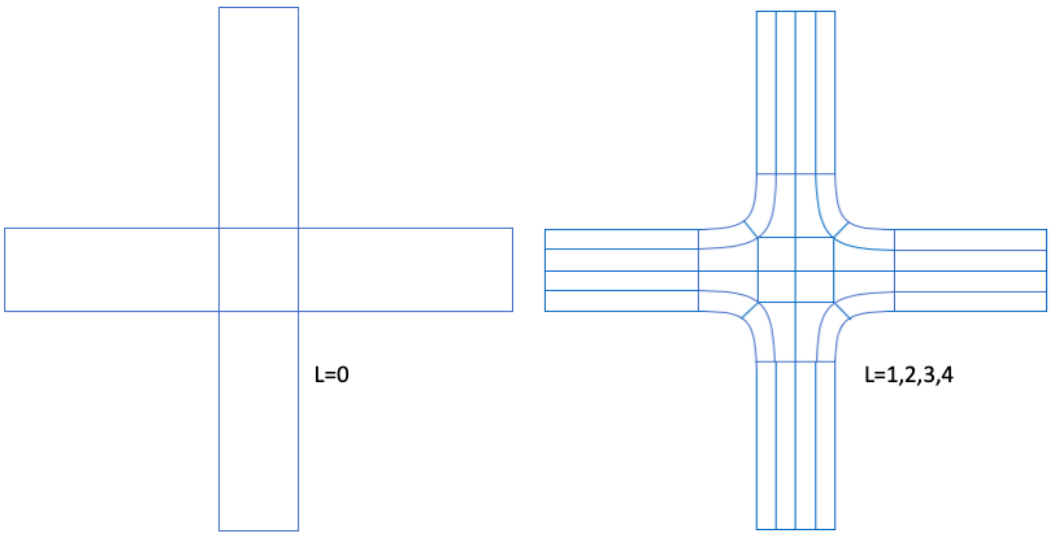

Figure 7.2: The sketch for different mesh block strategies used for sharp corner and different hyperbolic corner lengths.

Note that the mesh strategy used for the cross-slot with the hyperbolic corner for different lengths are the same. However, the position of the division within the hyperbolic section that divides the corners into two blocks depends on the hyperbolic length of the corner so that the mesh issues such as the high skewness of the cell can be minimized.

7.3 Effect of hyperbolic length in two-dimensional cross-slot

In this section, the influence of the hyperbolic corner length on the prediction of the extension-rate and stretch in the thin and fat tube for the RDP model along the outlet centre-line of the geometry are presented. The same constitutive parameters are used as in the previous chapter and as presented in Table 5.1 with other parameters set to $\beta^* = 0.0$, $\beta_{th} = 1.0$, $\delta = -0.5$ and $\eta_S = 0.01$. The mesh information for different hyperbolic corner lengths is presented in Table 7.2.

Table 7.2: Mesh information for the whole cross-slot geometry for different hyperbolic corner lengths.

L	$L = 0$	$L = 1$	$L = 2$	$L = 3$	$L = 4$
Points	30368	42402	42402	75442	116482
Cells	14841	20800	20800	37200	57660
Faces	59706	83600	83600	149320	231040
Internal faces	29340	41200	41200	73880	114560

The size and complexity of the domain increases as a consequence of the increase in the hyperbolic curvature length. Thus more cells are required for longer hyperbolic lengths so that a smooth numerical simulation can be ensured. The hyperbolic corner length with $L = 1$ and $L = 2$ are however able to be simulated using the same mesh dimensions. Figure 7.3 shows the velocity and total polymeric stress profile across the upstream channel taken at $y = 1.5 + L$ that is one unit away from the hyperbolic slot region.

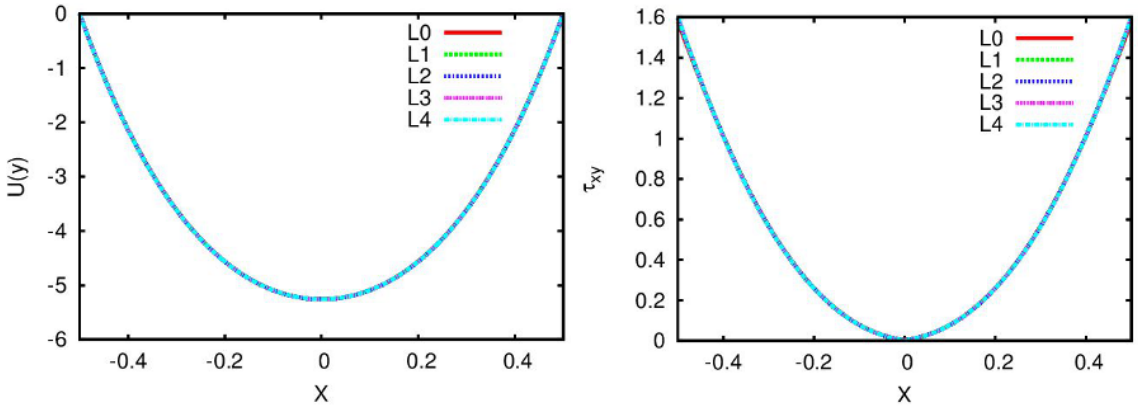

Figure 7.3: The fully-developed velocity and total polymeric stress profile (for $xy-$component) for different hyperbolic corner lengths taken at the upstream channel along the $y = 1.5 + L$ given the VFR ≈ 3.65.

Figure 7.3 revealed that the length of the straight channel upstream is sufficient to develop the fully-developed flow for both velocity and stress profile. We next present the profile of extension-rate taken at the centre-line.

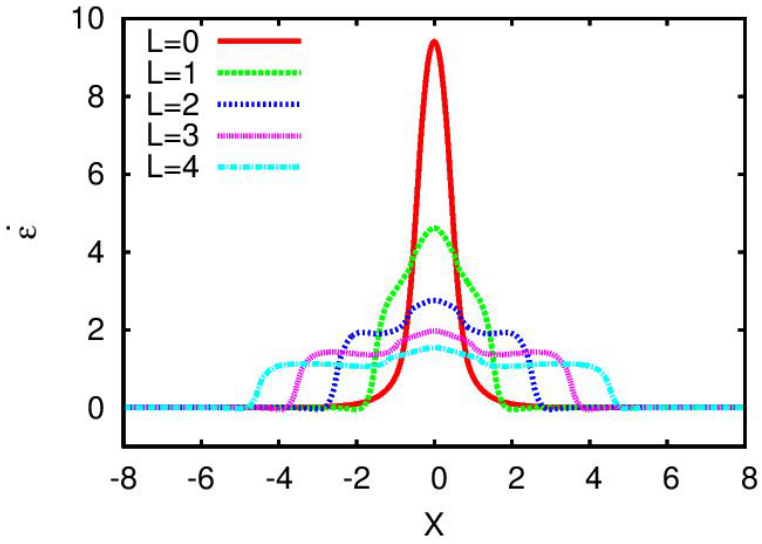

Figure 7.4: The extension-rate at the centre-line ($y = 0$) for different hyperbolic corner lengths in a cross-slot flow for VFR ≈ 3.65 with $\lambda_{D,L} = 10$, $\lambda_{R,L} = 0.2$, $\lambda_{D,S} = 0.1$ and $\lambda_{R,S} = 0.05$.

Figure 7.4 shows the prediction of the extension-rate along the centre-line of the outlet channels for different hyperbolic lengths, with the same VFR. The extension-rate is most pronounced at the stagnation point, $x = y = 0$. Along the outlet centre-line, the elongational

flow is created as a result of the changing flow direction from the inlet arms to the outlet arms. The extension-rate is highest at the stagnation point and reduces to zero at the end of the hyperbolic section. However there is an increase in the uniformity for the extension-rate within the length of the hyperbolic curve. From Figure 7.4, a region of almost constant extension-rate is observed for $L \geq 2$. As the hyperbolic length increases, the extension-rate within the hyperbolic length decreases slightly.

The predictions of the stretch in the cross-slot geometry with sharp and hyperbolic corners are presented in separate figures as the scale of the stretch in a cross-slot with sharp corner is much higher compared to the prediction made by the cross-slot with hyperbolic corners.

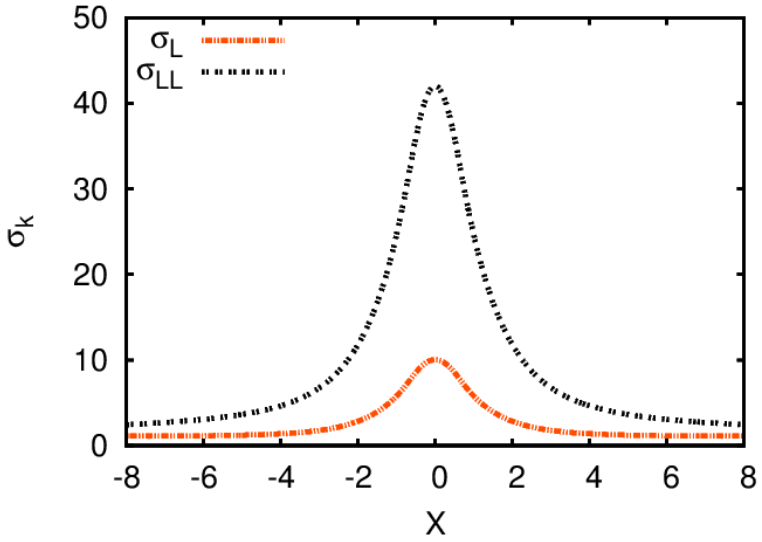

Figure 7.5: The stretch comparison for both thin and fat tubes at the centre-line ($y = 0$) for cross-slot geometry with sharp corner for $\Delta P = 43.8$ that gives VFR ≈ 3.65 with $\lambda_{D,L} = 10.0$, $\lambda_{R,L} = 0.2$, $\lambda_{D,S} = 0.1$ and $\lambda_{R,S} = 0.05$.

In Figure 7.5, the stretch in the thin and fat tube along the centre-line is shown for cross-slot with a sharp corner. The prediction of the fat and thin tube stretch made by the RDP model is about four times higher in the fat tube comparing to the thin tube. Comparing Figure 7.5 to Figure 7.6, the stretch predicted in both tubes are larger in the cross-slot with sharp corner compared to the stretch predicted using different hyperbolic lengths as a consequence of the higher extension-rate at the stagnation point shown in Figure 7.4.

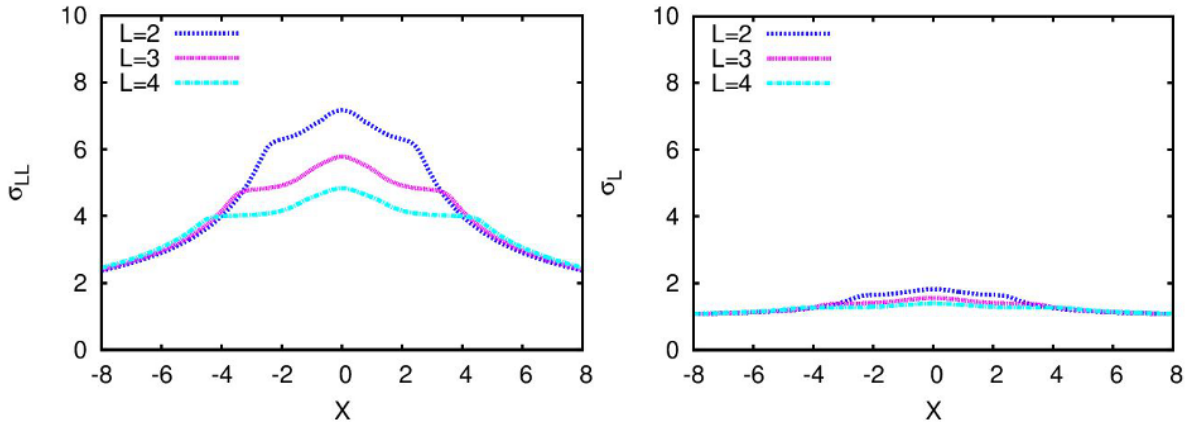

Figure 7.6: The stretch comparison for the fat and thin tubes along the centre-line ($y = 0$) of the cross-slot geometry with different hyperbolic corner lengths when VFR ≈ 3.65 with $\lambda_{D,L} = 10.0$, $\lambda_{R,L} = 0.2$, $\lambda_{D,S} = 0.1$ and $\lambda_{R,S} = 0.05$.

Figure 7.6 presents the stretch in the fat and thin tubes along the centre-line for different hyperbolic lengths corner. Note from Figure 7.4 that the extension-rate for these geometries ranges from 2 to 3.5 in the hyperbolic section, so that $\dot{\varepsilon}\lambda_{R,L} < 1$. Thus at steady-state (from Section 5.6) we expect $\sigma_L = (1 - \dot{\varepsilon}\lambda_{R,L})^{-1}$ while σ_{LL} will be larger by a factor of approximately $\phi_L^{-1/2}$.

The calculated stress birefringence with the same contour interval, (i.e. contour interval = 0.5) for the cross-slot with different hyperbolic lengths are presented in Figure 7.7 where the stress contours are shown for the central section of the geometry from half-way in the upstream channel to half-way in the downstream channel. The density of the stress contours away from the centre-line is similar for all lengths in both upstream and downstream arms as a consequence of the shear flow. However, in the outlet centre-line, a birefringence strand is observed due to the high stresses generated by the elongational flow. Looking at $L = 0$, the density of the stress contours is most pronounced in the cross-slot region compared to the other hyperbolic lengths. This indicates that the highest stress is produced within this region as a consequence of the strong elongational flow at the stagnation point, the history of which is inherited along the outlet centre-line of the geometry. This agrees with the extension-rate and stretch for the fat and thin tubes plotted in Figure 7.5 and 7.6 respectively. There is also high stress observed at the sharp corners due to the singularity in the velocity gradient at these points.

When the hyperbolic shape is applied to the corners, a smoother region is created and

this reduces the stress both near the stagnation point and at the walls. This is demonstrated by the decrease in the number of stress fringes within the slot, as can be seen from Figure 7.7, when the length of the hyperbolic corner is increased. Based on the results presented in this section, the $L = 2$ hyperbolic corner length is sufficiently long to generate the uniform extension-rate within the hyperbolic region and short enough to avoid larger shear effect near the wall. Therefore, the cross-slot with hyperbolic corner $L = 2$ is chosen as the base geometry to further investigate the effect of different extension-rate, effect of chain coupling, effect of blend composition effect and the effect of channel depths provided in the next sections. However, in order to examine the effect of changing the shape of the corner a comparison between the cross-slot with hyperbolic corner, $L = 2$ and cross-slot with rounded corner having a radius, R=R/H is presented beforehand to look at the effect on the extension-rate, the stretch in fat and thin tubes along the centre-line.

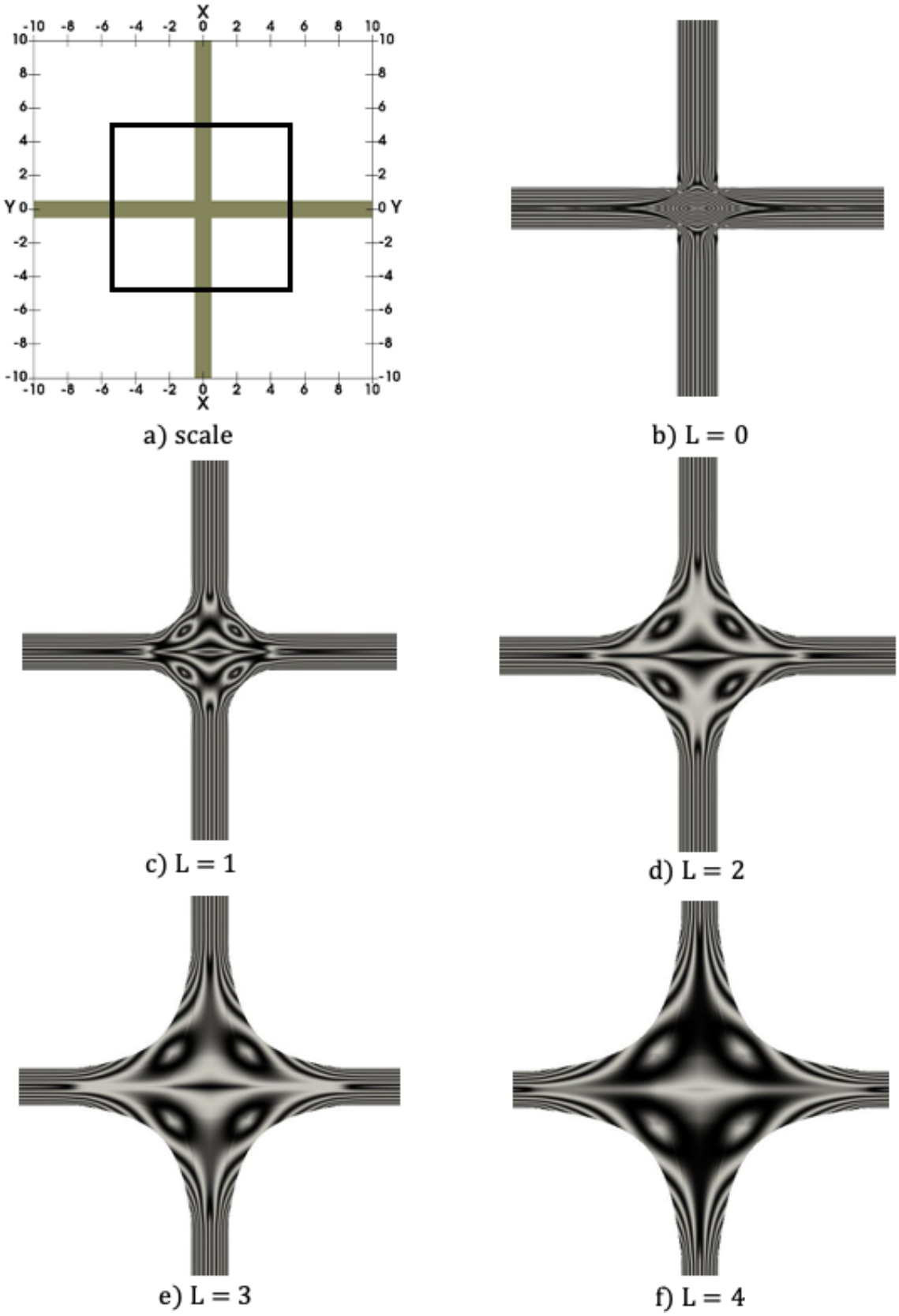

Figure 7.7: The birefringence pattern for different hyperbolic corner lengths with contour interval 0.5 predicted by the RDP model given the VFR ≈ 3.65 with $\lambda_{D,L} = 10.0$, $\lambda_{R,L} = 0.2$, $\lambda_{D,S} = 0.1$ and $\lambda_{R,S} = 0.05$.

Figure 7.8 shows a comparison of the extension rate between the cross-slot with hyperbolic corner and rounded corner. Here, we used R=2 for the radius of the rounded corner for a comparable results. The fluid is flowing through the slot with the same VFR that is about VFR ≈ 3.65. From the figure, it can be seen that the extension rate is quite similar to a comparison of the extension rate between the rounded corner showing higher extension-rate within the rounded region and the stagnation point comparing to the one predicted by hyperbolic corner. However, in terms of the uniformity of the extension-rate, there is a wider range of constant extension-rate observed for the cross-slot with hyperbolic corner which is within the hyperbolic region comparing the rounded corner.

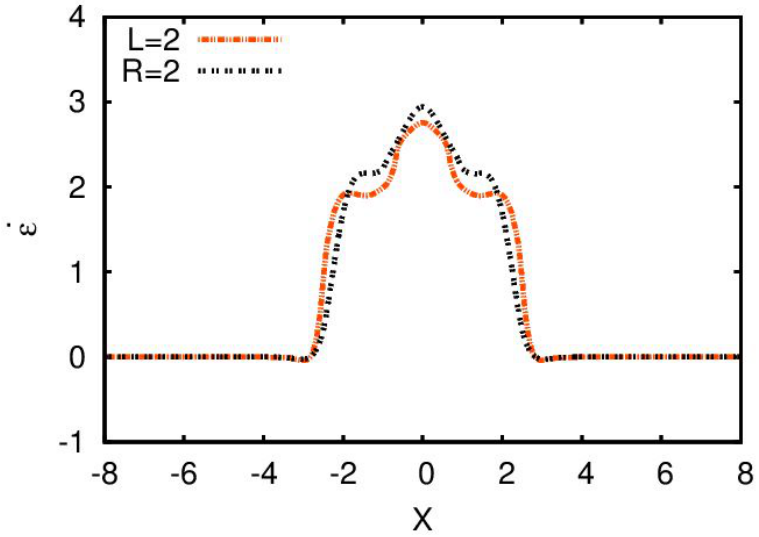

Figure 7.8: The extension-rate predicted by hyperbolic corner with a) $L = 2$ and rounded corner when radius b) R=2 given the VFR ≈ 3.65 with $\lambda_{D,L} = 10.0$, $\lambda_{R,L} = 0.2$, $\lambda_{D,S} = 0.1$ and $\lambda_{R,S} = 0.05$.

In Figure 7.9, the stretch for both fat and tubes measured along the centre-line are presented for both hyperbolic and rounded corner. From the figure, it can be seen that the rounded corner predicts slightly higher stretches as a consequence of the higher extension-rate predicted in the rounded corner. From Figure 7.9, there is a smooth increment of the stretch within the hyperbolic region while the profile observed for the rounded corner within the rounded region inherits the profile from the extension-rate.

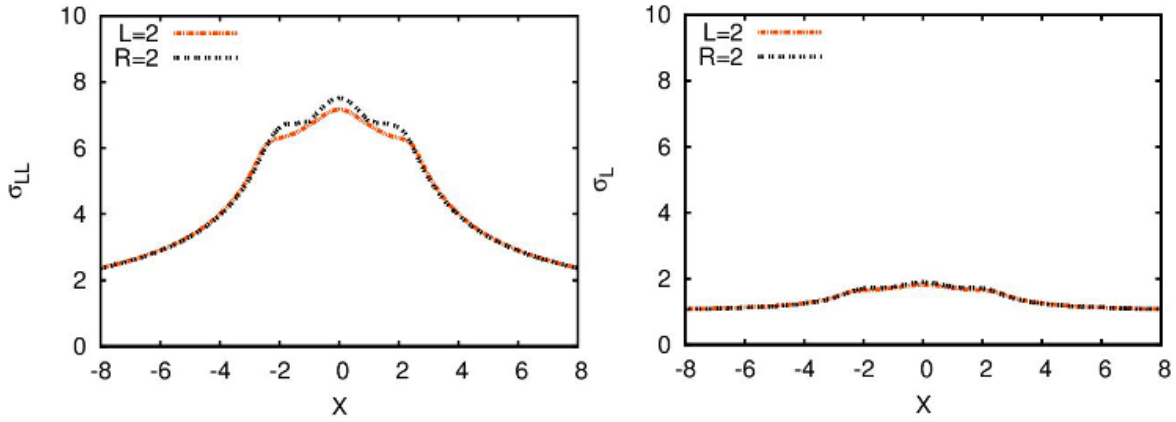

Figure 7.9: The fat and thin tubes stretch predicted by hyperbolic corner with a) $L = 2$ and rounded corner with radius b) R=2 given the VFR ≈ 3.65 when $\lambda_{D,L} = 10.0$, $\lambda_{R,L} = 0.2$, $\lambda_{D,S} = 0.1$ and $\lambda_{R,S} = 0.05$.

Looking at the birefringence pattern depicted in Figure 7.10, both hyperbolic and rounded corners show a similar pattern except in the region within the slot near the centre-line where the cross-slot with hyperbolic corner has a single white fringe at the stagnation point and a single black fringe away from the stagnation point. In a cross-slot with a rounded corner in Figure 7.10b, within the area of stagnation point, there are two fringes observed (i.e. one black and one white) near the centre-line and away from the stagnation point. This suggests that the rounded corner produces higher stress within near and along the centre-line as a consequence of the higher extension-rate within this region. This observation is consistent with the results shown in Figure 7.8 and 7.9.

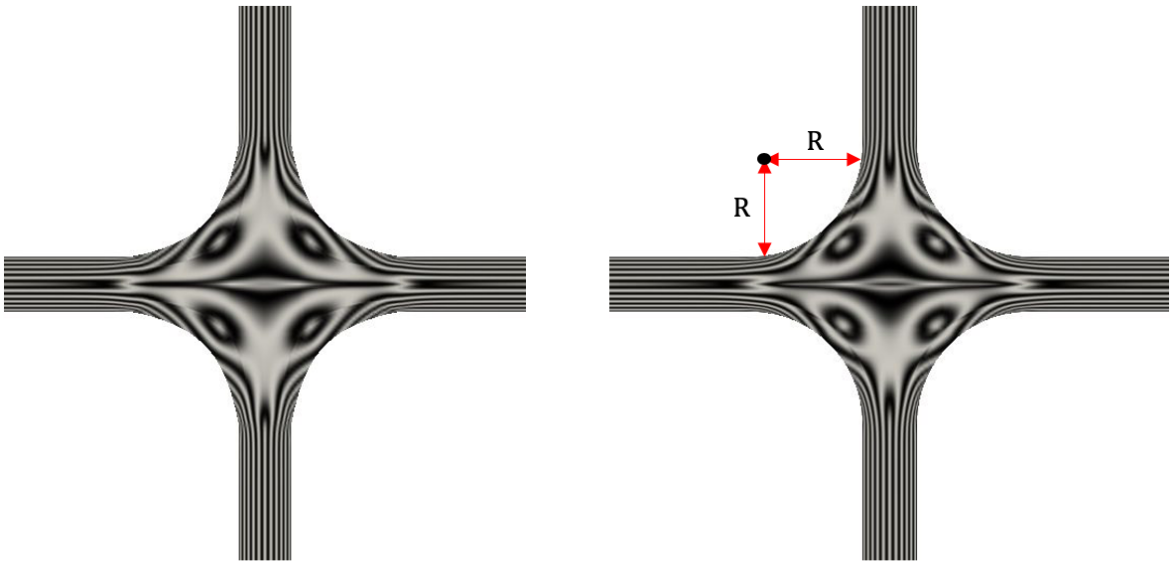

Figure 7.10: The birefringence pattern for hyperbolic corner when a) L=2 and rounded corner with radius, b) R=2 given the VFR ≈ 3.65 with contour interval 0.5 and $\lambda_{D,L} = 10.0$, $\lambda_{R,L} = 0.2$, $\lambda_{D,S} = 0.1$ and $\lambda_{R,S} = 0.05$.

7.4 Effect of different extension-rate

In this section, the effect of extension-rate on the prediction of stretch for the fat and thin tubes with the stress birefringence are discussed. Three different pressure drops, giving different volumetric flow-rates and extension-rates, are considered in this case. The details of the pressure drop imposed for $L = 2$ for the following extension-rates $\dot{\varepsilon} = 0.05, \dot{\varepsilon} = 1.0, \dot{\varepsilon} = 2.5$ are $\Delta P = 1.3, \Delta P = 22$ and $\Delta P = 43.8$ respectively.

Figure 7.11 displays the extension-rate along the outlet centre-line for different pressure drops. In this figure, the legend refers to the extension-rate along the section of hyperbolic curve where an almost constant strain-rate is found. The profile of the extension-rate is similar for all three values but the higher extension-rate, $\dot{\varepsilon} = 2.5$, shows a small undershoot both before and after the hyperbolic corner because of the modification of the flow caused by the polymeric stress. This can clearly be seen from the normalised extension-rate at constant flow-rate when the data is plotted on each other shown from the RHS of the figure.

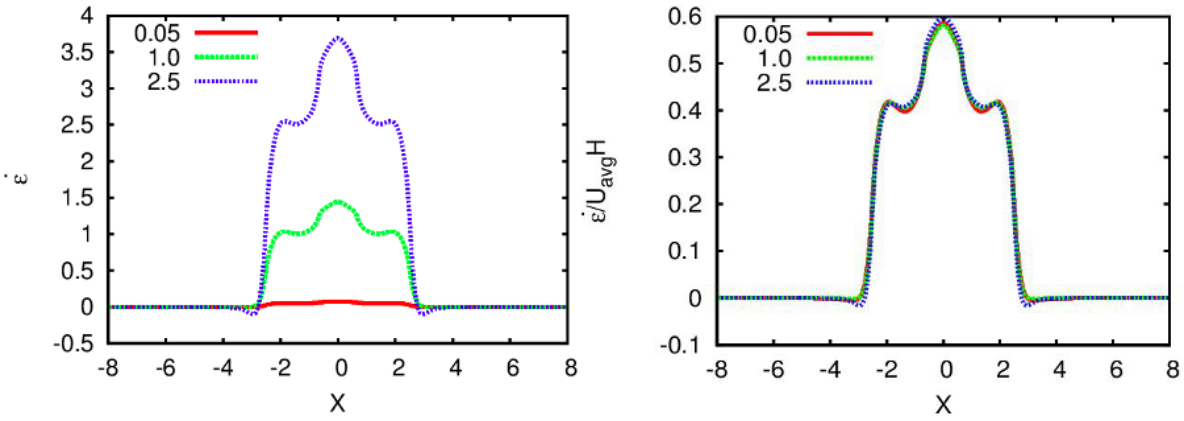

Figure 7.11: Extension-rate (LHS) and normalised extension-rate (RHS) along the outlet centre-line of the cross-slot with the hyperbolic corner given length, $L = 2$, for different pressure drops when $\lambda_{D,L} = 10.0$, $\lambda_{R,L} = 0.2$, $\lambda_{D,S} = 0.1$ and $\lambda_{R,S} = 0.05$. The legend value corresponds to the extension-rate in region of the hyperbolic curve.

The stretch for both fat and thin tubes are presented in Figure 7.12. As expected, the stretch is maximum at the stagnation point which has the highest extension-rate. The lowest extension-rate $\dot{\varepsilon} = 0.05$, does not show any stretching in both tubes because the flow is still in the slow regime and behaving like a Newtonian fluid. The extension-rate, $\dot{\varepsilon} = 1.0$, however, is high enough to create stretch in both tubes, as a consequence of the enhanced stretch relaxation time, even though $\dot{\varepsilon}\lambda_{R,L} < 1$. At the end of the hyperbolic section the stretch relaxes as the extension-rate returns to zero.

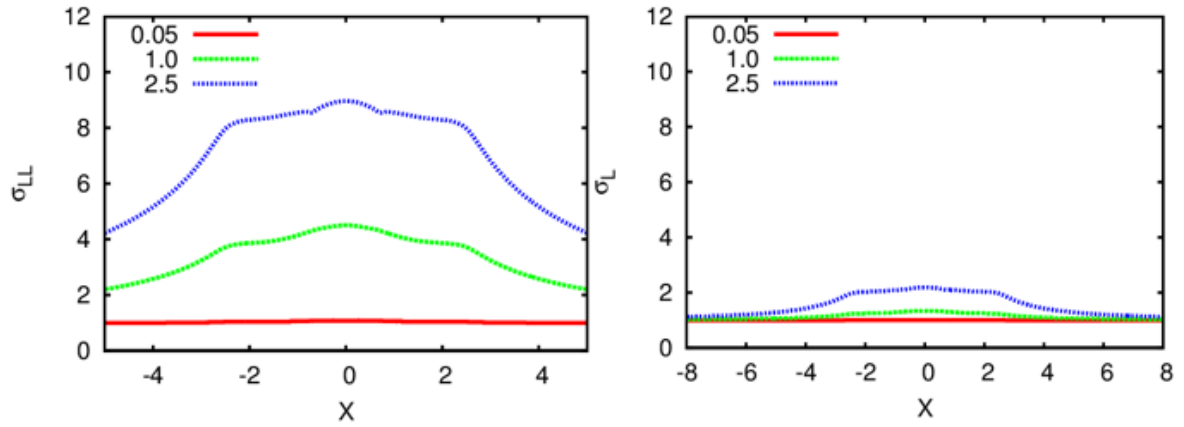

Figure 7.12: Effect of extension-rate for stretch of the fat and thin tubes along the outlet centre-line predicted by the RDP model.

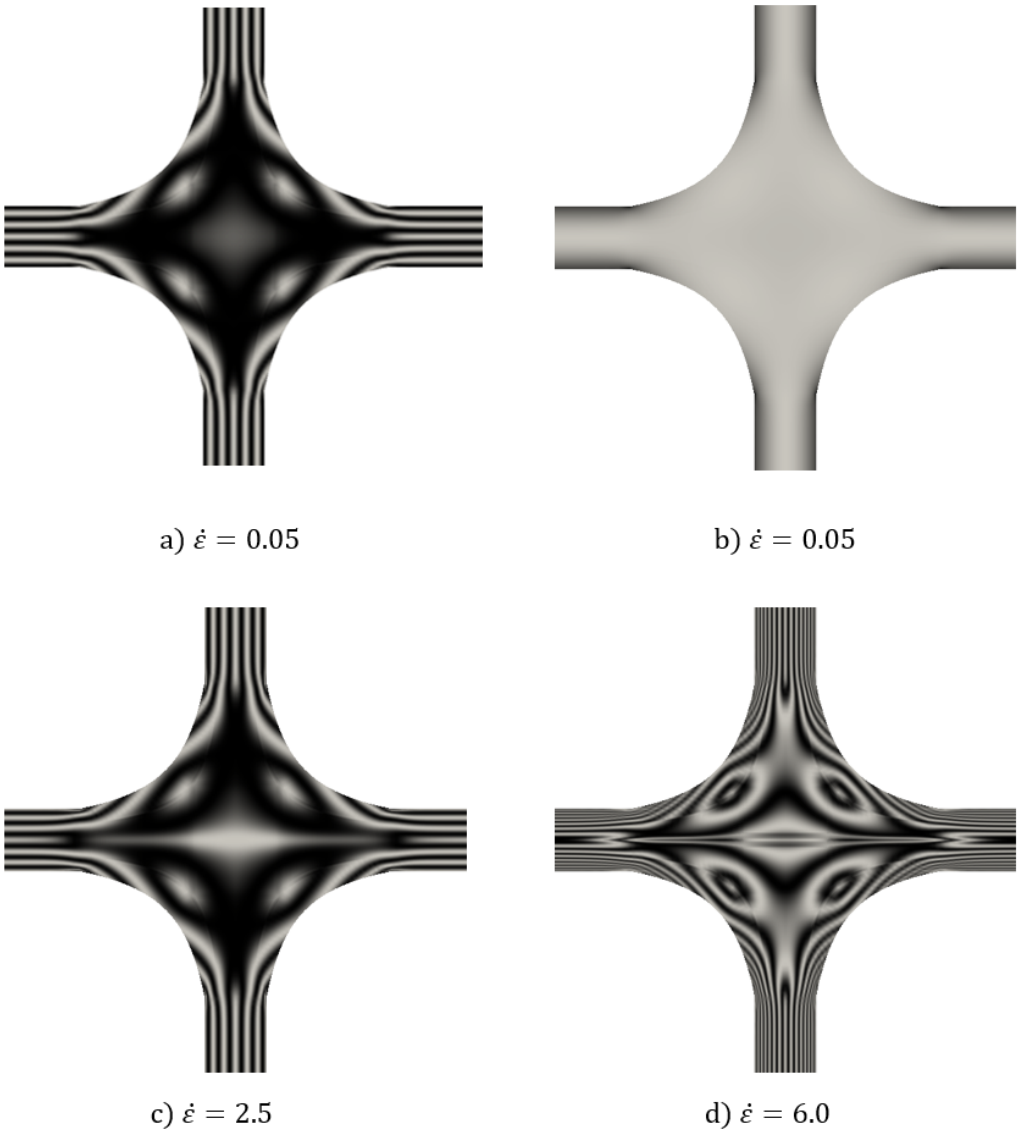

Figure 7.13: The birefringence contour predicted by RDP model for different extension-rate with contour interval 0.5 for figure (b),(c),(d) given $\lambda_{D,L} = 10.0$, $\lambda_{R,L} = 0.2$, $\lambda_{D,S} = 0.1$ and $\lambda_{R,S} = 0.05$. In figure (a) a small contour interval (i.e. 0.03) is used for $\dot{\varepsilon} = 0.05$.

The birefringence contour for different extension-rates are presented in Figure 7.13. Figure 7.13a uses a smaller contour interval of 0.03 compared with 0.5 used in Figures 7.13b,c,d in order to show the stress distribution at this much slower rate. The birefringence pattern predicted by $\dot{\varepsilon} = 0.05$ has four-fold symmetry as the flow is in the slow regime where the fluid is Newtonian. As the extension-rate is increased we observe both an increase in the number of birefringence contours shown by the figure, but also a change in the pattern with the four-fold symmetry lost due to the appearance of the birefringent strand along the

outlet centre-line.

7.5 Effect of coupled and uncoupled blends

This section presents the comparison between the coupled and uncoupled blend models, the RDP and its equivalent mRP model having the same linear rheology. Figure 7.14 shows the extension-rate and stretch for the long-long chain interaction. From the left-hand figure, the extension-rate profile does not show much difference. However, the RDP model has a slightly lower extension-rate at the stagnation point due to its higher resistance to extensional flow. The velocity profile across the upstream and downstream regions as shown in Figure 7.15 also show the same trend, where both regions have slightly lower velocity approaching the centre-line predicted by the RDP model. Both the upstream and downstream regions however show an identical velocity profile.

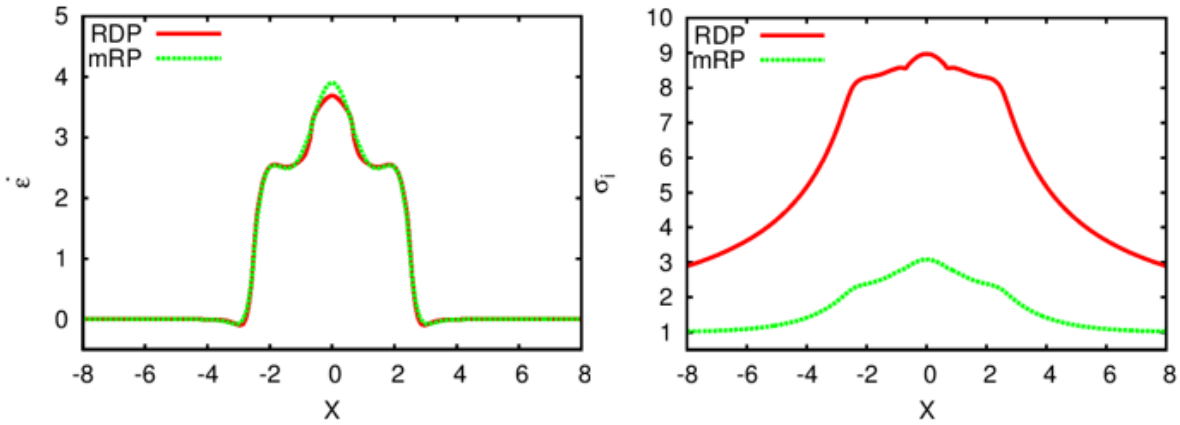

Figure 7.14: The extension-rate and stretch for the long-long interaction predicted by mRP and RDP models for hyperbolic corner length, $L = 2$ given pressure drop imposed $\Delta P = 43.8$ with $\lambda_{D,L} = 10.0$, $\lambda_{R,L} = 0.2$, $\lambda_{D,S} = 0.1$ and $\lambda_{R,S} = 0.05$.

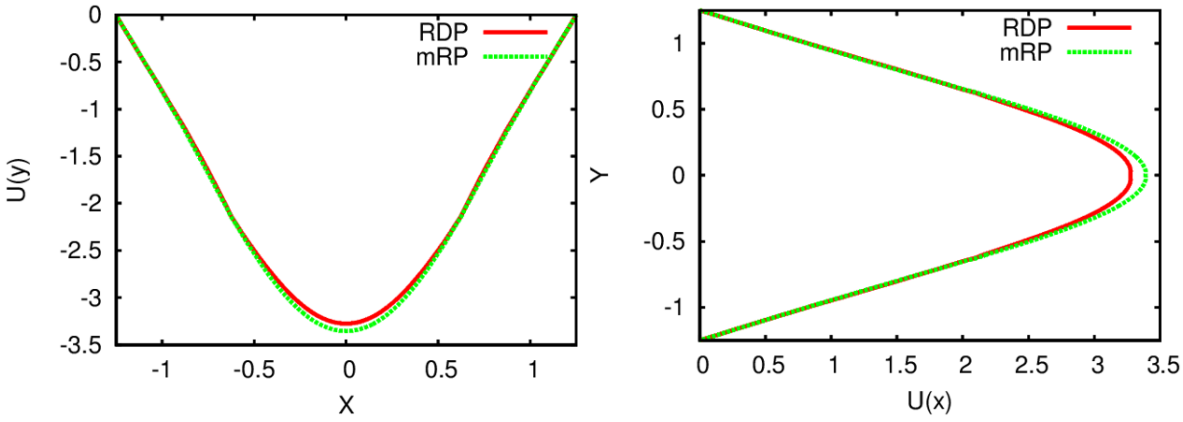

a) At $y = 1$ b) At $x = 1$

Figure 7.15: The velocity profile across the upstream and downstream section for $y = 1$ and $x = 1$ respectively comparing both RDP and mRP models given pressure drop imposed $\Delta P = 43.8$ with $\lambda_{D,L} = 10.0$, $\lambda_{R,L} = 0.2$, $\lambda_{D,S} = 0.1$ and $\lambda_{R,S} = 0.05$.

The stretch in the fat tube formed by the long-long chain interaction in RDP is equivalent to the stretch predicted by the first mode with the longest relaxation time in the mRP model. The stretch along the outlet centre-line predicted by these models are displayed in the right-hand Figure 7.14. The figure reveals that the stretch predicted by the RDP model is three times higher than the mRP model along the centre-line, even though the extension-rate is slightly higher for the mRP model. The enhanced stretch relaxation that is captured by the RDP model explains this prediction. For the mRP model the steady-state stretch in extensional channel flow is given by $\sigma_{M1} < \frac{1}{1-\dot{\varepsilon}\lambda_{R,i}}$, which is similar to that of the thin tube in the RDP model, whereas for the RDP model the stretch is enhanced by a factor of approximately $\phi_L^{-1/2}$. The molecular stretch relaxes beyond the hyperbolic corner. However, in the RDP model this relaxes at the enhanced stretch relaxation rate and so remains stretched along the outlet centre-line in the straight channel region.

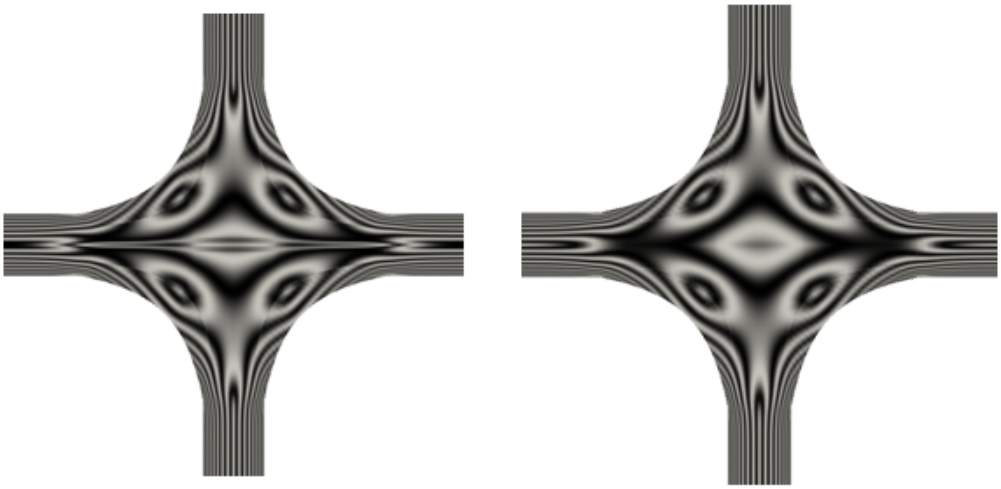

Figure 7.16: The birefringence contour predicted by RDP and mRP model with contour interval 0.5 given pressure drop imposed $\Delta P = 43.8$ with $\lambda_{D,L} = 10.0$, $\lambda_{R,L} = 0.2$, $\lambda_{D,S} = 0.1$ and $\lambda_{R,S} = 0.05$.

Figure 7.16 shows the birefringence contour generated when $\dot{\varepsilon} = 2.5$. The birefringence predicted by both models is almost identical except for the region close to the outlet centre-line. Here, the density of the birefringence contours is higher in the RDP model, compared to the prediction made by the mRP model, with the RDP model showing a birefringent strand that is absent in the mRP model.

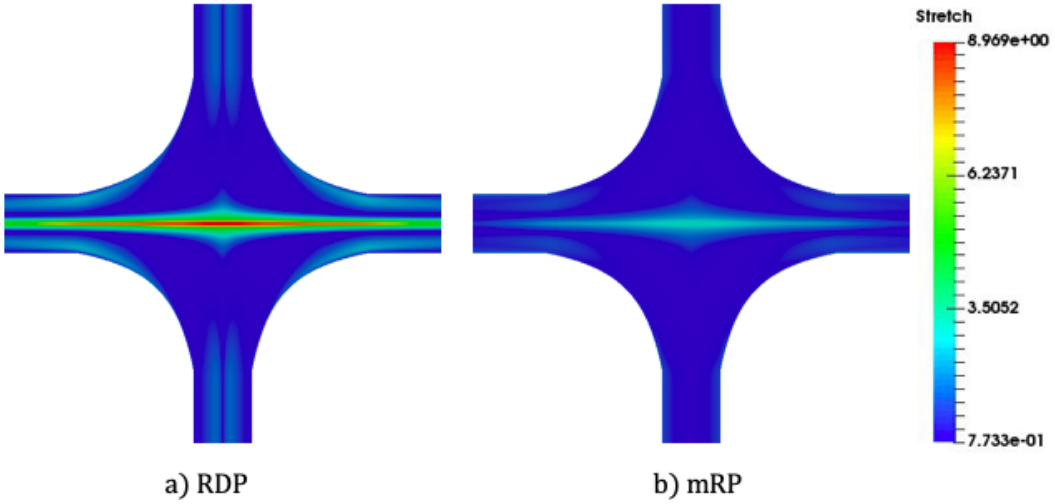

Figure 7.17: The stretch contour of the whole cross-slot for the fat tube predicted by the RDP and mRP model at $\dot{\varepsilon} = 2.5$ given pressure drop imposed $\Delta P = 43.8$ with $\lambda_{D,L} = 10.0$, $\lambda_{R,L} = 0.2$, $\lambda_{D,S} = 0.1$ and $\lambda_{R,S} = 0.05$.

This corresponds to the fat tube stretch field in a cross-slot presented in Figure 7.17 for both RDP and mRP models. No significant stretch is observed within the inlet region of the cross-slot arms. For both models the highest stretch occurs along the outlet centre-line at and downstream of the stagnation point as a result of the strong extensional flow created in this region. However, as shown in Figure 7.14 and Figure 7.17, the enhanced stretch relaxation in the RDP model gives a much greater stretch at this extension-rate than is produced in the mRP model.

7.6 Effect of blend composition in the two-dimensional cross-slot

In this section the results of varying the blend composition in the two-dimensional cross-slot flow are presented. The polymeric viscosity for the short and long chains for the different blends are recorded in Table 7.3 along with the pressure drop required to give a VFR of 4.8.

Table 7.3: Viscosity contribution from the short and long chains for the different blend compositions, together with the pressure drop required to give a VFR of 4.8. The relaxation times are given by $\lambda_{D,L} = 10, \lambda_{R,L} = 0.2, \lambda_{D,S} = 0.1, \lambda_{R,S} = 0.05$.

Blend	ϕ_S	ϕ_L	$\eta_{P,S}$	$\eta_{P,L}$	ΔP
A	0.95	0.05	0.095	0.5	43.8
B	0.9	0.1	0.09	1.0	45.0
C	0.8	0.2	0.08	2.0	47.5

Figure 7.18 shows the extension-rate along the centre-line for the two-dimensional cross-slot with hyperbolic corner length, $L = 2$, for the three different blends. From the figure, the extension-rate at the lower long chain fractions (i.e. $\phi_L = 5\%, 10\%$) do not show much difference within the hyperbolic corner, with the exception of the extension-rate at the stagnation point which is lower for $\phi_L = 10\%$.

The $\phi_L = 20\%$ blend produces a greater modification to the extension-rate and loses the uniformity of the extension-rate in the region of the hyperbolic corner. This is because the proportion of the long chains leads to a more significant modification of the flow along the outlet centre-line due to the enhanced resistance to extensional flow compared to lower ϕ_L.

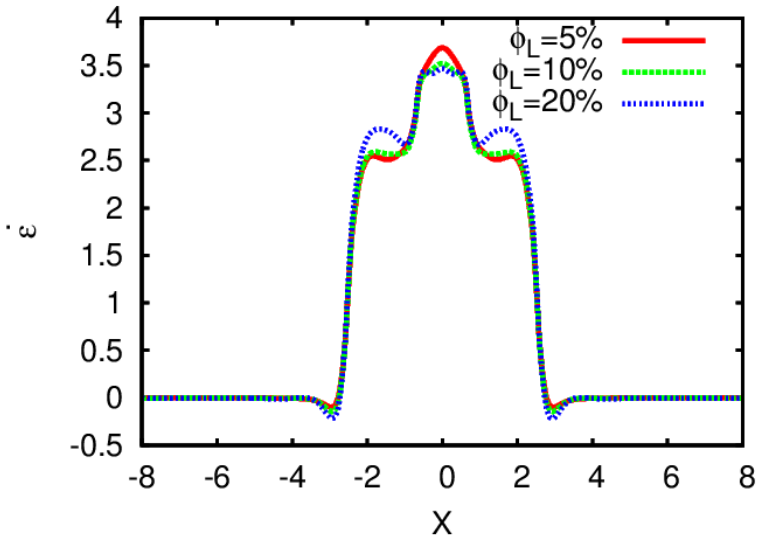

Figure 7.18: The extension-rate predicted by the RDP model along the outlet centre-line of the cross-slot geometry with hyperbolic corner with length, $L = 2$ for different blend compositions flowing with the same volumetric flow-rate of 4.8 when $\lambda_{D,L} = 10, \lambda_{R,L} = 0.2, \lambda_{D,S} = 0.1, \lambda_{R,S} = 0.05$.

Figure 7.19 shows the fat and thin tube stretches along the outlet centre-line. The prediction shows the same trends as found for the hyperbolic contraction flow where the stretch in the fat tube decreases with increasing long chain fraction while the thin tube stretch increases. Decreasing the proportion of long chains enhances the stretch relaxation time in the tube made up of the long-long chain interaction. The details of the discussion are similar to the explanation described in Section 6.5.

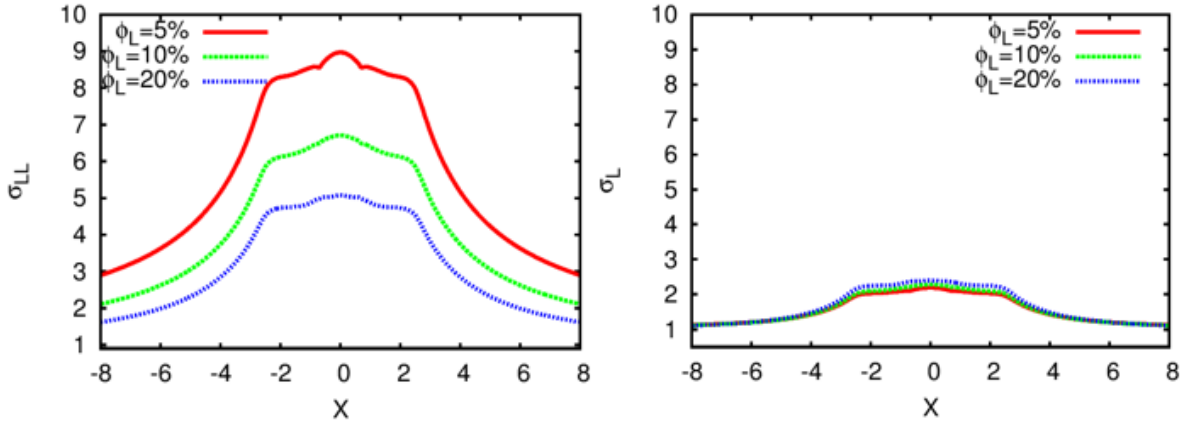

Figure 7.19: The stretch predicted by the RDP model along the centre-line of the cross-slot geometry with hyperbolic corner with length, $L = 2$ for different blend compositions flowing with the same volumetric flow-rate of 4.8 given $\lambda_{D,L} = 10.0$, $\lambda_{R,L} = 0.2$, $\lambda_{D,S} = 0.1$ and $\lambda_{R,S} = 0.05$.

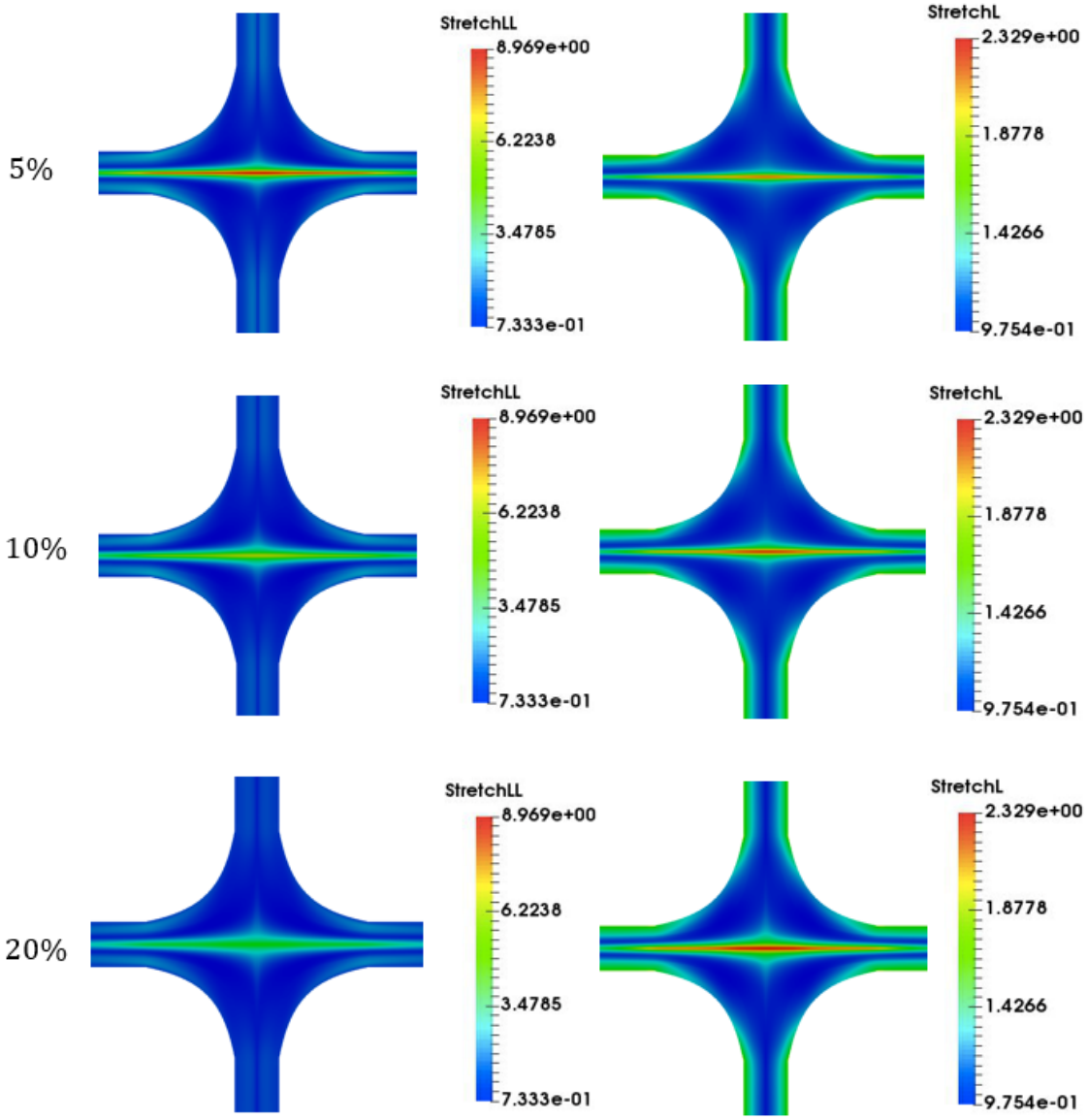

Figure 7.20: The stretch contour for both thin and fat tubes predicted by the RDP model for different blend compositions when $\lambda_{D,L} = 10, \lambda_{R,L} = 0.2, \lambda_{D,S} = 0.1, \lambda_{R,S} = 0.05$.

The distribution of stretch in both the fat and thin tubes within the cross-slot for the different blend compositions are presented in Figure 7.20. The trend of the stretch in both fat and thin tubes can be clearly be seen as the blend composition is increased (going down the figure). Looking at the cross-section of the outlet channel we observe a different distribution of stretch between the two tubes. In the fat tube it is observed that the stretch is concentrated at the centre-line due to the strong elongational flow in this region. Away from the centre-line, the stretch first decreases and then increases again. However, near the wall, the stretch is low. In contrast the maximum thin tube stretch in this region is

generated at the wall of the geometry due to the shear flow.

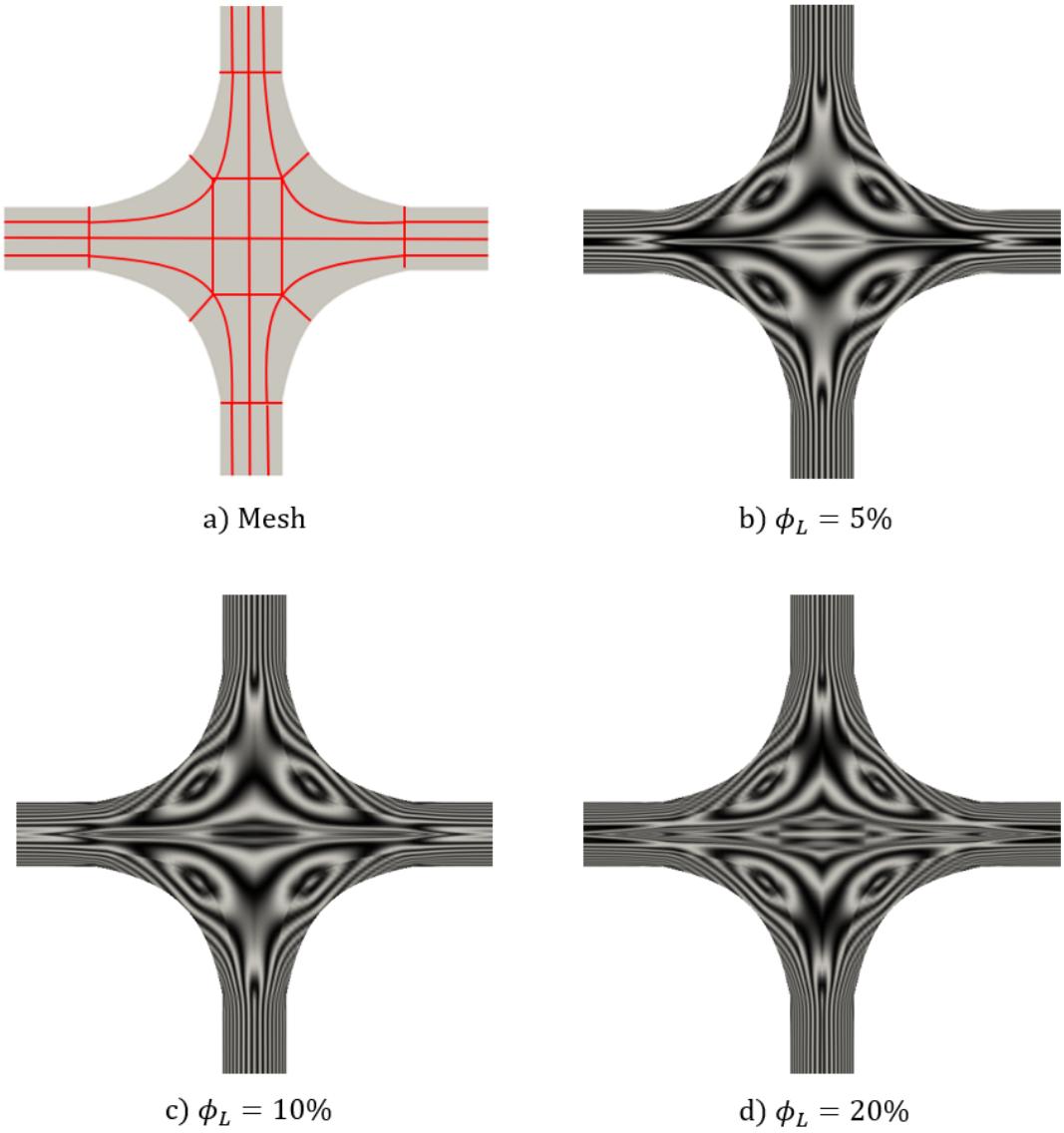

Figure 7.21: The birefringence contour predicted by the RDP model for different volume fractions with contour interval 0.5 with the same VFR of 4.8 when $\lambda_{D,L} = 10, \lambda_{R,L} = 0.2, \lambda_{D,S} = 0.1, \lambda_{R,S} = 0.05$.

Figure 7.21 shows the simulated birefringence contours generated by different blends. Note that, the density of the stress fringes is increasing in line with the increase of the long chain concentration. The significant difference of the birefringence contour is observed around the outlet centre-line region, where the stress generated at the stagnation point is advected downstream.

7.7 Hyperbolic contraction flow versus cross-slot flow

In this section, the comparison between hyperbolic contraction (one-dimensional flow) and cross-slot (two-dimensional flow) is presented. The main difference between these flows is the presence of the stagnation point at the centre of the cross-slot, which provides a point of infinite residence time.

The flow rates in the two devices are adjusted to give the same extension-rate, $\dot{\varepsilon} = 2.5$ within the hyperbolic region, with contraction length, $L = 5$, for hyperbolic contraction flow (HCF) and contraction length corner, $L = 2$, for cross-slot flow (CSF) as these give similar lengths of extensional flow along the centre-line. However the transit time for a polymer through these devices is quite different. The schematic diagram for both flows is presented in Figure 7.22.

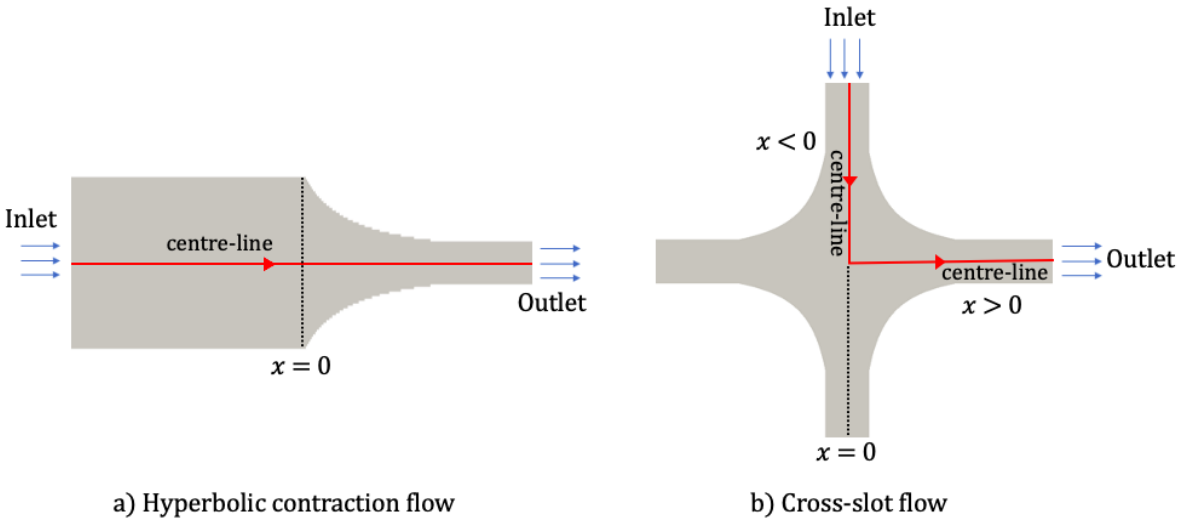

Figure 7.22: The schematic diagram for hyperbolic contraction flow and cross-slot flow with the flow direction.

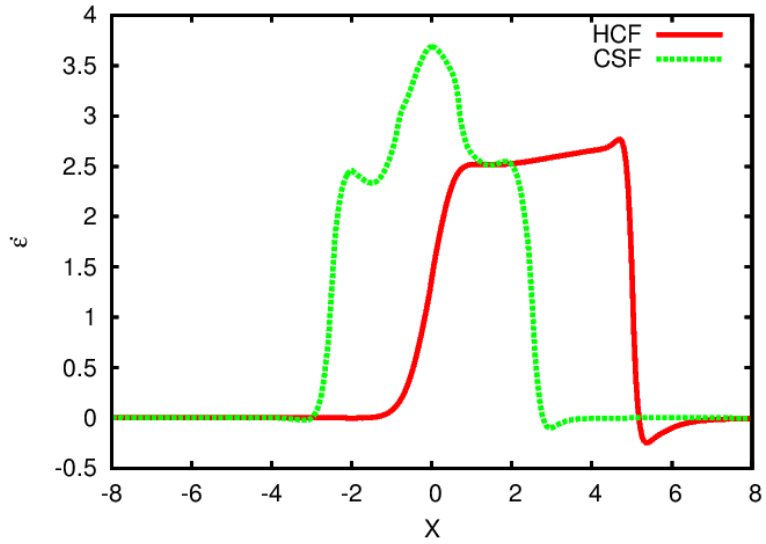

Figure 7.23: The extension-rate along the centre-line for one-dimensional flow (HCF) with two-dimensional flow (CSF) with pressure drop, $\Delta P = 256$ and $\Delta P = 43.8$ respectively to give $\dot{\varepsilon} \approx 2.5$ within the hyperbolic region when $\lambda_{D,L} = 10, \lambda_{R,L} = 0.2, \lambda_{D,S} = 0.1, \lambda_{R,S} = 0.05$.

Figure 7.23 presents the strain-rate profile along the centre-line. Note that, the value $x = 0$ is the beginning of the contraction for hyperbolic contraction flow while in cross-slot flow, it is the centre of the geometry where the stagnation point is defined. In order to show the extension-rate and stretch upstream of the stagnation point for the cross-slot, negative values correspond to points on the $y-$axis rather than the negative $x-$axis. This is shown in Figure 7.22b. There is a slight asymmetry in the extension-rate between the inlet and outlet centre-line observed in Figure 7.23 for CSF as a consequence of the polymeric stresses.

In the HCF, the flow accelerates through the contraction with extension-rate gradually increasing beyond $x = 0$ and achieving an almost extension-rate from about $x = 0.3$ within the contracting region.

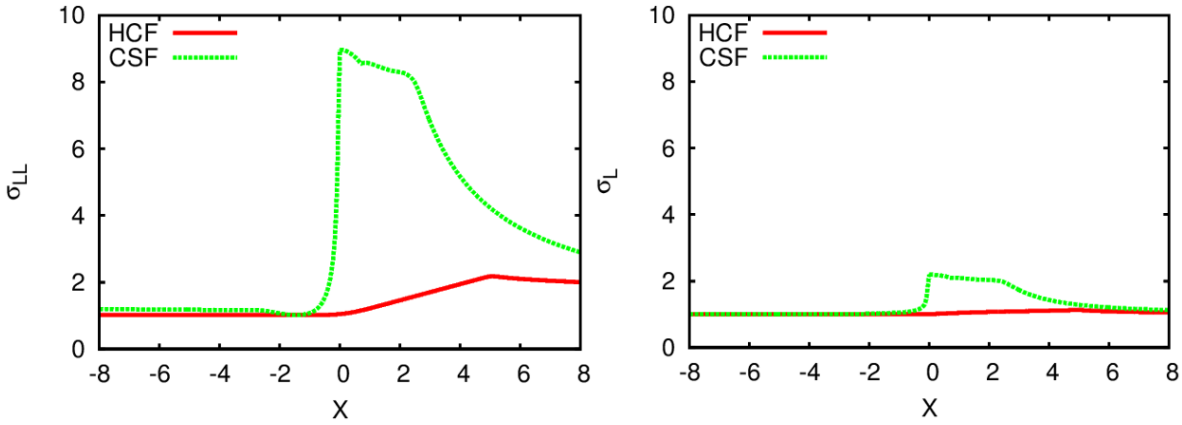

Figure 7.24: The stretch for the fat (LHS) and thin (RHS) tubes along the centre-line for one-dimensional flow (HCF) and two-dimensional flow (CSF) with $\dot{\varepsilon} = 2.5$ when $\lambda_{D,L} = 10, \lambda_{R,L} = 0.2, \lambda_{D,S} = 0.1, \lambda_{R,S} = 0.05$.

In Figure 7.24, the stretch in the fat and thin tube for both flow cases are presented. For the HCF, the thin and fat tubes are unstretched in the upstream channel and gradually stretch within the contraction before the stretch relaxes in the straight downstream channel (note that velocity in this downstream channel is 4 times that of the upstream channel).

In CSF, there is a rapid increase in both the thin and fat tube stretch approaching the stagnation point. Along the outlet centre-line, the stretch in both tubes is the highest at the stagnation point and relaxes downstream as the extension-rate reduces before relaxing further once it reaches the downstream channel. The main difference between these two geometries is that in the CSF, the residence time in the neighbourhood of the stagnation point is sufficient for the polymers to achieve their equilibrium stretch, whereas the HCF measures the transient growth of stretch.

7.8 Effect of cross-slot depth in the three-dimensional cross-slot

So far we have assumed that the cross-slot is sufficiently deep that flow in the centre is unaffected by the presence of side-walls. In this section, the effect of the presence of side-wall in a three-dimensional cross-slot flow is presented. The hyperbolic corner with length, $L = 2$, is used and with the channel half-depth, given by $d = 0.25, 0.5, 1.0, 2.0$ where $d = D/2$ is the channel depth measured from the centre-line to the side-wall. Figure 7.25 shows the

velocity profile across a quarter domain of the cross-slot. The centre-line for the $x-$ and $y-$direction with the channel depth, D is also shown in this figure.

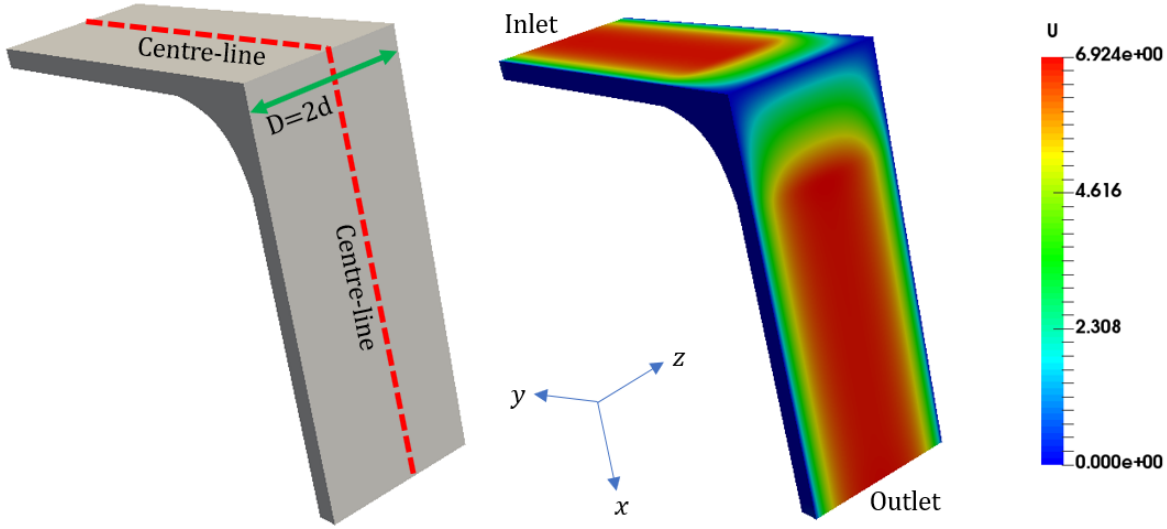

Figure 7.25: The quarter domain for the three-dimensional cross-slot taken from the first quadrant that has been tilted to illustrate the velocity field across the channel depth, $D = 2d$ given pressure drop, ΔP=43.8 when $\lambda_{D,L} = 10, \lambda_{R,L} = 0.2, \lambda_{D,S} = 0.1, \lambda_{R,S} = 0.05$ for $D = 4$ that is $d = 2$.

Figure 7.26 shows the velocity profile along the centre-line on the centre-plane when $y = 0$ and $z = d$, at a pressure drop ΔP=43.8. Comparing the velocity as a function of channel depth, the slowest flow is observed for the cross-slot with the smallest depth, $d = 0.25$. This is to be expected as the smallest depth restricts the motion of the fluid through the slot and the cross-stream flow. This leads to a reduction in the extension-rate both at the stagnation point and downstream.

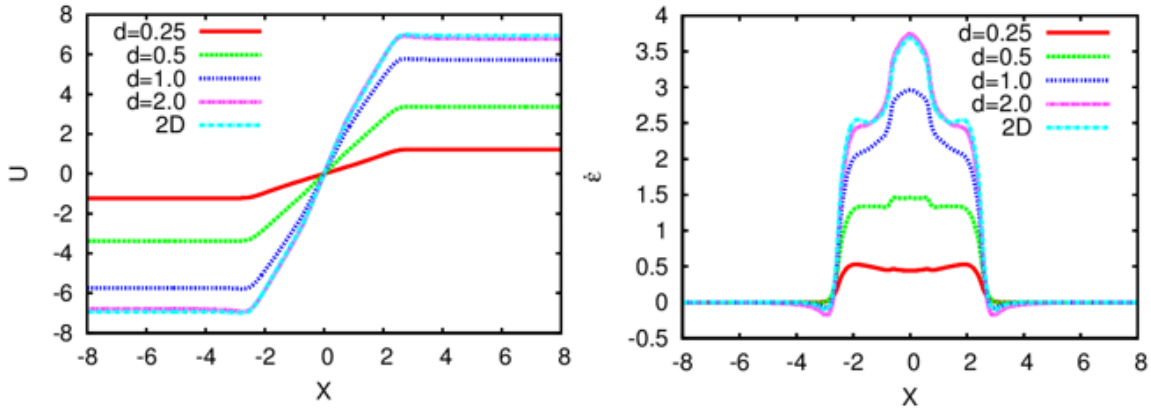

Figure 7.26: The influence of the channel depth in a three-dimensional cross-slot flow for the velocity and the extension-rate along the centre-line given $\lambda_{D,L} = 10.0, \lambda_{R,L} = 0.2, \lambda_{D,S} = 0.1$ and $\lambda_{R,S} = 0.05$ with 5% long chain concentration with $\Delta P = 43.8$.

The effect of the presence of the side-wall reduces as the channel depth increases and the prediction approaches the two-dimensional numerical approximation for $d = 2$.

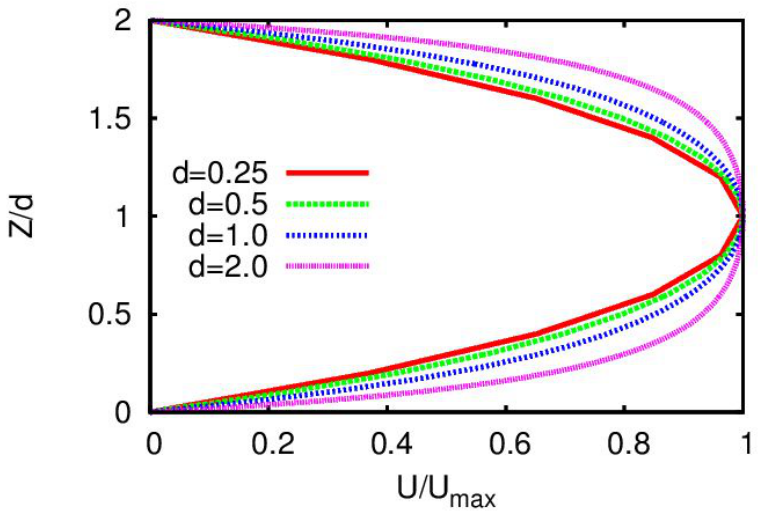

Figure 7.27: The cross-section in z-direction from the wall of the front plane to wall of the back plane in the half-way downstream region ($x = 6.25$) for three-dimensional cross-slot flow when $\lambda_{D,L} = 10.0, \lambda_{R,L} = 0.2, \lambda_{D,S} = 0.1$ and $\lambda_{R,S} = 0.05$ for 5% long chain concentration with $\Delta P = 43.8$.

Figure 7.27 shows the velocity profile across the channel in the $z-$direction for the different channel depths. The channel with smaller depths show a parabolic velocity profile indicating the influence of the presence of the side walls that disturbs the flow moving in the $x-$direction. The blunted velocity profile towards the centre-line, shown by depth $d = 2.0$, indicates this depth is wide enough for the effects of the side walls on the flow along the

centre-plane to be neglected.

7.9 Conclusion

In this chapter, the behaviour of the RDP model in a cross-slot geometry with a hyperbolic corner is studied. Several relevant effects are investigated including the geometrical effects of hyperbolic corner length and presence of side walls, as well as the effects of blend composition and differences from the uncoupled mRP model. Overall the results presented in this chapter show the same trend as discussed in Chapter 6 for the hyperbolic contraction flow.

The differences between the hyperbolic contraction flow and the cross-slot flow measured at the same extension-rate arise from the difference in residence times along the centre-line of the geometries. The presence of the stagnation point in a cross-slot geometry produces significantly higher stretch than the hyperbolic contraction geometry, even though the same extension-rate is applied, as the increased residence time allows the polymers to achieve their steady-state extension.

The resulting high polymeric stresses, both at the stagnation point and along the outlet centre-line, result in a loss of the four-fold symmetry in the flow birefringence distribution. However in all the cases shown in this chapter the flow and stress pattern remain symmetric about reflections in the x and y axes. For some constitutive equations for polymer solutions, such as Oldroyd-B and FENE-P it is found [35], [123] that the flow loses this reflectional symmetry above a critical Deborah number. In the next chapter, we investigate whether this can also happen for the RP and RDP models.

Chapter 8

The bifurcation of the flow in a cross-slot geometry

This chapter examines whether the flow bifurcation in a two-dimensional cross-slot geometry, found for the UCM and Oldroyd-B models for polymer solutions, are also seen for the single-mode Rolie-Poly [57] and RDP [23] constitutive models which better represent entangled polymer melts. At the beginning of the chapter, the simulation approach used in this work (i.e. the pressure ramping protocol as a boundary condition for pressure at the inlet) is validated against the published results [35] for UCM and Oldroyd-B [103] constitutive models. This is then followed by the results for the Rolie-Poly and RDP model with the discussion of relevant effects in both models to determine the critical Deborah number for the onset of this flow bifurcation. This includes the effect of varying stretch relaxation time, λ_R, in a single-mode Rolie-Poly model. In the RDP model, the comparison between different blend compositions of the long chain is presented.

8.1 Motivation

The steady-state flow bifurcation of the flow of a polymeric solution through a cross-slot was first reported by Arratia et al. [8] experimentally when comparing the flow of a Newtonian fluid with a polyacrylamide polymer solution at low Reynolds number through a microfluidic cross-channel flow. They found a spatial symmetry breaking bifurcation for the flow of the

polymer solution above a critical Deborah number. This experimental finding inspired Poole et al. [115] to investigate this flow numerically. They found that the asymmetric transition of the flow could be predicted for the UCM model in the absence of inertia. Rocha et al. [123] extended this work to consider the FENE-CR and FENE-P models to look at the effect of the finite extensibility and the concentration of the polymer. They also compared a cross-slot with sharp and rounded corners and reported that the influence of the rounded corner is not significant. They reported that the critical Deborah number decreases at higher finite extensibility and as the polymer viscosity increases. Cruz et al. [35] further extended the study of this flow bifurcation for different viscoelastic models that include the UCM, Oldroyd-B, [103] and PTT model [111] to determine the critical Deborah number. They suggested the prediction of this flow bifurcation as a new viscoelastic numerical benchmark flow problem. Pimenta and Alves [113] subsequently provided the cross-slot flow as a tutorial example in the RheoTool toolbox and solve the problem using the `rheoFoam` solver for a velocity driven flow where the fixed value of the velocity is used at the inlet of the geometry for the UCM model.

This flow bifurcation has not been studied for tube theory based constitutive models such as Rolie-Poly and RDP models. Moreover experiments on polymer melts, such as those of Auhl et al. [10], do not report this flow bifurcation. The cross-slot with a sharp corner will only be considered in this chapter since the cross-slot with rounded corner does not give significant changes to the prediction as reported in Rocha et al. [123] and Cruz et al. [35]. Different from the approach used in the literature, pressure boundary conditions are used here, where the boundary conditions specified are similar to Table 7.1.

8.2 Validation with published results

The simulations and pressure ramping approach used in this work are validated against the published results [35] by reproducing the prediction of flow bifurcation for the UCM model (viscosity ratio, $\beta = 0.0$) and Oldroyd-B model with $\beta = 1/9$ and fluid relaxation time for both models is $\lambda = 0.33$. The validation is made by calculating the bifurcation parameter, DQ [115] against Deborah number.

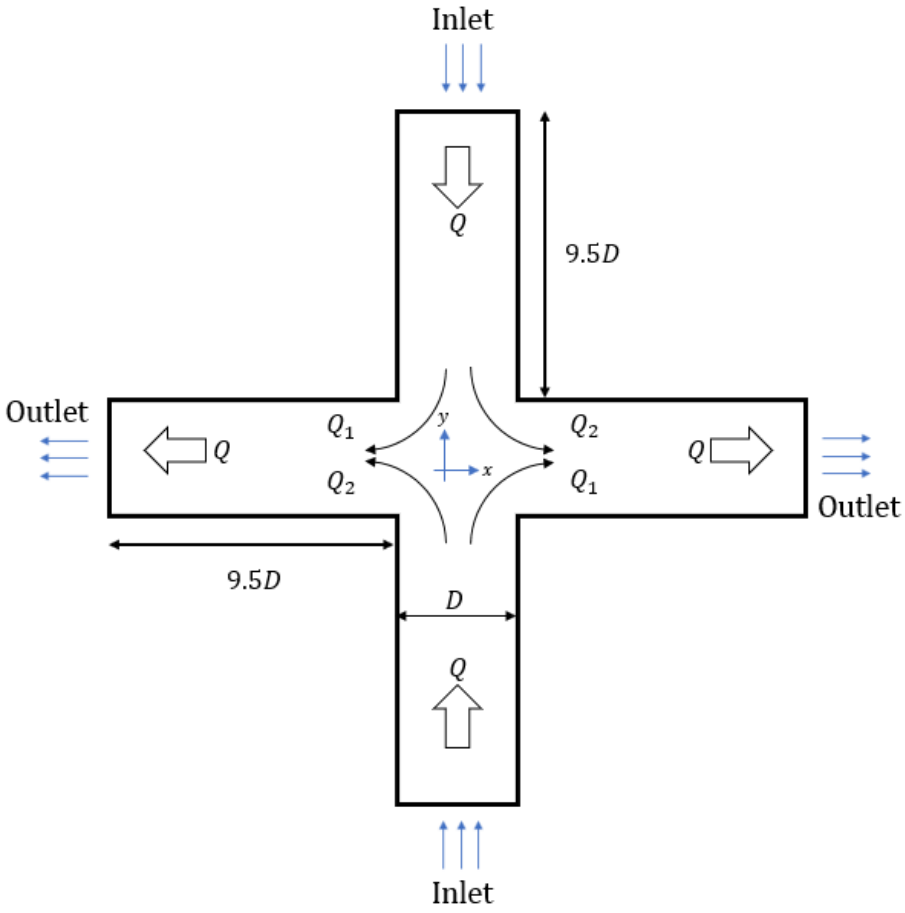

Figure 8.1: The cross-slot geometrical definition with flow-rate.

This parameter indicates the degree of the asymmetry of the flow and is defined as DQ= $\frac{Q_2-Q_1}{Q}$ where $Q = Q_1 + Q_2$ is the total flow rate in each arm of the cross-slot and Q_1 and Q_2 as indicated from Figure 8.1 is the flow rate in the left-hand outlet channel originating from the top and bottom inlets respectively. The Deborah number is defined as De= $\lambda U/D = \lambda Q/D^2$ where λ is the fluid relaxation time and $D = 1$ is the channel width. A value DQ=0.0 indicates the symmetric flow of Chapter 7. On the other hand, when the flow is fully bifurcated, DQ=$\pm$1.0 indicates that all the flow from one inlet goes through the same outlet.

Note that due to the symmetry of the geometry the bifurcation can happen in either direction so DQ can be both positive and negative. An example of how this bifurcation appears in the velocity colour plot for the UCM model is presented in Figure 8.2 showing how the asymmetry develops as the Deborah number is increased. From the figure, we can see the steady transition of the flow up to De=0.330. Notice that this change takes place

over a small range of Deborah numbers.

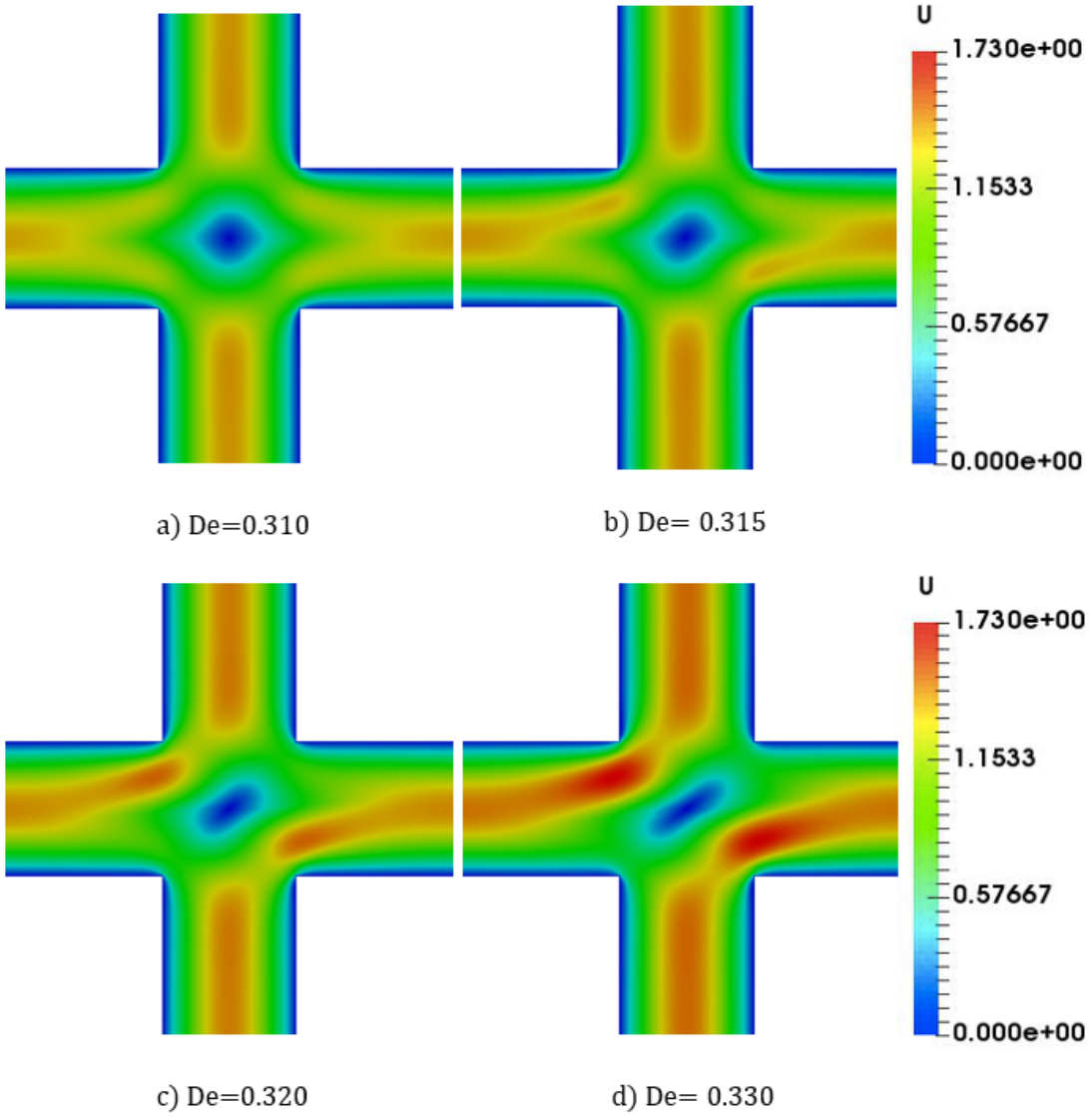

Figure 8.2: The steady-state flow transition from symmetry (De=0.310) to highly asymmetric case (De=0.330) for the UCM model when $\lambda = 0.33$.

Next, a numerical comparison between the published results and the current work are presented in Table 8.1 and 8.2 recording the bifurcation parameter value, DQ, as a function of Deborah number for UCM and Oldroyd-B models respectively.

Table 8.1: The UCM model data for Deborah number with bifurcation parameter, DQ [115] at different Deborah number comparing current work with published results [35].

De	DQ-Cruz et al. [35]	DQ-Current work
0.000	0.000	0.000
0.100	0.000	0.000
0.200	0.000	0.000
0.300	0.000	0.000
0.305	0.000	0.000
0.310	0.000	0.000
0.315	0.138	0.110
0.320	0.270	0.247
0.330	0.415	0.402

Table 8.2: The Oldroyd-B model data with $\beta = 1/9$ at different Deborah number comparing current work with published results [35].

De	DQ-Cruz et al. [35]	DQ-Current work
0.000	0.000	0.000
0.100	0.000	0.000
0.200	0.000	0.000
0.300	0.000	0.000
0.340	0.000	0.000
0.345	0.000	0.000
0.350	0.000	0.000
0.355	0.000	0.003
0.360	0.000	0.056
0.370	0.221	0.201
0.380	0.381	0.352
0.400	0.550	0.521
0.420	0.653	0.628

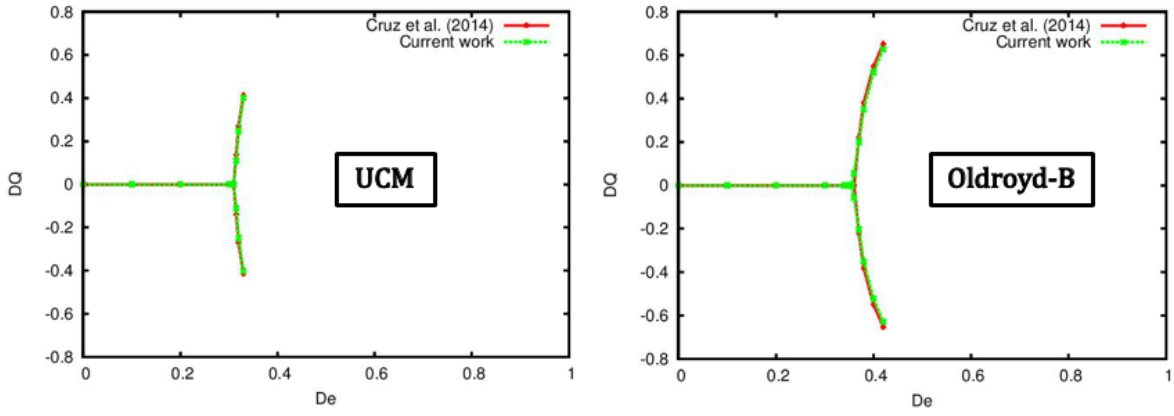

Figure 8.3: Bifurcation pattern for the Oldroyd-B and UCM follows the trend presented in the published article [35].

The calculations were performed using the mesh shown in Figure 8.4 which is similar to the mesh used in the tutorial example. This mesh has 14 841 hexahedral cells with 51 cells across the channel. The odd number of cells is chosen so that the stagnation point, where the local Weissenberg number at this point is evaluated, lies at the centre of a cell.

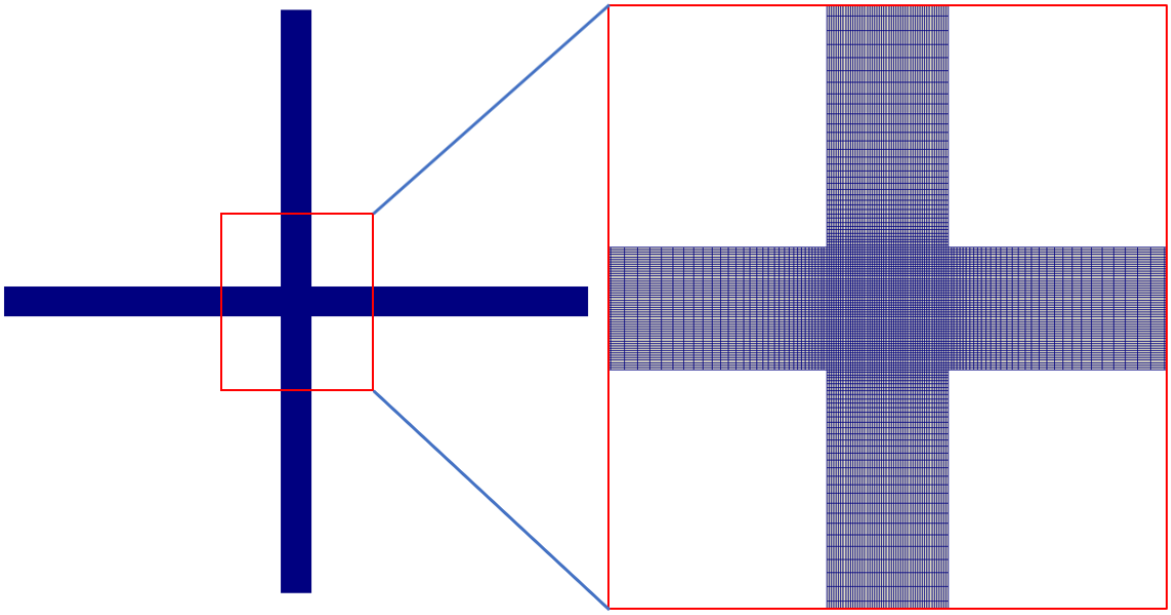

Figure 8.4: The 14 841 cell mesh used for the simulations.

The number of cells used by Cruz et al. [35] is 12 801 and is similar to the number 14 841 used here. Figure 8.3 shows a good agreement between the prediction made by both approaches. The slight difference of the prediction between the published data and current work data may be a consequence of differences in the numerical scheme, such as the stress-velocity coupling in the `rheoFoam` solver introduced by Pimenta and Alves [113] in order to improve the numerical stability.

8.3 The flow bifurcation for the RP model

In this section, the monodisperse Rolie-Poly model is considered where the influence of the ratio of the stretch and reptation relaxation times on the symmetry breaking flow is observed. The local Weissenberg number as a function of Deborah number is also presented and discussed.

8.3.1 Effect of varying relaxation time

As the RP model has two different relaxation times for stretch and orientation there are two possible definitions for the Deborah number. On the assumption that the bifurcation is associated with chain stretch the Deborah number is defined as De= $\lambda_R Q/D^2$. Other parameters are set to $\beta^* = 0.0$ and solvent viscosity ratio, $\beta = 1/9$. This ratio is inversely proportional to the number of entanglements, so is small for a highly entangled melt and approaches unity for unentangled chains. Note that, the dimensionless local Weissenberg number is measured at the stagnation point and is defined as $\mathrm{Wi}_0 = \lambda^{**}\dot{\varepsilon}$, where $\lambda^{**} = \lambda_R/\lambda_D$ (or $\lambda^{**} = 1/3Z$) given $\lambda_D = 1.0$ and the expression for $\dot{\varepsilon}$ is defined in equation (8.2). Table 8.3 records the data for the single-mode Rolie-Poly model with different relaxation times for De ≤ 1.599.

Table 8.3: The single-mode Rolie-Poly model data for a cross-slot with different relaxation time ratios, λ^{**} with $\beta = 1/9$. Osc stands for unsteady oscillatory flow.

$\lambda^{**} = 0.2$			$\lambda^{**} = 0.4$			$\lambda^{**} = 0.6$		
De	Wi_0	DQ	De	Wi_0	DQ	De	Wi_0	DQ
0.000	0.000	0.000	0.000	0.000	0.000	0.000	0.000	0.000
0.092	1.097	0.000	0.150	1.168	0.000	0.197	1.192	0.000
0.150	1.645	0.000	0.263	1.652	0.000	0.298	1.613	0.000
0.215	2.143	0.000	0.332	2.045	0.000	0.412	1.936	0.000
0.281	2.569	0.000	0.431	2.333	0.000	0.530	2.158	0.000
0.348	2.920	0.000	0.725	2.768	0.000	0.649	2.304	0.000
0.414	3.200	0.000	0.818	2.833	0.000	0.707	2.356	0.000
0.447	3.318	0.000	0.908	2.878	0.000	0.765	2.399	0.003
0.480	3.421	0.000	0.952	2.895	0.000	0.774	2.435	0.052
0.544	3.594	0.000	0.978	2.904	0.000	0.780	2.550	0.120
0.607	3.729	0.000	0.995	2.910	0.000	0.804	2.739	0.197
0.668	3.835	0.000	1.012	2.915	0.000	0.818	2.901	0.247
0.728	3.917	0.000	1.038	2.922	0.001	0.832	3.035	0.281
0.780	3.982	0.000	1.046	2.924	0.002	0.846	3.167	0.310
0.958	4.105	0.000	1.054	2.928	0.006	0.850	3.200	0.312
1.171	4.176	0.000	1.063	2.948	0.019	0.860	3.297	0.334
1.222	4.185	0.000	1.071	2.970	0.027	0.874	3.422	0.356
1.322	4.196	0.000	1.079	2.993	0.035	0.888	3.541	0.376
1.418	4.202	0.000	1.097	3.038	0.042	0.902	3.659	0.393
1.512	4.203	0.000	1.113	3.114	0.052	0.916	3.772	0.409
1.599	Osc	Osc	1.131	3.200	0.070	0.959	Osc	Osc
-	-	-	1.147	3.267	0.081	-	-	-
-	-	-	1.164	3.331	0.091	-	-	-
-	-	-	1.204	Osc	Osc	-	-	-

In Figure 8.5, we plot the bifurcation parameter against the Deborah number for different λ^{**}. The results from the table and graph reveal that the onset of asymmetric flow is not purely a function of the stretch relaxation time, but depends also on the relaxation time ratio. For $\lambda^{**} = 0.2$ the flow remains symmetric up to De=1.512 before the oscillatory flow is observed at De=1.599 which is the highest Deborah number considered.

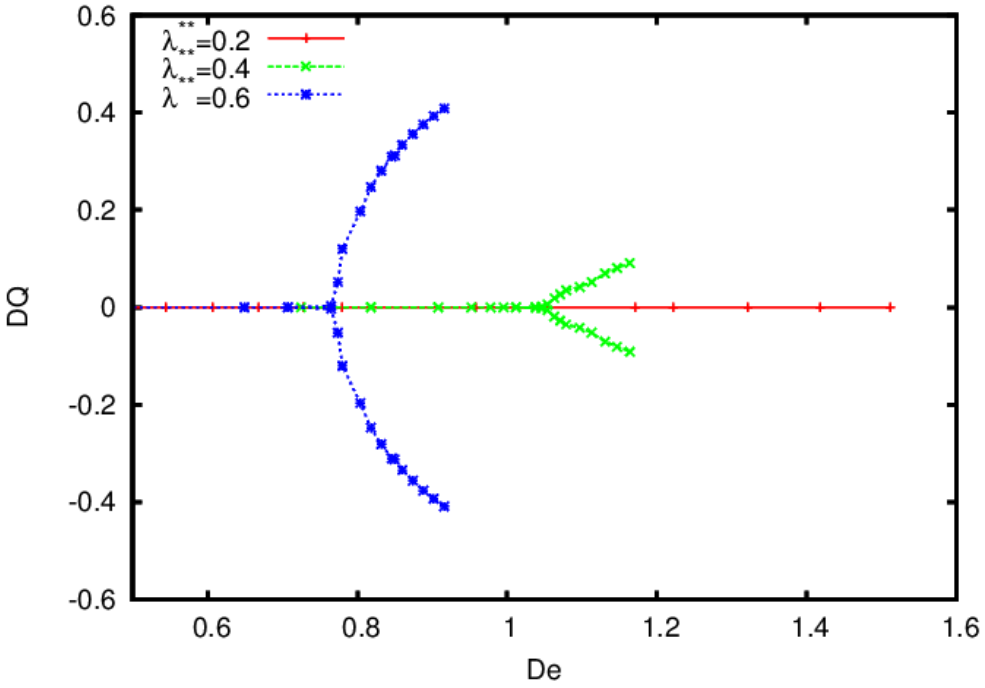

Figure 8.5: Bifurcation pattern for the single-mode RP model with different stretch relaxation time.

The emergence or the onset of the flow asymmetry for $\lambda_R = 0.4\lambda_D$ is observed to start at critical Deborah number $\mathrm{De}_{cr} = 1.038$ becoming more obvious at De=1.063 and above. For $\lambda_R = 0.6\lambda_D$, the steady symmetry breaking flow is observed above a critical Deborah number $\mathrm{De}_{cr} = 0.75$. Here, the asymmetric flow is more obvious with maximum splitting of the flow, DQ=0.409, before the simulation fails to converge at De=0.959. Thus as λ^{**} increases we find that the critical Deborah number decreases and the rate at which DQ grows with Deborah number increases.

Here, the Deborah number is based on the volumetric flow-rate rather than the strain-rate at the stagnation point, so we can instead define a local Weissenberg number based on the strain-rate at the stagnation point. When the flow is symmetric the strain-rate is given by $\dot{\varepsilon}_0 = (\partial u/\partial x)|_0 = -(\partial v/\partial y)|_0$. However, once the flow becomes asymmetric the velocity gradient will no longer be diagonal. The local strain-rate for a general two-dimensional incompressible flow is given by the

$$\mathbf{D} = \begin{pmatrix} \frac{\partial u}{\partial x} & \frac{1}{2}(\frac{\partial u}{\partial y} + \frac{\partial v}{\partial x}) \\ \frac{1}{2}(\frac{\partial v}{\partial x} + \frac{\partial u}{\partial y}) & \frac{\partial v}{\partial y} \end{pmatrix} = \begin{pmatrix} a & b \\ b & -a \end{pmatrix} \tag{8.1}$$

where $a = \frac{\partial u}{\partial x} = -\frac{\partial v}{\partial y}$ and $b = \frac{1}{2}(\frac{\partial u}{\partial y} + \frac{\partial v}{\partial x})$. Taking the positive eigenvalue, $\dot{\varepsilon}$, of equation (8.1), we have

$$\dot{\varepsilon}_0 = \frac{1}{2}\sqrt{\left[\left(\frac{\partial u}{\partial x}\bigg|_0 - \frac{\partial v}{\partial y}\bigg|_0\right)^2 + \left(\frac{\partial u}{\partial y}\bigg|_0 + \frac{\partial v}{\partial x}\bigg|_0\right)^2\right]}. \tag{8.2}$$

which gives a scalar measure of the strain-rate. Note that this is different from the definition used by Cruz et al. [35] who used the velocity gradient rather than the strain-rate to determine Weissenberg number.

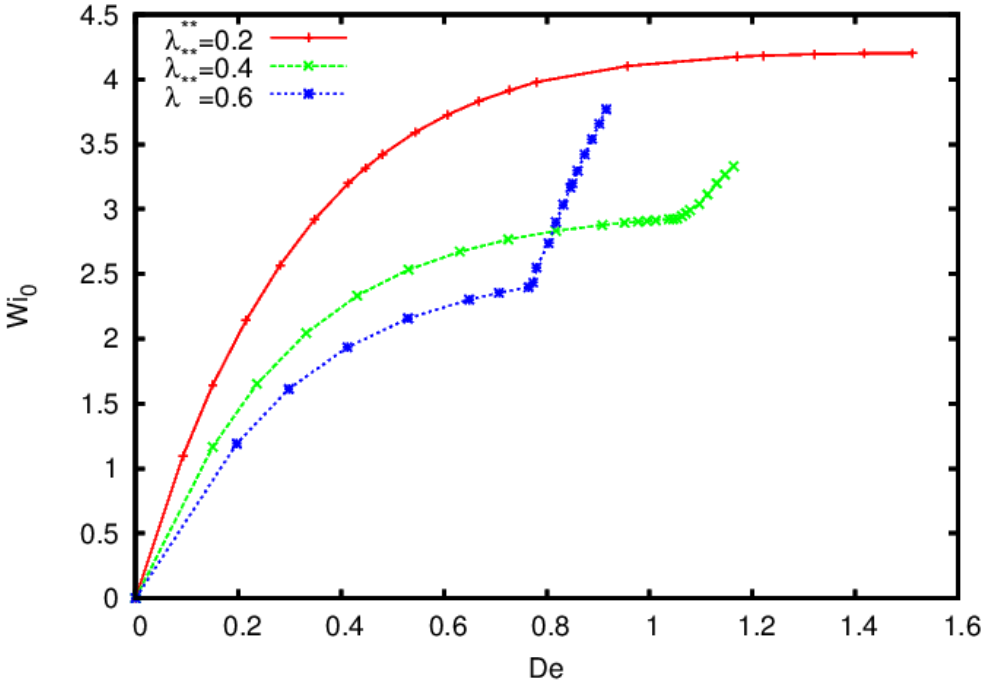

Figure 8.6: The Weissenberg number as a function of Deborah number, calculated as the product of the stretch relaxation time and strain-rate at the stagnation point for the Rolie-Poly model with $\beta = 1/9$.

In Figure 8.6, the local (stretch) Weissenberg number is plotted as a function Deborah number. As the Deborah number increases the rate of increase of the Weissenberg number with Deborah number decreases as the extensional stresses generated at the stagnation point modify the flow to reduce the extension-rate there. However, at the point where the flow becomes asymmetric there is a change in gradient with the Weissenberg number increasing more rapidly with strain-rate.

In summary, for the RP model we only observe flow asymmetry when the stretch and orientation relaxation times are similar, which is the limit of unentangled chains. This would

explain why the flow bifurcation is found experimentally for polymer solutions but has not been reported for polymer melts.

8.4 The bifurcation of the RDP model

The bidisperse RDP model is considered in this section where the effect of the varying long chain fraction on the flow bifurcation is investigated. The results of the previous section for the RP model found that flow bifurcations were only seen when the ratio of the stretch to orientation relaxation times was of order unity. One key property of the RDP model is that the effective stretch relaxation time is enhanced by dilution of the long chains, which raises a question as to whether this affects the onset of flow bifurcation. The local (stretch) Weissenberg number measured at the stagnation point as a function of Deborah number and stretch for both thin and fat tubes are presented and discussed.

8.4.1 The effect of varying concentration

Table 8.4, 8.5 and 8.6 record the data for local Weissenberg number that is obtained from the stretch relaxation time of the long chain and the bifurcation parameter over Deborah number for different mesh refinements (coarser to finer) and different long chain fractions i.e. $\phi_L = 5\%$, $\phi_L = 10\%$ and $\phi_L = 20\%$ respectively. The number of element in the coarser mesh (M1) is 14 841 cells, medium (M2) is 28 045 cells and finer (M3) is 45 045 cells. While the long chain fraction, ϕ_L is varying, other parameters are set as in previous chapters to $\lambda_{D,L} = 10$, $\lambda_{R,L} = 0.2$, $\lambda_{D,S} = 0.1$, $\lambda_{R,S} = 0.05$, $\beta^* = 0.0$, and $\eta_S = 0.01$ with the Deborah and Weissenberg numbers based on $\lambda_{R,L}$.

Table 8.4: The bidisperse RDP model data for a cross-slot with long chain fraction ϕ_L=5% for different mesh resolutions.

ΔP	M1			M2			M3		
	De	DQ	Wi_0	De	DQ	Wi_0	De	DQ	Wi_0
0	0.000	0.000	0.000	0.000	0.000	0.000	0.000	0.000	0.000
10	0.131	0.000	1.403	0.131	0.000	1.398	0.131	0.000	1.396
20	0.278	0.000	2.947	0.278	0.000	2.933	0.278	0.000	2.925
30	0.450	0.000	4.651	0.449	0.000	4.592	0.449	0.000	4.580
40	0.649	0.000	5.746	0.649	0.000	5.750	0.649	0.000	5.757
42	0.691	0.000	5.847	0.691	0.000	5.856	0.692	0.000	5.866
44	0.734	0.000	5.924	0.734	0.000	5.935	0.735	0.000	5.947
46	0.778	0.000	5.983	0.779	0.000	5.996	0.779	0.000	6.009
48	0.822	0.000	6.030	0.823	0.000	6.044	0.825	0.000	6.057
50	0.868	0.000	6.068	0.869	0.000	6.083	0.871	0.000	6.096
52	0.915	0.031	6.699	0.917	0.022	6.698	0.918	0.017	6.675

Table 8.5: The bidisperse RDP model data for a cross-slot with long chain fraction ϕ_L=10% for different mesh resolutions.

ΔP	M1			M2			M3		
	De	DQ	Wi_0	De	DQ	Wi_0	De	DQ	Wi_0
0	0.000	0.000	0.000	0.000	0.000	0.000	0.000	0.000	0.000
10	0.120	0.000	1.275	0.119	0.000	1.267	0.119	0.000	1.262
20	0.260	0.000	2.690	0.259	0.000	2.662	0.259	0.000	2.647
30	0.423	0.000	4.160	0.423	0.000	4.100	0.423	0.000	4.070
40	0.614	0.000	5.262	0.614	0.000	5.210	0.614	0.000	5.184
42	0.655	0.000	5.398	0.655	0.000	5.352	0.655	0.000	5.331
44	0.696	0.000	5.510	0.697	0.000	5.471	0.697	0.000	5.453
46	0.738	0.000	5.601	0.739	0.000	5.569	0.740	0.000	5.555
48	0.781	0.000	5.677	0.782	0.000	5.650	0.784	0.000	5.639
50	0.824	0.000	5.741	0.827	0.000	5.718	0.828	0.000	5.710
52	0.870	0.030	6.206	0.872	0.021	6.129	0.874	0.015	6.072
54	0.915	0.039	6.608	0.918	0.027	6.561	0.920	0.021	6.532
56	0.961	0.040	6.663	0.964	0.027	6.523	0.966	0.020	6.458
58	1.004	0.041	6.667	1.010	0.029	6.499	1.013	0.021	6.423
60	1.052	0.048	6.751	1.056	0.031	6.510	1.061	0.023	6.412

Table 8.6: The bidisperse RDP model data for a cross-slot with long chain fraction ϕ_L=20% for different mesh resolutions.

ΔP	M1			M2			M3		
	De	DQ	Wi_0	De	DQ	Wi_0	De	DQ	Wi_0
0	0.000	0.000	0.000	0.000	0.000	0.000	0.000	0.000	0.000
10	0.096	0.000	1.041	0.096	0.000	1.033	0.096	0.000	1.029
20	0.227	0.000	2.282	0.227	0.000	2.246	0.227	0.000	2.230
30	0.381	0.000	3.507	0.380	0.000	3.414	0.380	0.000	3.370
40	0.560	0.000	4.508	0.560	0.000	4.347	0.560	0.000	4.310
42	0.599	0.000	4.659	0.599	0.000	4.524	0.599	0.000	4.458
44	0.638	0.000	4.792	0.638	0.000	4.659	0.639	0.000	4.593
46	0.677	0.000	4.909	0.679	0.000	4.779	0.679	0.000	4.713
48	0.718	0.000	5.011	0.720	0.000	4.885	0.720	0.000	4.821
50	0.758	0.004	5.105	0.761	0.000	4.980	0.762	0.000	4.917
52	0.804	0.030	5.539	0.804	0.019	5.301	0.805	0.000	5.003
54	0.843	0.038	5.808	0.847	0.019	5.573	0.849	0.017	5.373
56	0.886	0.046	6.090	0.890	0.031	5.847	0.893	0.022	5.632
58	0.929	0.054	6.413	0.934	0.038	6.168	0.937	0.026	5.922
60	0.972	0.062	6.784	0.979	0.045	6.549	0.982	0.031	6.275
70	1.192	0.102	9.038	1.204	0.078	8.885	1.210	0.059	8.575
80	1.415	0.148	11.587	1.436	0.132	11.761	1.446	0.121	11.751
90	1.637	0.203	14.014	1.672	0.210	14.366	1.689	0.207	14.891
100	1.861	0.272	16.285	1.918	0.315	17.561	1.948	0.328	18.155
110	2.094	0.351	18.808	2.194	0.436	21.479	2.250	0.477	22.911
120	2.340	0.430	21.790	2.531	0.572	27.370	2.623	0.634	30.528
130	2.608	0.505	25.562	2.900	0.699	33.701	3.056	0.757	38.418

The same pressure drop values recorded from the first column of the table are used for different meshes and different blend compositions. Comparing the data for different meshes recorded in Table 8.4, 8.5 and 8.6 shows the convergence of the solution as the mesh is refined. Results for pressure drops beyond $\Delta P = 52$ for $\phi_L = 5\%$ and $\Delta P = 60$ for $\phi_L = 10\%$ are excluded because for these values a numerical instability is observed for at least one of the mesh refinements. This instability is discussed further in Section 8.5.

Figure 8.7 shows the local Weissenberg number measured at the stagnation point against Deborah number, where the Deborah number is defined as De=$\lambda_{R,L}Q/D^2$ in keeping with the definition used in earlier sections. This is presented in Figure 8.7a for $\phi_L = 20\%$ with different mesh resolutions. We present the effect of varying long chain concentration ϕ_L, in

Figure 8.7b using the finest resolution, M3.

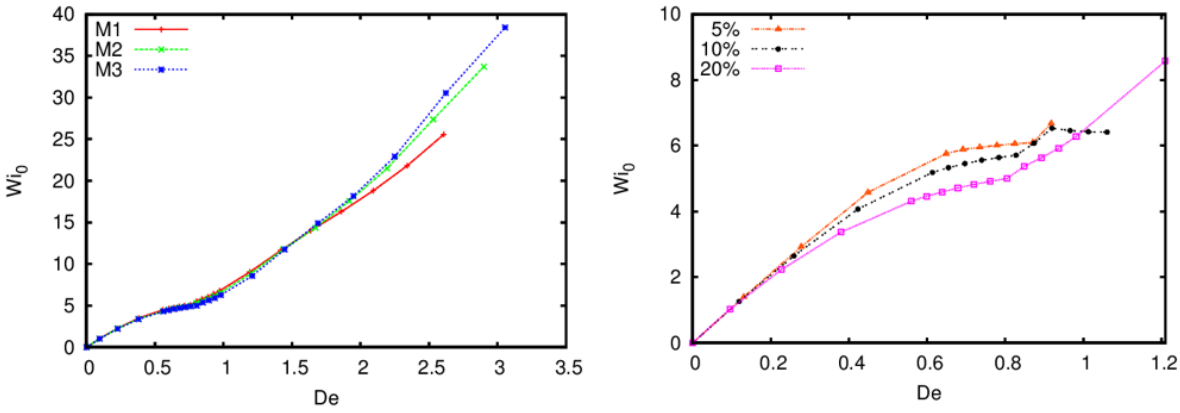

a) $\phi_L = 20\%$ b) Varying ϕ_L using M3

Figure 8.7: The local Weissenberg number measured at the stagnation point over Deborah number predicted by RDP model with different blend composition.

In Figure 8.7a the results for all different mesh resolutions agree well when the Deborah number is less than the unity. Beyond De=1.0, we see an increasing discrepancy between the different meshes with increasing Deborah number, but with a smaller discrepancy between the two finer meshes suggesting that results are converging with mesh refinement. This can also be seen from the corresponding Table 8.6. The agreement between different mesh resolutions is also observed for other blend compositions i.e. $\phi_L = 5\%$ and $\phi_L = 10\%$ as recorded from the Table 8.4 and 8.5 respectively.

A graph for different blend compositions plotted in Figure 8.7b shows that when De < 0.2, the different long chain contributions show the same linear prediction for the Weissenberg number as a function of Deborah number. However, beyond De $= 0.2$, the non-linear relationship between the dimensionless numbers is observed where $\phi_L = 5\%$ predicts the highest local Weissenberg compared to $\phi_L = 10\%$ and $\phi_L = 20\%$.

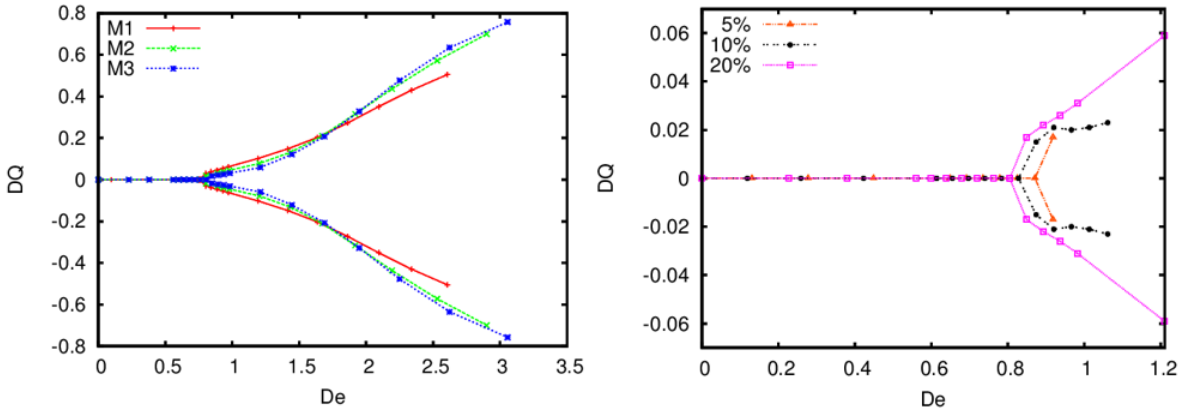

a) ϕ_L = 20% b) Varying ϕ_L using M3

Figure 8.8: The asymmetry parameter, DQ as a function of Deborah number for different volume fraction a) $\phi_L = 20\%$ and b) comparing different ϕ_L using M3.

Figure 8.8a shows the asymmetry parameter DQ plotted against Deborah number for $\phi_L = 20\%$ with different mesh resolutions. From the figure, we can see that the degree of the flow bifurcation shown by meshes M2 and M3 are close indicating mesh convergence. In terms of the critical Deborah number, the coarser mesh gives a lower critical Deborah number. However, the difference between the other two meshes is small. The critical Deborah number for 20% long chain concentration obtained by the finer mesh is $\mathrm{De}_{cr} = 0.849$.

Figure 8.8b shows the flow bifurcation for different long chain concentration plotted on a same graph using M3 mesh. In this figure, the onset of the asymmetric flow for all the long chain fractions is between 0.8 and 1.0. Even though the critical Deborah number for all the three volume fractions are about the same, the value of the bifurcation parameter DQ is different above the critical value as shown in Figure 8.8b. Among the three long chain concentrations, $\phi_L = 20\%$ gives the highest flow asymmetry with DQ=0.026 at De=0.937, whereas for the corresponding value at $\phi_L = 5\%$, DQ=0.017. Note that for the long chains the equivalent $\lambda^{**} = \frac{\lambda_{R,L}}{\lambda_{D,L}}$ is 0.02 which is much smaller than the values for which we found bifurcations for the RP model. Taking into account the effect of enhanced stretch relaxation the effective values of λ^{**} vary from 0.1 to 0.4 as ϕ_L decreases from 20% to 5%. However, decreasing ϕ_L reduces the relative stress contribution from the longer chains, which may be the reason why the onset occurs at a similar critical Deborah number for different values of ϕ_L.

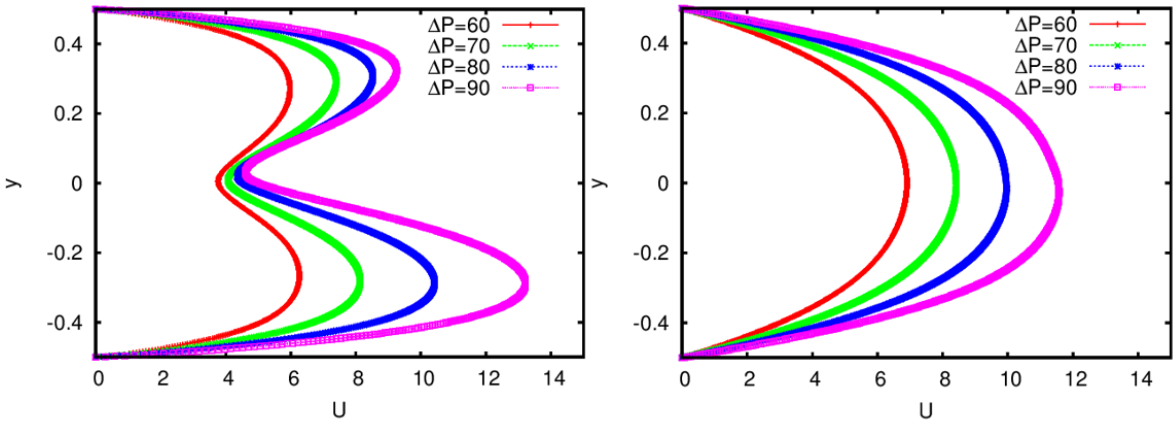

a) $x = 0.5$ b) $x = 3.5$

Figure 8.9: The velocity profile at steady-state across the downstream channel at a) $x = 0.5$ (beginning of the downstream channel) and b) $x = 3.5$ for $\phi_L = 20\%$ with different pressure drop values imposed using M3 mesh refinement.

Figure 8.9 shows the velocity profile across the downstream straight channel taken at $x = 0.5$ and $x = 3.5$ for $\phi_L = 20\%$ for pressure drop values between 60 and 90. We can see from the figure that the velocity profile at the beginning of the straight channel shows a double hump that becomes increasing asymmetric as flow asymmetry increases. The minimum corresponds to the location of the streamline that comes from the stagnation point which generates high elastic stresses that resist the extensional flow in this region. For very low Deborah number, however, this minimum is not found because the elastic stress is not significant and flow is in the Newtonian regime. Treating the centre-line as the line of symmetry, the symmetry breaking of the flow can be seen for the higher pressure drops, as the velocity profile in the lower negative y region has higher flow-rate compared to the upper positive y region. However further downstream in the straight channel, at $x = 3.5$, the flow relaxes back to the profile expected for channel flow.

Table 8.7, 8.8 and 8.9 record the data for the stretch in the thin and fat tubes for different long chain fractions with different mesh refinements at the stagnation point of the cross-slot geometry.

Table 8.7: The bidisperse RDP model data for fat and thin tube stretch in a cross-slot with long chain fraction, $\phi_L = 5\%$.

PD	M1			M2			M3		
	Wi_0	σ_L	σ_{LL}	Wi_0	σ_L	σ_{LL}	Wi_0	σ_L	σ_{LL}
0	0.000	1.000	1.000	0.000	1.000	1.000	0.000	1.000	1.000
10	1.403	1.624	6.149	1.398	1.647	6.282	1.396	1.661	6.362
20	2.947	2.906	12.325	2.933	3.084	13.193	2.925	3.225	13.868
30	4.651	5.794	25.150	4.592	6.277	27.393	4.580	6.700	29.348
40	5.746	13.228	58.351	5.750	14.466	63.906	5.757	15.605	69.021
42	5.847	15.094	66.705	5.856	16.570	73.317	5.866	17.928	79.408
44	5.924	16.957	75.038	5.935	18.678	82.744	5.947	20.262	89.844
46	5.983	18.795	83.260	5.996	20.765	92.072	6.009	22.575	100.182
48	6.030	20.604	91.340	6.044	22.820	101.253	6.057	24.855	110.365
50	6.068	24.775	109.995	6.083	24.841	110.281	6.096	27.096	120.375
52	6.699	23.767	105.321	6.698	26.525	117.682	6.675	30.487	128.988

Table 8.8: The bidisperse RDP model data for fat and thin tube stretch in a cross-slot with long chain fraction, $\phi_L = 10\%$.

PD	M1			M2			M3		
	Wi_0	σ_L	σ_{LL}	Wi_0	σ_L	σ_{LL}	Wi_0	σ_L	σ_{LL}
0	0.000	1.000	1.000	0.000	1.000	1.000	0.000	1.000	1.000
10	1.275	1.570	4.195	1.267	1.579	4.230	1.262	1.583	4.249
20	2.690	2.874	8.682	2.662	3.002	9.121	2.647	3.100	9.450
30	4.160	5.428	16.790	4.100	5.805	18.037	4.070	6.140	19.131
40	5.262	10.274	32.024	5.210	11.024	34.439	5.184	11.755	36.786
42	5.398	11.464	35.771	5.352	12.317	38.509	5.331	13.154	41.187
44	5.510	12.680	39.603	5.471	13.648	42.697	5.453	14.598	45.730
46	5.601	13.907	43.469	5.569	14.998	46.948	5.555	16.069	50.353
48	5.677	15.135	47.335	5.650	16.355	51.220	5.639	17.545	55.010
50	5.741	16.357	51.183	5.718	17.710	55.484	5.710	19.026	59.670
52	6.206	17.442	54.523	6.129	18.977	59.416	6.072	20.444	64.090
54	6.608	18.546	57.940	6.561	20.225	63.290	6.532	21.821	68.379
56	6.663	19.563	61.150	6.523	21.304	66.715	6.458	22.970	72.026
58	6.667	20.513	64.169	6.499	22.334	69.981	6.423	24.084	75.553
60	6.751	21.439	67.086	6.510	23.330	73.129	6.412	25.164	78.965

Table 8.9: The bidisperse RDP model data for fat and thin tube stretch in a cross-slot with long chain fraction, $\phi_L = 20\%$.

PD	M1			M2			M3		
	Wi_0	σ_L	σ_{LL}	Wi_0	σ_L	σ_{LL}	Wi_0	σ_L	σ_{LL}
0	0.000	1.000	1.000	0.000	1.000	1.000	0.000	1.000	1.000
10	1.041	1.436	2.662	1.033	1.432	2.662	1.029	1.435	2.662
20	2.282	2.576	5.496	2.246	2.621	5.607	2.230	2.653	5.682
30	3.507	4.645	10.207	3.414	4.815	10.606	3.370	4.977	10.979
40	4.508	7.922	17.518	4.347	8.222	18.224	4.310	8.574	19.032
42	4.659	8.694	19.237	4.524	9.025	20.012	4.458	9.422	20.922
44	4.792	9.486	21.004	4.659	9.855	21.860	4.593	10.299	22.877
46	4.909	10.298	22.803	4.779	10.705	23.750	4.713	11.198	24.879
48	5.011	11.117	24.623	4.885	11.569	25.672	4.821	12.114	26.917
50	5.105	11.941	26.458	4.980	12.441	27.611	4.917	13.040	28.977
52	5.539	12.820	28.353	5.301	13.376	29.660	5.003	13.973	31.051
54	5.808	13.667	30.207	5.573	14.300	31.691	5.373	14.988	33.281
56	6.090	14.493	32.011	5.847	15.199	33.663	5.632	15.953	35.407
58	6.413	15.301	33.770	6.168	16.083	35.595	5.922	16.902	37.497
60	6.784	16.090	35.479	6.549	16.948	37.475	6.275	17.841	39.551
70	9.038	19.831	43.358	8.885	21.040	46.212	8.575	22.319	49.191
80	11.587	23.200	50.090	11.761	24.647	53.366	11.751	26.193	56.922
90	14.014	26.158	55.802	14.366	27.596	58.900	14.891	29.253	62.677
100	16.285	28.609	60.765	17.561	29.665	62.874	18.155	31.051	65.957
110	18.808	30.491	64.772	21.479	30.464	64.194	22.911	31.084	64.778
120	21.790	31.794	67.507	27.370	30.315	62.001	30.528	30.661	61.439
130	25.562	32.652	68.698	33.701	30.348	61.209	38.418	29.895	58.442

Figure 8.10 and Figure 8.11 show the stretch in the thin and fat tubes and the local Weissenberg number plotted from the data in the Tables 8.7, 8.8 and 8.9. Figure 8.10a and Figure 8.11a present the thin and fat tube stretch as a function of local Weissenberg number for the 20% long chain contribution for different mesh resolutions. While Figure 8.10b and 8.11b show the prediction made by varying long chain fractions obtained using the M3 mesh.

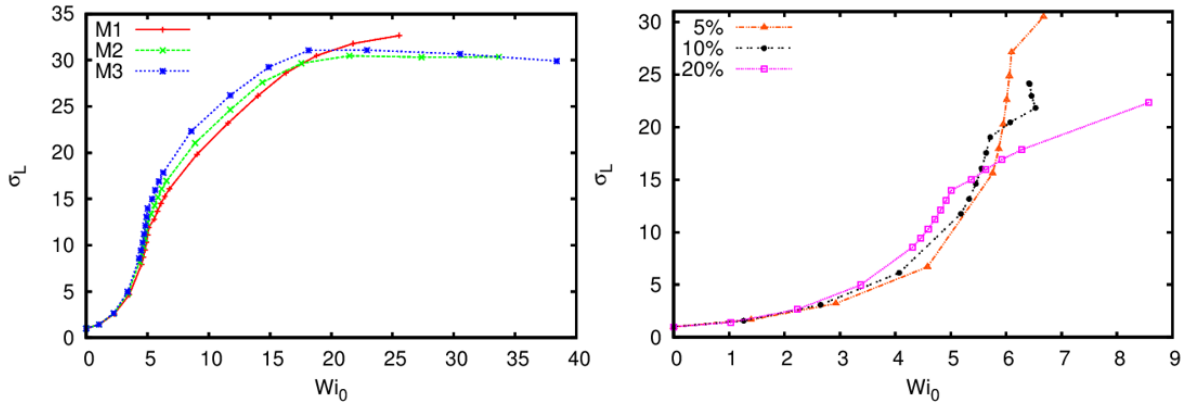

a) $\phi_L = 20\%$ b) Varying ϕ_L using M3

Figure 8.10: The stretch in the thin tube predicted by RDP model versus local Weissenberg number measured at the stagnation point for different blend compositions.

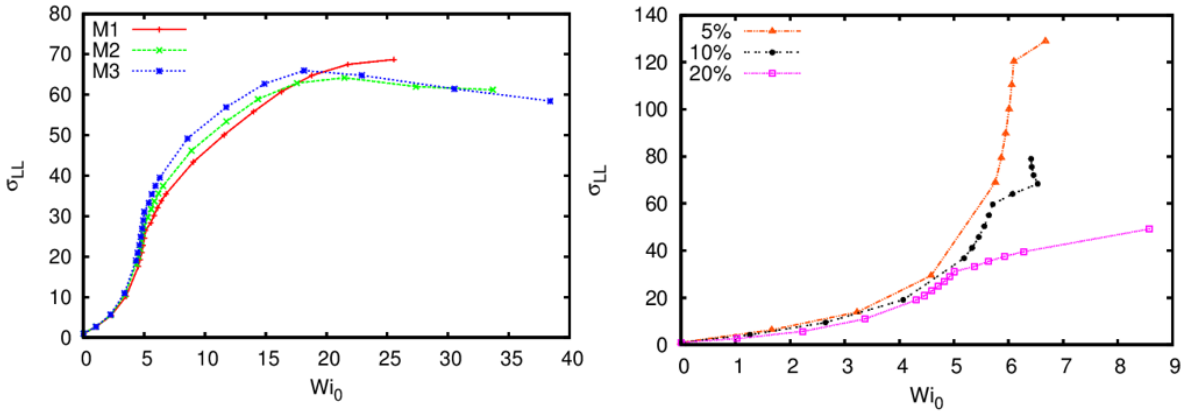

a) $\phi_L = 20\%$ b) Varying ϕ_L using M3

Figure 8.11: The stretch in the fat tube predicted by RDP model versus local Weissenberg number measured at the stagnation point for different blend compositions.

The stretch in the thin and fat tube in Figure 8.10a and 8.11a follows a similar trend when plotted against the local Weissenberg number with an increasing gradient for Weissenberg numbers up to 5 before leveling off once the flow becomes asymmetric. For the 20% blend the stretch in the fat tube is about double the stretch in the thin tube. Mesh convergence is observed below Wi_0=17.0, with the M3 mesh showing the highest stretch.

Comparing Figure 8.10b and 8.11b, opposite trends are found between stretch in the thin and fat tube when varying blend composition (which are plotted using the M3 mesh). Below Wi_0=5.0, when the flow is symmetric, the thin tube stretch increases with the long chain volume fraction, whereas the fat tube stretch decreases as the long chain volume

fraction increases. There is also a crossing over of the thin tube stretch for 20% long chain fraction in between Wi_0=5.0 and Wi_0=6.0, as shown in Figure 8.10a, that is not observed in the fat tube stretch which corresponds to the case where the flow becomes asymmetric. At higher local Weissenberg number, the stretch in both tubes shows a similar trend where the highest long chain fraction predicts the lowest stretch.

Note that, we have observed and discussed the effect of different relaxation time ratios for single mode RP model in the previous section and presented the results for the effect of varying volume fraction for the RDP model in this section. We also looked at the effect of the chain coupling for 5% long chain blends with 95% short chain where we found that there is no flow bifurcation observed and the simulation crashes at high Deborah number when mRP model is used. However, the results are not reported in this thesis as there is no significant flow bifurcation observed using this model probably because the chain interaction is neglected in this model. At high Deborah number, we encounter a numerical instability and convergence issue especially for small amount long-chain composition and this is discussed in the next section.

8.5 Numerical instability and mesh convergence issues

In this section we discuss the reasons that contribute to numerical instability issues observed at higher pressure drop value for $\phi_L = 5\%$ and $\phi_L = 10\%$. In order to determine the steady-state solution we compute the time dependent evolution of the flow from rest using a pressure ramp.

The time dependence of the strain-rate at the stagnation point for different blend compositions can be observed by plotting the graph of the transient local Weissenberg number as shown in Figure 8.12.

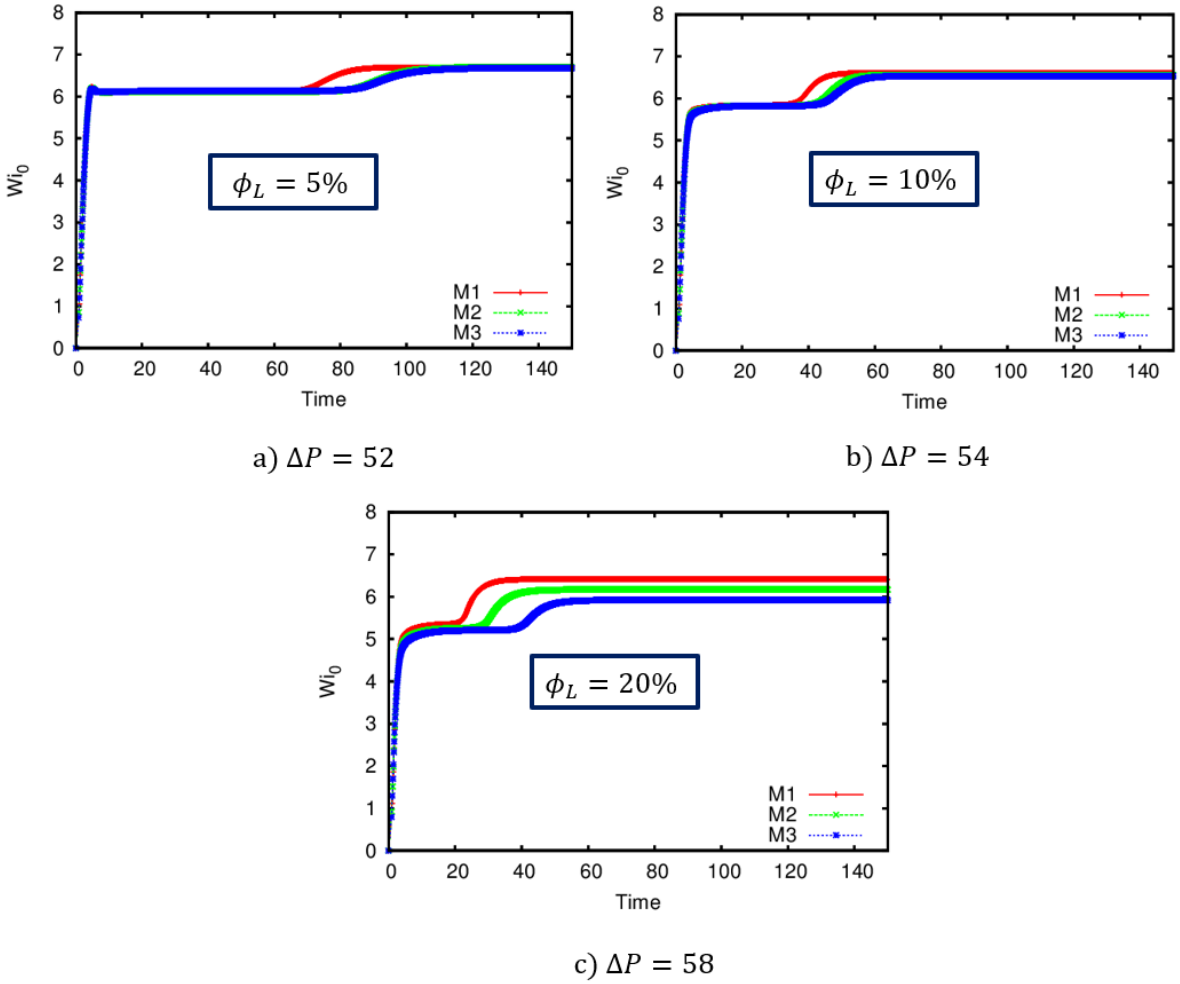

Figure 8.12: The transient local Weissenberg number for different blend compositions at similar flow rates slightly above the critical Deborah number.

Figure 8.12 shows the transient local Weissenberg number measured at the stagnation point for different blend compositions for different mesh refinements with pressure drop, $\Delta P = 52$, $\Delta P = 54$ and $\Delta P = 58$ for $\phi_L = 5\%$, $\phi_L = 10\%$ and $\phi_L = 20\%$ respectively which are just above the critical Deborah number for asymmetric flow. We can see that the Weissenberg number first evolves towards a "quasi" steady-state value in which the flow remains symmetric. This is followed by a transition from the symmetric flow to a symmetry breaking flow at the stagnation point. This second true steady-state represents the stationary asymmetric flow. This can be observed in Figure 8.13 where the velocity distribution at $t = 20$ and $t = 80$ is plotted for 20% long chain contribution. Similar results are found for the $\phi_L = 5\%$ and $\phi_L = 10\%$ blends.

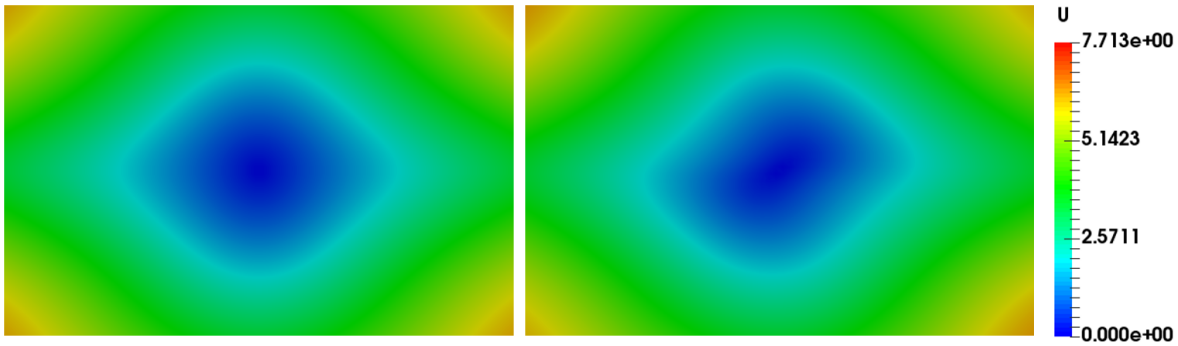

a) t=20 b) t=80

Figure 8.13: The velocity contour at a stagnation point for $\phi_L = 20\%$ using M3 mesh refinement taken at different times where the steady-state is observed with $\Delta P = 58$.

The bifurcation parameter at $t = 80$ is DQ=0.026 as recorded in Table 8.6 while at $t = 20$ with DQ=0. The transition occurs earlier for the coarse mesh, possibly as a consequence of the greater noise in the solution. However in Figure 8.12a we see that the three meshes gives the same final steady-state values for the Weissenberg number.

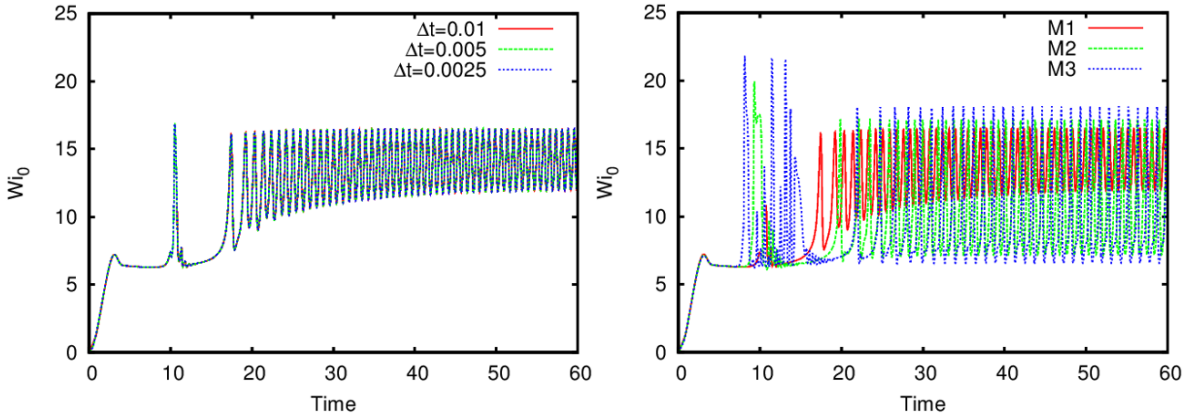

a) Varying Δt b) Varying mesh

Figure 8.14: The transient local Weissenberg number for $\phi_L = 5\%$ by varying time-step resolution and mesh resolution with pressure drop, $\Delta P = 80$.

However as we increase the pressure drop for the 5% blend we observe that the solution becomes unsteady. To investigate this phenomenon we have varied both time-step and spatial resolution in Figure 8.14. The results presented in Figure 8.14 are obtained for 5% long chain blend with a pressure drop $\Delta P = 80$. Figure 8.14a shows that the instability is insensitive to the time-step values ranging from $\Delta t = 1.0 \times 10^{-2}$ to $\Delta t = 2.5 \times 10^{-3}$. Here,

we used the M1 mesh resolution.

The effect of the varying the mesh resolution is presented in Figure 8.14b for the time-step $\Delta t = 1 \times 10^{-2}$. Refining the mesh has the effect of increasing both the amplitude and frequency of the oscillation as shown in Figure 8.14b where a slight changes is observed in the frequency. Since we are not able to obtain mesh independent results we are not able to conclude whether this is a consequence of the constitutive model or the numerical solution. Visually the flow appears steady, except for a small region around the stagnation point.

8.6 Conclusion

In this chapter, we have shown that bifurcation to an asymmetric flow, previously found for the Oldroyd-B and FENE models, is also observed for both the single-mode Rolie-Poly and RDP constitutive models. However the critical Deborah number is higher and the amplitude is smaller than is found for models where orientation and stretch have the same rate of relaxation. In particular we find that in the RP model the bifurcation is only found when the stretch relaxation time is of similar size to the orientation relaxation time, which would explain why the phenomenon has not been reported for entangled polymer melts. One possible explanation for this is that shear-thinning inhibits the formation of the flow bifurcation. However, Rocha et al. [123] found the opposite by comparing the FENE-CR and FENE-P model where the FENE-P model shows the formation of bifurcation at lower Deborah number than the equivalent FENE-CR model.

On the other hand, symmetry breaking is observed in the RDP model in cases where the ratio of the stretch to orientation relaxation time of the long chain fraction is small. Whilst this may be the effect of the enhanced stretch relaxation, the critical Deborah number for the three different blend compositions is approximately the same even though the effective stretch relaxation times differ by a factor of 4. We also found that the blends with lower long chain concentrations, that is $\phi_L = 5\%$ and $\phi_L = 10\%$, showed a numerical instability at higher Deborah numbers. Further work is needed to fully understand this phenomenon.

Chapter 9

Conclusion

In this final chapter, we present the conclusion, highlighting the contributions of this work and some potential ways in which it could be extended for future research.

9.1 Summary

In this thesis, we have studied the behaviour of entangled linear polymer blend using a recently published viscoelastic model, the bidisperse RDP model of Boudara et al. [23]. The main objectives of this thesis are to test whether this model is suitable for simulations in complex flow geometries and to understand the response of this model under elongational flow created in two different flow geometries, the hyperbolic contraction flow and the cross-slot flow that are used experimentally to determine extensional flow properties. In particular, the extent to which the hyperbolic curve is able to produce a constant extension-rate within a localised region of the flow.

Chapter 1 is the introductory chapter that provides the aims and objectives of this research, the background study of the project including the model description and the numerical techniques used. The review of the related work and overview of the outline of the thesis chapters are presented in this chapter.

Chapter 2 presents the OpenFOAM CFD software and focuses on the viscoelastic flow simulations. This includes a comparison of the two different libraries available to solve viscoelastic flow problems, `viscoselasticFluidFoam` and `rheoFoam` and our reasons for choosing the latter. The method and techniques used are also described in this chapter. A

description of the OpenFOAM structure is also provided in this chapter and a description of the pre-processing files. The new constitutive model compilation procedures are also presented.

In Chapter 3, we consider the solution of a Newtonian flow through a straight channel in one- and two-dimensional using different numerical approaches. This includes the finite difference method and the finite element method with different time discretisation techniques considered. The accuracy of the developed codes was validated against the available analytical solution to determine the error behaviour as a function of the spatial and temporal step-size. The work is then extended to include non-Newtonian flow for the Oldroyd-B model that is solved for the one-dimensional channel flow problem using a finite difference code. The flow was also solved using OpenFOAM where the results obtained using different numerical approaches, the FDM and FVM are validated against the analytical solution available in Duarte et al. [47]. This chapter demonstrates the agreement between the codes developed in C++ for the FDM and FEM numerical methods with the results obtained using the finite volume-based OpenFOAM solver for Newtonian flow using `icoFoam` and for non-Newtonian viscoelastic flows using the `rheoFoam` library.

Chapter 4 describes polymer melt flow through a hyperbolic contraction geometry. In this chapter, the Rolie-Poly model was implemented within the OpenFOAM software. The details of the implementation are described in Section 4.2. The implementation of the model is validated by solving the benchmark 4:1 planar sudden contraction for a multimode Rolie-Poly model and compared with previously published results [129] for this model. The work was then extended to look at the behaviour of this model in the hyperbolic contraction flow using different contraction lengths with the aim to determine the range of flow geometries that give a uniform extension-rate within the hyperbolic region. The results and contraction design conclusion are presented and discussed.

The conventional way of handling polydispersity of the fluid is based on the linear superposition of modes. This neglects the interaction dynamics between chains of different molecular lengths. These interactions are included in the RDP model. Chapter 5 considers the rheological behaviour of the bidisperse RDP and the equivalent mRP model. The mathematical description of the model was first presented the details of the implementation

of the model within the software are available in Appendix B. The implementation of the model is then validated with the published results [23] to check the correctness of the implementation. The equivalent mRP model was chosen to have the same linear viscoelastic limit as the RDP model in order to represent the linear relaxation predicted by double reptation. This requires three Rolie-Poly modes (mRP) rather than two. While the transient shear viscosity of the two models is similar, in transient extensional flow effects of the enhanced stretch in the RDP model can be seen.

In Chapter 6, the hyperbolic contraction flow for the RDP model and mRP model were considered. Based on the conclusions drawn from Chapter 4 on the suitable contraction length that generates an approximately uniform extension-rate within the contraction along the centre-line, the dimensional contraction length, $L = 5$ was used to observe other relevant effects. These include the effect of imposed pressure drop, the effect of contraction ratio, the differences between the results for the RDP and mRP model, the effect of varying blend compositions and the three-dimensional effects due to different channel depths. Our simulations demonstrate that the hyperbolic contraction geometry is able to generate a region of uniform extensional flow along the axis provided that the channel depth is sufficiently large to avoid the three-dimensional effects. This extensional flow is able to produce stretching of the polymer segments within the model. While the contraction ratio sets the extensional strain, the extension-rate is determined by the contraction length and imposed pressure drop. The enhanced stretch relaxation time that is captured by the RDP model leads to the generation of molecular stretch along the centre-line within the contracting region even though the extension-rate along the centre-line within the contracting region is below the inverse of the stretch relaxation time. We also presented the mathematical analysis to explain the different behaviour shown by the thin and fat tubes across the channel within the contracting region. We demonstrated that the prediction made the thin and fat tubes along the centre-line show the opposite trend as the blend composition is varied.

In Chapter 7, the results for the cross-slot flow with hyperbolic corner lengths predicted by the RDP model is presented. Several relevant effects including the effect of the hyperbolic corner length, extension-rate, blend composition, the difference between the RDP and mRP model and the three-dimensional geometry with different channel depths were presented

and discussed. A similar trend to the hyperbolic contraction flow of prediction for different effects was observed in the cross-slot flow. Our results demonstrated that with the same extension-rate generated within the hyperbolic region, the stretch is more pronounced in cross-slot flow due to the increase in residence time at the stagnation point.

Chapter 8 presents the study on a flow bifurcation in a cross-slot geometry with sharp corner for the single mode Rolie-Poly model and the bidisperse RDP model. For the single mode Rolie-Poly, we found that the degree of the flow bifurcation and the critical Deborah number depends on the ratio of the stretch to orientation relaxation times with higher values of this ratio having a lower critical Deborah number and higher degree of flow bifurcation. The flow bifurcation for the RDP model was observed for different blend compositions where our results demonstrated that the critical Deborah number is approximately the same for different blending ratios but that the degree of the bifurcation is more pronounced for higher long chain fraction. We also found a numerical instability at the stagnation point at higher pressure drop value for lower long chain concentration which prevented the illustration of the RDP behaviour in a wider range of Deborah number. This issue is unresolved and will be a part of the future direction to understand the cause of the numerical oscillation that takes place within this regime.

9.2 Achievements

The main achievements of this thesis can be summarised as follows.

1. We successfully implemented the Rolie-Poly and Rolie-Double-Poly model within the OpenFOAM software through the RheoTool toolbox. We validated the implementation against the published results for the benchmark 4:1 planar contraction for the RP model and the rheological behaviour computed on a single computational cell for the RDP model. In both cases close agreement was observed. This demonstrates both the utility of the RheoTool toolbox and the suitability of the RDP model for flow simulation.

2. We have explored further the rheological consequences of the coupling between the dynamics of polymer chains of different lengths introduced in the RDP model by

comparing with an equivalent multimode Rolie-Poly model that has the same linear viscoelastic response as given by double reptation theory [44] but excludes the coupling between stretch modes. Here, we observed that the RDP with the chain coupling effect exhibits the enhanced stretch relaxation time and the transient extensional viscosity grows above the linear viscoelastic envelope (for sufficiently high extension-rate) which is absent in the mRP model.

3. We modelled the RDP flow in the hyperbolic contraction geometry and presented the behaviour of the RDP focusing on the differences between the polymer stretch predictions both along the centre-line where the flow is purely elongational and in the mixed shear and extensional flow elsewhere in the contraction. We found that, the contraction ratio sets the extensional strain, while the strain-rate is determined by the contraction length. We extended the work to the three-dimensional domain where the influence of the cross-stream flow resulting from the presence of side-walls was modelled for different channel depths and we found for the flow to be effectively planar, the ratio of half geometry to channel depth is about quarter for 4:1 and 1:1.6 for 10:1 contraction ratio.

4. We modelled the RDP flow in the cross-slot geometry with hyperbolic corners and reported the behaviour of the RDP model by observing the stress birefringence field and the prediction made along the centre-line for extension-rate and polymer chains extension. We showed that the uniform extension-rate is observed within the hyperbolic region along the centre-line and spike approaching the stagnation point due to higher extensional strain in that region. The loss of the four-fold symmetry from the stress birefringence pattern is observed for sufficiently high pressure drop as a consequence of the elastic effect in the RDP model. The increased in the residence time in cross-slot flow (comparing to the hyperbolic contraction flow) along the centre-line allows polymer chains in fat and thin tubes to achieve higher chain stretch even though the same extension-rate is imposed.

5. We showed that the steady flow bifurcation found for polymer solutions is also predicted by the RP and RDP models. However in the RP model this phenomenon is

only seen for weakly entangled polymers where the stretch and orientation relaxation times are similar. This would explain why this phenomenon is not reported for polymer melts. For the RDP model, we see that the degree of flow bifurcation increases as the long chain composition is increased and the critical Deborah number is lower for higher long chain composition.

9.3 Future Work

In this section, we point out some potential open problems of the current work as part of the future direction of this research that we believe is worth investigating. These can be summarized as follows.

1. In the current work all the modes include stretch. However, this requires using a timestep that is able to resolve the stretch relaxation of the short chains. There is another version of the RP model that neglects the stretch term [57] and using this to model the short chains might enable longer time steps to be used.

2. The finite extensibility function, $f_E(\sigma)$ was not included (set to unity) in this work for the sake of simplicity but would be straightforward to add to the RP and RDP model to limit the extension at higher extension-rate particularly at the stagnation point of the cross-slot.

3. In this thesis we have only considered two species of polymer chains S and L. However the general RDP model has N modes requiring N^2 configuration tensors. We could extend the current work to include the RDP model with more than two-modes within OpenFOAM and model the behaviour in the geometrical flow in two- and three-dimensions to see whether it is feasible to use such a model for a three-dimensional problem in OpenFOAM.

4. With multiple modes it would be possible to make a quantitative comparison between the numerical simulation and flow experiments on polydisperse polymer melts. This would reveal whether the coupling between modes produce significant improvements in the prediction of the flow of industrial grade polymers.

5. The numerical instability issues found in the cross-slot flow bifurcation with a sharp corner require further investigation. One method for stabilisation would be to implement the log-conformation approach for the RDP model to check whether the numerical oscillation could be resolved by this technique.

6. The study of flow bifurcation in the cross-slot device could be extended to observe the effect of introducing hyperbolic corners or adding a cylinder at the centre to remove the stagnation point as was recently consider by Davoodi et al. [38].

References

[1] Ansys Polyflow. URL: `https://www.ansys.com/en-gb/products/fluids/ansys-polyflow`.

[2] ARC3 - Advanced Research Computing. URL: `https://arc.leeds.ac.uk/systems/arc3/`.

[3] Comsol Multiphysics 5.4. URL: `https://uk.comsol.com/`.

[4] D. J. Acheson. *Elementary Fluid Dynamics*. Oxford:Clarendon Press, 1990.

[5] M. A. Alves. Design of a Cross-Slot flow channel for Extensional Viscosity Measurements. In *AIP Conference Proceedings*, volume 1027, pages 240–242. AIP, 2008.

[6] M. A. Alves, P. J. Oliveira, and F. T. Pinho. A convergent and universally bounded interpolation scheme for the treatment of advection. *International Journal for Numerical Methods in Fluids*, 41(1):47–75, 2003.

[7] P. D. Ariel. A new finite-difference algorithm for computing the boundary layer flow of viscoelastic fluids in hydromagnetics. *Computer Methods in Applied Mechanics and Engineering*, 124(1-2):1–13, 1995.

[8] P. E. Arratia, C. C. Thomas, J. Diorio, and J. P. Gollub. Elastic instabilities of polymer solutions in cross-channel flow. *Physical review letters*, 96(14):144502, 2006.

[9] D. Auhl, P. Chambon, T. C. B. McLeish, and D. J. Read. Elongational flow of blends of long and short polymers: Effective stretch relaxation time. *Physical Review Letters*, 103(13):136001, 2009.

[10] D. Auhl, D. M. Hoyle, D. Hassell, T. D. Lord, O. G. Harlen, M. R. Mackley, and T. C. B. McLeish. Cross-slot extensional rheometry and the steady-state extensional response of long chain branched polymer melts. *Journal of Rheology*, 55(4):875–900, 2011.

[11] A. A. Azahar, O. G. Harlen, and M. A. Walkley. Modelling contraction flows of bi-disperse polymer blends using the Rolie-Poly and Rolie-Double-Poly equations. *Korea-Australia Rheology Journal*, 31(4):203–209, 2019.

[12] J. Azaiez, R. Guenette, and A. Ait-Kadi. Entry flow calculations using multi-mode models. *Journal of Non-Newtonian Fluid Mechanics*, 66(2-3):271–281, 1996.

[13] J. Azaiez, R. Guenette, and A. Ait-Kadi. Investigation of the abrupt contraction flow of fiber suspensions in polymeric fluids. *Journal of Non-Newtonian Fluid Mechanics*, 73(3):289–316, 1997.

[14] D. G. Baird, T. W. Chan, C. McGrady, and S. M. Mazahir. Evaluation of the use of a semi-hyperbolic die for measuring elongational viscosity of polymer melts. *Applied Rheology*, 20(3):47–58, 2010.

[15] D. G. Baird and J. Huang. Elongational viscosity measurements using a semi-hyperbolic die. *Applied Rheology*, 16(6):312–320, 2006.

[16] Y. Belhamadia, A. Fortin, and É. Chamberland. Anisotropic mesh adaptation for the solution of the stefan problem. *Journal of Computational Physics*, 194(1):233–255, 2004.

[17] F. V. Berghen and H. Bersini. CONDOR, a new parallel, constrained extension of Powell's UOBYQA algorithm: Experimental results and comparison with the DFO algorithm. *Journal of Computational and Applied Mathematics*, 181(1):157–175, 2005.

[18] B. Bernstein, K. A. Feigl, and E. T. Olsen. Steady flows of viscoelastic fluids in axisymmetric abrupt contraction geometry: a comparison of numerical results. *Journal of Rheology*, 38(1):53–71, 1994.

[19] R. B. Bird, R. C. Armstrong, and O. Hassager. *Dynamics of polymeric liquids. Vol. 1, 2nd Ed: Fluid mechanics.* John Wiley and Sons Inc., 1987.

[20] R. B. Bird, P. J. Dotson, and N. L. Johnson. Polymer solution rheology based on a finitely extensible bead—spring chain model. *Journal of Non-Newtonian Fluid Mechanics*, 7(2-3):213–235, 1980.

[21] G. B. Bishko, O. G. Harlen, T. C. B. McLeish, and T. M. Nicholson. Numerical simulation of the transient flow of branched polymer melts through a planar contraction using the pom–pom'model. *Journal of Non-Newtonian Fluid Mechanics*, 82(2-3):255–273, 1999.

[22] A. C. Bogaerds, W. M. Verbeeten, G. W. Peters, and F. P. Baaijens. 3D viscoelastic analysis of a polymer solution in a complex flow. *Computer methods in applied mechanics and engineering*, 180(3-4):413–430, 1999.

[23] V. A. Boudara, J. D. Peterson, L. G. Leal, and D. J. Read. Nonlinear rheology of polydisperse blends of entangled linear polymers: Rolie-Double-Poly models. *Journal of Rheology*, 63(1):71–91, 2019.

[24] C. A. Brebbia, J. C. F. Telles, and L. C. Wrobel. *Boundary element techniques: theory and applications in engineering.* Springer Science & Business Media, 2012.

[25] L. Campo-Deaño, F. J. Galindo-Rosales, F. T. Pinho, M. A. Alves, and M. S. Oliveira. Flow of low viscosity Boger fluids through a microfluidic hyperbolic contraction. *Journal of Non-Newtonian Fluid Mechanics*, 166(21-22):1286–1296, 2011.

[26] S. T. Chaffin and J. M. Rees. Viscoelastic Hele-Shaw flow in a cross-slot geometry. *European Journal of Mechanics-B/Fluids*, 68:45–54, 2018.

[27] L. F. Chen, J. Zang, A. J. Hillis, G. C. Morgan, and A. R. Plummer. Numerical investigation of wave–structure interaction using OpenFOAM. *Ocean Engineering*, 88:91–109, 2014.

[28] X. Chen, H. Marschall, M. Schäfer, and D. Bothe. A comparison of stabilisation approaches for finite-volume simulation of viscoelastic fluid flow. *International Journal of Computational Fluid Dynamics*, 27(6-7):229–250, 2013.

[29] M. D. Chilcott and J. M. Rallison. Creeping flow of dilute polymer solutions past cylinders and spheres. *Journal of Non-Newtonian Fluid Mechanics*, 29:381–432, 1988.

[30] F. N. Cogswell. Converging flow and stretching flow: a compilation. *Journal of Non-Newtonian Fluid Mechanics*, 4(1-2):23–38, 1978.

[31] J. R. Collier, O. Romanoschi, and S. Petrovan. Elongational rheology of polymer melts and solutions. *Journal of Applied Polymer Science*, 69(12):2357–2367, 1998.

[32] R. Comminal, J. H. Hattel, M. A. Alves, and J. Spangenberg. Vortex behavior of the oldroyd-b fluid in the 4-1 planar contraction simulated with the streamfunction–log-conformation formulation. *Journal of Non-Newtonian Fluid Mechanics*, 237:1–15, 2016.

[33] J. Crank and P. Nicolson. A practical method for numerical evaluation of solutions of partial differential equations of the heat-conduction type. In *Mathematical Proceedings of the Cambridge Philosophical Society*, volume 43, pages 50–67. Cambridge University Press, 1947.

[34] D. O. A. Cruz and F. T. Pinho. Fully-developed pipe and planar flows of multimode viscoelastic fluids. *Journal of Non-Newtonian Fluid Mechanics*, 141(2-3):85–98, 2007.

[35] F. A. Cruz, R. J. Poole, A. M. Afonso, F. T. Pinho, P. J. Oliveira, and M. A. Alves. A new viscoelastic benchmark flow: Stationary bifurcation in a cross-slot. *Journal of Non-Newtonian Fluid Mechanics*, 214:57–68, 2014.

[36] L. d'Agostino. Laminar Viscous Flow: Fully Developed Duct Flows. 2010.

[37] Polymer Properties Database. Crystallization Behaviour of Polymers. URL: `https://polymerdatabase.com/polymer\%20physics/Crystalline\%20Polymers.html`.

[38] M. Davoodi, A. F. Domingues, and R. J. Poole. Control of a purely elastic symmetry-breaking flow instability in cross-slot geometries. *Journal of Fluid Mechanics*, 881:1123–1157, 2019.

[39] P. G. de Gennes. Reptation of a polymer chain in the presence of fixed obstacles. *The journal of Chemical Physics*, 55(2):572–579, 1971.

[40] J. M. Dealy, D. J. Read, and R. D. Larson. *Structure and Rheology of Molten Polymers: From Structure to Flow Behavior and Back Again*. Hanser Publications, 2 edition, 2018.

[41] B. Debbaut, J. M. Marchal, and M. J. Crochet. Numerical simulation of highly viscoelastic flows through an abrupt contraction. *Journal of Non-Newtonian Fluid Mechanics*, 29:119–146, 1988.

[42] B. Debbaut and T. Marchal. Numerical simulation of extrusion process and die design for industrial profile, using multimode pom–pom model. *Plastics, rubber and composites*, 37(2-4):142–150, 2008.

[43] H. Demir. Numerical modelling of viscoelastic cavity driven flow using finite difference simulations. *Applied mathematics and computation*, 166(1):64–83, 2005.

[44] J. Des Cloizeaux. Double reptation vs. simple reptation in polymer melts. *EPL (Europhysics Letters)*, 5(5):437, 1988.

[45] M. Doi and S. F. Edwards. *The theory of polymer dynamics*, volume 73. Oxford University Press, 1988.

[46] I. G. Donev and B. D. Reddy. Time-dependent finite element simulations of a shear-thinning viscoelastic fluid with application to blood flow. *International Journal for Numerical Methods in Fluids*, 75(9):668–686, 2014.

[47] A. S. R. Duarte, A. I. Miranda, and P. J. Oliveira. Numerical and analytical modeling of unsteady viscoelastic flows: The start-up and pulsating test case problems. *Journal of Non-Newtonian Fluid Mechanics*, 154(2-3):153–169, 2008.

[48] R. E. Evans and K. Walters. Further remarks on the lip-vortex mechanism of vortex enhancement in planar-contraction flows. *Journal of Non-Newtonian Fluid Mechanics*, 32(1):95–105, 1989.

[49] R. Fattal and R. Kupferman. Constitutive laws for the matrix-logarithm of the conformation tensor. *Journal of Non-Newtonian Fluid Mechanics*, 123(2-3):281–285, 2004.

[50] R. Fattal and R. Kupferman. Time-dependent simulation of viscoelastic flows at high Weissenberg number using the log-conformation representation. *Journal of Non-Newtonian Fluid Mechanics*, 126(1):23–37, 2005.

[51] J. L. Favero. Viscoelastic flow simulation in OpenFOAM. URL: `http://powerlab.fsb.hr/ped/kturbo/OpenFOAM/slides/viscoelasticFluidFoam.pdf`.

[52] J. L. Favero, A. R. Secchi, N. S. M. Cardozo, and H. Jasak. Viscoelastic flow simulation: development of a methodology of analysis using the software OpenFOAM and differential constitutive equations. In *Computer Aided Chemical Engineering*, volume 27, pages 915–920. Elsevier, 2009.

[53] J. L. Favero, A. R. Secchi, N. S. M. Cardozo, and H. Jasak. Viscoelastic flow analysis using the software OpenFOAM and differential constitutive equations. *Journal of Non-Newtonian Fluid Mechanics*, 165(23-24):1625–1636, 2010.

[54] J. L. Favero, A. R. Secchi, N. S. M. Cardozo, and H. Jasak. Viscoelastic fluid analysis in internal and in free surface flows using the software OpenFOAM. *Computers & chemical engineering*, 34(12):1984–1993, 2010.

[55] K. Gardner, E. R. Pike, M. J. Miles, A. Keller, and K. Tanaka. Photon-correlation velocimetry of polystyrene solutions in extensional flow fields. *Polymer*, 23(10):1435–1442, 1982.

[56] H. Giesekus. A simple constitutive equation for polymer fluids based on the concept of deformation-dependent tensorial mobility. *Journal of Non-Newtonian Fluid Mechanics*, 11(1-2):69–109, 1982.

[57] R. S. Graham, A. E. Likhtman, T. C. B. McLeish, and S. T. Milner. Microscopic theory of linear, entangled polymer chains under rapid deformation including chain stretch and convective constraint release. *Journal of Rheology*, 47(5):1171–1200, 2003.

[58] B. Gschaider, H. Nilson, H. Rushe, H. Jasak, M. Beaudoin, and V. Skuric. SOURCEFORGE: foam-extend Open Source CFD Toolbox. URL: `https://sourceforge.net/projects/foam-extend/`.

[59] R. Guénette and M. Fortin. A new mixed finite element method for computing viscoelastic flows. *Journal of Non-Newtonian Fluid Mechanics*, 60(1):27–52, 1995.

[60] I. Guranov, A. Ćoćić, and M. Lečić. Numerical Studies of Viscoelastic Flow Using the Software OpenFOAM. *PAMM*, 13(1):591–592, 2013.

[61] F. Habla, H. Marschall, O. Hinrichsen, L. Dietsche, H. Jasak, and J. L. Favero. Numerical simulation of viscoelastic two-phase flows using openfoam®. *Chemical engineering science*, 66(22):5487–5496, 2011.

[62] F. Habla, M. W. Tan, J. Haßlberger, and O. Hinrichsen. Numerical simulation of the viscoelastic flow in a three-dimensional lid-driven cavity using the log-conformation reformulation in openfoam®. *Journal of Non-Newtonian Fluid Mechanics*, 212:47–62, 2014.

[63] O. G. Harlen, J. M. Rallison, and M. D. Chilcott. High-Deborah-number flows of dilute polymer solutions. *Journal of Non-Newtonian Fluid Mechanics*, 34(3):319–349, 1990.

[64] O. G. Harlen, J. M. Rallison, and P. Szabo. A split Lagrangian-Eulerian method for simulating transient viscoelastic flows. *Journal of Non-Newtonian Fluid Mechanics*, 60(1):81–104, 1995.

[65] D. G. Hassell, D. Auhl, T. C. B. McLeish, and M. R. Mackley. The effect of viscoelasticity on stress fields within polyethylene melt flow for a cross-slot and contraction–expansion slit geometry. *Rheologica Acta*, 47(7):821–834, 2008.

[66] D. G. Hassell, J. Embery, T. C. B. McLeish, and M. R. Mackley. An experimental evaluation of the formation of an instability in monodisperse and polydisperse polystyrenes. *Journal of Non-Newtonian Fluid Mechanics*, 157(1-2):1–14, 2009.

[67] S. J. Haward, M. S. N. Oliveira, M. A. Alves, and G. H. McKinley. Optimized cross-slot flow geometry for microfluidic extensional rheometry. *Physical Review Letters*, 109(12):128301, 2012.

[68] P. Higuera, J. L. Lara, and I. J. Losada. Realistic wave generation and active wave absorption for Navier–Stokes models: Application to OpenFOAM®. *Coastal Engineering*, 71:102–118, 2013.

[69] L. Holmes, J. L. Favero, and T. Osswald. Numerical simulation of three-dimensional viscoelastic planar contraction flow using the software OpenFOAM. *Computers & Chemical Engineering*, 37:64–73, 2012.

[70] D. M. Hoyle, Q. Huang, D. Auhl, D. Hassell, H. K. Rasmussen, A. L. Skov, O. G. Harlen, O. Hassager, and T. C. B. McLeish. Transient overshoot extensional rheology of long-chain branched polyethylenes: Experimental and numerical comparisons between filament stretching and cross-slot flow. *Journal of Rheology*, 57(1):293–313, 2013.

[71] R. I. Issa. Solution of the implicitly discretised fluid flow equations by operator-splitting. *Journal of Computational Physics*, 62(1):40–65, 1986.

[72] N. G. Jacobsen, D. R. Fuhrman, and J. Fredsøe. A wave generation toolbox for the open-source CFD library: OpenFoam®. *International Journal for Numerical Methods in Fluids*, 70(9):1073–1088, 2012.

[73] D. F. James. Flow in a converging channel at moderate Reynolds numbers. *AIChE journal*, 37(1):59–64, 1991.

[74] D. F. James, G. M. Chandler, and S. J. Armour. A converging channel rheometer for the measurement of extensional viscosity. *Journal of Non-Newtonian Fluid Mechanics*, 35(2-3):421–443, 1990.

[75] H. Jasak, A. Jemcov, Z. Tukovic, et al. OpenFOAM: A C++ library for complex physics simulations. In *International workshop on coupled methods in numerical dynamics*, volume 1000, pages 1–20. IUC Dubrovnik, Croatia, 2007.

[76] Y. Kawaguchi, W. Q. Tao, and H. Ozoe. Checkerboard pressure predictions due to the underrelaxation factor and time step size for a nonstaggered grid with momentum interpolation method. *Numerical Heat Transfer: Part B: Fundamentals*, 41(1):85–94, 2002.

[77] M. Kawahara and N. Takeuchi. Mixed finite element method for analysis of viscoelastic fluid flow. *Computers & Fluids*, 5(1):33–45, 1977.

[78] H. C. Kim, A. Pendse, and J. R. Collier. Polymer melt lubricated elongational flow. *Journal of Rheology*, 38(4):831–845, 1994.

[79] J. M. Kim, C. Kim, J. H. Kim, C. Chung, K. H. Ahn, and S. J. Lee. High-resolution finite element simulation of 4: 1 planar contraction flow of viscoelastic fluid. *Journal of Non-Newtonian Fluid Mechanics*, 129(1):23–37, 2005.

[80] D. A. Kopriva. *Implementing spectral methods for partial differential equations: Algorithms for scientists and engineers*. Springer Science & Business Media, 2009.

[81] C. Kunkelmann and P. Stephan. CFD simulation of boiling flows using the volume-of-fluid method within OpenFOAM. *Numerical Heat Transfer, Part A: Applications*, 56(8):631–646, 2009.

[82] A. Lanzaro, Z. Li, and X. F. Yuan. Quantitative characterization of high molecular weight polymer solutions in microfluidic hyperbolic contraction flow. *Microfluidics and Nanofluidics*, 18(5-6):819–828, 2015.

[83] R. G. Larson, T. Sridhar, L. G. Leal, G. H. McKinley, A. E. Likhtman, and T. C. B. McLeish. Definitions of entanglement spacing and time constants in the tube model. *Journal of Rheology*, 47(3):809–818, 2003.

[84] H. C. Lee. A nonlinear weighted least-squares finite element method for the Oldroyd-B viscoelastic flow. *Applied Mathematics and Computation*, 219(1):421–434, 2012.

[85] A. E. Likhtman and R. S. Graham. Simple constitutive equation for linear polymer melts derived from molecular theory: Rolie–Poly equation. *Journal of Non-Newtonian Fluid Mechanics*, 114(1):1–12, 2003.

[86] A. E. Likhtman and J Ramirez. Rheology of Entangled Polymers: Toolkit for Analysis of Theory and Experiment. URL: `http://www.reptate.com/`.

[87] Q. Liu, J. Ouyang, C. Jiang, X. Zhuang, and W. Li. Finite volume simulations of behavior for polystyrene in a cross-slot flow based on Rolie-Poly model. *Rheologica Acta*, 55(2):137–154, 2016.

[88] Q. S. Liu, Y. Q. Liu, C. T. Jiang, and X. H. Wang. Numerical simulation of viscoelastic flows during injection mold filling based on Rolie–Poly model. *Journal of Non-Newtonian Fluid Mechanics*, 263:140–153, 2019.

[89] T. D. Lord, L. Scelsi, D. G. Hassell, M. R. Mackley, J. Embery, D. Auhl, O. G. Harlen, R. Tenchev, P. K. Jimack, and M. A. Walkley. The matching of 3D Rolie-Poly viscoelastic numerical simulations with experimental polymer melt flow within a slit and a cross-slot geometry. *Journal of Rheology*, 54(2):355–373, 2010.

[90] A. Lyazid, O. Scrivener, and R. Teitgen. Velocity field in an elongational polymer solution flow. In *Rheology*, pages 141–148. Springer, 1980.

[91] G. Marrucci. Dynamics of entanglements: A nonlinear model consistent with the Cox-Merz rule. *Journal of Non-Newtonian Fluid Mechanics*, 62(2-3):279–289, 1996.

[92] I. Martin-Fabiani. What polymer are: A world of plastic spaghetti, October 2015. URL: `http://www.labiotheque.org/2015/10/what-polymers-are-world-of-plastic.html`.

[93] J. C. Maxwell. Iv. on the dynamical theory of gases. *Philosophical transactions of the Royal Society of London*, (157):49–88, 1867.

[94] T. C. B. McLeish and R. G. Larson. Molecular constitutive equations for a class of branched polymers: The pom-pom polymer. *Journal of Rheology*, 42(1):81–110, 1998.

[95] F. A. Morrison et al. *Understanding rheology*. Topics in Chemical Engineering, 2001.

[96] F. Moukalled, A. A. Aziz, and M. Darwish. Performance comparison of the nwf and dc methods for implementing high-resolution schemes in a fully coupled incompressible flow solver. *Applied Mathematics and Computation*, 217(11):5041–5054, 2011.

[97] Y. Mu, G. Zhao, A. Chen, G. Dong, and S. Li. Finite element simulation of three-dimensional viscoelastic planar contraction flow with multi-mode FENE-P constitutive model. *Polymer Bulletin*, 71(12):3131–3150, 2014.

[98] L. Nadau and A. Sequeira. Numerical simulations of shear dependent viscoelastic flows with a combined finite element–finite volume method. *Computers & Mathematics with Applications*, 53(3-4):547–568, 2007.

[99] M. Nyström, H. R. T. Jahromi, M. Stading, and M. F. Webster. Numerical simulations of Boger fluids through different contraction configurations for the development of a measuring system for extensional viscosity. *Rheologica acta*, 51(8):713–727, 2012.

[100] M. Nyström, H. R. T. Jahromi, M. Stading, and M. F. Webster. Hyperbolic contraction measuring systems for extensional flow. *Mechanics of Time-Dependent Materials*, 21(3):455–479, 2017.

[101] M. Nyström, H. T. Jahromi, M. Stading, and M. F. Webster. Extensional Flow through Hyperbolic Contraction Studied Both Numerically and Experimentally. *Annu. Trans. Nordic Rheol.*, 21:15–20, 2013.

[102] T. J. Ober, S. J. Haward, C. J. Pipe, J. Soulages, and G. H. McKinley. Microfluidic extensional rheometry using a hyperbolic contraction geometry. *Rheologica Acta*, 52(6):529–546, 2013.

[103] J. G. Oldroyd. On the formulation of rheological equations of state. *Proceedings of the Royal Society of London. Series A. Mathematical and Physical Sciences*, 200(1063):523–541, 1950.

[104] M. S. N. Oliveira, M. A. Alves, F. T. Pinho, and G. H. McKinley. Viscous flow through microfabricated hyperbolic contractions. *Experiments in fluids*, 43(2-3):437–451, 2007.

[105] J. Ortega and W. Rheinbolt. Numerical Solutions of Non-linear Systems of Equations, 1970.

[106] R. G. Owens and T. N. Phillips. *Computational rheology*, volume 14. World Scientific, 2002.

[107] S. V. Patankar and D. B. Spalding. A calculation procedure for heat, mass and momentum transfer in three-dimensional parabolic flows. In *Numerical Prediction of Flow, Heat Transfer, Turbulence and Combustion*, pages 54–73. Elsevier, 1983.

[108] D. W. Peaceman and H. H. Rachford, Jr. The numerical solution of parabolic and elliptic differential equations. *Journal of the Society for Industrial and Applied Mathematics*, 3(1):28–41, 1955.

[109] M. G. N. Perera and K. Walters. Long range memory effects in flows involving abrupt changes in geometry: Part 2: The expansion/contraction/expansion problem. *Journal of Non-Newtonian Fluid Mechanics*, 2(2):191–204, 1977.

[110] M. G. N. Perera and K. Walters. Long-range memory effects in flows involving abrupt changes in geometry: Part i: flows associated with I-shaped and T-shaped geometries. *Journal of Non-Newtonian Fluid Mechanics*, 2(1):49–81, 1977.

[111] N. Phan-Thien. A nonlinear network viscoelastic model. *Journal of Rheology*, 22(3):259–283, 1978.

[112] T. N. Phillips and A. J. Williams. Viscoelastic flow through a planar contraction using a semi-lagrangian finite volume method. *Journal of Non-Newtonian Fluid Mechanics*, 87(2-3):215–246, 1999.

[113] F. Pimenta and M. A. Alves. Stabilization of an open-source finite-volume solver for viscoelastic fluid flows. *Journal of Non-Newtonian Fluid Mechanics*, 239:85–104, 2017.

[114] R. J. Poole. The deborah and weissenberg numbers. *British Soc. Rheol. Rheol. Bull*, 53:32–39, 2012.

[115] R. J. Poole, M. A. Alves, and P. J. Oliveira. Purely elastic flow asymmetries. *Physical review letters*, 99(16):164503, 2007.

[116] B. Purnode and M. J. Crochet. Flows of polymer solutions through contractions Part 1: flows of polyacrylamide solutions through planar contractions. *Journal of Non-Newtonian Fluid Mechanics*, 65(2-3):269–289, 1996.

[117] L. M. Quinzani, R. C. Armstrong, and R. A. Brown. Birefringence and laser-doppler velocimetry (LDV) studies of viscoelastic flow through a planar contraction. *Journal of Non-Newtonian Fluid Mechanics*, 52(1):1–36, 1994.

[118] L. M. Quinzani, R. C. Armstrong, and R. A. Brown. Use of coupled birefringence and LDV studies of flow through a planar contraction to test constitutive equations for concentrated polymer solutions. *Journal of Rheology*, 39(6):1201–1228, 1995.

[119] D. J. Read, K. Jagannathan, S. K. Sukumaran, and D. Auhl. A full-chain constitutive model for bidisperse blends of linear polymers. *Journal of Rheology*, 56(4):823–873, 2012.

[120] J. Remmelgas, P. Singh, and L. G. Leal. Computational studies of nonlinear elastic dumbbell models of Boger fluids in a cross-slot flow. *Journal of Non-Newtonian Fluid Mechanics*, 88(1-2):31–61, 1999.

[121] C. M. Rhie and W. L. Chow. Numerical study of the turbulent flow past an airfoil with trailing edge separation. *AIAA journal*, 21(11):1525–1532, 1983.

[122] B. Riviere. *Discontinuous Galerkin methods for solving elliptic and parabolic equations: theory and implementation*. SIAM, 2008.

[123] G. N. Rocha, R. J. Poole, M. A. Alves, and P. J. Oliveira. On extensibility effects in the cross-slot flow bifurcation. *Journal of Non-Newtonian Fluid Mechanics*, 156(1-2):58–69, 2009.

[124] J. F. Schoonen, F. H. Swartjes, G. W. Peters, F. P. Baaijens, and H. E. Meijer. A 3D numerical/experimental study on a stagnation flow of a polyisobutylene solution. *Journal of Non-Newtonian Fluid Mechanics*, 79(2-3):529–561, 1998.

[125] O. Scrivener, C. Berner, R. Cressely, R. Hocquart, R. Sellin, and N. S. Vlachos. Dynamical behaviour of drag-reducing polymer solutions. *Journal of Non-Newtonian Fluid Mechanics*, 5:475–495, 1979.

[126] P. Singh and L. G. Leal. Finite element simulation of flow around a $3\pi 2$ corner using the FENE dumbbell model. *Journal of Non-Newtonian Fluid Mechanics*, 58(2-3):279–313, 1995.

[127] M. Stading and L. Bohlin. Measurements of extensional flow properties of semi-solid foods in contraction flow. In *Proceedings of the 2nd International Symposium on Food Rheology and Structure*, volume 2, pages 117–120. Laboratory of Food Process Engineering, ETH: Zurich, 2000.

[128] M. Stading and L. Bohlin. Contraction flow measurements of extensional properties. *Annual Transactions-Nordic Rheology Society*, 8:181–186, 2001.

[129] R. Tenchev, T. Gough, O. G. Harlen, P. K. Jimack, D. H. Klein, and M. A. Walkley. Three dimensional finite element analysis of the flow of polymer melts. *Journal of Non-Newtonian Fluid Mechanics*, 166(5-6):307–320, 2011.

[130] R. Tenchev, O. G. Harlen, P. K. Jimack, and M. A. Walkley. Finite element modelling of two-and three-dimensional viscoelastic polymer flows. *Trends in Engineering Computational Technology, edited by M. Papadrakakis, and BHV Topping (Saxe-Coburg, Edinburgh, UK, 2008)*, pages 81–101, 2008.

[131] N. P. Thien and R. I. Tanner. A new constitutive equation derived from network theory. *Journal of Non-Newtonian Fluid Mechanics*, 2(4):353–365, 1977.

[132] L. H. Thomas. Elliptic problems in linear difference equations over a network. *Watson Sci. Comput. Lab. Rept., Columbia University, New York*, 1, 1949.

[133] M. F. Tomé, N. Mangiavacchi, J. A. Cuminato, A. Castelo, and S. Mckee. A finite difference technique for simulating unsteady viscoelastic free surface flows. *Journal of Non-Newtonian Fluid Mechanics*, 106(2-3):61–106, 2002.

[134] R. Valette, M. R. Mackley, and G. H. F. del Castillo. Matching time dependent pressure driven flows with a Rolie Poly numerical simulation. *Journal of Non-Newtonian Fluid Mechanics*, 136(2-3):118–125, 2006.

[135] J. P. Van Doormaal and G. D. Raithby. Enhancements of the simple method for predicting incompressible fluid flows. *Numerical heat transfer*, 7(2):147–163, 1984.

[136] W. M. H. Verbeeten, G. W. M. Peters, and F. P. T. Baaijens. Differential constitutive equations for polymer melts: the extended Pom–Pom model. *Journal of Rheology*, 45(4):823–843, 2001.

[137] M. A. Walkley, P. H. Gaskell, P. K. Jimack, M. A. Kelmanson, and J. L. Summers. Finite element simulation of three-dimensional free-surface flow problems. *Journal of Scientific Computing*, 24(2):147–162, 2005.

[138] H. G. Weller, G. Tabor, H. Jasak, and C. Fureby. A tensorial approach to computational continuum mechanics using object-oriented techniques. *Computers in physics*, 12(6):620–631, 1998.

[139] K. Wikström and L. Bohlin. Extensional flow studies of wheat flour dough. i. experimental method for measurements in contraction flow geometry and application to flours varying in breadmaking performance. *Journal of Cereal Science*, 29(3):217–226, 1999.

[140] K. Yapici, B. Karasozen, and Y. Uludag. Finite volume simulation of viscoelastic laminar flow in a lid-driven cavity. *Journal of Non-Newtonian Fluid Mechanics*, 164(1-3):51–65, 2009.

[141] J. Y. Yoo and Y. Na. A numerical study of the planar contraction flow of a viscoelastic fluid using the SIMPLER algorithm. *Journal of Non-Newtonian Fluid Mechanics*, 39(1):89–106, 1991.

[142] S. Yoon, M. A. Walkley, and O. G. Harlen. Two particle interactions in a confined viscoelastic fluid under shear. *Journal of Non-Newtonian Fluid Mechanics*, 185:39–48, 2012.

[143] B. Yu, W. Q. Tao, J. J. Wei, Y. Kawaguchi, T. Tagawa, and H. Ozoe. Discussion on momentum interpolation method for collocated grids of incompressible flow. *Numerical Heat Transfer: Part B: Fundamentals*, 42(2):141–166, 2002.

[144] K. Zografos, F. Pimenta, M. A. Alves, and M. S. N. Oliveira. Microfluidic converging/diverging channels optimised for homogeneous extensional deformation. *Biomicrofluidics*, 10(4):043508, 2016.

Appendix A

The algorithm for the numerical schemes

Algorithm 1: Algorithm for the FTCS scheme

Data: The one-dimensional Channel flow problem

Result: The approximate solution using FTCS numerical scheme

Declare the header;

Declare the variable;

Initialization;

Read in the value for the mesh grid, (m) and number of the time step, (nt) ;

Define the initial $u[y, 0]$ and boundary condition $u[-1, t] = u$ and $u[1, t] = u$ for the domain $-1 < y < 1$ and $t > 0$. The domain and the value at the boundary condition u is depends on the problem to be solved;

for *k = 1,2, ..., nt* **do**

  for *j=1,2, ..., m-2* **do**

    $unew[j] = r\nu(uold[j] - 2uold[j] + uold[j]) + uold[j] + dt;$

  end

  $uold[j] = unew[j];$

end

Algorithm 2: Algorithm for the BTCS scheme

Data: The one-dimensional Channel flow problem

Result: The approximate solution using BTCS numerical scheme

Declare the header;

Declare the variable;

Initialization;

Read in the value for the mesh grid, (m) and number of the time step, (nt) ;

Calculate the value of the r, Δt and Δy based on the value of m and nt;

Initialization of the vectors $a, b, c, d, u, \alpha, s, y$ in solving the system of linear equation.;

Define the initial $u[y, 0]$ and boundary condition $u[-1, t] = u$ and $u[1, t] = u$ for the domain $-1 < y < 1$ and $t > 0$. The domain and the value at the boundary condition u is depends on the problem to be solved;

for *k = 1,2, ..., nt* **do**

  for *j=0,1, ..., m-2* **do**

    $d[j] = u[j] + dt$;

    solve the system of linear equation $\mathbf{Au^{k+1}} = \mathbf{d}$ obtained from the BTCS scheme where $\mathbf{A}$ is the tridiadonal matrix obtained from the schemes. The three main vectors needed in solving the tridiagonal matrix are $\mathbf{a} = \{r\}$, $\mathbf{b} = \{1 + 2r\}$ and $\mathbf{c} = \{r\}$.;

  end

  $u[j] = Thomas(a, b, c, d)$;

end

Algorithm 3: Algorithm for the Thomas algorithm

Data: Vectors defined in main body (**a,b,c,d**)

Result: Return the approximate solution $u_{i,j}^{k+1}$

Declare and initialize the vectors α and s ;

Initialization for $\alpha[1] = b[1]$ and $s[1] = d[1]$;

for *j=2,3,..., m-2* **do**

  $\alpha[j] = b[j] - (\frac{a[j]c[j-1]}{\alpha[j-1])}$;

  $s[j] = d[j] + (\frac{a[j]s[j-1]}{\alpha[j-1]})$

end

for *j=m-2, m-3, ..., 1* **do**

  if $i = m - 2$ **then**

    $u[j] = \frac{s[j]}{\alpha[j]}$;

  else

    $u[j] = \frac{s[j]+c[j]u[j+1]}{\alpha[j]}$

  end

  return $u[j]$

end

Algorithm 4: Algorithm for the Crank-Nicolson scheme

Data: The one-dimensional Channel flow problem

Result: The approximate solution using Crank-Nicolson numerical scheme

Declare the header;

Declare the variable;

Initialization;

Read in the value for the mesh grid, (m) and number of the time step, (nt) ;

Calculate the value of the r, Δt and Δy based on the value of m and nt;

Initialization of the vectors $a, b, c, d, u, \alpha, s, x$ in solving the system of linear equation.;

Define the initial $u[y, 0]$ and boundary condition $u[0, t] = u$ and $u[1, t] = u$ for the domain $-1 < y < 1$ and $t > 0$. The domain and the value at the boundary condition u is depends on the problem to be solved;

for *k = 1,2, ..., nt* **do**

  for *j=0,1, ..., m-2* **do**

    $d[j] = r\nu u[j-1] + (2 - 2r\nu)u[j] + r\nu u[j+1] + 2dt$;

    solve the system of linear equation $\mathbf{A}\bar{\mathbf{u}}^{\mathbf{k+1}} = \mathbf{d}$ obtained from the Crank-Nicolson scheme where $\mathbf{A}$ is the tridiadonal matrix obtained from the schemes. The three main vectors needed in solving the tridiagonal matrix are $\mathbf{a} = \{r\nu\}$, $\mathbf{b} = \{2 + 2r\nu\}$ and $\mathbf{c} = \{r\nu\}$.;

  end

  $u[j] = Thomas(a, b, c, d)$;

end

Solve the linear system using Thomas algorithm ;

Algorithm 5: Algorithm for ADI scheme

Data: The 2D channel flow problem

Result: The approximate solution using ADI numerical scheme

Declare the header;

Declare the functions prototype;

Declare the variable which include the array and pointers for 2D;

Initialization;

Read in the value for the mesh grid for x and y, N (same value of mesh grid), Δt and number of time steps (ts);

Calculate the value for r_x, r_y Δx and Δy based on the input data;

Declare and initialize the vectors involved for the two steps in ADI (depending on the read in value for the mesh grid);

Allocate the memory and initialize for 2D array ($unew[i][j]$);

Define the initial and boundary conditions;

for *k = 1,2, ..., nt* **do**

  Calling a function ***Step1*** to calculate the value the value of $\mathbf{u_{i,j}^{k+\frac{1}{2}}}$;

  Calling a function ***Step2*** by passing the value obtain in ***Step1*** to calculate the approximate value at $\mathbf{u_{i,j}^{k+1}}$;

  Update the value $uold[i][j] = unew[i][j]$ (for current time step) in order to obtain the new approximate value for the next time step;

end

Deallocate the memory;

Algorithm 6: Algorithm for ***Step1*** in ADI scheme

Data: vectors defined in main body (**a,b,c,d**), $uold[i][j]$, r_y, N

Result: The approximate solution at $u_{i,j}^{k+\frac{1}{2}}$

Allocate the memory and initialize for 2D array ($uhalf[i][j]$);

for *j = 1,2,...,N-2* **do**

  for *i= 1,2,...,N-2* **do**

    calculate the value for $d[i]$

    $d[i] = \frac{r_y}{2}(uold[i-1][j] + uold[i+1][j]) + (1 - r_y)uold[i][j] + \frac{\Delta t}{2}$;

    Solve the linear system $\mathbf{A}\ \mathbf{u_{i,j}^{k+\frac{1}{2}}} = \mathbf{d}$ obtained from the scheme in Step 1 where $\mathbf{A}$ is tridiagonal matrix with three main vectors are $\mathbf{a} = \{\frac{r_x}{2}\}$, $\mathbf{b} = \{1 + r_x\}$ and $\mathbf{c} = \{\frac{r_x}{2}\}$;

    Calling a function ***Thomas*** (Thomas Algorithm) to calculate the approximate solution at $\mathbf{u_{i,j}^{k+\frac{1}{2}}}$;

  end

end

Algorithm 7: Algorithm for ***Step2*** in ADI scheme

Data: vectors defined in main body (**a1,b1,c1,d1**), $uhalf[i][j]$, r_x, N

Result: The approximate solution at $u_{i,j}^{k+1}$

Allocate the memory and initialize for 2D array ($unew[i][j]$);

for *i = 1,2,...,N-2* **do**

  for *j= 1,2,...,N-2* **do**

    calculate the value for $d1[j]$

    $d1[j] = \frac{r_x}{2}(uhalf[i][j-1] + uhalf[i][j+1]) + (1 - r_x)uhalf[i][j] + \frac{\Delta t}{2}$;

    Solve the linear system $\mathbf{A}\ \mathbf{u_{i,j}^{k+1}} = \mathbf{d1}$ obtained from the scheme in Step 2 where $\mathbf{A}$ is tridiagonal matrix with three main vectors are $\mathbf{a1} = \{\frac{r_y}{2}\}$, $\mathbf{b1} = \{1 + r_y\}$ and $\mathbf{c1} = \{\frac{r_y}{2}\}$;

    Calling a function ***Thomas*** (Thomas Algorithm) to calculate the approximate solution at $\mathbf{u_{i,j}^{k+1}}$;

  end

end

Algorithm 8: Algorithm for one-dimensional finite element scheme.

Data: The one-dimensional Channel flow problem

Result: The approximate solution using finite element

```
Declare the header;
Declare the functions and variables;
Initialization;
Read in the value for the mesh grid, (m) and the number of the time step, (nt) ;
Calculate the value of Δt and Δy based on the value of m and nt ;
for k = 1,2, ..., nt do
    for j=0,1, ..., m-2 do
        Initialization of the vectors involve in the stiffness matrix, mass matrix and
         other relevant vectors involved in the numerical scheme. ;
        Define the initial u[y, 0] = u and boundary condition, u[−1, t] = u and
         u[1, t] = u for the domain −1 < y < 1 and t > 0. ;
        for j=1, ..., m-3 do
            Assemble the inner matrix for stiffness, mass matrix and vector f.
             Vector f is solved using a Simpson's method with appropriate shape
             function N;
        end
        Declaration for the upper boundary condition;
        for j=1, ..., m-2 do
            Calculate the matrix on the left-hand side of the schemes and assign the
             tridiagonal matrix to 3 different vectors. ;
        end
        for j=1, ..., m-2 do
            Calculate the vectors on the right-hand side of the numerical schemes.
        end
        Solve the linear system, Ku = f using Thomas algorithm to get u[j]. ;
    end
    Update the value of u[j].
end
```

Algorithm 9: Algorithm for 2D finite element scheme.

Data: The two-dimensional Channel flow problem

Result: The approximate solution using finite element

Declare the header;
Declare the functions and variables;
Read in the coordinates and connectivity array from the pfile and qfile (the example of the file names);
Initialization;
for *e=0, ..., nels-1* **do**
    Assign the nodes of the domain based on data for connectivity array in pfile;
end
for *e=0, ..., np* **do**
    Assign the coordinate for each of the points (both interior and boundary) from qfile. ;
end
Declare the initial condition.;
for *w=1, ..., finalTime/dt* **do**
    Initialization for the matrix of the interior nodes;
    Declare the boundary condition;
    for *e=0, ..., nels-1* **do**
        Assign the nodes of the element with respective coordinates;
        Assemble the stiffness matrix, $\mathbf{K}_{J,I}^{(e)} = \int_{\Omega_e} \underline{\nabla} N_J^{(e)} \cdot \underline{\nabla} N_I^{(e)} d\underline{x}$;
        Assemble the mass matrix, $\mathbf{M}_{J,I}^{(e)} = \int_{\Omega_e} N_J^{(e)} \cdot N_I^{(e)} d\underline{x}$;
        Assemble the RHS vector, $f(\underline{x}) = \int_{\Omega_e} F(\underline{x}) N_j(\underline{x}) d\underline{x}$;
    end
    Matrix addition of the LHS of the numerical schemes;
    Product of matrix and vector for the LHS of the schemes;
    Do (Crout) LU factorization, $\mathbf{LU}(u) = f$ to obtain the estimated value for u[j];
    Update the value of u[j];
end

Appendix B

The Rolie-Double-Poly.C file

Member functions in Rolie-Double-Poly.C file

```
//***************** Member Functions *****************//

void Foam::constitutiveEqs::Rolie_Double_Poly::correct()

{

volTensorField L = fvc::grad(U());


volTensorField CSS = tauSS_ & L;

volTensorField CLL = tauLL_ & L;

volTensorField CSL = tauSL_ & L;

volTensorField CLS = tauLS_ & L;


volSymmTensorField twoD = twoSymm(L);


StretchS_ = Foam::sqrt(1+tr(tauS_)*lambdaDS_/3/etaPS_);

StretchL_ = Foam::sqrt(1+tr(tauL_)*lambdaDL_/3/etaPL_);

StretchLL_ = Foam::sqrt(1+tr(tauLL_)*lambdaDL_/3/etaPL_);


volScalarField gSigma_S = 2*(1-1/StretchS_);

volScalarField gSigma_L = 2*(1-1/StretchL_);
```

```
volScalarField fSigma_S = gSigma_S*
(1+beta_*Foam::pow(StretchS_,2*delta_));

volScalarField fSigma_L = gSigma_L*
(1+beta_*Foam::pow(StretchL_,2*delta_));

//**** Solving polymeric tensor contribution ****//
//============= Short-Short interaction ============//
fvSymmTensorMatrix tauSS_Eqn
(
fvm::ddt(tauSS_) + fvm::div(phi(), tauSS_)
==
etaPS_/lambdaDS_*twoD + twoSymm(CSS) - fvm::Sp((1+betaThermal_)/
lambdaDS_ +1/lambdaRS_*fSigma_S*extensFuncS_, tauSS_)
- etaPS_/(lambdaDS_*lambdaRS_)*gSigma_S*I_
);
tauSS_Eqn.relax();
tauSS_Eqn.solve();

//============== Long-Long interaction ==============//
fvSymmTensorMatrix tauLL_Eqn
(
fvm::ddt(tauLL_) + fvm::div(phi(), tauLL_)
==
etaPL_/lambdaDL_*twoD + twoSymm(CLL) - fvm::Sp((1+betaThermal_)/
lambdaDL_ +1/lambdaRL_*fSigma_L*extensFuncL_, tauLL_)
- etaPL_/(lambdaDL_*lambdaRL_)*gSigma_L*I_
);
tauLL_Eqn.relax();
tauLL_Eqn.solve();
```

```
//=============== Short-Long interaction ==============//

fvSymmTensorMatrix tauSL_Eqn

(

fvm::ddt(tauSL_) + fvm::div(phi(), tauSL_)

==

etaPS_/lambdaDS_*twoD + twoSymm(CSL) - fvm::Sp(1/lambdaDS_

+gSigma_S/lambdaRS_*extensFuncS_ + betaThermal_/lambdaDL_ +

(beta_*gSigma_L*extensFuncL_*

Foam::pow(StretchS_,2*delta_))/lambdaRL_, tauSL_)

- etaPS_*gSigma_S*extensFuncS_*I_)/

(lambdaDS_*lambdaRS_)

);

tauSL_Eqn.relax();

tauSL_Eqn.solve();


//=============== Long-Short interaction ==============//

fvSymmTensorMatrix tauLS_Eqn

(

fvm::ddt(tauLS_) + fvm::div(phi(), tauLS_)

==

etaPL_/lambdaDL_*twoD + twoSymm(CLS) - fvm::Sp(1/lambdaDL_

+gSigma_L/lambdaRL_*extensFuncL_ + betaThermal_/lambdaDS_ +

(beta_*gSigma_S*extensFuncS_*

Foam::pow(StretchL_,2*delta_))/lambdaRS_, tauLS_)

- etaPL_*gSigma_L*extensFuncL_*I_)/

(lambdaDL_*lambdaRL_)

);
```

```
tauLS_Eqn.relax();

tauLS_Eqn.solve();


//============== Break down stress =============//

tauS_ = volFrac_*tauSS_ +(1-volFrac_)*tauSL_;

tauL_ = (1-volFrac_)*tauLL_ + volFrac_*tauLS_;


//========== Total stress contribution ===========//

tau_ = tauL_ + tauS_;

tau_.correctBoundaryConditions();


totalStress_ = etaS_*twoD + tau_;


//================== Birefringence ==================//

birefringence_ = Foam::sqrt(Foam::pow(totalStress_.

component(symmTensor::XX)-

totalStress_.component(symmTensor::YY),2) +

4*Foam::pow(totalStress_.component(symmTensor::XY),2));

}
```